SEMI-ANALYTICAL SOLUTION TO A FRACTURED WELL IN AN ASYMMETRIC RESERVOIR WITH A FINITE CONDUCTIVITY FAULT

By

Faisal M. Althawad

BSc, MSc.

Submitted for the degree of **Doctor of Philosophy** in

Petroleum Engineering

Heriot-Watt University

Institute of Petroleum Engineering

May 2016

IN THE NAME OF ALLAH, THE MOST GRACIOUS,

THE MOST MERCIFUL.

MASTER OF THE DAY OF JUDGEMENT,

IT IS YOU WE WORSHIP,

AND IT IS YOU WE ASK FOR HELP,

GUIDE US TO THE STRAIGHT WAY.

ABSTRACT

The primary scope of this study is to develop a novel compound semi-analytical solution for the general case of a well intersecting a vertical fracture near a finite conductivity fault in an asymmetric reservoir adjoining the fracture/fault model. A number of field cases have highlighted the existence of such complex flow geometries and the importance of developing appropriate solutions for their accurate modelling and performance predictions. In addition, the existence of intersected fractures is commonly observed over the increasing number of image and production logs (hard data), yet, the amount of these data are very limited relative to the field size. Consequently, dynamic data has become a primary tool for the identification, characterisation and modelling of such geological features, and thus, pressure signatures have become gradually more important. Nevertheless, currently there is no analytical solution to interpret such well test data signature(s), and hence, numerical simulation of the flow in such complex geometries is considered, which is cumbersome and often impractical.

The method of investigation consists of solving the flow domain of five flow units namely; (i) reservoir Region-1; that defines flow from un-faulted side of the fractured well, (ii) a Fractured-well, which allows fluids to flow into and along the fracture towards the well, (iii) reservoir Region-2; that defines flow between the fractured well and the fault, (iv) a nearby Fault, which allows fluids to flow along, across and towards the fractured well, and (vi) reservoir Region-3; that defines flow in the matrix beyond the fault. It should be noted that the author's aim is to have a solution to the pressure versus time and space in general and wellbore pressure with time in particular. Laplace and Fourier transformations were applied to the five equations governing the two-dimensional flow in this domain.

The major divisions of consists of development of semi-analytical solution to the following flow systems: a well intersecting a finite conductivity fracture in a composite reservoir, a well intersecting a finite conductivity fracture near a finite conductivity fault in an asymmetric three-region reservoir and the flux distribution and effective fracture half-length alongside fracture.

The reliability of the proposed solution has been demonstrated in a systematic approach by performing a number of sensitivities of varying model parameters and then using a number of synthetic cases and real field examples. Modelling of the flow behaviour at

earliest times by performing a number of sensitivities of varying model parameters and then validated the stability and the integrity of the solution, respectively. The calculated flux distribution and the effective fracture half-length reasonably matched the corresponding values input into numerical simulations that generated the synthetic well test signatures. The solution also provided acceptable interpretation of the real field data matching reasonably the corresponding numerical well test exercise routinely performed for such complex geometries. It offers more flexible schemes to easily carry out modelling with larger positive impact on hydrocarbon reservoir management and development decisions.

DEDICATION

I, with deepest respect, dedicate this work to my beloved Mother, MUDHAWI ALQERNAS, who continually prayed for me since birth. I always wanted to tell her: MUM “it is over”. My mother passed away on Friday May 9, 2014.

I would also dedicate it to my wonderful wife: Samar, daughters: Lubna and Mudhawi and Sons: Mua’ath, Anas and AbdullRahman.

ACKNOWLEDGMENTS

I would like first to acknowledge my supervisor, Professor Mahmoud Jamiolahmady; I want to express my sincere appreciation to him, for giving me the keys of his knowledge and patience, and for his contribution to this work. He spent his valuable time guiding me throughout my work. I am honoured to work under such supervision and simple words cannot express my gratitude and appreciation to him.

I also like to acknowledge my examiners Professors Patrick Corbett, Ann Muggeridge and Medhat Kamal for spending the time to read through the dissertation and to accept examining me despite their other important obligations. My sincere appreciation and acknowledgment goes to my dear friend Dr. Rahman, Anisur, for his continuous inspiration and valuable technical support throughout the years of my study. The same goes to my friends Dr. Mohammed Ben Issaka and Hasan Nourdeen.

I was also, overwhelmed by the support I received from my management in Saudi Aramco, with special thanks to Khalid Alsubaie, Aus Altaweel, Khalid Zainalabedin, Nabeel Alafaleq, Mohammed Alqahtani, Khalid Alburaik, and Amin Alnasser for giving me the opportunity to pursue my higher degree.

DECLARATION STATEMENT

ACADEMIC REGISTRY
Research Thesis Submission

Name*:*	FAISAL M. ALTHAWAD		
School/PGI:	Institute of Petroleum Engineering of Heriot-watt University		
Version: *(i.e. First, Resubmission, Final)*	Final	Degree Sought (Award **and** Subject area)	(G119-PEE) PhD (Petroleum Engineering)

Declaration

In accordance with the appropriate regulations I hereby submit my thesis and I declare that:

1) the thesis embodies the results of my own work and has been composed by myself
2) where appropriate, I have made acknowledgement of the work of others and have made reference to work carried out in collaboration with other persons
3) the thesis is the correct version of the thesis for submission and is the same version as any electronic versions submitted*.
4) my thesis for the award referred to, deposited in the Heriot-Watt University Library, should be made available for loan or photocopying and be available via the Institutional Repository, subject to such conditions as the Librarian may require
5) I understand that as a student of the University I am required to abide by the Regulations of the University and to conform to its discipline.

* *Please note that it is the responsibility of the candidate to ensure that the correct version of the thesis is submitted.*

Signature of Candidate*:*		Date:	

Submission

Submitted By *(name in capitals):*	FAISAL M. ALTHAWAD
Signature of Individual Submitting:	
Date Submitted:	

For Completion in the Student Service Centre (SSC)

Received in the SSC by *(name in capitals):*			
Method of Submission (Handed in to SSC; posted through internal/external mail):			
E-thesis Submitted (mandatory for final theses)			
Signature:		Date:	

TABLE OF CONTENTS

ABSTRACT *3*

DEDICATION *5*

ACKNOWLEDGMENTS *6*

DECLARATION STATEMENT *7*

TABLE OF CONTENTS *8*

LISTS OF FIGURES *13*

LISTS OF TABLES *18*

LISTS OF SYMBOLS *20*

CHAPTER 1 – INTRODUCTION 22

1.1 BACKGROUND *22*

1.2 PROBLEM STATEMENT *23*

Analytical versus numerical solutions *24*

1.3 FIELD EXAMPLE *25*

Geological and production data *25*

Pressure transient analysis of the field example *27*

1.4 THESIS OUTLINE *28*

2. CHAPTER 2 – LITERATURE REVIEW 30

2.1 OVERVIEW OF PRESSURE TRANSIENT ANALYSIS *30*

2.2 FAULTS, FRACTURES AND FRACTURED RESERVOIRS *31*

2.3 FLUX DISTRIBUTION ALONG FINITE-LENGTH FRACTURES *35*

2.4 FLUX DISTRIBUTION ALONG INFINITE-LENGTH FAULTS *38*

2.5 COMPARISON BETWEEN THREE IMPORTANT PUBLICATIONS IN RELATION TO THIS STUDY *38*

Summary *42*

3. CHAPTER 3 - SEMI-ANALYTICAL SOLUTION TO A WELL INTERSECTING A FINITE CONDUCTIVITY FRACTURE IN AN ASYMMETRIC RESERVOIR 43

3.1 OVERVIEW *43*

3.2 A FINITE CONDUCTIVITY FRACTURE IN AN ASYMMETRIC RESERVOIR *43*

3.2.1 SOLUTION ASSUMPTIONS *44*

3.2.2 DERIVATION OF GOVERNING EQUATIONS *45*

Region-1 ..... *45*

Region-2 ..... *46*

Region-n 46
FINITE CONDUCTIVITY FRACTURE 46
Flow along Fracture 48
Flow into Fracture from Regions 1&2 49
Region-1 49
Region-2 49
3.3 DIMENSIONLESS FORMS 49
Dimensionless parameters 50
Region-1 53
Region-2 53
Region-n 53
3.4 VALIDATION TO CINCO-LEY'S SOLUTION 54
Initial Conditions: 56
Boundary Conditions: 57
TRANSFORMATIONS 57
3.4.1 LAPLACE TRANSFORMATION 57
Region-1 57
Fracture 57
Region-2 57
3.4.2 FOURIER TRANSFORMATION 58
Region-1 58
Fracture 58
Region-2 58
3.4.3 HELMHOLTZ EQUATION 58
Region-1 59
Region-2 60
3.5 SOLVING FOR FRACTURED WELLBORE PRESSURE IN FOURIER DOMAIN 60
Region-1 61
Region-2 61
3.6 FINAL FRACTURED WELLBORE PRESSURE EQUATION 62
3.7 COMPUTER CODING 64
3.7.1 HANDLING DIMENSIONLESS SKIN AND WELLBORE STORAGE (WBS) 64
3.7.2 SOLUTION SCENARIOS 64
3.7.3 SOLUTION PARAMETERS 64

3.8 Overall Solution Behaviour: Observations and Discussions *64*
3.8.1 Sensitivity runs *69*
Summary *71*
4. CHAPTER 4 – SEMI-ANALYTICAL SOLUTION TO A WELL INTERSECTING A FINITE CONDUCTIVITY FRACTURE NEAR A FINITE CONDUCTIVITY FAULT IN AN ASYMMETRIC RESERVOIR 72
4.1 Introduction *72*
4.2 Mathematical narrative *73*
4.3 Mathematical Solution Set-up *74*
4.4 Diffusivity Equations *75*
4.4.1 Solution Assumptions *75*
4.4.2 Fractured-well diffusivity equation between two linear-composite reservoir *76*
4.4.3 Finite Conductivity Fault in an Asymmetric Reservoir *77*
4.4.4 Convert variables to dimensionless form *79*
4.4.5 Assemble the governing equations in space and time *82*
Region-1: *82*
Fracture: *82*
Region-2: *82*
Fault: *82*
Region-3: *82*
Transformations *83*
4.4.6 Laplace Transformation *83*
Region-1 ..... *83*
Fracture *83*
Region-2 ..... *83*
Fault: *83*
Region-3: *83*
4.4.7 Fourier Transformation *83*
Region-1: *84*
Fracture: *84*
Region-2: *84*
Fault: *84*
Region-3: *84*

4.5 Helmholtz Equation Solution *84*
Region-1: *84*
Region-2: *85*
Region-3: *86*
4.6 Solving for the Final Equation *86*
4.6.1 Interface conditions *87*
4.6.2 Differential Equations *87*
Region-2: *87*
Region-3: *87*
Region-2: *88*
Region-1: *89*
4.7 Equation Validation *92*
4.7.1 Final fractured-well pressure equation for asymmetric reservoir *94*
4.7.2 Fractured well pressure equation for symmetric reservoir *95*
4.8 Overall Solution Behaviour: Observations and Discussions *96*
4.8.1 Sensitivity runs *99*
Summary *110*
5. CHAPTER 5 – FLUX DISTRIBUTION AND EFFECTIVE FRACTURE HALF-LENGTH ESTIMATION 111
5.1 Introduction *111*
5.2 Flux Distribution along a Finite Conductivity Fracture *112*
5.2.1 Flux distribution from one side of the fracture on x-y plane *113*
5.2.2 Flux distribution from two sides of the fracture on x-y plane *115*
5.2.3 Flux distribution from two sides of the fracture along y-axis *116*
5.2.4 Fracture Flux Distribution along fracture *117*
5.3 Overall Solution Behaviour: Observations and Discussions *117*
5.3.1 Sensitivity Runs *118*
Summary *131*
6. CHAPTER 6 – SOLUTION COMPETENCY AND VALIDATION USING SYNTHETIC AND FIELD DATA 133
6.1 Solution for Different Reservoir Complexities *133*
6.1.1 Homogenous Reservoir *133*
6.1.2 Three-Region Linear Composite System *133*
6.2 Dimensionless Parameters *133*

6.3 Dimensionless Skin and Wellbore Storage (WBS) *135*
6.4 Solution Parameters *135*
6.5 Validation of Solution via Numerical, Analytical and Field Cases *136*
6.5.1 Analytical Cases *136*
Analytical data from the commercial well-test Software: Analytical Data Set-1 . *136*
6.5.2 Numerical cases *138*
6.5.3 Field Cases *149*
Summary *169*
7. CHAPTER 7 – CONCLUSIONS, OBSERVATIONS AND RECOMMENDATIONS . 170
7.1 Conclusions *170*
7.2 Major Findings *173*
7.3 Business Impact *176*
7.4 Recommendations for Future work *177*
Well skin using the effective radius method *177*
Superposition for varying rates *177*
Fault face-skin deformation *177*
Fault core effect *179*
Non-Darcy flow systems *183*
Main Program *183*
REFERENCES *184*

LISTS OF FIGURES

Figure 1: A schematic representation of an intersected fracture in a reservoir with a fault defining the model to be developed in this thesis. 22

Figure 2: A Formation Analysis Log and a Production Log across a horizontal well in an oil-bearing carbonate reservoir (after Althawad and Jamiolahmady, 2014). 23

Figure 3: The production history of the well over a 10-year period (after Althawad et al., 2001). 24

Figure 4: The vertical seismic line of the field example (after Althawad et al., 2001)..... 26

Figure 5: The Production Logging Tool (PLT) clearly shows nearly 80% of the production is coming from the hydraulic fracture at the top of the reservoir (after Althawad et al., 2001). 26

Figure 6: The derivative plot of the subject well with four flow regimes reflecting the hydraulic fracture (after Althawad et al., 2001). Currently no analytical model exists to explain this response. 27

Figure 7- Stabilised flux distribution along infinite conductivity vertical fracture at various times using a numerical model (after Gringarten et al., 1974)..... 36

Figure 8- Flux Distribution of active and observation fractured wells at high conductivity value (100π) and 90° (after Meehan, 1989). 36

Figure 9- Flux Distribution of active and observation fractured wells at low conductivity value of π and 90° (after Meehan, 1989)..... 37

Figure 10- Flux Distribution along an infinite-length fault plane from left and right hand sides (after Maghsood and Cinco-Ley, 1995)..... 38

Figure 11- Schematic of a fracture model geometry (after Cinco et al., 1978). 39

Figure 12- Schematic of a fault model (after Maghsood and Cinco-Ley, 1995). 39

Figure 13- Schematic of a fault model (after Rahman et al., 2003)..... 40

Figure 14: Schematic of flow distribution for a finite conductivity fracture of a non-uniform flux in a composite reservoir, describes the flow problem of the Frac-model. 44

Figure 15: Schematic of material balance for Region-1, along both x- and y-planes..... 45

Figure 16: Definition sketch of the Frac-model solution. 46

Figure 17: Schematic shows fluid flow along and into fracture as per Cinco-Ley (1981) where fracture is located in a homogenous isotropic reservoir..... 54

Figure 18: Schematic shows fluid flow along and into fracture with a source term. 55

Figure 19: Argument of flow to well and the exponential (e^x) effect on flow direction considered in the solution..... 59

Figure 20: Type-curve by the Frac-model of dimensionless pressure-derivative versus dimensionless time for different dimensionless fracture conductivity..... 65

Figure 21: Type-curve by the Frac-model of dimensionless pressure and pressure-derivative versus dimensionless time for different dimensionless fracture conductivity. 65

Figure 22- Dimensionless time vs. dimensionless pressure derivative exhibiting the Early Fracture Linear Flow regime by the Frac-model. 66

Figure 23 Fracture Linear Flow only in the case of no matrix flow into fracture by the Frac-model. 68

Figure 24- Dimensionless time vs. dimensionless pressure and pressure derivative, by the Frac-model, with Wellbore Storage using Kucuk and Ayestaran's (1985) dimensionless equations.. 68

Figure 25- Dimensionless time vs. dimensionless pressure and pressure derivative curves by the Frac-model. 69

Figure 26- Derivative overlay of a vertical well in a homogenous reservoir and a fractured well in an asymmetric reservoir, by the Frac-model, where both reservoirs have the same average permeability of 10 md. 70

Figure 27: An aerial outcrop image (50 km north of Riyadh), describes the flow problem of the FracFault-model. 72

Figure 28: A 3-D sketch representing the model geometry of the FracFault. 73

Figure 29: Definition sketch of the FracFault-model solution. 75

Figure 30: Schematic of flow distribution for a finite conductivity fault in bounded by an asymmetric reservoir. 77

Figure 31: Flow from the three regions towards the well and its relation to the solution of Helmholtz equation. 85

Figure 32- Dimensionless pressure and pressure derivative vs. dimensionless time. 97

Figure 33- Dimensionless pressure derivative versus dimensionless time by the FracFault-model for a more realistic case. 98

Figure 34- Dimensionless time vs. dimensionless pressure derivative by the FracFault-model exhibiting the Early Fracture Linear Flow regime. 98

Figure 35- Dimensionless time vs. dimensionless pressure for the three sets. 100

Figure 36- A well model in a linear composite reservoir with an increasing mobility. 101

Figure 37- A well model in a linear composite reservoir with a decreasing mobility. 102

Figure 38- A fractured-well model in a linear composite reservoir with increasing mobility.. 103

Figure 39- A fractured-well model in a linear composite reservoir with decreasing mobility. 104

Figure 40- Dimensionless time vs. dimensionless pressure for the three sets. 105

Figure 41- A fractured-well in a reservoir with a finite conductivity fault at different distances from the well. 106

Figure 42- A fractured-well in a reservoir with a finite conductivity fault at different fault conductivities. 107

Figure 43- A fractured well near a fault in a linear composite reservoir with differing mobility at Region-3. 108

Figure 44- The curves reflect a fractured-well in a reservoir with a finite conductivity fault with different fracture and fault conductivities and well-bore storage. 109

Figure 45- A fractured-well in a reservoir with a finite conductivity fault with different fracture and fault conductivities, well-bore storage and skin. 109

Figure 46- A fractured-well numerical model by Ecrin-KAPPA Software, illustrates the pressure drop per unit distance around a finite conductivity fractured-well. 111

Figure 47- Schematic of fracture pressure distribution along the fracture and as a function of fracture conductivity at a constant rate. 112

Figure 48- Schematic of the flux along a finite conductivity fracture. 113

Figure 49- Dimensionless Pressure Derivative versus Dimensionless Time at different fracture conductivities. 118

Figure 50- Matrix “Linear” flux distribution along the fracture on the y-plane. 119

Figure 51- Matrix “Diagonal” flux distribution along the fracture on the x-y plane. 120

Figure 52- Both “Linear” and “Diagonal” Matrix flux distribution along the fracture on the x-y plane. 120

Figure 53- Matrix flux accumulation sensitivity case for differing matrix permeability. 121

Figure 54- Matrix flux accumulation sensitivity case for differing fracture conductivity. 122

Figure 55- Fracture pressure distribution alongside the fracture and fracture half-length estimation at different fracture conductivities and a well-rate of 2π bpd. 123

Figure 56- Fracture flux distribution alongside the fracture and fracture half-length estimation at different fracture conductivities and a well-rate of 2π bpd. 124

Figure 57- Matrix Linear flux distribution alongside the fracture and fracture half-length estimation at different fracture conductivities and a well-rate of 2π bpd. 125

Figure 58- Dimensionless fracture pressure along fracture aperture versus fracture half-length estimation at different matrix permeabilities. 126

Figure 59- Dimensionless linear flux distribution alongside the fracture and fracture plane at different matrix permeabilities. 127

Figure 60- Dimensionless flux distribution alongside the fracture and fracture half-length estimation for a composite reservoir. 128

Figure 61- Dimensionless flux distribution along the fracture aperture for composite reservoir. 128

Figure 62- Matrix flux distribution versus effective fracture half-length at different well rates. 129

Figure 63- Fracture flux distribution versus effective fracture half-length at different well rates. 130

Figure 64: The fractured well is located in the centre between Regions 1 and 2. 134

Figure 65: Region-2 is separating the fractured-well from the fault. 135

Figure 66- Pressure and derivative match of the synthetic data-1 with a type curve of the numerical model available in the used well-test package. 137

Figure 67- Pressure distribution in a circular, 2D, numerical model of a drawdown test from a vertical well using Ecrin-Software by KAPPA Engineering. 140

Figure 68- Pressure and derivative match of the Synthetic data-1 from the FracFault-model with a numerical model from Ecrin-Software package. 141

Figure 69- Pressure and derivative match from the FracFault-model with Synthetic Numerical Data. 143

Figure 70- Dimensionless fracture flux distribution alongside the fracture and fracture half-length estimation using the FracFault-model. 144

Figure 71- Pressure and derivative match using the Frac-model with Synthetic Numerical Model. 144

Figure 72- Schematic of a well located in a reservoir with a finite conductivity fault for synthetic data set-3. 146

Figure 73- Pressure and derivative match of the FracFault-model and the numerical model available in the used well-test package for synthetic data set-3. 146

Figure 74- Numerical model with different grid sizes around and between the fracture and fault. 147

Figure 75- Pressure and derivative match using the FracFault-model to Synthetic Numerical Data. 148

Figure 76- Fracture flux distribution alongside the fracture and fracture half-length estimation. 149

Figure 77- Pressure and derivative match of the field data set-1 with a type curve of the solution proposed by the FracFault-model. 151

Figure 78- Pressure and derivative match of the field data set-1 with a type curve of the Cinco et al. (1978) solution available in the used well-test package. 151

Figure 79 Formation Analysis Log. 152

Figure 80: Horizontal Trajectory of 2050 ft. 153

Figure 81- Flux distribution alongside the fracture and fracture half-length estimation of the given field case using the FracFault-model. 154

Figure 82- Pressure and derivative match of the field case with a type curve of the solution proposed by the FracFault-model. 155

Figure 83- 2D Geometry Plot Pressure Distribution field data set-2 by the used software. 155

Figure 84- Pressure and derivative match of the field case-2 with a type curve of the numerical model from software available in the used well-test package. 156

Figure 85- Pressure and derivative match using the FracFault-model to field data set-3. 157

Figure 86- 2D Geometry Plot Pressure Distribution field data set-3, by the used commercial software. 158

Figure 87- Pressure and derivative match using numerical model with different skin values of (-1.3, 0 and 5), from the used commercial software to field data set-3. 158

Figure 88- Pressure and derivative match using the FracFault-model to field data set-4. 160

Figure 89- 2D-Geometry Plot Pressure Distribution field data set-4 by the used commercial software. 160

Figure 90- Pressure and derivative match using numerical model with different skin values of (-0.7, 0 and 5), from the used commercial software to field data set 4. 161

Figure 91- Pressure and derivative match to field data set-5 using the FracFault-model, with similar fracture and fault conductivity values. 163

Figure 92- Pressure and derivative match to field data set-5 using the FracFault-model with different fracture and fault conductivity values. 163

Figure 93- Pressure and derivative match to field data set-5 using the commercial software. . 164

Figure 94: The derivative plot of the subject well with four flow regimes, reflecting the hydraulic and natural fractures. 165

Figure 95: (PEBI) grids generated around well and along fracture and nearby fault by Saphir-KAPPA-Software. 166

Figure 96: Numerical model match to the pressure data by Saphir-KAPPA-Software. 167

Figure 97- Pressure and derivative match of the field data set-6 with a type curve of the solution proposed by the FracFault-model. 168

Figure 98- Fracture pressure distribution alongside the fracture and fracture half-length estimation. 168

Figure 99: Generalized derivative type-curve for a finite conductivity fault (after Maghsood and Cinco-Ley, 1995) 178

Figure 100: Generalised derivative type-curve for a finite conductivity fault (after Rahman et al., 2003) 178

Figure 101: Schematic of the fault components. 179

Figure 102: Schematic of the damaged zones around the fault (after Evans et al., 1997). 180

Figure 103: A numerically-built model of the damaged zones around the fault core. 180

Figure 104: Derivative plot reflecting effect of different leakage factors (0%, 5% & 100%) on flow profile. 181

Figure 105: Derivative plot reflecting effect of a 1% leakage factor on flow profile. 182

Figure 106: Field example from a braided fluvial reservoir in a North African fluvial reservoir example (after Corbett et al., 2005). 183

LISTS OF TABLES

Table 1: Well and reservoir properties of the field data set-1. 69

Table 2: Well and reservoir properties of the field data set-1. 136

Table 3: Comparison between the results obtained from the FracFault-model and the analytical model available in the used well-test package. 136

Table 4: Reservoir Properties of data set-1. 139

Table 5: Model Dimensions of data set-1. 139

Table 6: Comparison between the results of a numerically based model and the new solution. 141

Table 7: Well and reservoir properties of the field data set-1. 142

Table 8: Comparison between the results of a numerically based model and the new solution. 142

Table 9: Comparison between the results of a numerically-based model and this solution. 143

Table 10: Production data of the field data set-3. 145

Table 11: Well and reservoir properties of field data set-3. 145

Table 12: Comparison; between the results of the numerically based constructed model and the FracFault-model. 145

Table 13: Production data for the field data set-4. 147

Table 14: Well and reservoir properties of field data set-4. 147

Table 15: Comparison between the results of a numerically based model and the new solution. 148

Table 16: Well and reservoir properties of the field data set-1. 150

Table 17: Comparison between the results obtained for the field data set-1 by the solution proposed by the FracFault-model and the Cinco et al. (1978) solution available in the used well test package. 150

Table 18: Production data of the field data set-2. 153

Table 19: Well and reservoir properties of the field data set-2. 153

Table 20: Results obtained for the field data set by the approach proposed by the FracFault-model. 154

Table 21: Production data of the field data set-3. 156

Table 22: Well and reservoir properties of field data set-3. 156

Table 23: Comparison between the results obtained for the field data set-3 by the solution proposed by the FracFault-model and the numerical solution available in the used well test package. 157

Table 24: Production data for the field data set-4. 159

Table 25: Well and reservoir properties of field data set-4. 159

Table 26: Comparison between the results obtained for the field data set-4 by the solution proposed by the FracFault-model and the numerical solution available in the used well test package. 159

Table 27: Production data for the field data set-5. 162

Table 28: Well and reservoir properties of field data set-5. 162

Table 29: Comparison between the results obtained for the field data set-5 by the solution proposed by the FracFault-model and the numerical solution available in the used well test package. 162

Table 30: Production data for the field data set-6. 165

Table 31: Well and reservoir properties of the field data set-6. 165

Table 32: Comparison between the results obtained for the field data set-6 by the solution proposed by the FracFault-model and the numerical solution available in the used well test package. 167

Table 33: Comparison between this study and Cinco et al. (1978), Maghsood and Cinco-Ley, (1995) and Rahman et al. (2003). 172

a = Distance from origin, ft
B = Formation volume factor, RB/STB
C = Wellbore storage, bbls/psi
c_f = Formation compressibility, psi–1
c_t = Total compressibility, psi–1
d_F = Distance to fault, ft
d_f = Distance to fracture, ft
F_{CDf} = Dimensionless fracture conductivity
F_{Cf} = Dimensional fracture conductivity, md-ft
F_{CDF} = Dimensionless fault conductivity
F_{CF} = Dimensional fault conductivity, md-ft
h = Reservoir thickness, ft
k = Matrix permeability, md
k_f = Fracture permeability, md
k_F = Fault permeability, md
k_d = Dimensionless matrix permeability,
k_{df} = Dimensionless fracture permeability, md
$k_f .w_f$ = Fracture conductivity, md-ft
k_r = Reference permeability, md
k_n = (n) reservoir permeability, md
P_i = Initial formation pressure, psi
P_1 = Region-1 pressure, psi
P_2 = Region-2 pressure, psi
P_f = Fracture pressure, psi
P_{wf} = Flowing BHP, psi
P_d = dimensionless pressure
P_{d1} = Dimensionless Region-1 pressure
P_{d2} = Dimensionless Region-2 pressure
P_{df} = Dimensionless fracture pressure
P_{dwf} = Dimensionless fracture pressure
$\overline{p}$ = Pressure in Laplace domain
$\overline{\overline{p}}$ = Pressure in Fourier domain
q = Flow rate at surface, STB/D
r_w = Wellbore radius, ft
r_D = Dimensionless distance from the centre of wellbore, ft
S = Skin factor, dimensionless
s = Laplace parameter
t_D = Dimensionless time
t_{Df} = Fracture dimensionless time
w_f = Fracture width, ft

x_f = Fracture half-length, ft
x_{fe} = Effective fracture half-length, ft
x_d = Dimensionless x-planes
Δx = Finite Difference
q_x = Rate at (x) interface
$q_{\Delta x}$ = Accumulation over (Δx)
$q_{x+\Delta x}$ = Rate at ($x+\Delta x$) interface
$q_{d\,y}$ = Matrix flux on y-plane
$q_{d\,xy}$ = Matrix flux on x-y plane
Δp = Pressure change since start of transient test, psi
$p_{d\,f}$ = Dimensionless pressure
Δt = Time elapsed since start of test, hours
η = 0.0002637 k/$\phi\mu$ct, hydraulic diffusivity, ft^2/hr
η_{Df} = Fracture hydraulic diffusivity, dimensionless
η_D = Matrix hydraulic diffusivity, dimensionless
μ = Viscosity, cp
ϕ = Porosity, fraction
ρ = Fourier parameter

Subscripts

C =*Conductivity*
D =*Dimensionless*
ex =*External model or data*
i =*Iterations*
F =*Fault*
f =*Fracture*
n =*Number of parameters*
w =*Wellbore*

CHAPTER 1 – INTRODUCTION

1.1 Background

In current oil production operation ventures, it is becoming increasingly likely to encounter man-made fractures designed to create more surface area to the wellbore as well as natural fractures. In other words; more reservoir area, is in direct communication with the wellbore, hence a greater volume of fluid can be produced per unit time. While, in tight formations, fractures can enhance the recovery of hydrocarbons, in permeable formations, the highly permeable conduits they form could lead to a premature breakthrough of water or gas. Faulting may result in symmetric or also asymmetric reservoirs, i.e. different quality reservoirs across the fault plane, due to the displacement of reservoir blocks along the fault plane. A new flow scenario of a combined intersected fracture at early times and a conductive fault at late times has been observed repeatedly when pressure pulses propagate into the reservoir in many carbonate reservoirs. Figure 1 explains the definition sketch for the model to be developed in this thesis. The presence of such complex geology is also widely recognized through the growing number of image and production logs. The identification, characterisation and modelling of such signatures, have therefore, become important.

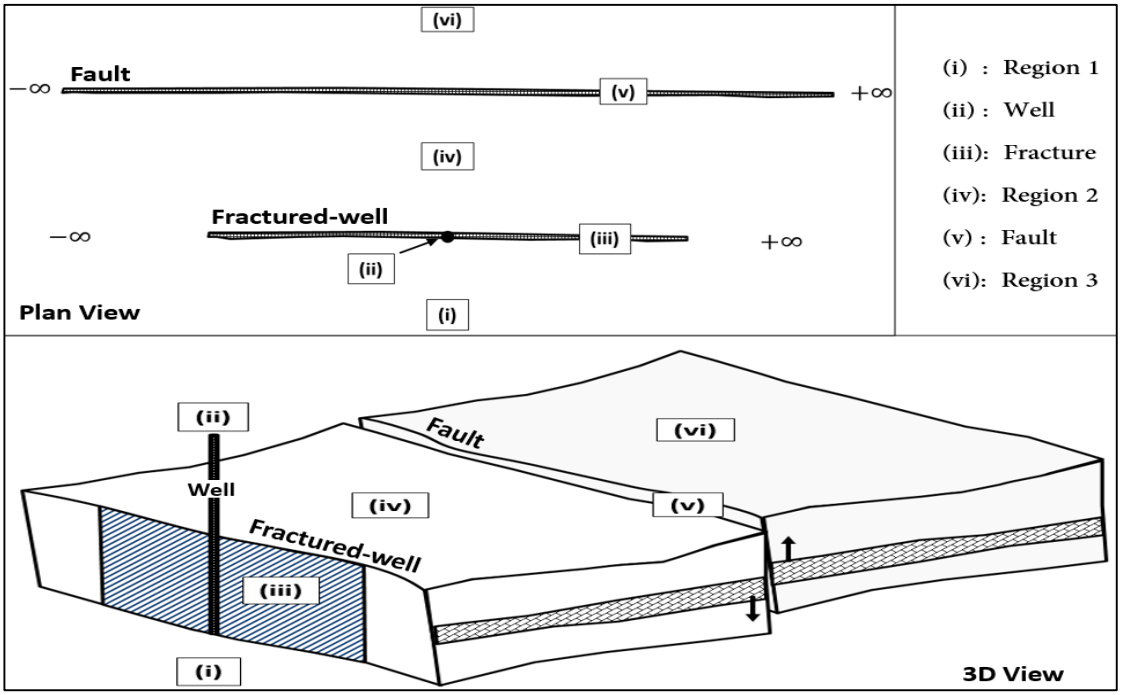

Figure 1: A schematic representation of an intersected fracture in a reservoir with a fault defining the model to be developed in this thesis.

1.2 Problem Statement

The main objective of this work is to introduce a set of practical mathematical solutions for a fractured-well in an asymmetric reservoir with a fault nearby. Many production logs have shown two different fault-blocks resulting from a reverse fault that offset two zones. Figure 2, illustrates a good example of a log across a horizontal well, showing two different zones (fault-blocks) resulting from a fault that offset two carbonate zones. This sequence juxtaposes different geologies across the intersected fault plane, whereby two different quality zones are aligned through the fracture plane.

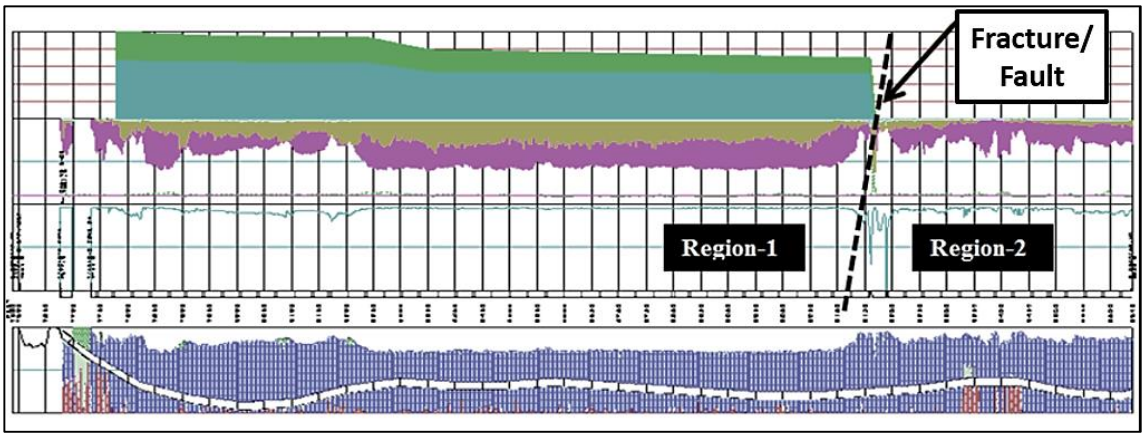

Figure 2: A Formation Analysis Log and a Production Log across a horizontal well in an oil-bearing carbonate reservoir (after Althawad and Jamiolahmady, 2014).

Faulting will result in a sudden displacement of rock along fault planes and yields a complex deformation that is associated with the fault plane and, possibly, a large-scale slippage, and thus, different quality fault blocks on both sides of the faulting. The case of symmetric reservoirs across faulting, which is most likely in the case of small fractures or strike-slip faults, has been discussed in the literature (Gringarten et al., 1974; Cinco et al., 1978). However, in the case of reverse or normal faulting with large throw (juxtaposing) different quality reservoirs will be juxtaposed across the fault plane, as in the case considered for the present study.

Evidence of possible fractures/faults in reservoir models also come from the production history, where the well has experienced a premature water breakthrough. In Figure 3, the production history since 1988 clearly shows that the water-cut follows the total production rate. This could be an indication of vertical water movement through high quality corridors (e.g. fractures/faults).

For the purposes of this well testing study, to simplify the terminology, the fracture and fault, Figure 1, are defined as follows:

A fracture : Is any fracture or fault intersecting the well,

A fault : Is any fracture or fault not intersecting the well.

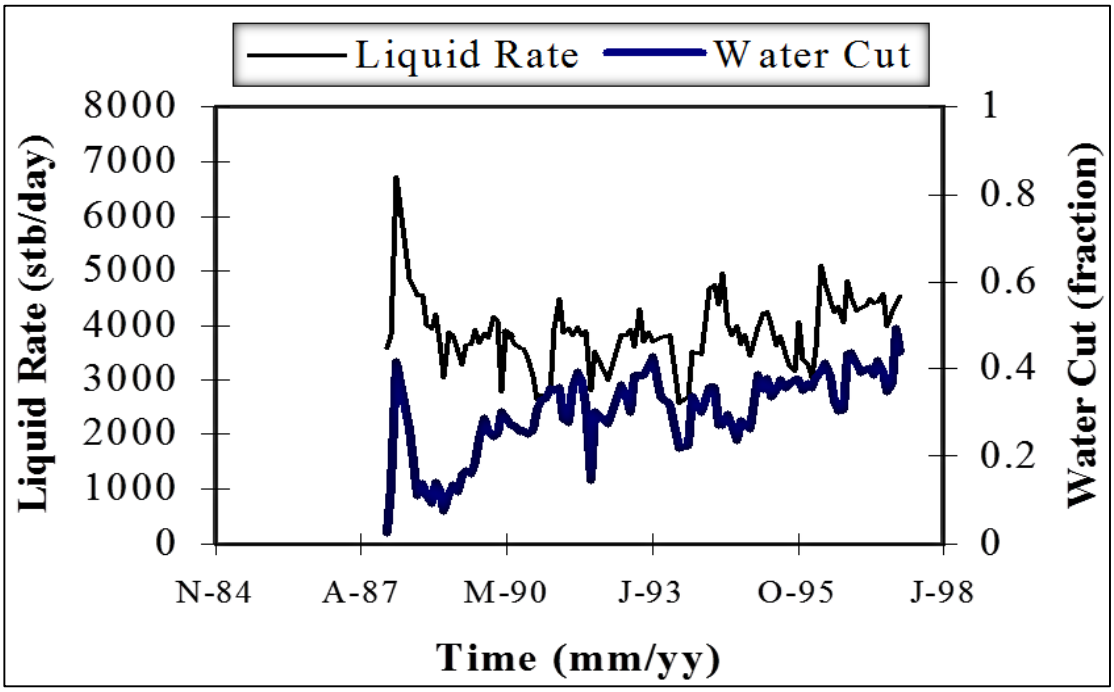

Figure 3: The production history of the well over a 10-year period (after Althawad et al., 2001).

It is worth mentioning that many carbonate reservoir blocks across fractures/faults are asymmetric, hence, resulting in great restrictions to the application of the traditional analytical well testing solutions, which are generally symmetric. Geologically, it is more likely that a fault will have different properties across it than a fracture.

Cinco et al. (1978) presented an analytical solution for the analysis of the transient pressure data in fractured wells of symmetric reservoirs. However, in the case of reverse or normal faulting with large throw, different quality reservoirs juxtapose across the fracture plane. In addition, with the growing use of Permanent Downhole Gauges (PDG) that record long term pressure data, it is becoming more likely to encounter far away multiple faults.

Analytical versus numerical solutions

Currently, there is no analytical solution to interpret the well test data signature from such a complex model, and therefore, numerical simulation of the flow in such complex

geometries is performed. Numerical models are recognized for their flexibility and ability to encompass complex geology and well geometries (e.g. multiple wells, fractures) efficiently. These are, hence, suitable for specific cases and are being increasingly used and likely to become even more widely utilised (Corbett et al., 2012; Aljuboori et al., 2015).

Nevertheless, it is worth mentioning that such numerical simulations are known for their limitations with regard to adequately representing major geological events and pronounced flow regimes. They are largely affected by grid sizes and geometries, especially when analysing wells with complex geological settings (Jackson et al., 2015). Without careful grid design, the expected flow regime might not be captured. Thus, the grids must be structured to follow the fluid flow, e.g. fracture linear flow followed by matrix radial flow, must be designed to have enough linear segments and be bounded by radial grids (Houzé et al., 2007), hence, subject to user knowledge.

On the other hand, modelling with analytical solutions is better for general cases. In addition, the evidence of fractures and faults from seismic, production, and pressure transient data and an increasing number of similar cases has strongly suggested developing more easy-to-use analytical/semi-analytical solutions to validate the special cases of numerical models and yield more accurate results. It is believed that the long-term benefits of these solutions will have a great business impact in the near future. Here a set of semi-analytical solutions for such scenarios are presented. To illustrate the statement problem in more depth, a field example is presented in the next section.

1.3 Field Example

Althawad et al. (2001) presented a field example that discusses a cased-hole vertical well penetrating a formation that consists of multiple oil-bearing reservoirs. The well is perforated in the lower two main structures, separated by a non-reservoir structure of nearly 400 ft. in thickness, and had been in production since 1948. The rate was 4660 bpd, with 20% water cut.

Geological and production data

Fracture/fault reservoir behaviour has been observed in tens of repeated pressure data tests. The vertical seismic line data shows major faults quite close to the well. The most

likely location of faulting is at the crest of the carbonate structure, where fracturing intensity seems to be the highest, Figure 4.

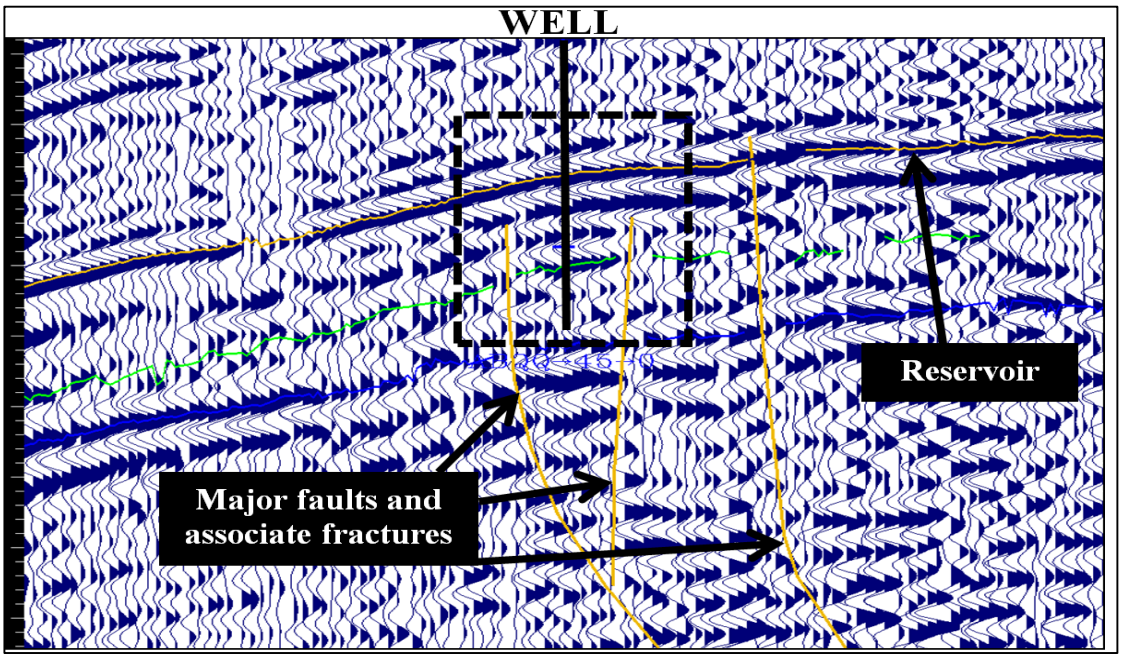

Figure 4: The vertical seismic line of the field example (after Althawad et al., 2001).

The well was hydraulically fractured with an acid matrix job, resulting in a low- finite conductivity fracture with a small fracture skin. The Production Logging Tool (PLT) clearly assessed the acid treatment and showed nearly 80% of the production was coming from the hydraulic fracture at the top of the reservoir, Figure 5.

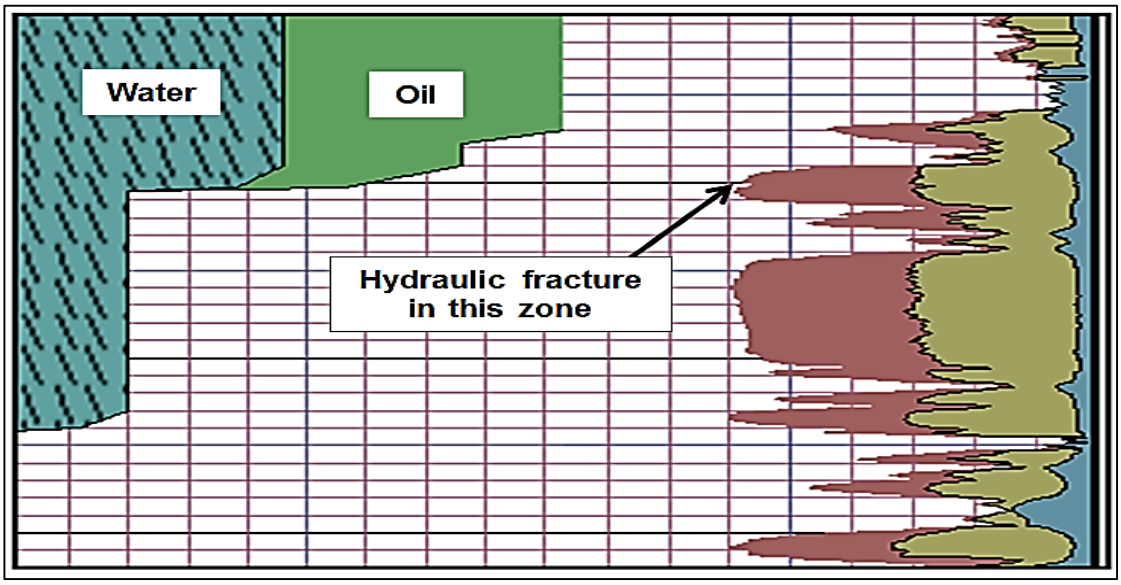

Figure 5: The Production Logging Tool (PLT) clearly shows nearly 80% of the production is coming from the hydraulic fracture at the top of the reservoir (after Althawad et al., 2001).

Pressure transient analysis of the field example

A post-acid well test job was conducted to further investigate and characterise the hydraulic and natural fractures and faults nearby. In a relatively tight, oil-bearing carbonate reservoir (1-3 md), an extended drawdown/build-up is required to evaluate and characterise the well and geology nearby. A 348-hour build-up (14-day) was carried out, with results shown in Figure 6. It is noted that after the wellbore storage and transition period, the derivative plot suggests three major responses: (1) finite conductivity fracture at early times, (2) positive fault skin (geoskin/geochoke) and (3) finite conductivity fault at late times. The first response shows the characteristics of a fracture (a quarter slope on both the pressure and derivative curves with a factor of four separating them) as a result of the acid job. The second indicates an upward increase in the derivative curve, just before the fault, reflecting a low permeability finite conductivity fault response close to the well. A negative unit slope is then clearly observed for about 30 hours, followed by a bilinear flow period lasting for the rest of the build-up period.

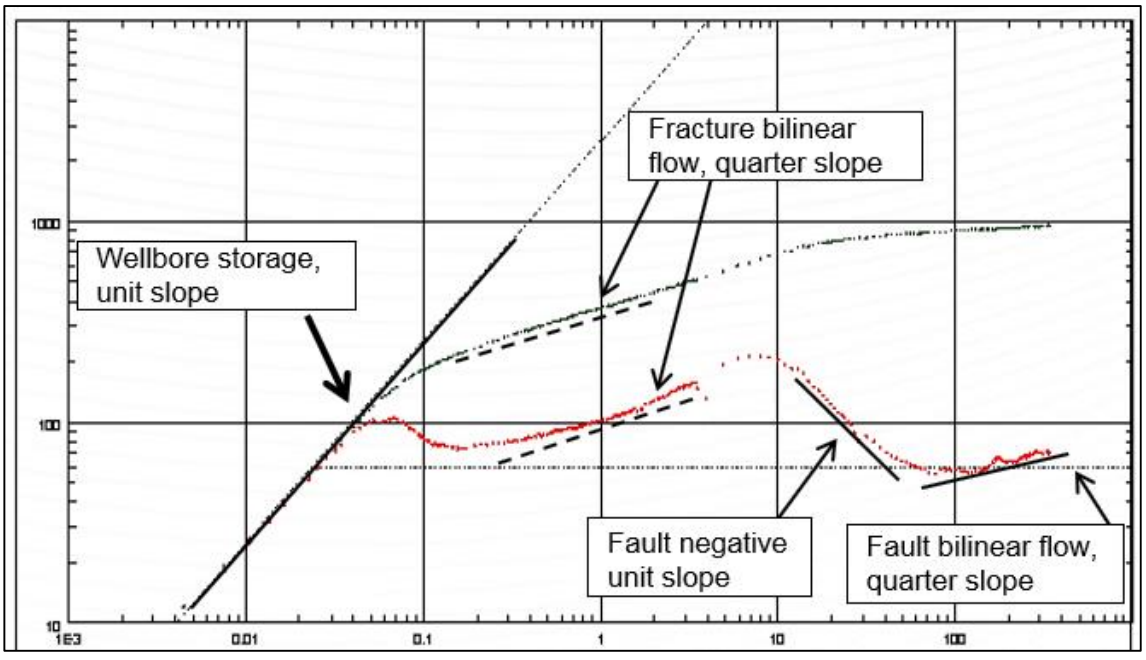

Figure 6: The derivative plot of the subject well with four flow regimes reflecting the hydraulic fracture (after Althawad et al., 2001). Currently no analytical model exists to explain this response.

A full analysis of this field case is presented in Chapter 6, using a numerically-based commercial software and the semi-analytical solution proposed by this study.

1.4 Thesis Outline

The present study introduces a semi-analytical approach and develops the flow solution for a well intersecting a finite conductivity vertical fracture near a finite conductivity fault in a three-region asymmetric reservoir. It should be noted that the author aims to obtain a solution for the pressure versus time and space in general and wellbore pressure versus time in particular.

Chapter 1 highlighted the presence and importance of such reservoirs, which are widely characterised by image and production logs, in addition to the increasing amount of horizontal and multilateral well drilling. Problem statement is discussed followed by a comparison between numerical and analytical approaches. The objectives of this study have been further clarified by presenting the corresponding field cases using geological to production data and production logs.

Chapter 2 includes a detailed literature review with special emphasis on the fractures, fractured reservoirs, and a brief discussion of fracture properties affecting reservoir performance. It also includes a comparison of the three most important publications in relation to this work. It highlighted the need for this solution, as it was not addressed in previous work.

Chapter 3 discusses the development of a semi-analytical solution to a fractured well with a finite conductivity fracture separating **two regions** of different mobilities and accounting, for the first time, for flow in the reservoir in the **x-y plane**. It should be noted that the assumed finite conductivity fracture is of infinite length and dictates a non-uniform inflow-flux distribution along the fracture.

Chapter 4 provides an added level of complexity to the solution, by solving for a fractured-well near finite conductivity fault in **a three-region** linear composite reservoir. In other words, the reservoir is assumed to be asymmetric, complementing the efforts carried over from Chapter 3. The three regions have their own specific permeabilities, separated by the fractured-well (between Regions 1 and 2) and the fault (between Regions 2 and 3). The solution also accounts for matrix flow in the x-y plane in all the three regions. The corresponding type-curve solution of dimensionless time versus dimensionless pressure and its log-derivative for different dimensionless fracture and fault conductivities are presented and discussed.

Chapter 5 introduces an approach to estimate the fracture and the matrix flux distributions in and alongside the fracture plane. It presents a new method to estimate the fracture **effective half-length** (x_{fe}), by deploying the flux term and solving it along the fracture length ($x - axis$) of an infinite length fracture. It also includes the effect of different parameters on the effective fracture half-length (x_{fe}) and flux distribution. There is also a validation exercise studying different synthetic, numerical and field cases with different complexities.

Chapter 6 first verifies the reliability of the proposed solutions, demonstrated in a systematic approach, using many analytically and numerically built synthetic cases. The confirmation of the validity of the proposed solution is then established further through analysing a number of field cases.

Chapter 7 is devoted to the main conclusions of this study, discussion of the business impact of such the proposed solutions and recommendations for future work in this area. It highlights the main outcomes and its differences with other similar studies and also discusses this study's limitations and the way forward to tackle some of them in future studies.

Appendices should the reader wishes to explore further details of the provided solutions.

CHAPTER 2 – LITERATURE REVIEW

This chapter summarises the key technical work that has been published as part of the efforts to provide solutions to assist in characterising reservoirs, in general, and diagnose geological features, with a focus on those related to this work in particular.

2.1 Overview of Pressure Transient Analysis

Pressure Transient Analysis evolved nearly 80 years after the introduction of Darcy's law, to study the hydraulic conductivity of the ground water in porous material (Darcy, 1856; Jacob and Cooper Jr., 1946; Jacob., 1940; Wenzel and Fishel, 1942; Cooper and Jacob, 1946). It became a recognized tool for well and reservoir characterisation and has been widely used since the invention of the "Semi-Log Plot", which was first introduced by Theis (1935) to assess transmissibility and storage coefficients for ground water flow problems (Cooper and Jacob, 1946; Stewart and Gupta, 1984). Later, the (Horner, 1951) plot was presented and widely accepted as a method for analysing pressure build-up data. Rock permeability and well skin are calculated from the straight line segment of the semi-log plots (Matthews and Russell, 1967; Lee, 1982; Landa et al., 1996). Type-Curve analysis has been used in the field of hydrology since 1930 (McKinley, 1971 and Ramey Jr., 1976). Another widely used aid to pressure-transient analysis is the plot of logarithmic pressure change vs. logarithmic elapsed (shut-in) time (Earlougher, 1977).

In the early 1980s, Bourdet et al. (1983) presented the "derivative", a diagnostic plot that led to a paradigm-shift in type-curve matching and made it more unique. The use of the derivative of pressure versus time is mathematically satisfying because the derivative is directly represented in one term of the diffusivity equation, which is the governing equation for the models of transient-pressure behaviour used in well-test analysis. The generated plot, which analytically generates reservoir response patterns for specified reservoir models, can also be matched to type curves (Pirard and Bocock, 1986; Gringarten, 1987; Bourdet et al., 1989; Bourdet, 2002). Moreover, trends, of pressure-transient data, can be obtained for a large variety of well and reservoir systems. However, when the semi-log pressure derivative is applied to other flow geometries, such as linear or spherical ones, the responses are not horizontal, making identification

of these flow regimes more difficult (Issaka and Ambastha, 1999). A polynomial pressure derivative was also introduced by Jelmert (1993) to simplify the identification of such flow regimes for homogenous reservoirs. The key advantage of type-curve analysis is its ability to match the entire pressure data, whereas the semi-log analysis uses only a portion of the data to obtain the information (Kamal, 2008). Suri et al. (2014) also used derivative and second derivative of transient pressure data to characterise the onshore Cambay basin and Bombay offshore basin off the western coast of India.

No doubt that there are many events affecting fracture characteristics and thus reservoir performance. The formation of fractures and their respective properties are contingent on many factors, such as the fracture's origin (i.e. tectonic activities) and digenesis processes, fluids occupying the pore spaces and reacting with the rock matrix. Lorenz et al. (1996) suggested that the nature of a fracture is determined by several factors, the orientation and magnitudes of the stresses, the number of stress events, the thickness of bedding, and the rock properties hosting the fracture. The fracture spacing is commonly equal to bed thickness, as a rule of thumb. The permeability is dominated by the larger fractures, which are less frequent and may form in different lithology and range from very poorly consolidated sediment to relatively ductile shales and coals, to carbonates and to brittle, well-cemented sandstones. Nelson (2001) points out that the characteristics of these fractures is a function of their mode of origin, the mechanical properties of the host rock, and subsurface diagenesis; therefore, the combined effect of these factors dictates the quality of these fractures. He highlighted that the fractures effect on fluid flow becomes important only when they occur in sufficient spacing or length.

2.2 Faults, Fractures and Fractured Reservoirs

McGuire and Sikora (1960) used an electric analyser prepared by Bruce (1943) in their study to assess well productivity from vertical fractures at different conductivities. They used a square drainage system of a fractured well with a range of fracture half-lengths. The results were very interesting and enlightening, where they showed that beyond certain fracture conductivity, the productivity stabilises and is independent of the fracture half-length. In other words, the focus should be on increasing the fracture

conductivity, but interestingly, not exceeding a fracture conductivity of $(F_{Cf} = 1e4)$. A portion of the data was also published by Dyes et al. (1958).

Warren and Root (1963), developed an idealized model, a naturally fractured reservoir, to investigate the behaviour of a medium that contains primary and secondary porosities in fractured reservoirs. The first porosity describes the matrix porosity that only contributes to the pore volume and its contribution to the flow capacity is negligible. The second porosity describes the fracture/fissure porosity and contributes fully to the flow capacity. Their study suggested that two parameters describe/control the flow regimes in the "double porosity model", namely: Omega (ω) which is a measure of the fluid storativity of the secondary porosity, fractures/fissures, and Lambda (λ) a measure of the inter-porosity mobility between the matrix and the fractures/fissures. The behaviour of the naturally fractured reservoirs is a function of the fracture's aperture, intensity, shape and the fluid transfer to/from the matrix (Kamal, 2008).

Ramey Jr (1976) and Raghavan (1977) reviewed the work done on flow along and towards fractures and highlighted that intersecting fractures strongly affect transient flow behaviour of the well.

Cinco et al. (1978) introduced a new technique for describing pressure transient behaviour for wells intersecting finite conductivity vertical fractures. Their study resulted in a bi-linear flow due to the transient linear flows perpendicular to each other along fracture and formation. This is the first published work that accounts for transience along the fracture and is considered to be a pivotal work in the subsequent studies later including this work. That is, it is one of the works that presents a special case of the more complex system considered in this study.

Stewart and Gupta (1984) demonstrated a fault as a leaky barrier that was of numerically insignificant volume. They studied the effect of a partially sealing fault between an active well and observation wells using a two-dimensional single phase simulator that produced a set of log-log type-curves of dimensionless pressure and time for various values of fault transmissibility.

Yaxley (1987) presented analytical solutions for partially communicating faults. The solutions maybe used to improve the design and analysis of interference tests between

wells separated by partially communicating faults. The type curves generated the solution that should yield separate estimates of the formation transmissibility and fault transmissibility. Basically, Yaxely generalized the approach presented by Bixel et al. (1963) for reservoirs with a semi-impermeable linear discontinuity.

Houze et al. (1988) studied a combined model of a well intersecting an infinite conductivity fracture in a naturally fractured reservoir using a double-porosity model. Their study also provided pressure derivative plots along with a method of analysis.

Ambastha et al. (1989) modelled a linear fault as an infinitesimal-thickness skin boundary. Analytical solutions for pressure-transient behaviour for a composite reservoir were obtained and presented for strip and infinite reservoirs. Their conclusion was that the pressure response departs from the line-source solution, demonstrating a double-slope radial flow regime, and then reverts back to a semi-log linear pressure response parallel to the line-source solution at late times. It is important to note that the models prepared by Stewart and Gupta (1984), Yaxley (1987) and Ambastha et al. (1989) allow for fluid transfer across the fault plane only, but they do not account for fluid flow along the fault plane.

In the mid-nineties, Maghsood and Cinco-Ley (1995) presented an analytical solution for a non-intersected finite conductivity fault or fracture. Their solution defined the pressure distribution in a reservoir caused by drawdown of an active well near a non-intersecting fault. They accounted for fault conductivity within the fault and surrounded by a transverse fault skin. In their solution, the reservoir flow is considered on both sides of the fault, left and right, and the net flux in/out of the fault is zero. The fault plane has a thickness (w_f) and a permeability (k_f) and is located at a distance of (d_f) from the active well that produces at a constant rate. A region of altered permeability referred to as a fault skin, (s_f), is on both side of the fault. This altered region is to reflect the geological change on the sides of the fault plane due to possible juxtaposition with another formation with different properties. This work presents another special case of the more complex system considered in here.

Evans et al. (1997) points out that although well-developed damaged zones around the fault core may lead to enhanced fluid flow through a relatively thin tabular region parallel to the fault plane, the fault core still restricts fluid flow across the fault. Fault

zones could also act as conduits, barriers, or both at the same time, leading to distinctive flow regimes (Smith et al., 1990; Antonellini and Aydin, 1994; Caine et al., 1996). Once the fault is formed, its structure and ability to conduct fluids may vary over time and space (Allan, 1989; Bouvier et al, 1989; Pittman, 1981; Smith et al., 1990; Knipe, 1992; Harding and Tuminas, 1988; Bouvier et al., 1989). Some faults are conductive during their early times (Gibson, 1994; Schlische, 1995) and may vary to be non-conductive, sealing later in time.

Althawad et al. (2000) presented an integrated method for horizontal well placement in faulted reservoirs using Maghsood and Cinco-Ley's (1995) approach in characterising conductive faults nearby. Many horizontal wells were placed parallel to the conductive faults to avoid intersecting them and hence, premature water breakthrough. The solution was used in an integrated workflow along with the seismic data, in order to precisely locate the faults and geo-steer horizontal sections parallel to them.

A solution was also proposed by Boussila et al. (2003) for a well near a linear leaky fault in a double-porosity system (fractured reservoir). The fault is modelled as a small damaged baffle. They also presented pressure-derivative type-curves and validated the solution with field data. However, the models of both Maghsood and Cinco-Ley (1995) and Boussila et al. (2003) neglected the fault conductance to fluids along them.

Rahman et al. (2003) presented an important analytical solution for a well located near a finite-conductivity fault in a two-zone, composite reservoir. Their solution is distinctive, as it accounts for the transient flow along the fault plane. It exhibited a negative unit slope once the transient flow reaches the fault, reflecting a pressure support source for a considerable amount of time, followed by a quarter slope and a radial flow period reflecting the reservoir behind the fault. This is the third valuable contribution that presents a special case of the more complex system considered in this study.

Corbett et al. (2005) discussed "Geochoke" and their similarity to the damaged zones around a fault core. They stated that peaks of high permeability in braided fluvial systems could be misinterpreted as a fault response. They also noted that the "Geochoke" response could occur due to the limited restriction of flow that represents depletion of the high permeability zones and the delay in recharging from other patches away from the well. They demonstrated a pronounced humped middle time region in a

well test build-up from a field example. The work by Sagawa et al. (2000) had produced semi-analytical model for negative geoskin.

Mahdiyar et al. (2011) discussed how the "inertial effect" can significantly reduce the effective fracture conductivity, and they extended the application of previously developed formulae to non-Darcy flow systems by replacing absolute fracture conductivity with the effective fracture conductivity (Guppy et al., 1982a; Huang and Ayoub, 2007; Meyer and Jacot, 2005; Settari et al., 2002; Smith et al., 2004).

Althawad and Jamiolahmady (2014) also presented, as a result of the present study, a semi-analytical solution for a well intersecting a finite conductivity vertical fracture in an asymmetric reservoir. The solution is characterised by the distinctive feature of a fracture-linear at a very early time, reflecting the first fluid linear flow along the fracture and towards the well. This is followed by a bilinear flow, a quarter slope, demonstrating the fracture characteristics, followed by a radial flow, zero slope, articulating the quality of the two reservoirs (see also Chapter 3).

2.3 Flux Distribution along Finite-length Fractures

Calculating the flux alongside the fracture plane defines the nature of the flux distribution, fracture's conductivity and assist in estimating the fracture's effective half-length. Several scholars have introduced calculation methods for the flux distribution for a finite length fracture; however, in this study, the fracture is assumed to be of infinite length, hence, the calculated flux distribution (detailed in chapter 5) will be used to assess the fracture half-length and confirms its conductivity nature.

Gringarten et al. (1974) showed that the flux distribution for a vertical infinite conductivity fracture varies with time, initially, and then reaches stabilisation, steady state, at late time, where fluids are entering the fracture at a stabilised manner. Figure 7 (after Gringarten et al., 1974) presents the flux distribution resulting from a numerical simulation at various times, with an increase in flux around the fracture tip. If the fracture length is assumed to be infinite, as is the case in the present study, the flux will not be increasing but rather decreasing with length.

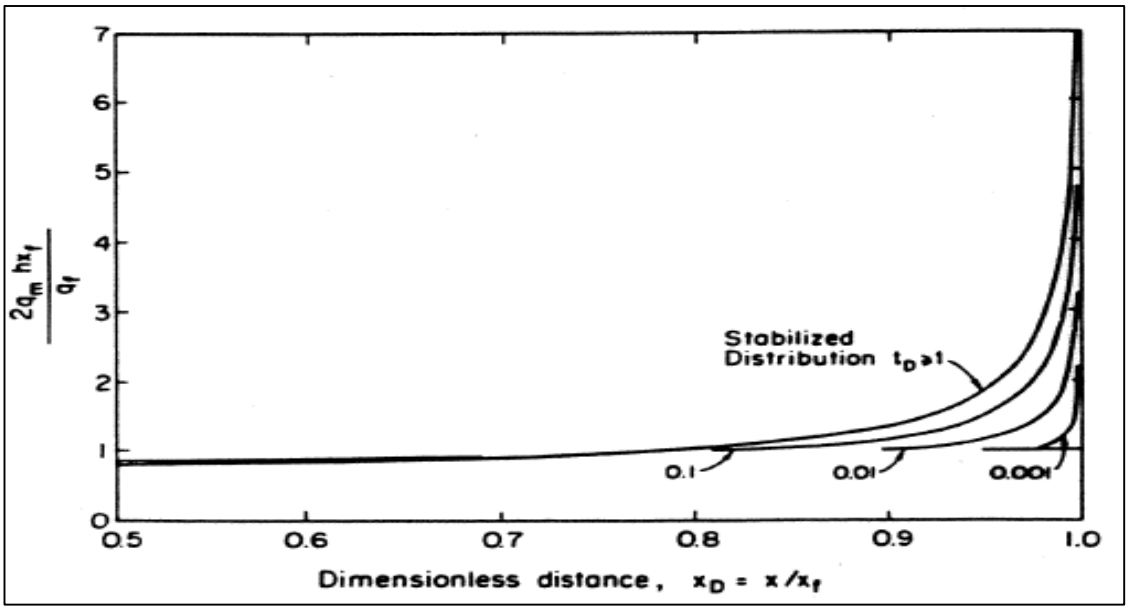

Figure 7- Stabilised flux distribution along infinite conductivity vertical fracture at various times using a numerical model (after Gringarten et al., 1974).

Meehan (1989), when studying the interference effect in fractured wells, calculated fluxes at the active fractured-well and observation well with varying azimuths ranging from 15° to 90° and a range of fracture conductivities. Their study illustrated early and late time fluxes for a high fracture conductivity case, $F_{CD}= 100\pi$, infinite conductivity, and verified that the flux is uniformly distributed along the fracture plane, Figure 8.

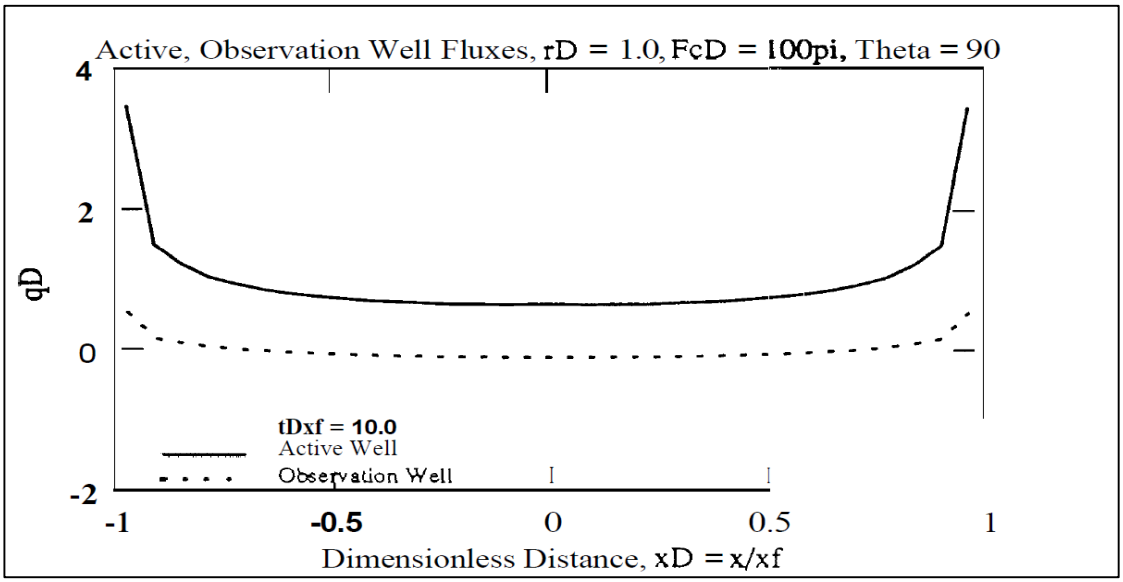

Figure 8- Flux Distribution of active and observation fractured wells at high conductivity value (100π) and 90° (after Meehan, 1989).

Therefore, the assumption is made that the fluid enters the fracture at a uniform flow rate per unit area of fracture face. Here, due to high conductivity of fracture, there is a negligible pressure drop along the fracture, causing a slight pressure gradient yielding a uniformly distributed flux.

Guppy et al. (1982b) noted that producing fractured wells at high flow rates can cause non-Darcy effects in the fracture. This results in pessimistic estimates of fracture conductivity (as much as 85% lower than the true conductivity) and different flux distribution. The same assumption is valid for highly propped fractures and damaged fracture-face cases.

Meehan (1989) also illustrated early and late time fluxes for a low fracture conductivity case $F_{CD}= \pi$. A clear declining flux distribution along the fracture plane is evident, i.e. it is non-uniformly distributed, for the low conductivity case, Figure 9.

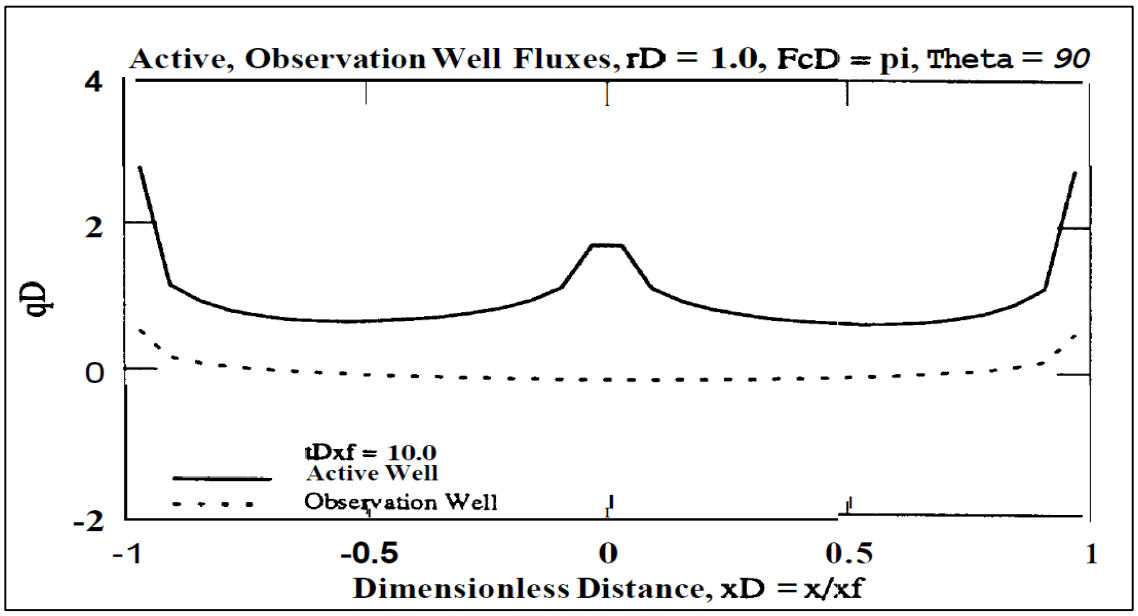

Figure 9- Flux Distribution of active and observation fractured wells at low conductivity value of π and 90° (after Meehan, 1989).

It is worth stating again that the above mentioned methods are limited to finite fracture lengths, and therefore reflect a tip effect, i.e. an increase in flux towards the toe of the fracture. This phenomenon is occurring due to the greater pressure drop (per unit distance) at the fracture tips.

2.4 Flux Distribution along Infinite-length Faults

Maghsood and Cinco-Ley (1995) studied the flux distribution along the non-intersecting fault and the effect of its conductivity on the source of fluids towards the reservoir and the producing well, Figure 10. They showed that, at low conductivity values, the fluid transfer is only across the fault, because fluxes from the right and the left-side reservoirs are identical and are of opposing signs. However, at high conductivity values, the fault acts as a source of fluid supply, dominating the fluid contribution over the matrix, for a constant rate solution.

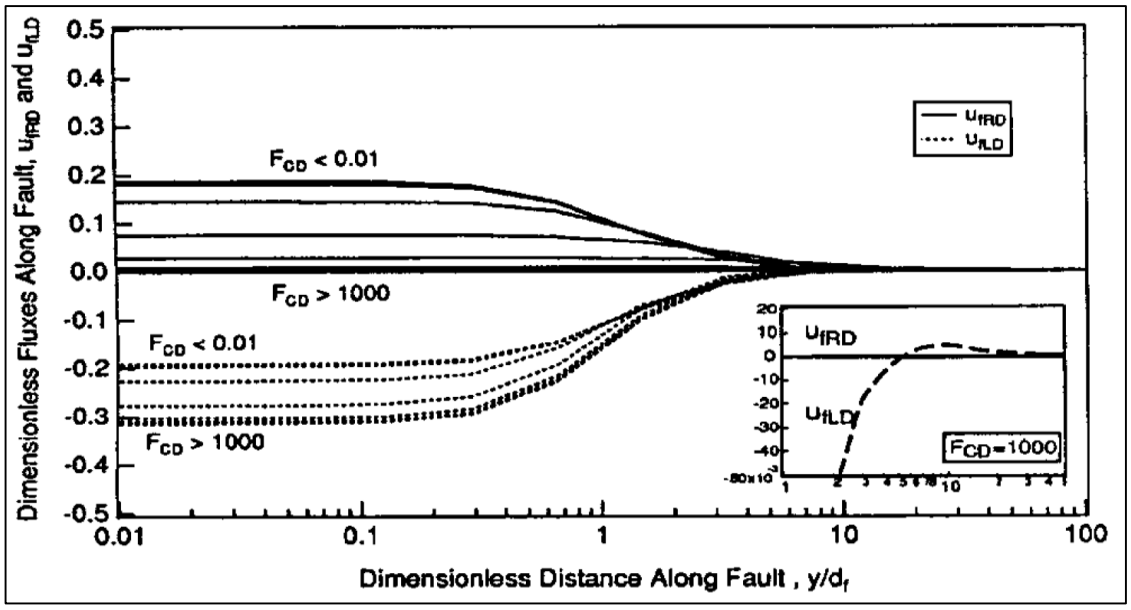

Figure 10- Flux Distribution along an infinite-length fault plane from left and right hand sides (after Maghsood and Cinco-Ley, 1995).

2.5 Comparison between Three Important Publications in Relation to this Study

Cinco et al. (1978) presented a semi-analytical solution for the analysis of the transient pressure data for fractured wells in symmetric reservoirs, which is most likely to occur in the case of small fractures or during a strike-slip faulting. A new technique was presented for analysing pressure transient data for wells intercepted by a finite conductivity vertical fracture. Their study resulted in a bi-linear flow due to the transient linear flows perpendicular to each other along fracture and formation, Figure 11.

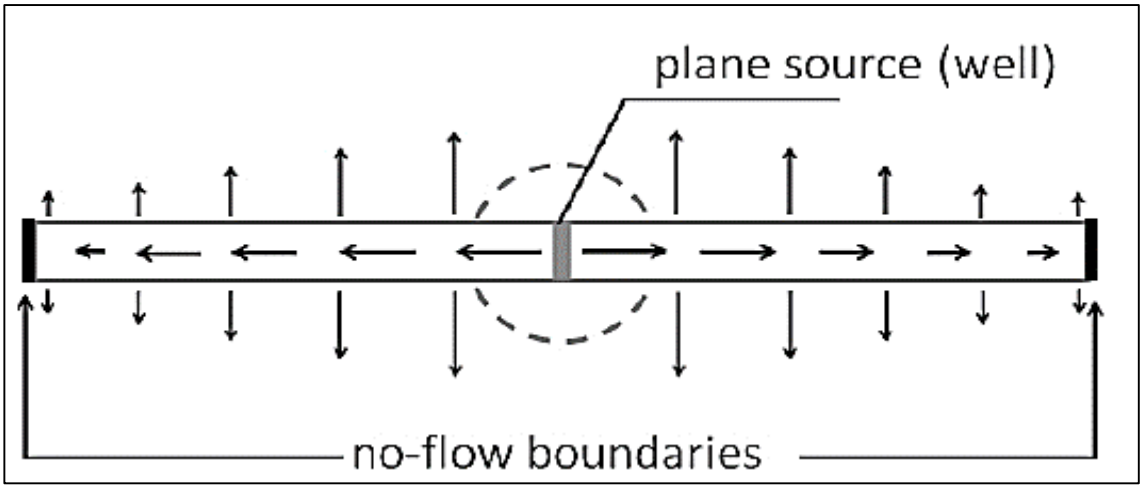

Figure 11- Schematic of a fracture model geometry (after Cinco et al., 1978).

Maghsood and Cinco-Ley (1995) presented an analytical solution for pressure distribution in a reservoir caused by drawdown of an active well near a non-intersecting finite conductivity fault or fracture by accounting for fault conductivity within the fault and surrounded by a transverse fault skin, Figure 12.

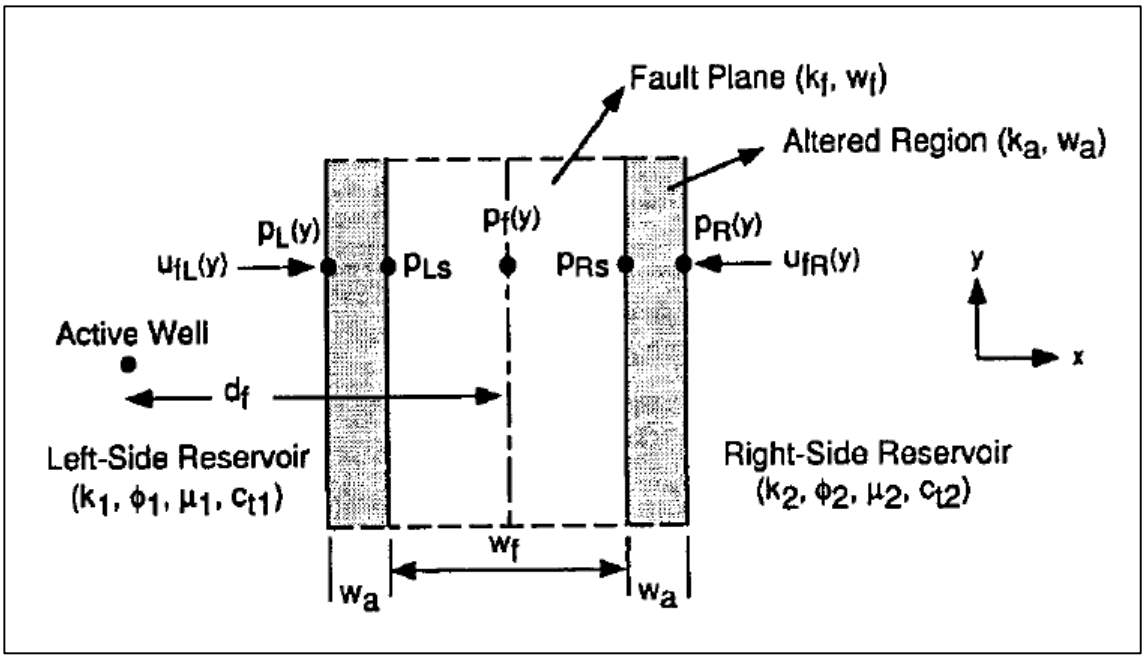

Figure 12- Schematic of a fault model (after Maghsood and Cinco-Ley, 1995).

The solution was obtained by dividing the flow domain into the reservoir and the fault flow partitions. The reservoir flow is considered on both sides of the fault, left and right, and the net flux in/out of the fault is zero, due to the belief that the fault does not have

any fluid storage capacity and that the thickness is very small, thus only linear flow along the fault is assumed:

$$q_f(y,t) = q_{fR}(y,t) + q_{fL}(y,t) \text{ and } \int_0^\infty q_f(y,t)\,dy = 0$$

where, $q_{fR}(y,t)$ and $q_{fL}(y,t)$, are fluxes into the fault plane from the reservoirs in the right and left sides, respectively. They also assumed that the transient flow along the fault is small, and therefore could be neglected. The fault plane has a thickness (w_f) and a permeability (k_f) and is located at a distance of (d_f) from the active well that produces at a constant rate. A region of altered permeability referred to as a fault skin (s_f), is considered on both sides of the fault (left, closer to the well, and right). This altered region is to reflect the geological change on the sides of the fault plane due to possible juxtaposition with another formation with different properties. In geological terms, it is possibly referred to as "damaged zones around fault core" or "Geochoke", as per Corbett et al. (2005).

An important advancement in modelling conductive faults was analytically presented by Rahman et al. (2003), for a well located near a finite-conductivity fault in a two-zone, composite reservoir, Figure 13.

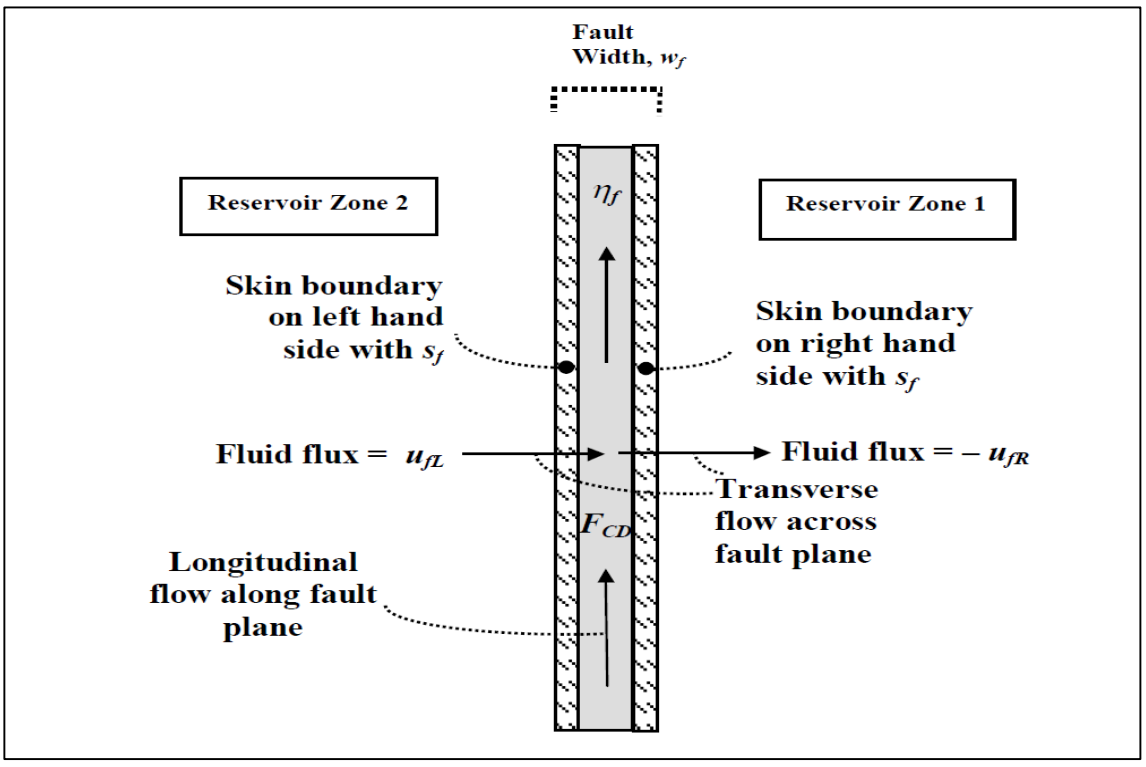

Figure 13- Schematic of a fault model (after Rahman et al., 2003).

Their solution is distinctive, as it accounts for the transient flow along the fault plane. They outlined a detailed computational procedure and compared it to a number of special cases in the literature. The solution provided avenues to better understanding of the transient flow along the conductive faults. It clearly demonstrated that a negative unit slope is obtained once the transient flow reaches the fault, reflecting a pressure support source for a considerable amount of time. This time is a function of the conductivity of the fault, i.e. the higher the conductivity, the longer it takes to support it. Afterwards, a quarter slope is evident, followed by a radial flow period reflecting the reservoir behind the fault. The quarter slope is a function of fault quality, as for F_{CD} < 1.0e5, a bilinear-flow regime appears after the end of the constant pressure support-like regime. However, for higher F_{CD} values, a slope of (½), indicating linear flow, is evident, which might be attributed to the fault having infinite conductivity. Their solution is theoretically identical to that of Maghsood and Cinco-Ley (1995) with two differences, which Rahman et al. (2003) accounted for namely: a two-region reservoir and transience along the fault zone.

This study presents a different solution for the pressure transient data of a more complex geological setting. It accounts for a fractured-well in a three-region reservoir with a finite conductivity fault. All the three regions are of specific dimensions and capacities, and hence, have distinctive mobilities. It also provides a novel method to estimate the fracture half-length (Effective Fracture Half-Length), in addition to fluxes from the matrix and the fracture. The solution can also be used to describe a three-region, linear, composite reservoir with or without a fractured-well. A summary of the similarities and differences between the above mentioned studies in relation to this study is also presented in part of the conclusions in Chapter 7.

Summary

Chapter 2 presented a detailed literature review with special emphasis on the fractures, fractured reservoirs and the possibility of having an asymmetric reservoir across the fractured well and faulted zone. The chapter ended with a comparison of the three most important publications in relation to this work. It highlighted the need for this solution, as it was not addressed in previous work.

The next chapter presents a new, semi-analytical solution to a well intersecting a finite conductivity fracture in a two-region composite reservoir.

CHAPTER 3 - SEMI-ANALYTICAL SOLUTION TO A WELL INTERSECTING A FINITE CONDUCTIVITY FRACTURE IN AN ASYMMETRIC RESERVOIR

3.1 Overview

The presence of fractures and faults plays a significant role in recovery and performance of tight reservoirs exploited with hydraulically fractured-wells. The identification, characterisation and modelling of conductive fractures have become increasingly important with increasing horizontal and multi-lateral well drilling and activities in production from naturally faulted geological settings and unconventional reservoirs. Typically, numerical well-test packages are used to match the pressure responses of such complex geology and well geometries (Hamdi et al., 2014). Faulting may result in symmetric reservoirs, i.e. the same quality across the fault plane, or asymmetric reservoirs, i.e. different quality reservoirs across the fault plane, due to the displacement of reservoir blocks along the fault plane.

3.2 A Finite Conductivity Fracture in an Asymmetric Reservoir

A semi-analytical approach has been followed to develop a new practically efficient flow solution for a well intersecting a finite conductivity vertical fracture in an asymmetric reservoir. This new model is defined as the “Frac” model.

The solution to the equations describing pressure distribution for a finite conductivity fracture in a composite reservoir, Figure 14, can be obtained by dividing the flow domain into three regions namely:

1. Reservoir Region-1,
2. Fractured-Well, and
3. Reservoir Region-2.

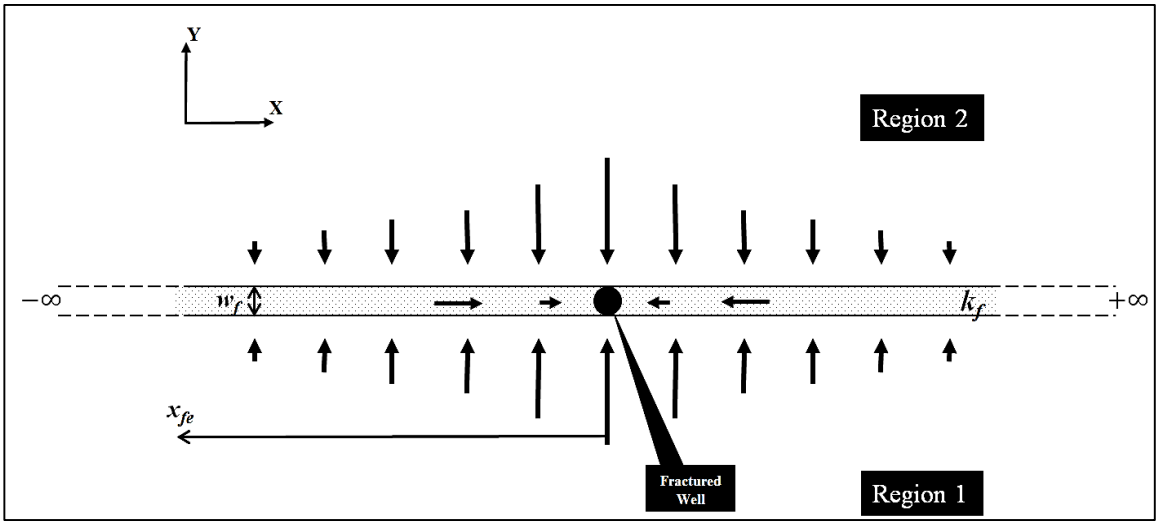

Figure 14: Schematic of flow distribution for a finite conductivity fracture of a non-uniform flux in a composite reservoir, describes the flow problem of the Frac-model.

3.2.1 Solution assumptions

The well model solution adopts the following assumptions:

- Vertical well penetrating a horizontal layer with an infinite drainage domain.
- The drainage domain is divided into two composite regions (fracture is splitting the two regions) with specific properties for each region.
- The porous volume is bounded by top and bottom impermeable boundaries:

  $(\frac{dp}{dz}\Big|_{z=0} = 0)$ and $(\frac{dp}{dz}\Big|_{z=h} = 0)$.

- Initially (at time zero) the flow domain is at initial pressure $(p_{(t,x,y)}\,|_{t=0} = p_i)$.
- Infinite length fracture $(-\infty < x < \infty)$.
- Semi-infinite along y-axis $(0 < y < \infty)\ and\ (-\infty < y < 0)$.
- Production occurs through a fully penetrating "uneven flux" vertical fracture with fracture conductivity of $(k_f . w_f)$.
- Reservoirs are homogenous $(\mathrm{k}_v = \mathrm{k}_h$ and isotropic within each side of the fracture.
- Single phase slightly compressible fluid (c_f), flows from single (φ) porous media to the fracture with constant viscosity (μ_f) and formation volume factor (B).
- Reservoir total compressibility is (c_t)
- The fluids' properties are independent of pressure.
- Gravity and capillary forces are neglected.

- The fracture half-length is assumed to be infinite, whereas the effective fracture half-length (x_f) is finite, whose value is determined using a unique procedure presented in the next chapter.

3.2.2 Derivation of governing equations

The diffusivity equations are derived for all regions. In this exercise and for fracture, initially, the well is ignored but then introduced in Section 3.6. Detailed derivation for the diffusivity equations describing the flow in Regions 1 and 2 are presented in Appendix-A.

Region-1

The fluid flow in Region-1 is represented in the x-y plane to account for matrix flow around the fracture, Figure 15.

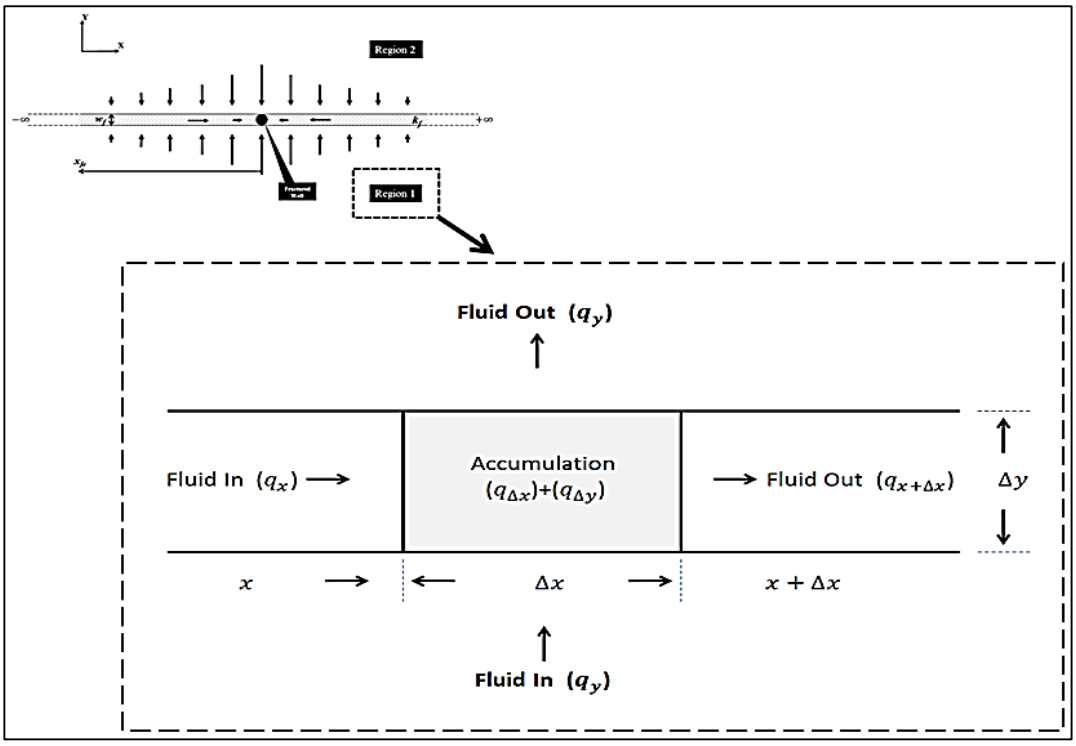

Figure 15: Schematic of material balance for Region-1, along both x- and y-planes.

Equation 1

$$\frac{\partial^2 p_1}{\partial x^2} + \frac{\partial^2 p_1}{\partial y^2} = 1/\eta_1 \cdot \left(\frac{\partial p_1}{\partial t}\right) \quad (1)$$

Region-2

Following an approach similar to that described in Appendix-A, the 2-D, Partial Differential Equation, for Region-2 is obtained

Equation 2

$$\frac{\partial^2 p_2}{\partial x^2} + \frac{\partial^2 p_2}{\partial y^2} = 1/\eta_2 \cdot \left(\frac{\partial p_2}{\partial t}\right) \quad (2)$$

Region-n

If a region n is defined to represent all matrix regions, then the 2-D, Partial Differential Equation, for Region-n is equation 3:

Equation 3

$$\frac{\partial^2 p_n}{\partial x^2} + \frac{\partial^2 p_n}{\partial y^2} = 1/\eta_f \cdot \left(\frac{\partial p_f}{\partial t}\right) \quad (3)$$

Where, $^1/_{\eta_f} = C \cdot \frac{c_t \cdot \varphi \cdot \mu}{k_f}$, $C = 0.000264$ and $(n)\ is\ Res\ 1, 2 \ldots, n$

Finite conductivity fracture

Figure 16, represents the fluid flow into and along the fracture and towards the well. The fluid flow into the fracture is the matrix contribution from Regions 1 and 2:

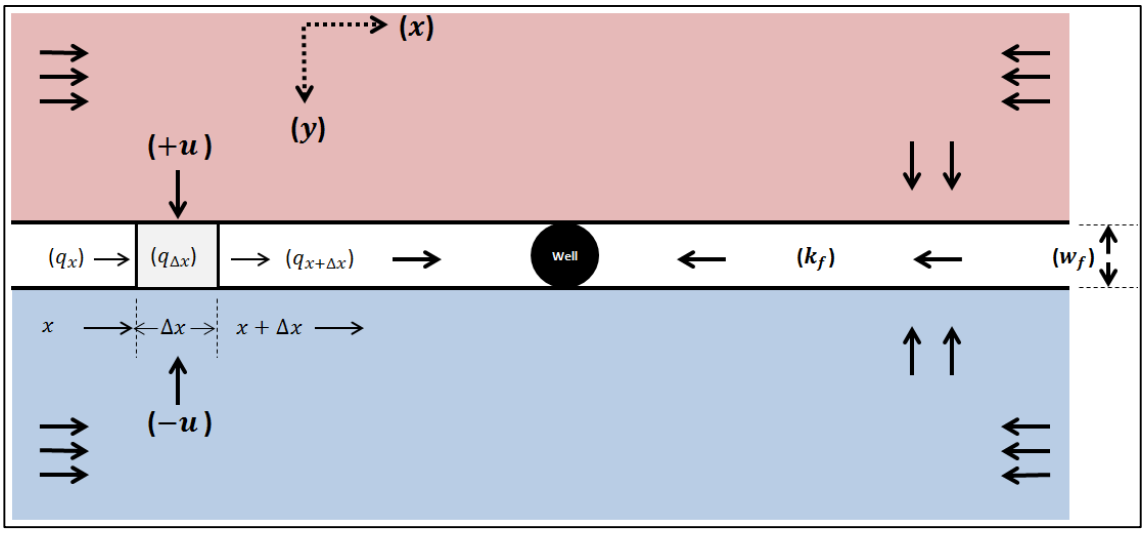

Figure 16: Definition sketch of the Frac-model solution.

(u_1&u_2), are the flow rate per unit area $\left(u = \frac{q}{A}\right)$ from Regions 1 and 2 to fracture, where, for:

Region-1: $-\infty < y < 0$

Region-2: $0 < y < \infty$

and $-\infty < x < \infty$ for both regions:

(Mass-in / Time) – (Mass-out / Time) = (Mass-Accumulation / Time)

$$(q_x \cdot \rho_x) + u_1(h \cdot \Delta x) \cdot \rho_y + u_2(h \cdot \Delta x) \cdot \rho_y - (q_{x+\Delta x} \cdot \rho_{x+\Delta x}) = q_{\Delta x} \cdot \rho_{\Delta x}$$

Taking into consideration the steps carried-over in Appendix-A, hence multiply by Δt:

$$(q_x \cdot \Delta t) - (q_{x+\Delta x} \cdot \Delta t) + (u_1 + u_2) \cdot (h \cdot \Delta x) \cdot \Delta t = q_{\Delta x} \cdot \Delta t$$

Equation 4

$$(q_x - q_{x+\Delta x}) \cdot \Delta t + (u_1 + u_2) \cdot (h \cdot \Delta x) \cdot \Delta t = q_{\Delta x} \cdot \Delta t \quad (4)$$

$$(q_x - q_{x+\Delta x}) \cdot \Delta t + (u_1 + u_2) \cdot (h \cdot \Delta x) \cdot \Delta t = q_{\Delta x} \cdot \Delta t = \Delta v$$

Introducing the compressibility equation:

where: $C = -\frac{1}{v}\frac{\Delta v}{\Delta p} \rightarrow \Delta v = - cv\, \Delta p$

into Equation 4 gives:

$$(q_x - q_{x+\Delta x}) \cdot (\Delta t) + (u_1 + u_2) \cdot (h \cdot \Delta x) \cdot \Delta t = - cv\, \Delta p = - c \cdot (w_f \cdot h \cdot \Delta x \cdot \varphi) \cdot (p_t - p_{t+\Delta t})$$

Divide by $(\Delta x \cdot \Delta t)$ and take limit as $\Delta x \rightarrow 0$ & $\Delta t \rightarrow 0$:

$$-\lim_{\Delta x \to 0}\left(\frac{q_{x+\Delta x} - q_x}{\Delta x}\right) + (u_1 + u_2) \cdot (h) = c \cdot (w_f \cdot h \cdot \varphi) \lim_{\Delta t \to 0}\left(\frac{p_{t+\Delta t} - p_t}{\Delta t}\right)$$

Equation 5

$$-\frac{dq}{dx} + (u_1 + u_2) \cdot (h) = c \cdot (w_f \cdot h \cdot \varphi)\frac{dp_f}{dt} \quad (5)$$

Flow along Fracture

Introduce Darcy's law along fracture:

$$q = -\frac{k_f A}{\mu} \cdot \frac{dp_f}{dx},$$

Differentiate both sides (w.r.t.) x:

$$\frac{d}{dx} \cdot q = -\frac{k_f A}{\mu} \cdot \left(\frac{d}{dx} \cdot \frac{dp_f}{dx}\right)$$

Equation 6

$$\frac{dq}{dx} = -\frac{k_f A}{\mu} \cdot \left(\frac{d^2 p_f}{dx^2}\right) \tag{6}$$

Substitute Equation 6 in Equation 5:

$$\frac{k_f A}{\mu} \cdot \left(\frac{\partial^2 p_f}{\partial x^2}\right) + (u_1 + u_2) \cdot (h) = c \cdot \left(w_f \cdot h \cdot \varphi\right) \frac{\partial p_f}{\partial t}$$

Since, $A\ is\ constant = w_f \cdot h$, then:

$$\frac{k_f}{\mu} \cdot w_f \left(\frac{\partial^2 p_f}{\partial x^2}\right) + (u_1 + u_2) = c \cdot \left(w_f \cdot \varphi\right) \frac{\partial p_f}{\partial t}$$

Re-arranging this two dimensional diffusivity equation for fluid flowing along fracture plane per unit area gives:

$$\frac{\partial^2 p_f}{\partial x^2} + (u_1 + u_2) \cdot \frac{\mu}{w_f \cdot k_f} = \frac{c\mu\varphi}{k_f} \cdot \left(\frac{\partial p_f}{\partial t}\right)$$

Or:

Equation 7

$$\frac{\partial^2 p_f}{\partial x^2} + (u_1 + u_2) \cdot \frac{\mu}{w_f \cdot k_f} = {}^{1}/_{\eta_f} \cdot \left(\frac{\partial p_f}{\partial t}\right) \tag{7}$$

where:

η_f: Hydraulic Diffusivity Constant along fracture

$w_f.k_f.$: Fracture conductivity (md.ft)

Flow into Fracture from Regions 1&2

Region-1

$(\mathbf{u_1})$**:**

Equation 8

$$u_1 = \frac{q}{A} = \frac{-k_1}{\mu} \cdot \left.\frac{dp_1}{dy}\right|_{y\to 0}, \text{Flow from } \textbf{Region 1} \text{ into fracture } (-\text{ve direction}) \quad (8)$$

Region-2

$(\mathbf{u_2})$**:**

Equation 9

$$u_2 = \frac{q}{A} = \frac{k_2}{\mu} \cdot \left.\frac{dp_2}{dy}\right|_{y\to 0}, \text{Flow from } \textbf{Region 2} \text{ into fracture } (+\text{ve direction}) \quad (9)$$

Substitute Equation 8 and Equation 9 into Equation 7 and re-arrange:

Equation 10

$$\frac{\partial^2 p_f}{\partial x^2} + \frac{1}{k_f \cdot w_f}\left[k_2 \left.\frac{\partial p_2}{\partial y}\right|_{y=0} - k_1 \left.\frac{\partial p_1}{\partial y}\right|_{y=0}\right] = 1/\eta_f \cdot \left(\frac{\partial p_f}{\partial t}\right) \quad (10)$$

where;

- Region-1is semi-infinite along y-axis $(-\infty < y < 0)$ and infinite along x-axis, $(-\infty < x < \infty)$
- Fractured-Well is infinite along x-axis $(-\infty < x < \infty)$
- Region-2 is semi-infinite along y-axis $(0 < y < \infty)$ and infinite along x-axis, $(-\infty < x < \infty)$.

Equation 10 is the diffusivity equation for a finite conductivity fracture in an asymmetric reservoir. The fracture is in-between two linear composite regions.

where: $1/\eta_f = \frac{c_t \cdot \varphi \cdot \mu}{k_f}$,

and $F_{Cf} = k_f \cdot w_f \ (md.ft)$ **.**

3.3 Dimensionless Forms

Here I simplify the problem by replacing the real variables with dimensionless variables, hence, resulting in a set of equations with a generalised solution.

Dimensionless parameters

The dimensionless parameters are defined as follows:

$x_D = \frac{x}{r_w} \rightarrow x = r_w \,.\, x_D$, and

Equation 11

$$dx = r_w \,.dx_D \tag{11}$$

$y_D = \frac{y}{r_w} \rightarrow y = r_w \,.\, y_D$, and,

Equation 12

$$dy = r_w \,.dy_D \tag{12}$$

$t_{D_f} = \frac{0.000264\, k_{rf} \cdot t}{(\varphi\ c_t\ \mu)_{rf}\ {r_w}^2}$, and $dt_{D_f} = \frac{0.000264\, k_{rf}}{(\varphi\ c_t\ \mu)_{rf}\ {r_w}^2} \cdot dt$

Equation 13

$$\Rightarrow\ dt = \frac{(\varphi\ c_t\ \mu)_{rf}\ {r_w}^2}{0.000264\, k_{rf}} \cdot dt_{D_f} \tag{13}$$

$p_{Dn} = \frac{k_{rn}\,.\ h[p_i - p_n]}{141.2 q\beta\mu}$,

Equation 14

$$\Rightarrow\ p_n = p_i - \frac{141.2\ q\beta\mu}{k_{rf}h}\ p_{Dn} \tag{14}$$

Dimensionless equations for fracture

Here, the terms in (Equation 10) are converted individually into dimensionless form before presenting the final equation in dimensionless form.

Fracture Pressure gradient along x-axis:

$\frac{\partial^2 p_f}{\partial x^2}$:

$p_{Df} = \frac{k_{rf}\,.\ h[p_i - p_f]}{141.2 q\beta\mu} \Rightarrow p_f = p_i - \frac{141.2\ q\beta\mu}{k_{rf}h}\ p_{Df}$ and $dp_f = -\frac{141.2\ q\beta\mu}{k_{rf}h}\ dp_{Df}$

And $\frac{dp_f}{dx} = 0 - \frac{141.2\ q\beta\mu}{k_{rf}h}\ \frac{dp_{Df}}{dx} = -\frac{141.2\ q\beta\mu}{k_{rf}h\ (r_w}\ \frac{dp_{Df}}{dx_D)}$, $(since\ dx = r_w \cdot\ dx_D)$

Equation 15

$$\Rightarrow \frac{d^2 p_f}{dx^2} = -\frac{141.2\ q\beta\mu}{k_{rf}.h\ {r_w}.^2} \cdot \frac{d^2 p_{Df}}{{dx_D}^2} \tag{15}$$

Matrix Flow into Fracture along y-axis:

$\left(\frac{\partial p_1}{\partial y}\ \&\ \frac{\partial p_2}{\partial y}\right)$**:**

$p_{D1} = \frac{k_r h[p_i - p_1]}{141.2 q\beta\mu} \Rightarrow p_1 = p_i - \frac{141.2\ q\beta\mu}{k_r h}\ p_{D1}$

Then:

$$\frac{dp_1}{dy} = 0 - \frac{141.2\ q\beta\mu}{k_r h}\ \cdot\ \frac{dp_{D1}}{dy}$$

Equation 16

$$\frac{dp_1}{dy} = -\frac{141.2\ q\beta\mu}{k_1 h\ r_w}\ \frac{dp_{D1}}{dy_D} \tag{16}$$

$(since\ dy = r_w .\cdot\ dy_D)$

Similarly:

$$\frac{dp_2}{dy} = 0 - \frac{141.2\ q\beta\mu}{k_r h}\ \cdot\ \frac{dp_{D2}}{dy}\ = -\frac{141.2\ q\beta\mu}{k_r h\ .\ (r_w}\ \frac{dp_{D2}}{dy_D)},$$

Equation 17

$$\frac{dp_2}{dy} = -\frac{141.2\ q\beta\mu}{k_r h\ .\ r_w}\ \frac{dp_{D2}}{dy_D} \tag{17}$$

$(since\ dy = r_w .\cdot\ dy_D)$

Fracture Pressure gradient versus time:

$\frac{\partial p_f}{\partial t}$:

$$\frac{dp_f}{dt} = 0 - \frac{141.2\ q\beta\mu}{k_{rf}\ .\ h}\cdot\ \frac{dp_{Df}}{dt}$$

Substitute Equation 13 for dt :

Equation 18

$$\frac{dp_f}{dt} = -\frac{141.2\ q\beta\mu}{k_{rf}\ h}\ \cdot\frac{0.000264\ k_{rf}}{(\varphi\ c_t\ \mu)_{rf}\ {r_w}^2}\cdot\frac{dp_{Df}}{dt_{D_f}} \tag{18}$$

Final Equation:

Substituting the dimensionless variables in Equation 13 to Equation 18 in Equation 10:

$$-\frac{141.2\ q\beta\mu}{k_{rf}.h\ {r_w}.^2}\ \cdot\ \frac{d^2 p_{Df}}{{dx_D}^2} + \frac{1}{k_f \cdot w_f}\left[-\frac{141.2\ q\beta\mu}{k_r h\ .\ r_w}\ \cdot\ \left(k_2 \frac{dp_{D2}}{dy_D}\Big|_{y=0} - k_1 \frac{dp_{D1}}{dy_D}\Big|_{y=0}\right)\right]$$

$$= \frac{\mathbf{1}}{\boldsymbol{\eta_f}} \cdot \left(-\frac{141.2\, q\beta\mu}{k_{rf}\, h} \cdot \frac{0.000264\, k_{rf}}{(\varphi\ c_t\ \mu)_{rf}\, r_w{}^2}\right) \cdot \frac{dp_{Df}}{dt_{D_f}}$$

gives the dimensionless form of PDE for Fracture:

$$\frac{\partial^2 p_{Df}}{\partial x_D{}^2} + \frac{1}{\frac{k_f\, w_f}{k_{rf}\ r_w}} \left[\left(\frac{k_2}{k_r}\right) \cdot \frac{\partial p_{D2}}{\partial y_D}\Big|_{y_D=0} - \left(\frac{k_1}{k_r}\right) \cdot \frac{\partial p_{D1}}{\partial y_D}\Big|_{y_D=0}\right] = 0.000264 \left(\frac{1}{\eta_f}\right) \cdot \left(\frac{k_{rf}}{(\varphi\ c_t\ \mu)_{rf}}\right) \frac{\partial p_{Df}}{\partial t_{Df}}$$

The fracture diffusivity equation in dimensionless form:

Equation 19

$$\frac{\boldsymbol{\partial^2 p_{Df}}}{\boldsymbol{\partial x_D{}^2}} + \frac{\mathbf{1}}{\boldsymbol{F_{CDf}}} \left[(\boldsymbol{k_{D2}}) \cdot \frac{\boldsymbol{\partial p_{D2}}}{\boldsymbol{\partial y_D}}\Big|_{\boldsymbol{y_D=0}} - (\boldsymbol{k_{D1}}) \cdot \frac{\boldsymbol{\partial p_{D1}}}{\boldsymbol{\partial y_D}}\Big|_{\boldsymbol{y_D=0}}\right] = \mathbf{1}/\boldsymbol{\eta_{Df}} \cdot \frac{\boldsymbol{\partial p_{Df}}}{\boldsymbol{\partial t_{Df}}} \quad (19)$$

where, repetition

$$\eta_{Df} = 0.000264 \cdot \left(\frac{(\varphi\ c_t\ \mu)_f}{k_f} \cdot \frac{k_{rf}}{(\varphi\ c_t\ \mu)_{rf}}\right) = 0.000264 \cdot \left(\frac{\eta_{rf}}{\eta_f}\right),\ 1/\eta_{Df} = \frac{1}{0.000264} \cdot \left(\frac{\eta_f}{\eta_{rf}}\right)$$

$$F_{CDf} = \frac{k_f\, w_f}{k_{fr}\ r_w},\ k_{fr} = \frac{k_1 + k_2}{2},\ k_{D2} = \frac{\boldsymbol{k_2}}{\boldsymbol{k_r}},\ k_{D1} = \frac{\boldsymbol{k_1}}{\boldsymbol{k_r}},\ k_r = 1.0$$

Fracture reference permeability

Dimensionless fracture conductivity is a measure of a fracture's ability to contribute to flow. In this study, the dimensionless fracture conductivity is a function of fracture conductivity ($k_f\ w_f$) divided by the well radius (r_w) and the arithmetic matrix permeability ($k_{rf} = \frac{k_1 + k_2}{2}$), since the well is located in the middle, between Regions 1 and 2. Hence, the calculation of the fracture dimensionless conductivity will be rational and reflects the influence of the two regions. In previous fracture solutions, F_{CDf}, was defined as ($F_{CDf} = \frac{k_f\, w_f}{k_m\ x_f}$), as the fracture was finite in length and located in a homogenous reservoir (symmetric) with flow direction from the matrix in the y-direction. In this study, I solve for a finite conductivity fracture with an infinite length, in an asymmetric reservoir on (*x-y plane*). It should be noted that, later in Chapter 5, a new approach to calculate the fracture half-length is discussed, and referred to as "the effective fracture half-length (x_{fe})".

Reservoir reference permeability

Any reference permeability (k_r) can be used to convert the reservoir permeability into dimensionless form, as long as it is consistent with the other regions. In this code,

($k_r = 1.0$) has been considered to retain the dimensionless permeability to be the same as the dimensional permeability.

Dimensionless Equations for Matrix Bounding the Fracture:

Similarly to what was the case for fracture, substituting the dimensionless variables in Equation 13 to Equation 18, in Equation 1, obtained obtained

Equation 2 and Equation 3, the corresponding PDEs in dimensionless form are:

Region-1

Equation 20

$$\frac{\partial^2 p_{\mathrm{D1}}}{\partial {x_D}^2} + \frac{\partial^2 p_{\mathrm{D1}}}{\partial {y_D}^2} = 1/\eta_{\mathrm{D1}} \cdot \left(\frac{\partial p_{\mathrm{D1}}}{\partial t_D}\right) \tag{20}$$

Region-2

Equation 21

$$\frac{\partial^2 p_{\mathrm{D2}}}{\partial {x_D}^2} + \frac{\partial^2 p_{\mathrm{D2}}}{\partial {y_D}^2} = 1/\eta_{\mathrm{D2}} \cdot \left(\frac{\partial p_{\mathrm{D2}}}{\partial t_D}\right) \tag{21}$$

Region-n

Equation 22

$$\frac{\partial^2 p_{\mathrm{Dn}}}{\partial {x_D}^2} + \frac{\partial^2 p_{\mathrm{Dn}}}{\partial {y_D}^2} = 1/\eta_{\mathrm{Dn}} \cdot \left(\frac{\partial p_{\mathrm{Dn}}}{\partial t_D}\right) \tag{22}$$

$$\eta_{Dn} = \left(\frac{\eta_r}{\eta_n}\right) = \left(\frac{(\varphi\ c_t\ \mu)_n}{k_n} \cdot \frac{k_r}{(\varphi\ c_t\ \mu)_r}\right)$$

$$1/\eta_{Dn} = \frac{1}{\left(\frac{\eta_r}{\eta_n}\right)}$$

3.4 Validation to Cinco-Ley's Solution

Cinco-Ley's solution assumes a finite length fracture; a symmetric system on both sides of the fracture and matrix flow towards the fracture along y-direction only. Whilst, this more general approach assumes an **asymmetric** system (two differing regions bounding the fracture), matrix flow towards the fracture is on ***x-y plane*** and for an infinite fracture length, Figure 17. Thus, if one applies the restricting conditions mentioned earlier for the Cinco-Ley model in the more general approach, Equation 19, the solution should become identical to that of the Cinco-Ley (1981) solution.

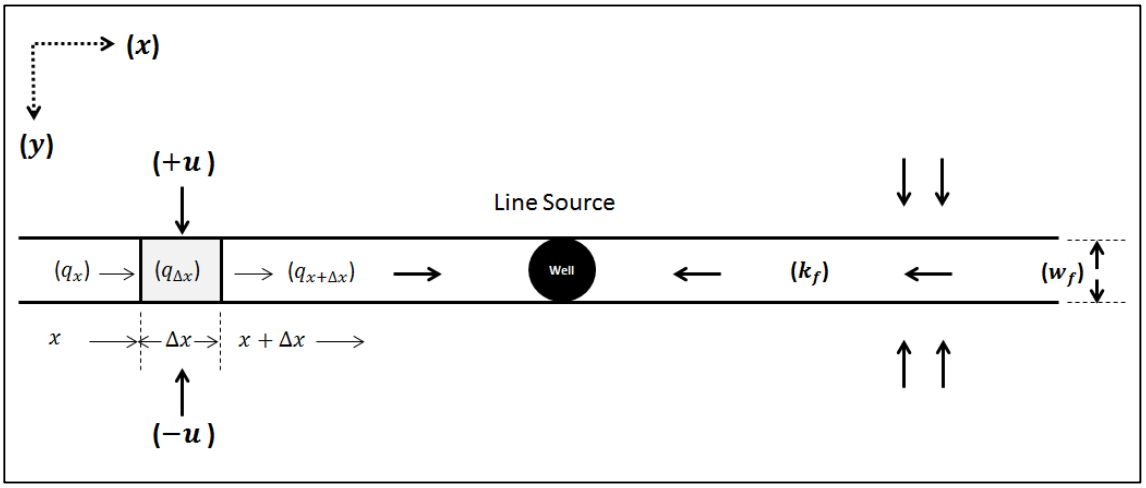

Figure 17: Schematic shows fluid flow along and into fracture as per Cinco-Ley (1981) where fracture is located in a homogenous isotropic reservoir.

That is, in Equation 19, if u_1=u_2; this gives the diffusivity equation for finite conductivity fracture (Appendix-B):

Equation 23

$$\frac{\partial^2 p_f}{\partial x^2} + \frac{2k}{k_f \cdot w_f} \left.\frac{\partial p}{\partial y}\right|_{y=0} = 1/\eta_f \cdot \left(\frac{\partial p_f}{\partial t}\right) \tag{23}$$

where: $1/\eta_f = C \cdot \frac{c_{tf} \cdot \varphi_f \cdot \mu}{k_f}$, $C = 0.000264$

Converting to dimensionless variables, as detailed above, will produce Cinco-Ley's Finite Conductivity Fracture Solution (Cinco et al., 1978):

- for a **symmetric** system on both sides of the fracture (i.e. $k_1 = k_2$),
- that accounts for **linear** flow along the **y-axis** only,
- with finite fracture length.

Equation 24

$$\frac{\partial^2 p_{Df}}{\partial x_D{}^2} + \frac{2}{(k_f \cdot w_f)_D} \frac{\partial p_D}{\partial y_D}\bigg|_{y_D=0} = 1/\eta_{fD} \cdot \left(\frac{\partial p_{Df}}{\partial t_{Dxf}}\right) \quad (24)$$

$0 < y < \infty$ And $0 < x < \infty$

where: $(k_f w_f)_D = \frac{k_f w_f}{k_r x_f}$

while this study:

(1) Assumes an **asymmetric** reservoir $k_1 \neq k_2$,

(2) Accounts for flow on **x-y plane**,

(3) Adopts an infinite fracture length case.

Equation 19

$$\frac{\partial^2 p_{Df}}{\partial x_D{}^2} + \frac{1}{F_{CDf}} \left[(k_{D2}) \cdot \frac{\partial p_{D2}}{\partial y_D}\bigg|_{y_D=0} - (k_{D1}) \cdot \frac{\partial p_{D1}}{\partial y_D}\bigg|_{y_D=0} \right] = 1/\eta_{Df} \cdot \frac{\partial p_{Df}}{\partial t_{Df}}$$

where: $(k_f w_f)_D = \frac{k_f w_f}{k_r r_w}$

3.5 Development of a Finite Conductivity Fracture Solution with a Source Term

The unit step function is a typical function used in engineering to model phenomena that are "switched" on and off. It is expressed mathematically as: $H(x-a)$, where (a) designates the shift from the origin. Here, Heaviside Unit Step function inserted for the plane source (i.e. fracture). Figure 18, shows the geometry including the source term:

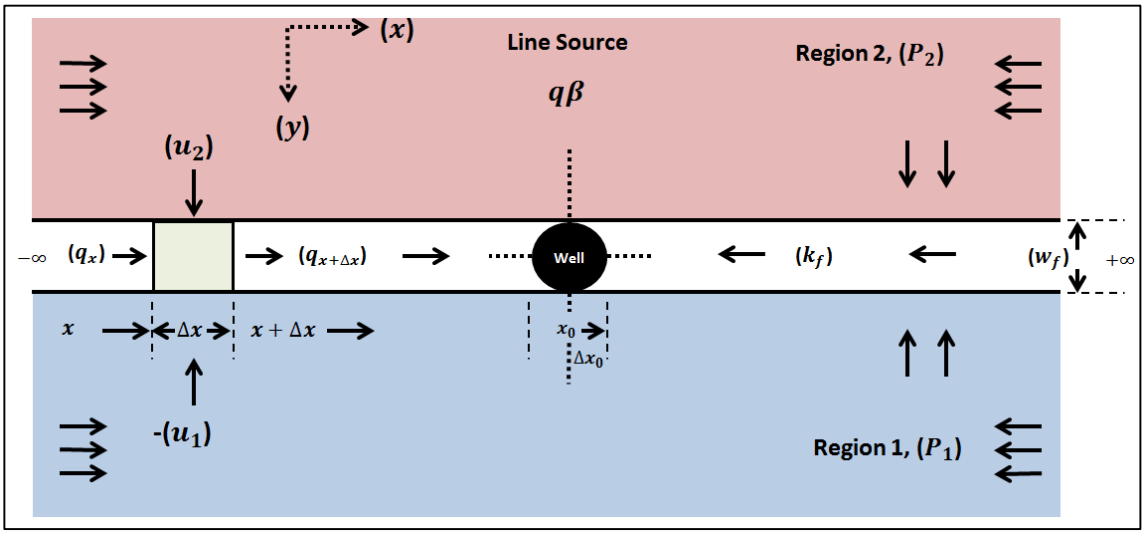

Figure 18: Schematic shows fluid flow along and into fracture with a source term.

Following the procedure mentioned above but including the source term q, the corresponding PDE, as detailed in (Appendix-C), gives the diffusivity equation for finite conductivity fracture:

Equation 25

$$\frac{\partial^2 p_f}{\partial x^2} + \frac{1}{k_f \cdot w_f}\left[k_2 \frac{\partial p_2}{\partial y}\Big|_{y=0} - k_1 \frac{\partial p_1}{\partial y}\Big|_{y=0}\right] + \frac{\mathrm{q}\beta\mu}{w_f \cdot k_f \cdot h} \cdot \frac{\partial \mathrm{H}(x_0 - \mathrm{a})}{\partial x} = 1/\eta_f \cdot \left(\frac{\partial p_f}{\partial t}\right) \quad (25)$$

where,

$a \;\&\; \Delta x_0 = 0$

$1/\eta_f = C \cdot \frac{c_t \cdot \varphi \cdot \mu}{k_f}, C = 0.000264$

By substituting the dimensional by the dimensionless variables, in Equation 11 to Equation 13, using $\left(\frac{\mathbf{141.2\ q\beta\mu}}{\boldsymbol{kh}} \cdot 2\pi\right)$ as a constant well-rate in field units, Equation 19 in dimensionless form with a source term, becomes equation 26:

Equation 26

$$\frac{\partial^2 p_{Df}}{\partial {x_D}^2} + \frac{1}{F_{CDf}}\left[(k_{D2}) \cdot \frac{\partial p_{D2}}{\partial y_D}\Big|_{y_D=0} - (k_{D1}) \cdot \frac{\partial p_{D1}}{\partial y_D}\Big|_{y_D=0}\right] + \frac{2\pi}{F_{CD}} \cdot \delta(x_D - a) = \left(1/\eta_{Df}\right) \cdot \frac{\partial p_{Df}}{\partial t_{Df}} \quad (26)$$

where, the well is at origin (a = 0),

$F_{CDF} = \frac{k_f\, w_f}{k_{rf}\; r_w}, k_{rf} = \frac{k_1 + k_2}{2}, k_{D3} = \frac{k_1}{k_r}, k_{D2} = \frac{k_2}{k_r}, k_r = 1.0$

$\eta_{Df} = \cdot \left(\frac{(\varphi\ c_t\ \mu)_f}{k_f} \cdot \frac{0.000264 \cdot k_{rf}}{(\varphi\ c_t\ \mu)_{rf}}\right) = 0.000264 \cdot \left(\frac{\eta_{rf}}{\eta_f}\right),$

$1/\eta_{Df} = \frac{1}{0.000264 \cdot \left(\frac{\eta_{rf}}{\eta_f}\right)},$

Initial Conditions:

$p_{D1} = p_{D2} = p_{Df} = 0 \qquad @\ t_{Df} = 0$

Boundary Conditions:

$@\ y_D = 0$

$p_{D1} = p_{D2} = p_{Df}$

$0 < \mathrm{y} < \infty$

$-\infty < \mathrm{y} < 0$

$-\infty < \mathrm{x} < \infty$

Transformations

The next step towards the solution is to apply Laplace (Marquis de Laplace, 1820) and Fourier (Grattan-Guinness and Fourier, 1972) transformations to all the given diffusivity equations as follows:

3.4.1 Laplace transformation

Take Laplace transformation of all equations with respect to dimensionless time (t_{Df}) in terms of parameter (s) :

Region-1

Equation 27

$$\frac{\partial^2 \overline{p}_{\mathrm{D1}}}{\partial {x_D}^2} + \frac{\partial^2 \overline{p}_{\mathrm{D1}}}{\partial {y_D}^2} = 1/\eta_{\mathrm{D1}} \cdot \left(s\overline{p}_{D1} - 0\right) \tag{27}$$

Fracture

Equation 28:

$$\frac{\partial^2 \overline{p}_{Df}}{\partial {x_D}^2} + \frac{1}{F_{CD}}\left[(k_{D2}) \cdot \left.\frac{\partial \overline{p}_{D2}}{\partial y_D}\right|_{y_D=0} - (k_{D1}) \cdot \left.\frac{\partial \overline{p}_{D1}}{\partial y_D}\right|_{y_D=0}\right] + \frac{2\pi}{F_{CD} \cdot s} \cdot \delta(x_D - a) = \left(1/\eta_{Df}\right) \cdot \left(s\overline{p}_{Df} - 0\right) \tag{28}$$

Region-2

Equation 29:

$$\frac{\partial^2 \overline{p}_{\mathrm{D2}}}{\partial {x_D}^2} + \frac{\partial^2 \overline{p}_{\mathrm{D2}}}{\partial {y_D}^2} = 1/\eta_{\mathrm{D2}} \cdot \left(s\overline{p}_{D2} - 0\right) \tag{29}$$

3.4.2 Fourier transformation

At this stage, I take the Fourier transform for all the equations with respect to space variable (x_D) in terms of parameter (ρ):

Region-1

$$-\rho^2\,\bar{\bar{p}}_{D1}+\frac{d^2\bar{\bar{p}}_{D1}}{dy_D{}^2}=\frac{s\cdot\bar{\bar{p}}_{D1}}{\eta_{D1}}$$

Equation 30:

$$\Rightarrow\quad \frac{d^2\bar{\bar{p}}_{D1}}{dy_D{}^2}=\left(\rho^2+\frac{s}{\eta_{D1}}\right)\,\bar{\bar{p}}_{D1} \tag{30}$$

Fracture

To take Fourier transform on the delta function, $\delta(x_D-a)$**:**

$$F\{f(t)\}=\frac{1}{\sqrt{2\pi}}\int_{-\infty}^{\infty} f(t)\cdot e^{-i\rho t}\,dt$$

Equation 31

$$F\{\delta(x_D-0)\}=\frac{1}{\sqrt{2\pi}}\int_{-\infty}^{\infty}\delta(x_D-0)\cdot e^{-i\rho x_D}\,dx_D\;=\;\frac{1}{\sqrt{2\pi}} \tag{31}$$

then,

Equation 32

$$-\rho^2\,\bar{\bar{p}}_{Df}+\frac{1}{F_{CD}}\left[(k_{D2})\cdot\left.\frac{\partial\bar{\bar{p}}_{D2}}{\partial y_D}\right|_{y_D=0}-(k_{D1})\cdot\left.\frac{\partial\bar{\bar{p}}_{D1}}{\partial y_D}\right|_{y_D=0}\right]+\frac{2\pi}{F_{CD}\,s}\cdot\frac{1}{\sqrt{2\pi}}=\left(\frac{s\cdot\bar{\bar{p}}_{Df}}{\eta_{Df}}\right) \tag{32}$$

Region-2

$$-\rho^2\,\bar{\bar{p}}_{D2}+\frac{d^2\bar{\bar{p}}_{D2}}{dy_D{}^2}=\frac{s\cdot\bar{\bar{p}}_{D2}}{\eta_{D2}}$$

Equation 33

$$\Rightarrow\quad \frac{d^2\bar{\bar{p}}_{D2}}{dy_D{}^2}=\left(\rho^2+\frac{s}{\eta_{D2}}\right)\,\bar{\bar{p}}_{D2} \tag{33}$$

3.4.3 Helmholtz equation

The above is a partial differential equation in both time and space, as Laplace and Fourier transformations were taken with respect to time variable (t_D) in terms of

parameter (s) and space variable (x_D) in terms of parameter (ρ), respectively. The Helmholtz equation, which results from applying the technique of separation of variables, can be used to further reduce the complexity of the solution (Khan et al., 2010) as shown below.

The Helmholtz equation can be written as follows:

$(\frac{d^2\mathrm{p}}{dy^2} = m \cdot \mathrm{p})$, can be written as: $p = C_1\, e^{+\sqrt{m}\,.\,y} + C_2\, e^{-\sqrt{m}\,.\,y}$

Hence,

Region-1

Equation 34

$$\overline{\overline{p}}_{D1} = C_1{}'\, e^{+\sqrt{\left(\rho^2+\frac{s}{\eta_{D1}}\right)}\,.\,y_D} + C_1{}''\, e^{-\sqrt{\left(\rho^2+\frac{s}{\eta_{D1}}\right)}\,.\,y_D} \qquad (34)$$

$$-\infty < y_D \leq 0$$

* See Appendix-D, for detailed initial and boundary conditions.

Since it is infinite at **Region-1** from one side of the fracture, y_D is $(-^{ve})$ as the flow is going up towards the fracture in a plan view. In a drawdown test, the pressure decreases with time, and thus to have the pressure decreasing with time, the power of "e" has to be negative Figure 19, and then Equation 34 becomes:

Equation 35

$$\overline{\overline{p}}_{D1} = C_1\, e^{+\sqrt{\left(\rho^2+\frac{s}{\eta_{D1}}\right)}\,.\,y_D} \qquad (35)$$

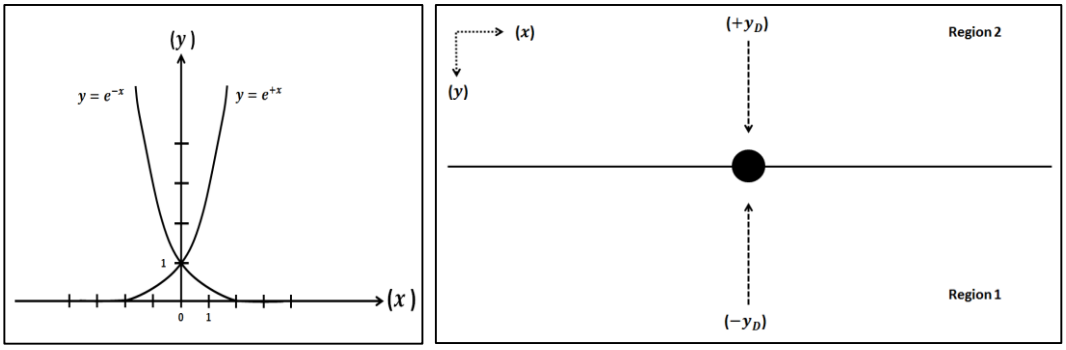

Figure 19: Argument of flow to well and the exponential (e^x) effect on flow direction considered in the solution.

Applying to boundary conditions @ $y_D = 0$, gives:

$p_{D1} = p_{D2} = p_{Df}$ And $\bar{\bar{p}}_{D1} = C_1$

Region-2

$$-\rho^2 \bar{\bar{p}}_{D2} + \frac{d^2\bar{\bar{p}}_{D2}}{dy_D{}^2} = \frac{s \cdot \bar{\bar{p}}_{D2}}{\eta_{D2}}$$

$$\Rightarrow \quad \frac{d^2\bar{\bar{p}}_{D2}}{dy_D{}^2} = \left(\rho^2 + \frac{s}{\eta_{D2}}\right) \bar{\bar{p}}_{D2}$$

The solution to the above Helmholtz equation is Equation 34.

Hence,

$$\bar{\bar{p}}_{D2} = C_2{}' \, e^{+\sqrt{\left(\rho^2+\frac{s}{\eta_{D2}}\right)} \cdot y_D} + C_2{}' \, e^{-\sqrt{\left(\rho^2+\frac{s}{\eta_{D2}}\right)} \cdot y_D}$$

$0 \leq y_D < \infty$

Since it is infinite at **Region-2** from one side, unlike **Region-1**, y_D is $(+^{ve})$, therefore, to have the pressure decreasing with time, the power of "e" has to be negative, then it becomes:

Equation 36

$$\bar{\bar{p}}_{D2} = C_2 \, e^{-\sqrt{\left(\rho^2+\frac{s}{\eta_{D2}}\right)} \cdot y_D} \tag{36}$$

Applying to boundary conditions results in:

@ $y_D = 0$,

$p_{D1} = p_{D2} = p_{Df}$ And $\bar{\bar{p}}_{D1} = C_1$ (Region 1)

$p_{D1} = p_{D2} = p_{Df}$ And $\bar{\bar{p}}_{D2} = C_2$ (Region 2)

$\Rightarrow \bar{\bar{p}}_{D1} = \bar{\bar{p}}_{D2} = \bar{\bar{p}}_{Df} = C_1 = C_2$

3.5 Solving for Fractured Wellbore Pressure in Fourier Domain

Differentiating Equation 35; Region-1 & Equation 36; Region-2, (w.r.t.) y_D gives:

Region-1

$$\frac{d\bar{\bar{p}}_{D1}}{dy_D} = C_1.\sqrt{\left(\rho^2+\frac{s}{\eta_{D1}}\right)}\,.e^{+\sqrt{\left(\rho^2+\frac{s}{\eta_{D1}}\right)}\,.\,y_D}$$

Applying boundary conditions:

Equation 37

$$\Rightarrow \quad \left.\frac{d\bar{\bar{p}}_{D1}}{dy_D}\right|_{y_D=0} = C_1.\sqrt{\left(\rho^2+\frac{s}{\eta_{D1}}\right)} = \bar{\bar{p}}_{Df}.\sqrt{\left(\rho^2+\frac{s}{\eta_{D1}}\right)} \tag{37}$$

Region-2

$$\frac{d\bar{\bar{p}}_{D2}}{dy_D} = -C_2.\sqrt{\left(\rho^2+\frac{s}{\eta_{D1}}\right)}\,.e^{-\sqrt{\left(\rho^2+\frac{s}{\eta_{D1}}\right)}\,.\,y_D}$$

Applying to boundary conditions:

Equation 38

$$\Rightarrow \quad \left.\frac{d\bar{\bar{p}}_{D2}}{dy_D}\right|_{y_D=0} = -C_2.\sqrt{\left(\rho^2+\frac{s}{\eta_{D2}}\right)} = -\bar{\bar{p}}_{Df}.\sqrt{\left(\rho^2+\frac{s}{\eta_{D2}}\right)} \tag{38}$$

Substitute Equation 37 & Equation 38 in Equation 32*:*

$$-\rho^2\,\bar{\bar{p}}_{Df} + \frac{1}{F_{CD}}\left[-(k_{D2})\cdot\bar{\bar{p}}_{Df}.\sqrt{\left(\rho^2+\frac{s}{\eta_{D2}}\right)} - (k_{D1})\cdot\bar{\bar{p}}_{Df}.\sqrt{\left(\rho^2+\frac{s}{\eta_{D1}}\right)}\right] + \frac{2\pi}{F_{CD}\cdot s}\cdot$$

$$\frac{1}{\sqrt{2\pi}} = \left(\frac{s\cdot\bar{\bar{p}}_{Df}}{\eta_{Df}}\right)$$

Solve for $\bar{\bar{p}}_{Df}$:

Equation 39

$$\Rightarrow \quad \bar{\bar{p}}_{Df} = \frac{\sqrt{2\pi}}{s.\left[F_{CD}.\left(\rho^2+\frac{s}{\eta_{Df}}\right)+(k_{D1}).\sqrt{\left(\rho^2+\frac{s}{\eta_{D1}}\right)}+(k_{D2}).\sqrt{\left(\rho^2+\frac{s}{\eta_{D2}}\right)}\right]} \tag{39}$$

Take inverse of Fourier transformation with respect to (ρ) for reverting it back to the variable (x_D) in Laplace domain:

from

$F^{-1}\left\{\overline{\overline{p}}_{Df}\right\} = \frac{1}{\sqrt{2\pi}} \int_{-\infty}^{\infty} \overline{\overline{p}}_{Df}\, e^{-i\rho x_D}\, d\rho = \overline{p}_{Df}\,(x_D, s)$, inverted back to Laplace space,

write

Equation 40

$$\overline{p}_{Df}\,(x_D = 0, s) = \frac{1}{\sqrt{2\pi}} \int_{-\infty}^{\infty} \overline{\overline{p}}_{Df}\, d\rho = \overline{p}_{wD}\,(s) \tag{40}$$

$$@\ x_D = 0 \ \ where, \ \ \overline{p}_{Df} = \overline{p}_{wD}$$

Substitute Equation 39 in Equation 40:

Equation 41

$$\overline{p}_{wD} = \frac{1}{s} \int_{-\infty}^{\infty} \frac{d\rho}{\left[\left(F_{CDf}\cdot\left(\rho^2+\frac{s}{\eta_{Df}}\right)\right)+\left((k_{D1})\cdot\sqrt{\left(\rho^2+\frac{s}{\eta_{D1}}\right)}\right)+\left((k_{D2})\cdot\sqrt{\left(\rho^2+\frac{s}{\eta_{D2}}\right)}\right)\right]} \tag{41}$$

3.6 Final Fractured Wellbore Pressure equation (Frac-model)

The above integration is an even function in (ρ) domain whilst (rho) cannot have negative values. The resultant expression for the wellbore pressure in Laplace domain is:

Equation 42

$$\overline{p}_{wD} = \frac{2}{s} \int_{0}^{\infty} \frac{d\rho}{\left[\left(F_{CDf}\cdot\left(\rho^2+\frac{s}{\eta_{Df}}\right)\right)+\left((k_{D1})\cdot\sqrt{\left(\rho^2+\frac{s}{\eta_{D1}}\right)}\right)+\left((k_{D2})\cdot\sqrt{\left(\rho^2+\frac{s}{\eta_{D2}}\right)}\right)\right]} \tag{42}$$

where:

η_{Df}, η_{D1} and η_{D2} are the dimensionless hydraulic diffusivity of fracture, Region-1 and Region-2, respectively, defined as:

$$\eta_{Df} = 0.000264 \cdot \left(\frac{(\varphi\ c_t\ \mu)_f}{k_f} \cdot \frac{k_{rf}}{(\varphi\ c_t\ \mu)_{rf}}\right) = 0.000264 \cdot \left(\frac{\eta_{rf}}{\eta_f}\right)$$

$$\eta_{D1} = \left(\frac{(\varphi\ c_t\ \mu)_1}{k_1} \cdot \frac{k_r}{(\varphi\ c_t\ \mu)_{r1}}\right) = \left(\frac{\eta_r}{\eta_1}\right)$$

$$\eta_{D2} = \left(\frac{(\varphi\ c_t\ \mu)_2}{k_2} \cdot \frac{k_r}{(\varphi\ c_t\ \mu)_{r2}}\right) = \left(\frac{\eta_r}{\eta_2}\right)$$

F_{CDf} is the dimensionless fracture conductivity described by:

$$F_{CDf} = \frac{k_f w_f}{k_{rf} r_w}$$

The fracture's reference permeability is the arithmetic average of the two adjoining regions (the well is located in the centre between the two regions):

$$k_{rf} = \frac{k_1 + k_2}{2},$$

The region's reference permeability is:

$$k_r = 1.0\ md,$$

And (k_{d1}) & (k_{d2}) are the dimensionless permeabilities for Regions 1 and 2:

$$k_{D1} = \frac{k_1}{k_r},\ k_{D2} = \frac{k_2}{k_r}.$$

3.7 Computer Coding

Frac-model Code: MATLAB software package was used to code the solution in the dimensionless form. The code is capable of running an unlimited number of different scenarios required to generate type curves which can be used to match pressure data of field cases. It also accounts for specific properties for the fracture and the two regions.

3.7.1 Handling Dimensionless Skin and Wellbore Storage (WBS)

Moreover, the solution is enabled with dimensionless skin and wellbore storage (WBS) using Kucuk and Ayestaran (1985) dimensionless equations and limited to positive skin only:

$$\overline{p}_{wD}\big|_{skin} = \overline{p}_{wD} + \frac{\text{skin}}{\text{s}}$$

$$\overline{p}_{wD}\big|_{WBS} = \frac{\overline{p}_{wD}}{1+C_D \cdot \text{s}^2 \cdot \overline{p}_{wD}},$$

where s is the Laplace parameter.

3.7.2 Solution Scenarios

The code is capable of handling:

- An Infinite-acting homogenous reservoir,
- A Finite conductivity, fractured well in homogenous reservoir,
- A Finite conductivity, fractured well between two reservoirs with different mobilities.

3.7.3 Solution Parameters

The solution will provide the following results

- Reservoir permeabilities: (k_1 and k_2)
- Dimensional fracture conductivity: $k_f \cdot w_f$
- Dimensionless fracture conductivity: ($F_{CDf} = \frac{k_f w_f}{k_{rf}\ r_w}$)

3.8 Overall Solution Behaviour: Observations and Discussions

The type curve solution of dimensionless pressure-derivative versus dimensionless time for different dimensionless fracture conductivity has been plotted in Figure 20, using Villinger's (1985) numerical inversion from the Laplace transform. The solution shows

some distinctive features: fractured-well pressure behaviour at early times, where the curve signifies a ¼ slope as a result of a bilinear flow reflecting two linear flow regimes along and into the fracture. Finally, a homogenous total behaviour, with an infinite acting radial flow (IARF) derivative stabilisation.

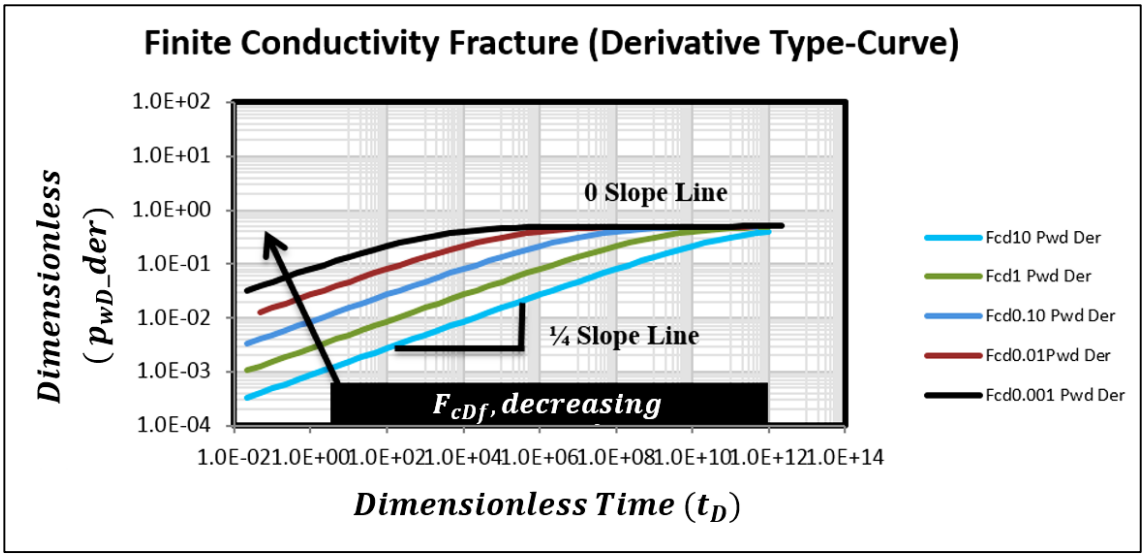

Figure 20: Type-curve by the Frac-model of dimensionless pressure-derivative versus dimensionless time for different dimensionless fracture conductivity.

The combined dimensionless pressure and pressure-derivative versus dimensionless time for different dimensionless fracture conductivity has been plotted in Figure 21.

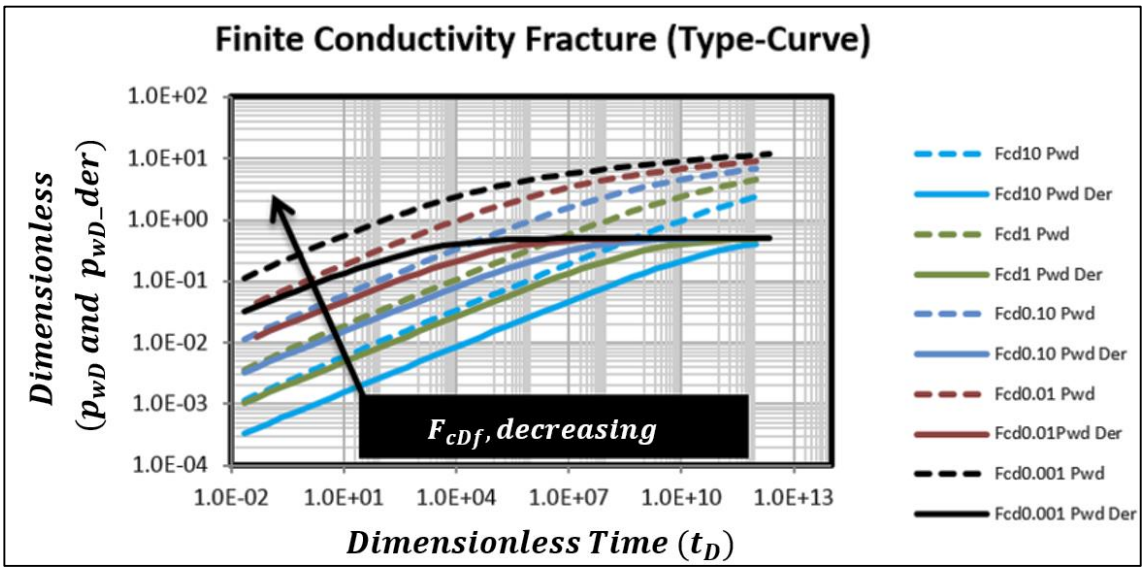

Figure 21: Type-curve by the Frac-model of dimensionless pressure and pressure-derivative versus dimensionless time for different dimensionless fracture conductivity.

Looking more closely at the type curves shown in Figure 22, it is noted that the pressure derivative curve exhibits a distinctive feature of an early fracture linear flow regime at a very early time (from $1e^{-8}$ to $1e^{-10}$). This feature, 1/2 slope, reflects the first fluid flow into the well from the fracture only, and validates the stability of the solution at very early times. It is worth mentioning that the normal operating hours are shaded from (from $2.8e^{1}$ to $6.7e^{7}$).

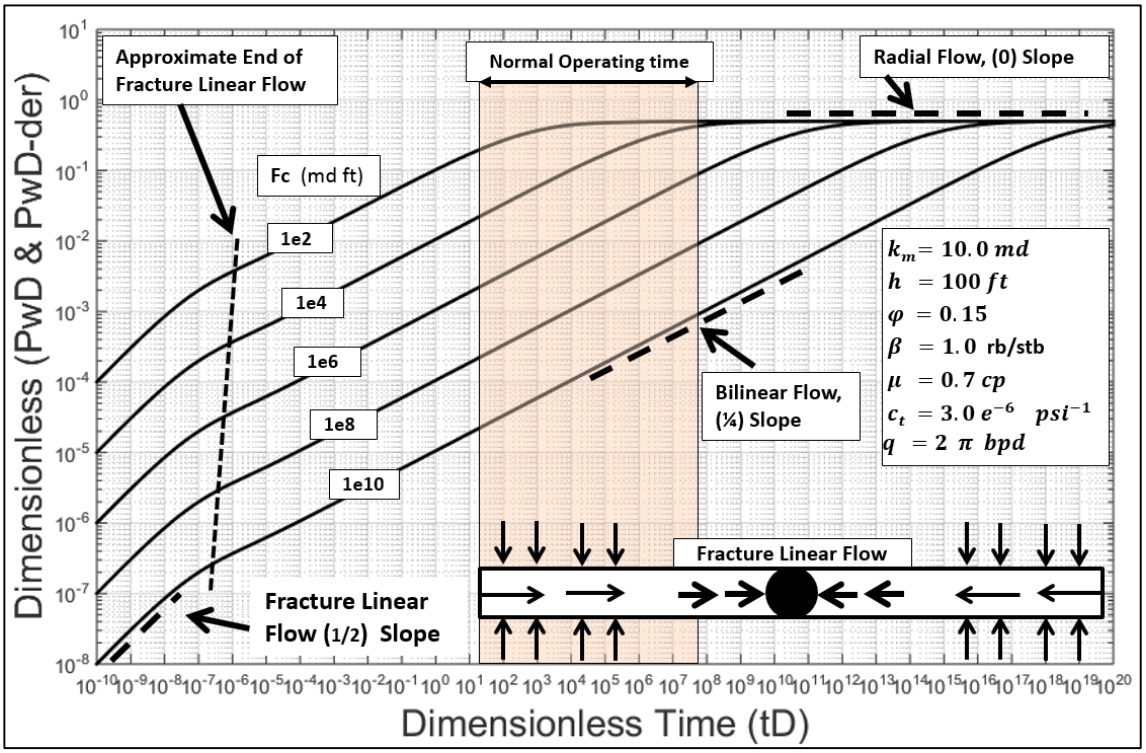

Figure 22- Dimensionless time vs. dimensionless pressure derivative exhibiting the Early Fracture Linear Flow regime by the Frac-model.

Fracture linear flow without matrix flow

According to Wattenbarger et al. (1998), "decline curves for tight gas wells show that linear flow may last for over 10 or 20 years. These decline curves may show outer boundary effects but no pseudo-radial flow" and they suggest that "a good assumption for large dimensionless fracture conductivity is F_{CD} >50". This is true for tight reservoirs; however, in cases where the presence of natural fractures or exploited hydraulically fractures, it is expected to obtain a fracture-flow domination, fracture-linear flow, and only a very weak matrix support may be obtained. However the present general solution, Frac-model, can handle the specific scenario proposed by Wattenbarger et al. (1998). That is, to only investigate the fracture linear flow

behaviour, the author assumed that the flow rate per unit area of the matrix permeabilities from both regions is approaching zero:

If:

$$\frac{\partial^2 p_{Df}}{\partial {x_D}^2} + \frac{1}{F_{CDf}}\left[(k_{D2}) \cdot \left.\frac{\partial p_{D2}}{\partial y_D}\right|_{y_D=0} - (k_{D1}) \cdot \left.\frac{\partial p_{D1}}{\partial y_D}\right|_{y_D=0}\right] + \frac{2\pi}{F_{CD}} \cdot \delta(x_D - a) = \left(1/\eta_{Df}\right) \cdot \frac{\partial p_{Df}}{\partial t_{Df}}$$

and

$$(k_{D2}) \cdot \left.\frac{dp_{D2}}{dy_D}\right|_{y_D=0} - (k_{D1}) \cdot \left.\frac{dp_{D1}}{dy_D}\right|_{y_D=0} \cong Zero$$

then:

$$F_{CDf} \cdot \frac{\partial^2 p_{Df}}{\partial {x_D}^2} + 2\pi \cdot \delta(x_D - a) = F_{CDf} \cdot \left(1/\eta_{Df}\right) \cdot \frac{\partial p_{Df}}{\partial t_{Df}}$$

$$\frac{\partial^2 p_{Df}}{\partial {x_D}^2} + \frac{2\pi \cdot \delta(x_D - a)}{F_{CDf}} = \cdot \left(1/\eta_{Df}\right) \cdot \frac{\partial p_{Df}}{\partial t_{Df}}$$

Laplace form: $\frac{\partial^2 \overline{p}_{Df}}{\partial {x_D}^2} + \frac{2\pi}{F_{CD} \cdot s} \cdot \delta(x_D - a) = \left(\frac{s \cdot \overline{p}_{Df}}{\eta_{Df}}\right)$

Laplace form: $-\rho^2 \, \overline{\overline{p}}_{Df} + \frac{2\pi}{F_{CD}\, s} \cdot \frac{1}{\sqrt{2\pi}} = \left(\frac{s \cdot \overline{\overline{p}}_{Df}}{\eta_{Df}}\right)$

Then:

Equation 43

$$\Rightarrow \quad \overline{p}_{Df} = \frac{2}{s} \int_0^\infty \frac{d\rho}{\left(F_{CDf} \cdot \left(\rho^2 + \frac{s}{\eta_{Df}}\right)\right)} \tag{43}$$

The dimensionless pressure and pressure-derivative versus dimensionless time for several fracture linear-flow (only) cases with different fracture conductivity are shown in Figure 23. The solution correctly shows the 1/2 slope lines dominating the entire flow period.

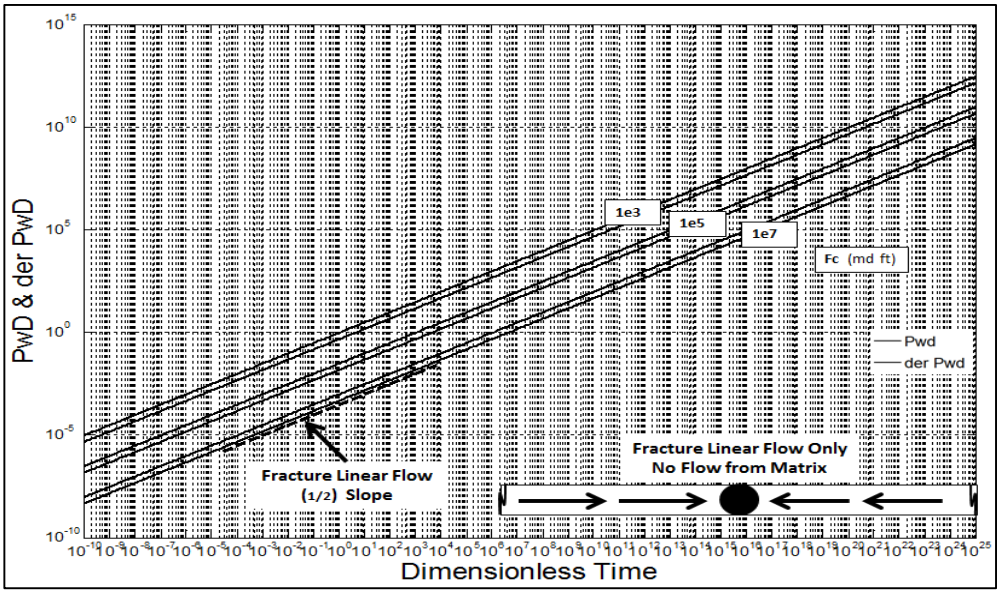

Figure 23 Fracture Linear Flow only in the case of no matrix flow into fracture by the Frac-model.

Fracture skin and wellbore storage

As mentioned above, the solution code is also empowered with dimensionless skin and wellbore storage (WBS) using Kucuk and Ayestaran's (1985) dimensionless equations. Such a scenario, albeit limited to positive skin only, is shown in Figure 24. It correctly shows the unit-slope and transition solution signatures of positive wellbore storage prior to ¼ bi-linear signature.

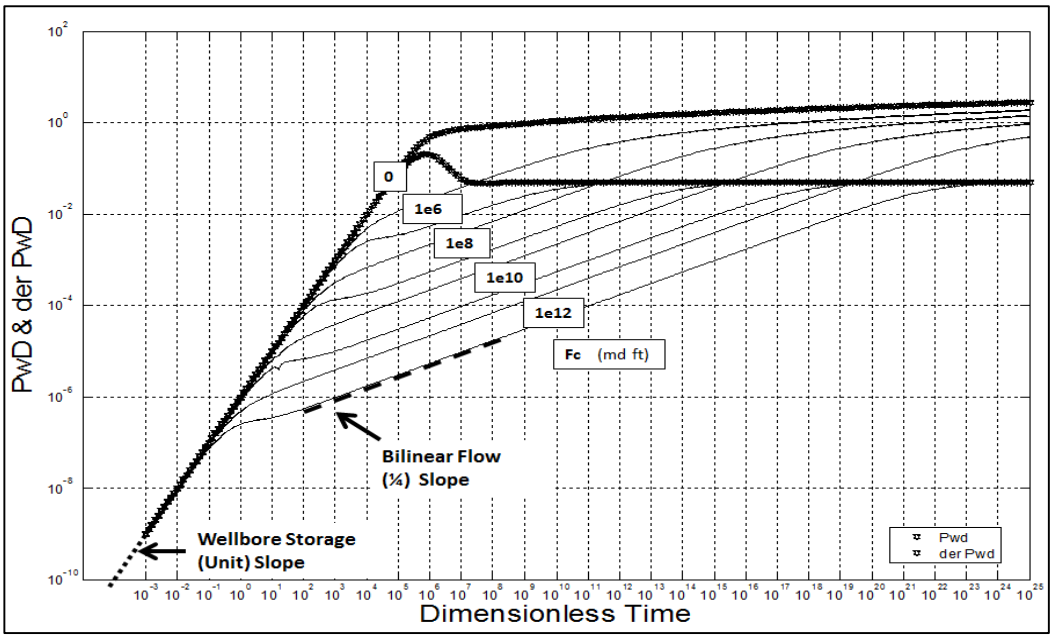

Figure 24- Dimensionless time vs. dimensionless pressure and pressure derivative, by the Frac-model, with Wellbore Storage using Kucuk and Ayestaran's (1985) dimensionless equations.

3.8.1 Sensitivity runs

Fractured well bounded by two similar regions: Case 1

The type curve solution of dimensionless pressure and its log-derivative versus dimensionless time for different dimensionless fracture conductivity in **a symmetric reservoir** ($k_1 = k_2$) has been plotted in Figure 25. *Table 1*, summarises well and reservoir properties. Here, both regions have similar permeabilities of $10\ md$ and thus the arithmetic average is also $10\ md$ with varying fracture conductivities, i.e. F_{Cf} =$1e^6, 1e^8, 1e^{10}\ and\ 1e^{12}\ md\ ft$. This case is compared to another case, of a well located in a homogenous reservoir (without a fracture) with a similar reservoir permeability. The solution correctly shows the ¼ slope bilinear flow signatures followed by the middle time stabilisation corresponding to the symmetric reservoir.

Table 1: Well and reservoir properties of the field data set-1.

Property	Value
Wellbore Radius, ft	0.3
Pay Zone, ft	100.0
Porosity, %	15.0
Formation Volume Factor, bbl/STB	1.0
Viscosity, cp	0.7
Total Compressibility, psi^{-1}	3. $0e^{-6}$

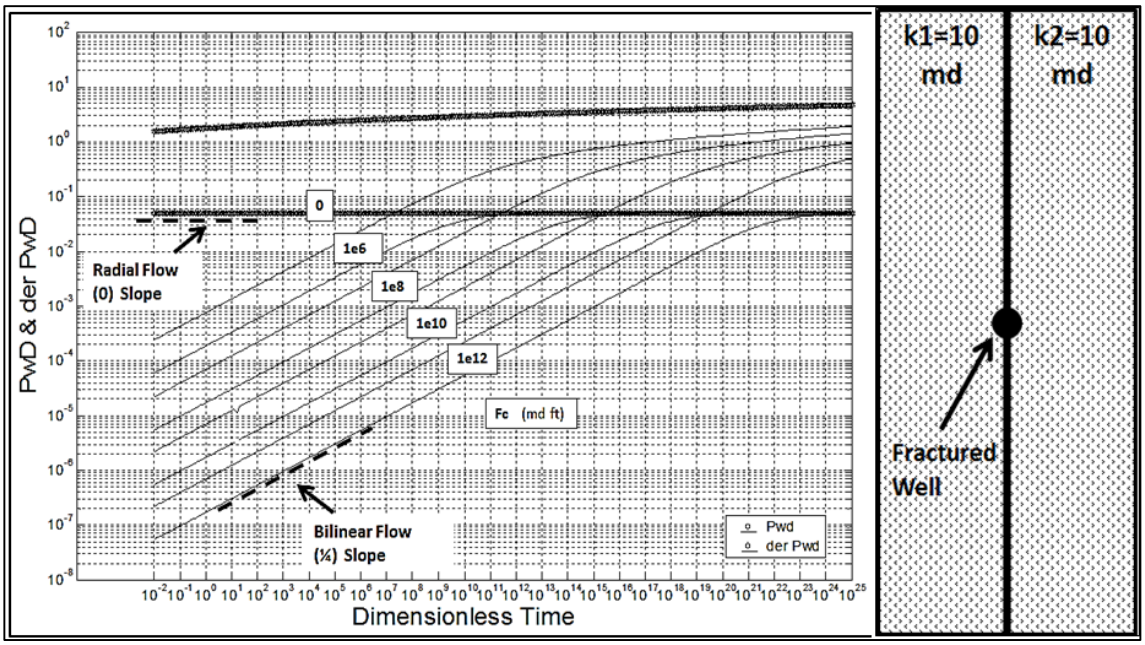

Figure 25- Dimensionless time vs. dimensionless pressure and pressure derivative curves by the Frac-model.

Fractured well bounded by two different regions: Case 2

For the same well and reservoir properties of the above example, Table 1, a synthetic case of a fractured-well ($F_{Cf} = 1e^6 md\ ft$) in **an asymmetric reservoir** was studied, where Region-1 and Region-2's permeabilities are 5 md and 15 md, respectively, and the average permeability calculated from this solution is the arithmetic average of 10 md. Again, it is compared to another case, of a well located in a homogenous reservoir (without a fracture) with an average reservoir permeability of 10 md. By superimposing the two pressure derivatives of both cases, a perfect overlay is achieved over the radial flow period, confirming the reliability of the average permeability calculation method by this solution, Figure 26. This was predicted, as the well is located in the centre, between the two regions.

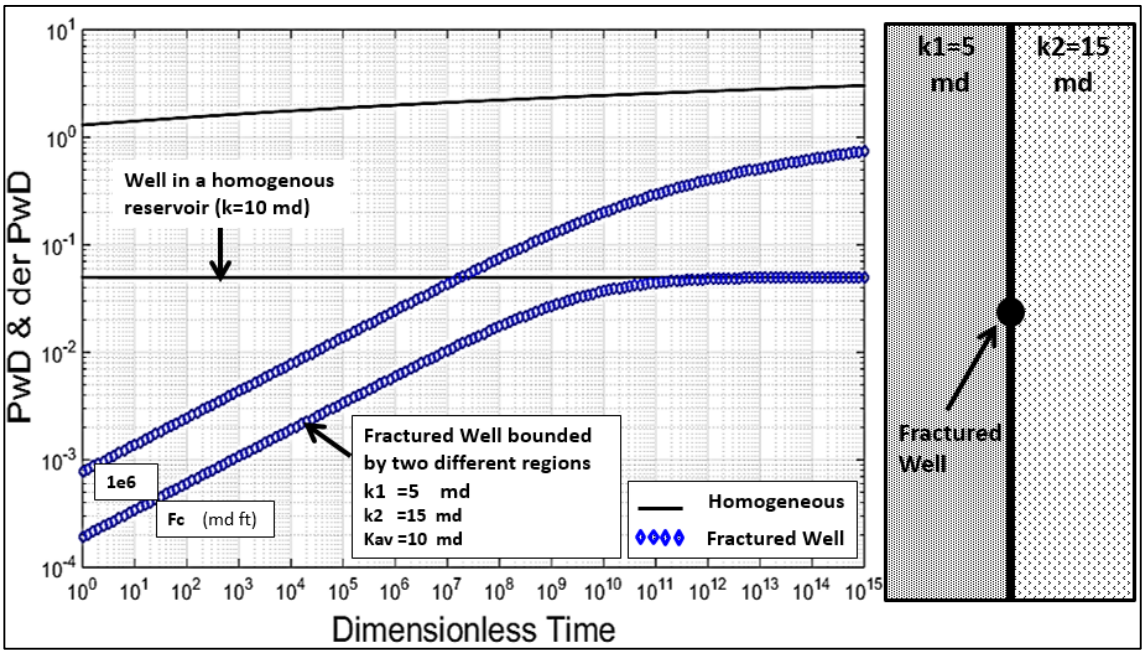

Figure 26- Derivative overlay of a vertical well in a homogenous reservoir and a fractured well in an asymmetric reservoir, by the Frac-model, where both reservoirs have the same average permeability of 10 md.

Summary

Chapter 3 has discussed the development of a semi-analytical solution to a fractured-well with a finite conductivity fracture separating two regions of different mobilities. A new solution is proposed to handle a finite conductivity fracture in **symmetric and asymmetric** reservoirs (two different regions bounding the fracture plane) accounting for the flow in the reservoir along the x-y plane. Here, the flow domain of the statement problem has been divided into three flow regions namely: (i) a reservoir Region-1, with its specific properties, that defines flow into the fracture from Region -1 in both x- and y-planes, (ii) a fracture, of infinite length, with its specific fracture properties, which allows fluids to flow along the fracture and towards the well and (iii) a reservoir Region-2, with its specific properties, that defines the fluid flow into the fracture from the top in the **x-y plane**.

The governing equations corresponding to these three flow regions were derived and converted to dimensionless form, which were then further simplified in the time and space domains by taking the Laplace and Fourier transformations, respectively. Since the flow domain is semi-infinite at Regions-1 and 2, the Helmholtz equation was used to further reduce the complexity of the solution and led to the resultant expression for the wellbore pressure in the Laplace domain. It should be noted that the assumed finite conductivity fracture dictates a non-uniform inflow-flux distribution along the fracture plane, as the fracture pressure (p_f) is smaller close to the well and larger towards the tip, or end of formation flow. The fracture half-length is assumed to be infinite, whereas the effective fracture half-length (x_f) is finite. The flux distribution and the effective half-length determination will be discussed in the next chapter. The corresponding type curves of dimensionless time and pressure were presented. The pressure derivative curve exhibits a distinctive feature of an early fracture linear flow regime at a very early time. This feature reflects the first fluid flow into the well from the fracture only, and validates the stability of the solution at very early times. This is followed by the characteristics of a bilinear slope (flow along and into the fracture), demonstrating the fracture characteristics, and then by a radial flow, zero slope, articulating the quality of the two reservoirs.

The next chapter will discuss an added complexity to the solution by solving for a fractured-well near finite conductivity fault in a three-region linear composite reservoir.

CHAPTER 4 – SEMI-ANALYTICAL SOLUTION TO A WELL INTERSECTING A FINITE CONDUCTIVITY FRACTURE NEAR A FINITE CONDUCTIVITY FAULT IN AN ASYMMETRIC RESERVOIR

4.1 Introduction

Complementing the efforts carried over from Chapters 3, here in Chapter 4, the reservoir is assumed to be asymmetric with a fractured well and a fault. The asymmetry is represented by three regions of different quality separating the fracture and the fault. Regions 1 and 2 are bounding the fractured well, whereas Regions 2 and 3 bound the fault nearby, Figure 27. This new model is defined as the "FracFault" model.

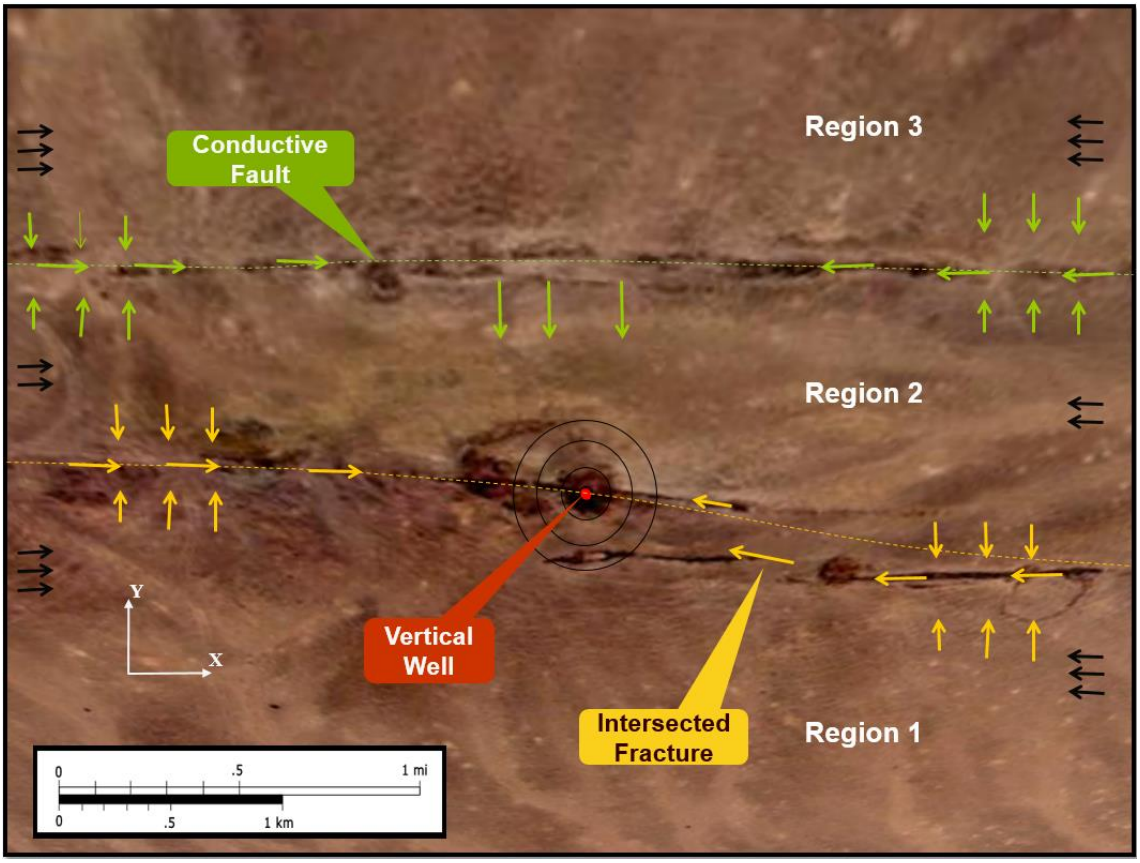

Figure 27: An aerial outcrop image (50 km north of Riyadh), describes the flow problem of the FracFault-model.

The proposed semi-analytical solution presented here offers general schemes to easily carry out modelling of such scenarios with increasing certainty and enhanced positive impact on management decisions regarding such reservoirs and is in-line with meeting the current needs of the industry. Furthermore, it serves as a good platform to address

the more general case of the presence of a fault with differing quality reservoir units across the fault plane. The proposed solution is supplemented by type curves of dimensionless time and pressure. The integrity is verified with synthetic models along with analytically and numerically built models, in addition to real field data.

The solution assumes an infinite outer reservoir boundary and lengths of both the fracture and fault. Regions 1 and 3 are semi-infinite on the y-axis, while, Region 2 is separating the fracture and fault, hence finite along y-axis, Figure 28. The quality of the regions (flow units) across the fault and the fractured-well, can be presented with different fracture, fault and reservoir properties.

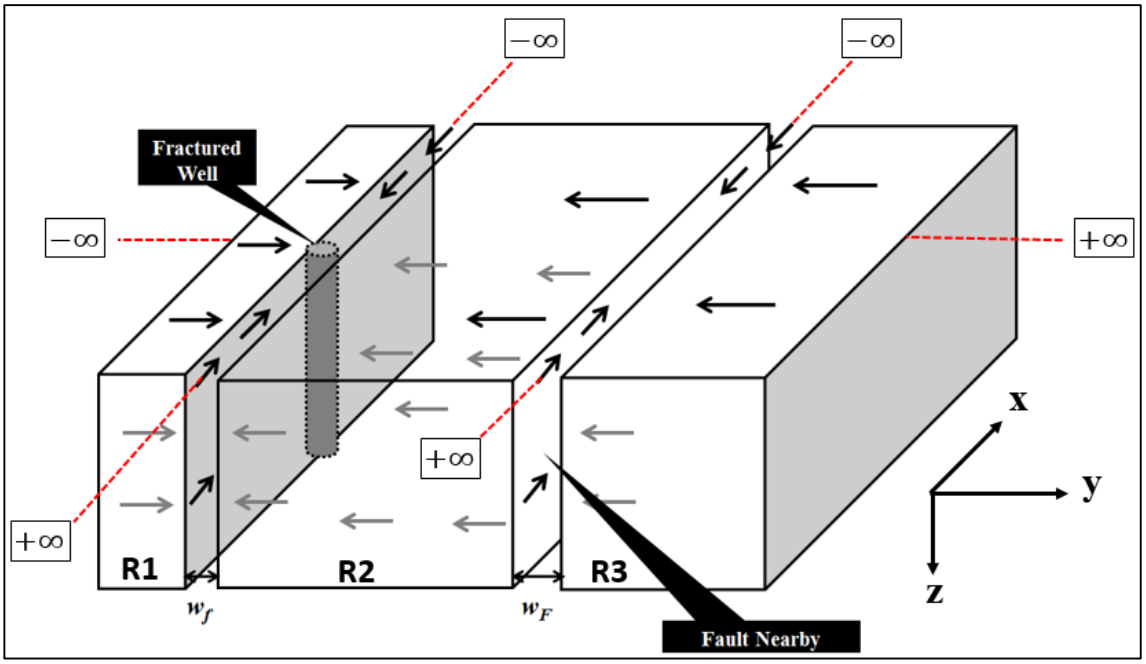

Figure 28: A 3-D sketch representing the model geometry of the FracFault.

4.2 Mathematical narrative

The flow domain of the statement problem has been divided into five flow areas namely: (i) reservoir Region-1 , with its specific properties, that defines the flow from the un-faulted side into and around the fractured well, (ii) well intersecting a finite conductivity Fracture, (iii) reservoir Region-2, with its specific properties which defines the flow between the fracture and the fault nearby, (iv) the finite conductivity fault nearby (with its specific properties), which allows fluids to flow along, across and towards the fracture and (v) reservoir Region-3, with its specific properties which defines flow into from beyond the fault.

The flow per unit area towards the well is defined to be positive from the faulted side and negative from the un-faulted side. It should be noted that the author's aim is to have a solution to the pressure versus time and space in general and wellbore pressure with time in particular. The task is designed to carry out a detailed analysis of the physics and propose an appropriate semi-analytical solution to the flow problem. This is achieved by:

- Deriving the equation for each region separately, converting variables to dimensionless forms and solving all five equations for the pressure at the well in both Laplace and Fourier domains for the following cases:
  a. Fractured-well in an asymmetric reservoir.
  b. Flux distribution and effective half-length estimation.
  c. Fractured-well in a symmetric reservoir with a finite conductivity fault nearby (parallel to the fractured well).
  d. Fractured-well in a two-region linear composite reservoir with a finite conductivity fault nearby.
  e. Fractured-well in a three-region linear composite reservoir with a finite conductivity fault nearby.

In a well-defined systematic approach, the model is simplified by adding the above mentioned reservoir units one at a time.

4.3 Mathematical Solution Set-up

The solution to the equations describing this flow problem presented in Figure 29, is divided into five regions namely:

1. **Region-1**: the reservoir of the un-faulted side with permeability k_1 and pressure p_1.
2. **Fractured Well**: fractured-well with fracture permeability $\boldsymbol{k}_{\mathrm{f}}$, fracture width $\mathrm{w_f}$ and fracture pressure p_{f}.
3. **Region-2:** the reservoir between fracture and fault with permeability $\mathrm{k_2}$and pressure $\mathrm{p_2}$.
4. **Fault**: nearby fault with fault permeability $\mathrm{k_F}$, fracture width $\mathrm{w_F}$ and fault pressure p_F.
5. **Region-3:** the reservoir beyond the fault with permeability $\mathrm{k_3}$and pressure $\mathrm{p_3}$.

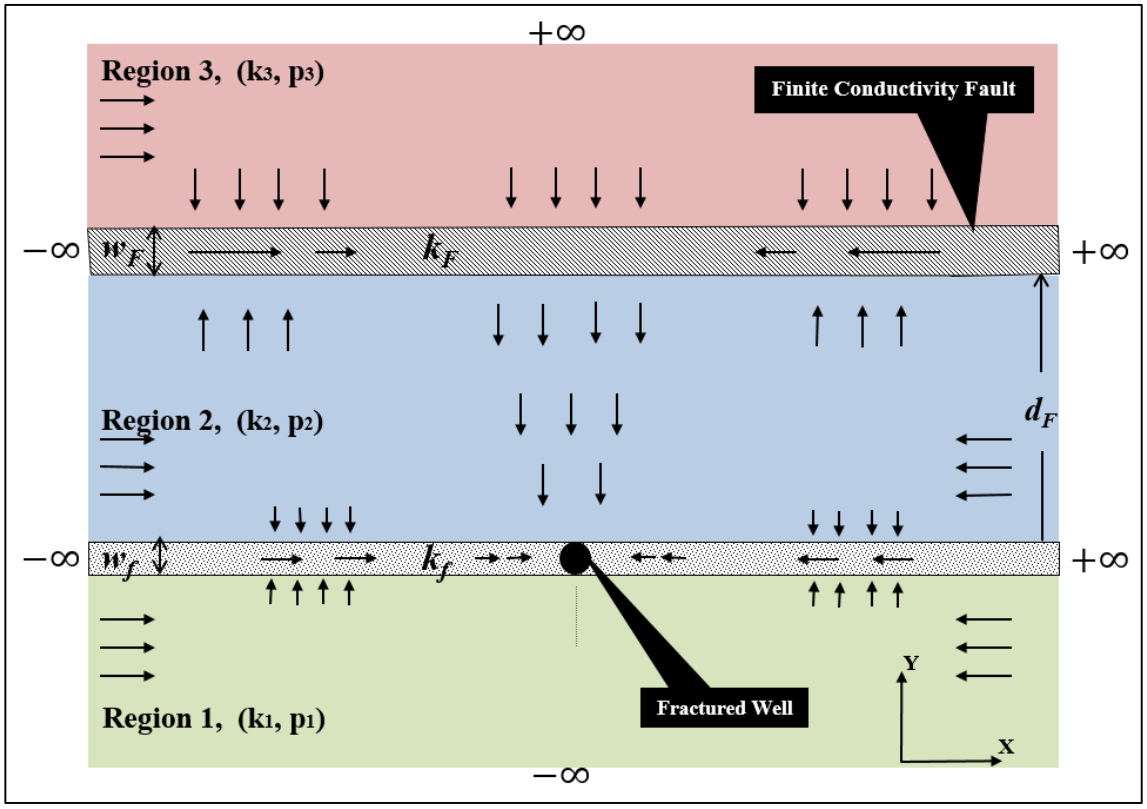

Figure 29: Definition sketch of the FracFault-model solution.

4.4 Diffusivity Equations

4.4.1 Solution Assumptions

The well model solution adopts the following assumptions:

- Vertical well penetrating a horizontal layer with an infinite drainage domain.
- The drainage domain is divided into three composite regions (fracture and fault are splitting the three regions) of similar properties.
- The porous volume is bounded by top and bottom impermeable boundaries.

$(\frac{dp}{dz}\Big|_{z=0} = 0)$ and $(\frac{dp}{dz}\Big|_{z=h} = 0)$.

- Initially (at time zero) at constant pressure $(p_{(x,\ y)}\ |_{t=0} = p_i)$.
- Fracture and faults are infinite in length, but semi-infinite along y-axis;
  Region 1: $(-\infty < y < 0)$,
  Region 2: $(0 < y < d_F)$, *and*
  Region 3: $(d_F < y < \infty)$.

- Production occurs through a fully penetrating "uneven flux" vertical fracture with fracture conductivity of ($k_f.w_f$).
- Reservoirs are homogenous and isotropic within each side of the fracture and reservoir.
- Single phase slightly compressible fluid (c_f), flows from porous media to the fracture with constant viscosity (μ_f) and formation volume factor (B).
- Reservoir total compressibility is (c_t)
- Fluid properties are independent of pressure.
- Gravity and capillary forces are neglected.

4.4.2 Fractured-well diffusivity equation between two linear-composite reservoir

In this chapter Regions 1, 2 and 3 are of different permeabilities:

$$\boldsymbol{k_{D1} \neq k_{D2} \neq k_{D3}}$$

Moreover, the flowrate from each region is not the same, as some of the fluid, from Region-2, is prone to flow towards the fault and the fractured well:

$$u_1 \neq u_2 \neq u_3$$

$$\Rightarrow \frac{dp_{D1}}{dy_D} \neq \frac{dp_{D2}}{dy_D} \neq \frac{dp_{D3}}{dy_D}$$

Hence, the fracture diffusivity equation for asymmetric reservoir is the same as Equation 26:

$$\frac{\partial^2 p_{Df}}{\partial {x_D}^2} + \frac{1}{F_{CD_f}}\left[(k_{D2}) \cdot \frac{\partial p_{D2}}{\partial y_D}\Big|_{y_D=0} - (k_{D1}) \cdot \frac{\partial p_{D1}}{\partial y_D}\Big|_{y_D=0}\right] + \frac{2\pi}{F_{CD_f}} \cdot \delta(x_D - a) = \left(1/\eta_{Df}\right) \cdot \frac{\partial p_{Df}}{\partial t_{Df}} \quad 31$$

Where,

$$k_{D1} = \frac{k_1}{k_r}, k_{D2} = \frac{k_2}{k_r}, k_r = 1.0$$

$$F_{CDf} = \frac{k_f \ w_f}{k_{rf} \ r_w}, \text{ where } k_{rf} = \frac{k_1 + k_2}{2}$$

$$\eta_{Df} = \left(\frac{(\varphi \ c_t \ \mu)_f}{k_F} \cdot \frac{0.000264 \cdot k_{rf}}{(\varphi \ c_t \ \mu)_{rf}}\right) = 0.000264 \cdot \left(\frac{\eta_{rf}}{\eta_f}\right)$$

4.4.3 Finite Conductivity Fault in an Asymmetric Reservoir

Figure 30 clarifies the statement problem for flow within the fault:

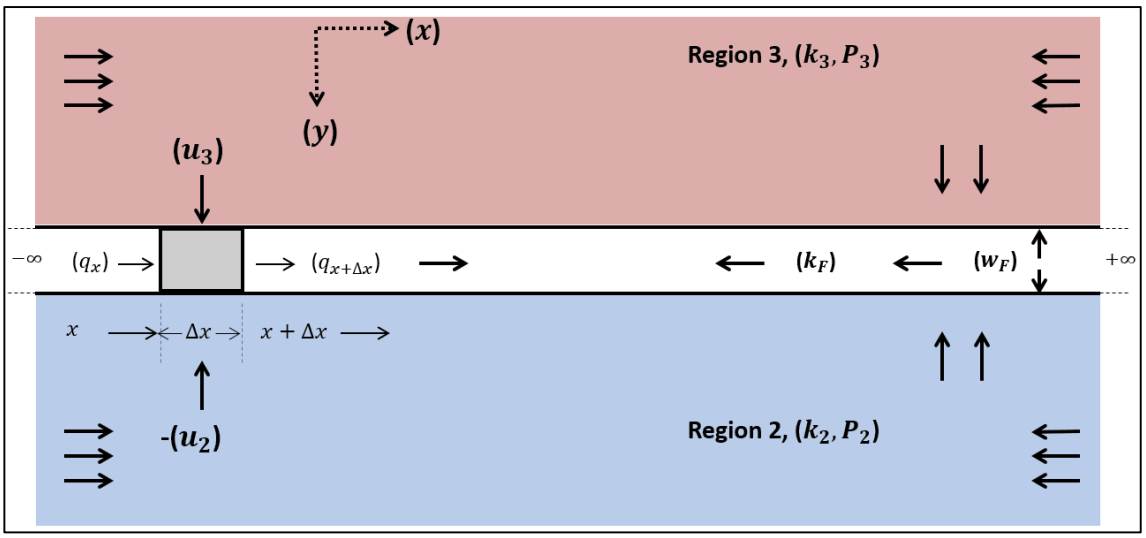

Figure 30: Schematic of flow distribution for a finite conductivity fault in bounded by an asymmetric reservoir.

In this figure, (u_2&u_3) are flow per unit area $\left(u = \frac{q}{A}\right)$, assuming a constant (non-uniform) flux along the fault plane, from the reservoir ($A = h \cdot \Delta x$).

Similarly, as in (Appendix-A), for slightly compressible fluid:

(Mass-in / Time) – (Mass-out / Time) = (Mass-Accumulation / Time)

$$(q_x \cdot \rho_x) - (q_{x+\Delta x} \cdot \rho_{x+\Delta x}) + u_2(h \cdot \Delta x) \cdot \rho_y + u_3(h \cdot \Delta x) \cdot \rho_y = q_{\Delta x} \cdot \rho_{\Delta x}$$

Multiply by Δt

$$(q_x \cdot \Delta t) - (q_{x+\Delta x} \cdot \Delta t) + (u_2 + u_3) \cdot (h \cdot \Delta x) \cdot \Delta t = q_{\Delta x} \cdot \Delta t = \Delta v$$

$$\left(q_x - q_{x+\Delta x}\right) \cdot (\Delta t) + (u_2 + u_3) \cdot (h \cdot \Delta x) \cdot \Delta t = cv\, \Delta p = c \cdot (w_F \cdot h \cdot \Delta x \cdot \varphi) \cdot (p_{t+\Delta t} - p_t)$$

Divide by $(\Delta x \cdot \Delta t)$ and take limit as $\Delta x \to 0$ & $\Delta t \to 0$:

$$-\lim_{\Delta x \to 0}\left(\frac{q_{x+\Delta x} - q_x}{\Delta x}\right) + (u_2 + u_3) \cdot (h) = c \cdot (w_F \cdot h \cdot \varphi) \lim_{\Delta t \to 0}\left(\frac{p_{t+\Delta t} - p_t}{\Delta t}\right)$$

Equation 44

$$-\frac{dq}{dx}+(u_2+u_3)\cdot(h)=c\cdot(w_F\cdot h\cdot\varphi)\frac{dp_F}{dt} \quad (44)$$

Introduce Darcy's law:

$$q=-\frac{k_F A}{\mu}\cdot\frac{dp_F}{dx},\ along\ fault$$

Differentiate both sides w.r.t. x:

$$\frac{d}{dx}\cdot q=-\frac{k_F A}{\mu}\cdot\left(\frac{d}{dx}\cdot\frac{dp_F}{dx}\right)$$

Equation 45

$$\frac{dq}{dx}=-\frac{k_F A}{\mu}\cdot\left(\frac{d^2p_F}{dx^2}\right) \quad (45)$$

Substitute Equation 45 in Equation 44:

$$\frac{k_F A}{\mu}\cdot\left(\frac{\partial^2 p_F}{\partial x^2}\right)+(u_2+u_3)\cdot(h)=c\cdot(w_F\cdot h\cdot\varphi)\frac{\partial p_F}{\partial t}$$

Since, $A=w_F\cdot h$, then:

$$\frac{k_F}{\mu}\cdot w_F\left(\frac{\partial^2 p_F}{\partial x^2}\right)+(u_2+u_3)=c\cdot(w_F\cdot\varphi)\frac{\partial p_F}{\partial t}$$

Re-arrange two dimensional diffusivity equations for fluid flowing along fracture plane per unit area:

$$\frac{\partial^2 p_F}{\partial x^2}+(u_2+u_3)\cdot\frac{\mu}{w_F\cdot k_F}=\frac{c\mu\varphi}{k_F}\cdot\left(\frac{\partial p_F}{\partial t}\right)$$

Or:

Equation 46

$$\frac{\partial^2 p_F}{\partial x^2}+(u_2+u_3)\cdot\frac{\mu}{w_F\cdot k_F}={}^{1}\!/_{\eta_F}\cdot\left(\frac{\partial p_F}{\partial t}\right) \quad (46)$$

Now**:**

From Darcy's equation:

For (u_2):

Equation 47

$$u_2 = \frac{q}{A} = -\frac{k_2}{\mu} \cdot \frac{dp_2}{dy}\Big|_{y \to d_F}, \text{Flow from } \mathbf{Region - 2} \text{ into fault (oppisite direction)} \quad (47)$$

For (u_3):

Equation 48

$$u_3 = \frac{q}{A} = \frac{k_3}{\mu} \cdot \frac{dp_3}{dy}\Big|_{y \to d_F}, \text{Flow from } \mathbf{Region - 3} \text{ into fault (normal direction)} \quad (48)$$

Substitute Equation 47 & Equation 48 into Equation 46 and re-arranging the equation:

Equation 49

$$\frac{\partial^2 p_F}{\partial x^2} + \frac{1}{k_F \cdot w_F}\left[k_3 \frac{\partial p_3}{\partial y}\Big|_{y=d_F} - k_2 \frac{\partial p_2}{\partial y}\Big|_{y=d_F}\right] = 1/\eta_F \cdot \left(\frac{\partial p_F}{\partial t}\right) \quad (49)$$

which is the diffusivity equation for a finite conductivity fracture,

where:

η_F: Hydraulic Diffusivity constant along fault

$F_{CF} = k_F \cdot w_F\ (md.ft)$: Fault conductivity, dimensional (md.ft)

$$1/\eta_F = C \cdot \frac{(\varphi \mu c_t)_F}{k_F},\ C = 0.000264$$

4.4.4 Convert variables to dimensionless form

$x_D = \frac{x}{r_w} \rightarrow x = r_w .\ x_D$, and $dx = r_w .dx_D$

$y_D = \frac{y}{r_w} \rightarrow y = r_w \ \cdot\ y_D$, and $dy = r_w .dy_D$

$t_{D_F} = \frac{0.000264\ k_{rF}\ t}{(\varphi \mu c_t)_F\ {r_w}^2}$, and $dt_{D_F} = \frac{0.000264\ k_{rF}}{(\varphi \mu c_t)_F\ {r_w}^2} \cdot dt$

Equation 50

$$\Rightarrow\ dt = \frac{(\varphi \mu c_t)_F \cdot {r_w}^2}{0.000264\ k_{rF}} \cdot dt_{D_F} \quad (50)$$

Flow along fault

$\frac{\partial^2 p_F}{\partial x^2}$:

$p_{DF} = \frac{k_{rF}\ .\ h[p_i - p_F]}{141.2\ q\beta\mu}$, $p_F = p_i - \frac{141.2\ q\beta\mu}{k_{rF} \cdot h}\ p_{DF}$ and $dp_F = -\frac{141.2\ q\beta\mu}{k_{rF} \cdot h}\ dp_{DF}$

And $\frac{dp_F}{dx} = 0 - \frac{141.2\ q\beta\mu}{k_{rF} \cdot h}\ \frac{dp_{DF}}{dx} = -\frac{141.2\ q\beta\mu}{k_{rF} \cdot h \cdot r_w}\ \frac{dp_{DF}}{dx_D}$, $(since\ dx = r_w\ \cdot\ dx_D)$

Equation 51

$$\frac{d^2 p_F}{dx^2} = -\frac{141.2\ q\beta\mu}{k_{rF}.h\ r_w.^2}\ \cdot\ \frac{d^2 p_{DF}}{dx_D{}^2} \tag{51}$$

Flow into fault:

($\frac{\boldsymbol{dp_1}}{\boldsymbol{dy}}$ & $\frac{\boldsymbol{dp_2}}{\boldsymbol{dy}}$)**:**

$p_{D1} = \frac{k_r h[p_i - p_1]}{141.2 q\beta\mu}$, $p_1 = p_i - \frac{141.2\ q\beta\mu}{k_r h}\ p_{D1}$

Then:

Equation 52

$$\frac{dp_2}{dy} = 0 - \frac{141.2\ q\beta\mu}{k_r h}\ \cdot\ \frac{dp_{D2}}{dy}\ = -\frac{141.2\ q\beta\mu}{k_r h\ r_w}\ \frac{dp_{D2}}{dy_D}\ ,\ (since\ dy = r_w\ \cdot\ dy_D) \tag{52}$$

Similarly:

Equation 53

$$\frac{dp_3}{dy} = 0 - \frac{141.2\ q\beta\mu}{k_r h}\ \cdot\ \frac{dp_{D3}}{dy}\ = -\frac{141.2\ q\beta\mu}{k_r h\ .\ r_w}\ \frac{dp_{D3}}{dy_D}\ ,\ (since\ \ dy = r_w\ \cdot\ dy_D) \tag{53}$$

Solve for transient pressure:

$\frac{\boldsymbol{dp_F}}{\boldsymbol{dt}}$**:**

$\frac{dp_F}{dt} = 0 - \frac{141.2\ q\beta\mu}{k_{rF}\ \cdot h}\ \cdot\ \frac{dp_{DF}}{dt}$

Substitute for dt from Equation 50:

Equation 54

$$\frac{dp_F}{dt} = -\frac{141.2\ q\beta\mu}{k_{rF} \cdot h}\ \cdot \frac{0.000264\ k_{rF}}{(\varphi\mu c_t)_F\ r_w{}^2} \cdot \frac{dp_{DF}}{dt_{D_F}} \tag{54}$$

substituting the dimensionless variables described by Equation 50 to Equation 54

in Equation 49:

Equation 55

$$-\frac{141.2\,q\beta\mu}{k_{rF}\cdot h\,{r_w}^2}\cdot\frac{d^2p_{DF}}{{dx_D}^2}+\frac{1}{k_F\cdot w_F}\left[-\frac{141.2\,q\beta\mu}{k_r h\cdot r_w}\cdot\left(k_3\left.\frac{dp_{D3}}{dy_D}\right|_{y=d_F}-k_2\left.\frac{dp_{D2}}{dy_D}\right|_{y=d_F}\right)\right]=$$

$$1/\eta_F\cdot\left(-\frac{141.2\,q\beta\mu}{k_{rF}\,h}\cdot\frac{0.000264\,k_{rF}}{(\varphi\mu c_t)_{rF}\;{r_w}^2}\right)\cdot\left(\frac{\partial p_F}{\partial t}\right) \quad (55)$$

gives the dimensionless form of PDE describing the flow along and into the fault, for asymmetric reservoirs:

Equation 56

$$\frac{\partial^2 p_{DF}}{\partial {x_D}^2}+\frac{1}{F_{CD_F}}\left[(k_{D3})\cdot\frac{\partial p_{D3}}{\partial y_D}-(k_{D2})\cdot\frac{\partial p_{D2}}{\partial y_D}\right]_{y_D=d_F}=(1/\eta_{DF})\cdot\frac{\partial p_{DF}}{\partial t_D} \quad (56)$$

where:

$k_{D2}=\frac{k_2}{k_r}$, $k_{D3}=\frac{k_3}{k_r}$ and $k_r=1.0\,md$

$d_F=distance\ to\ Fault\ (ft)$

$F_{CDF}=\frac{k_F\,w_F}{k_r\;r_w}$, $where\ k_{rF}=\frac{k_2+k_3}{2}$

$1/\eta_{DF}=\frac{1}{0.000264}\cdot\left(\frac{\eta_F}{\eta_{rF}}\right)$

4.4.5 Assemble the governing equations in space and time

The same equations as those presented in Chapter 3 for fracture and all three matrix regions, are listed below:

Region-1:

Equation 57

$$\frac{\partial^2 \mathrm{p_{D1}}}{\partial \mathrm{x_D}^2} + \frac{\partial^2 \mathrm{p_{D1}}}{\partial \mathrm{y_D}^2} = 1/\eta_{\mathrm{D1}} \cdot \left(\frac{\partial \mathrm{p_{D1}}}{\partial \mathrm{t_D}}\right) \tag{57}$$

(η_{D1}), capturing permeability of Region 1.

Fracture:

Equation 58

$$\frac{\partial^2 p_{Df}}{\partial {x_D}^2} + \frac{1}{F_{CD_f}}\left[(k_{D2}) \cdot \left.\frac{\partial p_{D2}}{\partial y_D}\right|_{y_D=0} - (k_{D1}) \cdot \left.\frac{\partial p_{D1}}{\partial y_D}\right|_{y_D=0}\right] + \frac{2\pi}{F_{CD_f}} \cdot \delta(x_D - a) = (1/\eta_{Df}) \cdot \frac{\partial p_{Df}}{\partial t_{Df}} \tag{58}$$

(k_{D1}) and (k_{D2}), capturing permeability of Region 1 and Region 2.

Region-2:

Equation 59

$$\frac{\partial^2 \mathrm{p_{D2}}}{\partial \mathrm{x_D}^2} + \frac{\partial^2 \mathrm{p_{D2}}}{\partial \mathrm{y_D}^2} = 1/\eta_{\mathrm{D2}} \cdot \left(\frac{\partial \mathrm{p_{D2}}}{\partial \mathrm{t_D}}\right) \tag{59}$$

(η_{D2}), capturing permeability of Region 2 only.

Fault:

Equation 60

$$\frac{\partial^2 p_{DF}}{\partial {x_D}^2} + \frac{1}{F_{CD_F}}\left[(k_{D3}) \ \frac{\partial p_{D3}}{\partial y_D} - (k_{D2}) \ \frac{\partial p_{D2}}{\partial y_D}\right]_{y_D=d_F} = (1/\eta_{DF}) \cdot \frac{\partial p_{DF}}{\partial t_D} \tag{60}$$

(k_{D2}) and (k_{D3}), capturing permeability of Region 2 and Regions 3.

Region-3:

Equation 61

$$\frac{\partial^2 \mathrm{p_{D3}}}{\partial \mathrm{x_D}^2} + \frac{\partial^2 \mathrm{p_{D3}}}{\partial \mathrm{y_D}^2} = 1/\eta_{\mathrm{D3}} \cdot \left(\frac{\partial \mathrm{p_{D3}}}{\partial \mathrm{t_D}}\right) \tag{61}$$

(η_{D3}), capturing permeability of Region 3 only.

Transformations

4.4.6 Laplace Transformation

Take the Laplace transform of all equations with respect to dimensionless time, t_{Df}, in terms of parameter (s):

Region-1

Equation 62

$$\frac{\partial^2 \overline{p}_{\mathrm{D1}}}{\partial {x_D}^2} + \frac{\partial^2 \overline{p}_{\mathrm{D1}}}{\partial {y_D}^2} = 1/\eta_{\mathrm{D1}} \cdot \left(s\overline{p}_{D1} - 0\right) \tag{62}$$

Fracture

Equation 63

$$\frac{\partial^2 \overline{p}_{Df}}{\partial {x_D}^2} + \frac{1}{F_{CD_f}}\left[(\boldsymbol{k_{D2}}) \cdot \frac{\partial \overline{p}_{D2}}{\partial y_D}\Big|_{y_D=0} - (\boldsymbol{k_{D1}}) \cdot \frac{\partial \overline{p}_{D1}}{\partial y_D}\Big|_{y_D=0}\right] + \frac{2\pi}{F_{CD_f} \cdot s} \cdot \boldsymbol{\delta(x_D - a)} = \left(\boldsymbol{1/\eta_{Df}}\right) \cdot \left(s\overline{p}_{Df} - 0\right) \tag{63}$$

Region-2

Equation 64

$$\frac{\partial^2 \overline{p}_{\mathrm{D2}}}{\partial {x_D}^2} + \frac{\partial^2 \overline{p}_{\mathrm{D2}}}{\partial {y_D}^2} = 1/\eta_{\mathrm{D2}} \cdot \left(s\overline{p}_{D2} - 0\right) \tag{64}$$

Fault:

Equation 65

$$\frac{\partial^2 \overline{p}_{DF}}{\partial {x_D}^2} + \frac{1}{F_{CD_F}}\left[(k_{D3})\ \frac{\partial \overline{p}_{D3}}{\partial y_D} - \ (k_{D2})\frac{\partial \overline{p}_{D2}}{\partial y_D}\right]_{y_D=d_F} = (1/\eta_{DF}) \cdot \left(s\overline{p}_{DF} - 0\right) \tag{65}$$

Region-3:

Equation 66

$$\frac{\partial^2 \overline{p}_{\mathrm{D3}}}{\partial {x_D}^2} + \frac{\partial^2 \overline{p}_{\mathrm{D3}}}{\partial {y_D}^2} = 1/\eta_{\mathrm{D3}} \cdot \left(s\overline{p}_{D3} - 0\right) \tag{66}$$

4.4.7 Fourier Transformation

Take the Fourier transform of all equations with respect to space variable, x_D, in terms of parameter (ρ):

Region-1:

$$-\rho^2\,\bar{\bar{p}}_{\mathrm{D1}}+\frac{d^2\bar{\bar{p}}_{\mathrm{D1}}}{dy_D{}^2}=\frac{s\cdot\bar{\bar{p}}_{\mathrm{D1}}}{\eta_{\mathrm{D1}}}$$

Equation 67

$$\Rightarrow\quad \frac{d^2\bar{\bar{p}}_{\mathrm{D1}}}{dy_D{}^2}=\left(\rho^2+\frac{s}{\eta_{\mathrm{D1}}}\right)\,\bar{\bar{p}}_{\mathrm{D1}} \tag{67}$$

Fracture:

Equation 68

$$-\rho^2\,\bar{\bar{p}}_{\mathrm{Df}}+\frac{1}{\mathrm{F_{CDf}}}\left[(\mathrm{k_{D2}})\cdot\left.\frac{\partial\bar{\bar{p}}_{\mathrm{D2}}}{\partial y_{\mathrm{D}}}\right|_{y_{\mathrm{D}}=0}-(\mathrm{k_{D1}})\cdot\left.\frac{\partial\bar{\bar{p}}_{\mathrm{D1}}}{\partial y_{\mathrm{D}}}\right|_{y_{\mathrm{D}}=0}\right]+\frac{\sqrt{2\pi}}{\mathrm{F_{CDf}\,.\,s}}=\left(\frac{\mathrm{s}\cdot\bar{\bar{p}}_{\mathrm{Df}}}{\eta_{\mathrm{Df}}}\right) \tag{68}$$

Region-2:

$$-\rho^2\,\bar{\bar{p}}_{\mathrm{D2}}+\frac{d^2\bar{\bar{p}}_{\mathrm{D2}}}{dy_D{}^2}=\frac{s\cdot\bar{\bar{p}}_{\mathrm{D2}}}{\eta_{\mathrm{D2}}}$$

Equation 69

$$\Rightarrow\quad \frac{d^2\bar{\bar{p}}_{\mathrm{D2}}}{dy_D{}^2}=\left(\rho^2+\frac{s}{\eta_{\mathrm{D2}}}\right)\,\bar{\bar{p}}_{\mathrm{D2}} \tag{69}$$

Fault:

Equation 70

$$-\rho^2\,\bar{\bar{p}}_{\mathrm{DF}}+\frac{1}{\boldsymbol{F_{CD_F}}}\left[(k_{D3})\,\frac{d\bar{\bar{p}}_{D3}}{dy_D}-(k_{D2})\,\frac{d\bar{\bar{p}}_{D2}}{dy_D}\right]_{y_D=d_F}=\left(\frac{\mathrm{s}\cdot\bar{\bar{p}}_{\mathrm{DF}}}{\eta_{\mathrm{DF}}}\right) \tag{70}$$

Region-3:

$$-\rho^2\,\bar{\bar{p}}_{\mathrm{D3}}+\frac{d^2\bar{\bar{p}}_{\mathrm{D3}}}{dy_D{}^2}=\frac{s\cdot\bar{\bar{p}}_{\mathrm{D3}}}{\eta_{\mathrm{D3}}}$$

Equation 71

$$\Rightarrow\quad \frac{d^2\bar{\bar{p}}_{\mathrm{D3}}}{dy_D{}^2}=\left(\rho^2+\frac{s}{\eta_{\mathrm{D3}}}\right)\,\bar{\bar{p}}_{\mathrm{D3}} \tag{71}$$

4.5 Helmholtz Equation Solution

Region-1:

$$-\rho^2\,\bar{\bar{p}}_{\mathrm{D1}}+\frac{d^2\bar{\bar{p}}_{\mathrm{D1}}}{dy_D{}^2}=\frac{s\cdot\bar{\bar{p}}_{\mathrm{D1}}}{\eta_{\mathrm{D1}}}$$

$$\Rightarrow \quad \frac{d^2\overline{\overline{p}}_{D1}}{dy_D{}^2} = \left(\rho^2 + \frac{s}{\eta_D}\right)\ \overline{\overline{p}}_{D1}$$

$$\overline{\overline{p}}_{D1} = C_1{}' \cdot e^{+\sqrt{\left(\rho^2+\frac{s}{\eta_D}\right)}\ \cdot\ y_D} + C_1{}'' \cdot e^{-\sqrt{\left(\rho^2+\frac{s}{\eta_D}\right)}\ \cdot\ y_D}$$

Since it is **semi-infinite** at Region-1 $(0 < y < -\infty)$, Figure 31**,** and y_D is (-ve). to have the pressure decreasing with time, then it becomes:

$$\overline{\overline{p}}_{D1} = C_1 \ \cdot e^{+\sqrt{\left(\rho^2+\frac{s}{\eta_D}\right)}\ \cdot\ y_D}$$

Equation 72

$$\overline{\overline{p}}_{D1} = C_1 \ \cdot e^{+\sqrt{m}\ \cdot\ y_D} \tag{72}$$

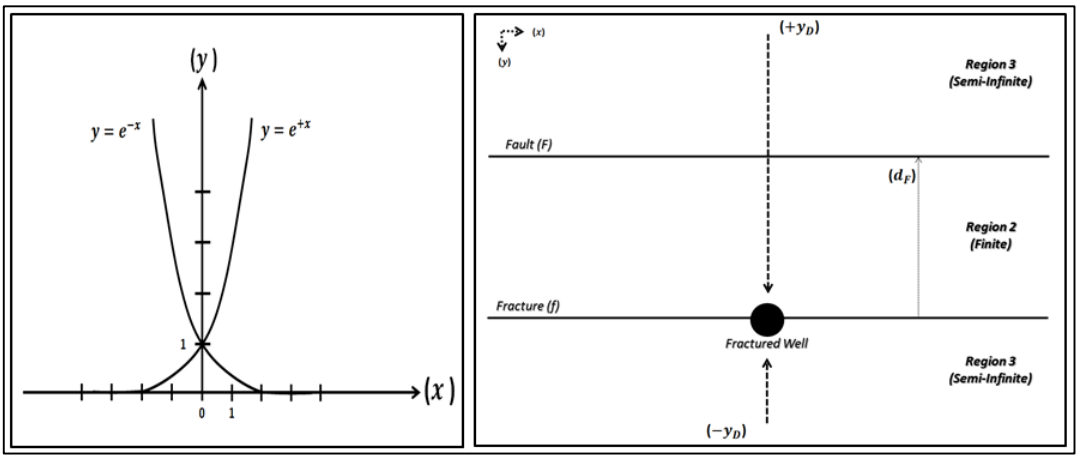

Figure 31: Flow from the three regions towards the well and its relation to the solution of Helmholtz equation.

Region-2:

$$-\rho^2\ \overline{\overline{p}}_{D2} + \frac{d^2\overline{\overline{p}}_{D2}}{dy_D{}^2} = \frac{s\cdot\overline{\overline{p}}_{D2}}{\eta_D}$$

$$\Rightarrow \quad \frac{d^2\overline{\overline{p}}_{D2}}{dy_D{}^2} = \left(\rho^2 + \frac{s}{\eta_D}\right)\ \overline{\overline{p}}_{D2}$$

Since it is **finite** at **Region-2** $(0 < y < d_F)$ and y_D is (+ve), the flow is along two opposite directions: towards the well and towards the fault; thus, both terms of the equation exist:

$$\overline{\overline{p}}_{D2} = C_2' \ \cdot e^{+\sqrt{\left(\rho^2+\frac{s}{\eta_D}\right)}\ \cdot\ y_D} + C_2'' \ \cdot e^{-\sqrt{\left(\rho^2+\frac{s}{\eta_D}\right)}\ \cdot\ y_D}$$

Equation 73

$$\overline{\overline{\mathrm{p}}}_{\mathrm{D2}} = C_2' \cdot \mathrm{e}^{+\sqrt{\mathrm{m}} \cdot \mathrm{y_D}} + C_2'' \cdot \mathrm{e}^{-\sqrt{\mathrm{m}} \cdot \mathrm{y_D}} \tag{73}$$

Region-3:

$$-\rho^2 \overline{\overline{p}}_{\mathrm{D3}} + \frac{d^2\overline{\overline{p}}_{\mathrm{D3}}}{dy_D{}^2} = \frac{s \cdot \overline{\overline{p}}_{\mathrm{D3}}}{\eta_{\mathrm{D}}}$$

$$\Rightarrow \quad \frac{d^2\overline{\overline{p}}_{\mathrm{D3}}}{dy_D{}^2} = \left(\rho^2 + \frac{s}{\eta_{\mathrm{D}}}\right) \overline{\overline{p}}_{\mathrm{D3}}$$

The solution to the above Helmholtz equation

$(\frac{d^2\mathrm{p}}{dy^2} = m \cdot \mathrm{p})$, can be written as: $\mathrm{p} = C' \cdot \mathrm{e}^{+\sqrt{\mathrm{m}} \cdot \mathrm{y}} + C'' \cdot \mathrm{e}^{-\sqrt{\mathrm{m}} \cdot \mathrm{y}}$

where, $m = \rho^2 + \frac{s}{\eta_{\mathrm{D23}}}$

Hence,

$$\overline{\overline{\mathrm{p}}}_{\mathrm{D3}} = C_3' \cdot \mathrm{e}^{+\sqrt{\left(\rho^2 + \frac{\mathrm{s}}{\eta_{\mathrm{D}}}\right)} \cdot (y_D - d_F)} + C_3'' \cdot \mathrm{e}^{-\sqrt{\left(\rho^2 + \frac{\mathrm{s}}{\eta_{\mathrm{D}}}\right)} \cdot (y_D - d_F)}$$

Since it is **semi-infinite** at **Region-3** ($d_F < y < \infty$), and $\mathrm{y_D}$ is ($+^{\mathrm{ve}}$): to have the pressure decreasing with time, then it becomes:

$$\overline{\overline{\mathrm{p}}}_{\mathrm{D3}} = \mathrm{C_3}\, \mathrm{e}^{-\sqrt{\left(\rho^2 + \frac{\mathrm{s}}{\eta_{\mathrm{D}}}\right)} \cdot (y_D - d_F)}$$

or

Equation 74

$$\overline{\overline{\mathrm{p}}}_{\mathrm{D3}} = \mathrm{C_3}\, \mathrm{e}^{-\sqrt{\mathrm{m}} \cdot (y_D - d_F)} \tag{74}$$

4.6 Solving for the Final Equation

It is needed to define the boundary conditions and the differentiation forms in order to solve for $\overline{\overline{\mathrm{p}}}_{\mathrm{DF}}$ in the fault equation, Appendix-D:

4.6.1 Interface conditions

From the interface conditions:

$@\ y_D = 0$:

$$\overline{\overline{p}}_{D1} = \overline{\overline{p}}_{D2} = \overline{\overline{p}}_{Df} = \mathrm{C_1}$$

$$\overline{\overline{p}}_{D2} = C_2' + C_2''$$

Equation 75

Solve for

$$\overline{\overline{p}}_{Df} = C_2' + C_2'' \tag{75}$$

$@\ y_D = d_F$:

$$\overline{\overline{p}}_{D3} = \mathrm{C_3}$$

4.6.2 Differential Equations

Differentiate Equation 73 & Equation 74 for Regions 2 and 3 with respect to $\mathrm{y_D}$ then substitute in the fault Equation 70 and solve for $\overline{\overline{\mathrm{p}}}_{\mathrm{DF}}$ at $\mathrm{y_D = d_F}$:

Region-2:

$$\overline{\overline{p}}_{D2}\Big|_{y_D} = C_2' \cdot e^{+\sqrt{m_2}\cdot y_D} + C_2'' \cdot e^{-\sqrt{m_2}\cdot y_D}$$

Equation 76

$$\overline{\overline{\mathrm{p}}}_{\mathrm{D2}}\Big|_{y_D=d_F} = C_2' \cdot \mathrm{e}^{+\sqrt{\mathrm{m_2}}\cdot \mathrm{d_F}} + C_2'' \cdot \mathrm{e}^{-\sqrt{\mathrm{m_2}}\cdot \mathrm{d_F}} \tag{76}$$

Equation 77

$$\frac{\mathrm{d}\overline{\overline{\mathrm{p}}}_{\mathrm{D2}}}{dy_D}\Big|_{y_D=d_F} = C_2' \cdot \sqrt{\mathrm{m_2}} \cdot \mathrm{e}^{+\sqrt{\mathrm{m_2}}\cdot d_F} - C_2'' \cdot \sqrt{\mathrm{m_2}} \cdot \mathrm{e}^{-\sqrt{\mathrm{m_2}}\cdot d_F} \tag{77}$$

Region-3:

Equation 78

$$\overline{\overline{p}}_{D3}\Big|_{y_D-d_F} = C_3 \cdot e^{-\sqrt{m_3}\cdot (y_D-d_F)} \tag{78}$$

$$\overline{\overline{p}}_{D3}\Big|_{y_D=d_F} = C_3 = \overline{\overline{p}}_{DF}$$

$$\left.\frac{d\bar{\bar{p}}_{D3}}{dy_D}\right|_{y_D-d_F} = -C_3 \cdot \sqrt{m_3} \cdot e^{-\sqrt{m_3}\,.(y_D-d_F)}$$

Equation 79

$$\left.\frac{\partial\bar{\bar{p}}_{D3}}{dy_D}\right|_{y_D=d_F} = -C_3 \cdot \sqrt{m_3} = -\bar{\bar{p}}_{DF} \cdot \sqrt{m_3} \qquad (79)$$

Then, substitute back in the Fault Equation 70:

Equation 80

$$\left.\bar{\bar{p}}_{DF}\right|_{y_D=d_F} = \frac{k_{D2}\left[C_2^{"} \cdot \sqrt{m_2} \cdot e^{-\sqrt{m_2}\,\cdot\, d_F} - C_2' \cdot \sqrt{m_2} \cdot e^{\sqrt{m_2}\,\cdot\, d_F}\right]}{F_{CD_F} \cdot m_F + k_{D3} \cdot \sqrt{m_3}} \qquad (80)$$

It is known that:

Equation 81

$$\Rightarrow \left.\bar{\bar{p}}_{DF}\right|_{y_D=d_F} = C_2' \cdot e^{+\sqrt{m_2}\,\cdot\, d_F} + C_2^{"} \cdot e^{-\sqrt{m_2}\,\cdot\, d_F} \qquad (81)$$

Then Equation 81 = Equation 80 and solve for $C_2^{"}$:

Equation 82

$$C_2^{"} = -C_2' \cdot \frac{e^{2\sqrt{m_2}\,\cdot\, d_F} \cdot \left[1 + \frac{k_{D2} \cdot \sqrt{m_2}}{F_{CD_F} \cdot m_F + k_{D3} \cdot \sqrt{m_3}}\right]}{\left[1 - \frac{k_{D2} \cdot \sqrt{m_2}}{F_{CD_F} \cdot m_F + k_{D3} \cdot \sqrt{m_3}}\right]} \quad \underline{\textbf{or}} \quad C_2^{"} = -C_2' \cdot X \qquad (82)$$

Differentiate Equation 72 & Equation 73 for Regions 1&2 with respect to y_D, then substitute in the fracture Equation 68 and solve for $\bar{\bar{p}}_{Df}$ at $y_D = 0$:

Region-2:

Equation 83

$$\left.\bar{\bar{p}}_{D2}\right|_{y_D} = C_2' \cdot e^{+\sqrt{m_2}\,\cdot\, y_D} + C_2^{"} \cdot e^{-\sqrt{m_2}\,\cdot\, y_D} \qquad (83)$$

and

$$\left.\bar{\bar{p}}_{D2}\right|_{y_D=0} = C_2' + C_2^{"}$$

From Equation 75:

$$\overline{\overline{p}}_{Df} = C_2' + C_2''$$

Equation 84

$$\left.\frac{d\overline{\overline{p}}_{D2}}{dy_D}\right|_{y_D} = C_2' \cdot \sqrt{m_2} \cdot e^{+\sqrt{m_{23}} \cdot y_D} - C_2'' \cdot \sqrt{m_2} \cdot e^{-\sqrt{m_2} \cdot y_D} \quad (84)$$

Equation 85

$$\left.\frac{d\overline{\overline{p}}_{D2}}{dy_D}\right|_{y_D=0} = C_2' \cdot \sqrt{m_2} - C_2'' \cdot \sqrt{m_2} \quad (85)$$

Region-1:

Equation 86

$$\left.\overline{\overline{p}}_{D1}\right|_{y_D} = C_1 \cdot e^{\sqrt{m_1} \cdot y_D} \quad (86)$$

$$\left.\overline{\overline{p}}_{D1}\right|_{y_D=0} = C_1 = \overline{\overline{p}}_{Df}$$

$$\left.\frac{\partial\overline{\overline{p}}_{D1}}{dy_D}\right|_{y_D} = C_1 \cdot \sqrt{m_1} \cdot e^{\sqrt{m_1} \cdot y_D}$$

Equation 87

$$\left.\frac{\partial\overline{\overline{p}}_{D1}}{dy_D}\right|_{y_D=0} = C_1 \cdot \sqrt{m_1} = \overline{\overline{p}}_{Df} \cdot \sqrt{m_1} \quad (87)$$

Then, substitute back in the fracture Equation 68:

Equation 88

$$\left.\overline{\overline{p}}_{Df}\right|_{y_D=0} = \frac{k_{D2}\left[C_2' \cdot \sqrt{m_2} - C_2'' \cdot \sqrt{m_2}\right] + \frac{\sqrt{2\pi}}{s}}{F_{CD_f} \cdot m_f + k_{D1} \cdot \sqrt{m_1}} \quad (88)$$

From the boundary condition, it is known that:

$$\left.\overline{\overline{p}}_{Df}\right|_{y_D=0} = \frac{k_{D2}\left[C_2' \cdot \sqrt{m_2} - C_2'' \cdot \sqrt{m_2}\right] + \frac{\sqrt{2\pi}}{s}}{F_{CD_f} \cdot m_f + k_{D1} \cdot \sqrt{m_1}} = C_2' + C_2''$$

and solve for C_2'':

Equation 89

$$C_2^{"} = C_2' \cdot \frac{\left[(F_{CD_f} \cdot m_f) + (k_{D1} \cdot \sqrt{m_1}) - (k_{D2} \cdot \sqrt{m_2})\right] + \frac{\sqrt{2\pi}}{s}}{\left[(F_{CD_f} \cdot m_f) + (k_{D1} \cdot \sqrt{m_1}) + (k_{D2} \cdot \sqrt{m_2})\right]} \quad \underline{\mathbf{or}} \quad C_2^{"} = \frac{C_2' \cdot Y + \sqrt{2\pi}}{Z} \tag{89}$$

Then Equation 89 = Equation 82 and solve for $C_2^{"}$:

$$-C_2' \cdot X = \frac{C_2' \cdot Y + \sqrt{2\pi}}{Z}$$

Then solve for C_2' and $C_2^{"}$

and

$$\overline{\overline{p}}_{Df} = C_2' + C_2^{"} = \frac{\sqrt{2\pi} \cdot (1 - \frac{1}{X})}{Z + \frac{Y}{X}}$$

$$\overline{\overline{p}}_{Df} = C_2' + C_2^{"} = \frac{\sqrt{2\pi} \cdot (1 - \frac{1}{X})}{Z + \frac{Y}{X}}$$

Then by substituting for X, Y and Z the final equation can be written as:

$$\overline{\overline{p}}_{Df} = \frac{\sqrt{2\pi}}{s} \frac{1 - \left[e^{-2\sqrt{m_2}} \cdot d_F \left[\frac{1 - \frac{k_{D2} \cdot \sqrt{m_2}}{F_{CD_F} \cdot m_F + k_{D3} \cdot \sqrt{m_3}}}{1 + \frac{k_{D2} \cdot \sqrt{m_2}}{F_{CD_F} \cdot m_F + k_{D3} \cdot \sqrt{m_3}}}\right]\right]}{\left[(F_{CD_f} \cdot m_f) + (k_{D1} \cdot \sqrt{m_1}) + (k_{D2} \cdot \sqrt{m_2})\right] + \left[e^{-2\sqrt{m_2}} \cdot d_F \left[\frac{1 - \frac{k_{D2} \cdot \sqrt{m_2}}{F_{CD_F} \cdot m_F + k_{D3} \cdot \sqrt{m_3}}}{1 + \frac{k_{D2} \cdot \sqrt{m_2}}{F_{CD_F} \cdot m_F + k_{D3} \cdot \sqrt{m_3}}}\right]\right] \cdot \left[(F_{CD_f} \cdot m_f) + (k_{D1} \cdot \sqrt{m_1}) - (k_{D2} \cdot \sqrt{m_2})\right]}$$

Equation 90

$$\bar{\bar{p}}_{Df} = \frac{\sqrt{2\pi}}{s} \cdot \frac{1 - \left[e^{-2\sqrt{m_2}} \cdot d_F \left[\frac{1 - \frac{k_{D2} \cdot \sqrt{\left(\rho^2 + \frac{s}{\eta_{D2}}\right)}}{F_{CD_F} \cdot \left(\rho^2 + \frac{s}{\eta_{DF}}\right) + k_{D3} \cdot \sqrt{\left(\rho^2 + \frac{s}{\eta_{D3}}\right)}}}{1 + \frac{k_{D2} \cdot \sqrt{\left(\rho^2 + \frac{s}{\eta_{D2}}\right)}}{F_{CD_F} \cdot \left(\rho^2 + \frac{s}{\eta_{DF}}\right) + k_{D3} \cdot \sqrt{\left(\rho^2 + \frac{s}{\eta_{D3}}\right)}}} \right] \right]}{\left[F_{CD_f} \left(\rho^2 + \frac{s}{\eta_{Df}}\right) + k_{D1} \sqrt{\left(\rho^2 + \frac{s}{\eta_{D1}}\right)} + k_{D2} \sqrt{\left(\rho^2 + \frac{s}{\eta_{D2}}\right)} \right] + \left[e^{-2\sqrt{m_2}} \cdot d_F \left[\frac{1 - \frac{k_{D2} \cdot \sqrt{\left(\rho^2 + \frac{s}{\eta_{D2}}\right)}}{F_{CD_F} \cdot \left(\rho^2 + \frac{s}{\eta_{DF}}\right) + k_{D3} \cdot \sqrt{\left(\rho^2 + \frac{s}{\eta_{D3}}\right)}}}{1 + \frac{k_{D2} \cdot \sqrt{\left(\rho^2 + \frac{s}{\eta_{D2}}\right)}}{F_{CD_F} \cdot \left(\rho^2 + \frac{s}{\eta_{DF}}\right) + k_{D3} \cdot \sqrt{\left(\rho^2 + \frac{s}{\eta_{D3}}\right)}}} \right] \right] \cdot \left[F_{CD_f} \left(\rho^2 + \frac{s}{\eta_{Df}}\right) + k_{D1} \sqrt{\left(\rho^2 + \frac{s}{\eta_{D1}}\right)} - k_{D2} \sqrt{\left(\rho^2 + \frac{s}{\eta_{D2}}\right)} \right]}$$

4.7 Equation Validation

If there is no fault, then: $w_F = 0$ and $k_{D2} = k_{D3}$

Hence: $F_{CDF} = \frac{k_F w_F}{k_r \; r_w} = 0$

where: $k_{D1} \neq k_{D2}$; thus:

$$\overline{\overline{p}}_{Df} = \frac{\sqrt{2\pi}}{s} \cdot \frac{1}{\left[\left(F_{CDf} \cdot \left(\rho^2 + \frac{s}{\eta_{Df}}\right)\right) + \left((k_{D1}) \cdot \sqrt{\left(\rho^2 + \frac{s}{\eta_{D1}}\right)}\right) + \left((k_{D2}) \cdot \sqrt{\left(\rho^2 + \frac{s}{\eta_{D2}}\right)}\right)\right]}$$

Equivalent to Equation 39

and if; $k_{D1} = k_{D2} = k_{D3}$ then:

Equation 91

$$\Rightarrow \overline{\overline{p}}_{Df} = \frac{\sqrt{2\pi}}{s} \cdot \frac{1}{\left[F_{CD_f} \cdot \left(\rho^2 + \frac{s}{\eta_{Df}}\right) + 2 \cdot k_D \cdot \sqrt{\left(\rho^2 + \frac{s}{\eta_D}\right)}\right]} \quad (91)$$

Take inverse of Fourier transformation with respect to ρ for reverting it back to the variable, x_D, in Laplace domain:

From

$F^{-1}\left\{\overline{\overline{p}}_{Df}\right\} = \frac{1}{\sqrt{2\pi}} \int_{-\infty}^{\infty} \overline{\overline{p}}_{Df} \, e^{-i\rho x_D} \, d\rho = \overline{p}_{Df}(x_D, s)$, inverted back to Laplace space

write,

Equation 92

$$\overline{p}_{Df}(x_D = 0, s) = \frac{1}{\sqrt{2\pi}} \int_{-\infty}^{\infty} \left(\overline{\overline{p}}_{Df}\right) d\rho = \overline{p}_{wD}(s) \quad (92)$$

$@ \; x_D = 0 \;\; where, \;\; \overline{p}_{Df} = \overline{p}_{wD}$

Substitute Equation 90,write,

Equation 92:

$$\overline{p}_{wD}=\frac{1}{s}\int_{-\infty}^{\infty}\frac{1-\left[e^{-2\sqrt{\left(\rho^2+\frac{s}{\eta_{D2}}\right)}}\cdot d_F\left[\frac{1-\frac{k_{D2}\cdot\sqrt{\left(\rho^2+\frac{s}{\eta_{D2}}\right)}}{F_{CD_F}\cdot\left(\rho^2+\frac{s}{\eta_{DF}}\right)+k_{D3}\cdot\sqrt{\left(\rho^2+\frac{s}{\eta_{D3}}\right)}}}{1+\frac{k_{D2}\cdot\sqrt{\left(\rho^2+\frac{s}{\eta_{D2}}\right)}}{F_{CD_F}\cdot\left(\rho^2+\frac{s}{\eta_{DF}}\right)+k_{D3}\cdot\sqrt{\left(\rho^2+\frac{s}{\eta_{D3}}\right)}}}\right]\right]}{\left[F_{CD_f}\cdot\left(\rho^2+\frac{s}{\eta_{Df}}\right)+k_{D1}\cdot\sqrt{\left(\rho^2+\frac{s}{\eta_{D1}}\right)}+k_{D2}\cdot\sqrt{\left(\rho^2+\frac{s}{\eta_{D2}}\right)}\right]+\left[e^{-2\sqrt{\left(\rho^2+\frac{s}{\eta_{D2}}\right)}}\cdot d_F\left[\frac{1-\frac{k_{D2}\cdot\sqrt{\left(\rho^2+\frac{s}{\eta_{D2}}\right)}}{F_{CD_F}\cdot\left(\rho^2+\frac{s}{\eta_{DF}}\right)+k_{D3}\cdot\sqrt{\left(\rho^2+\frac{s}{\eta_{D3}}\right)}}}{1+\frac{k_{D2}\cdot\sqrt{\left(\rho^2+\frac{s}{\eta_{D2}}\right)}}{F_{CD_F}\cdot\left(\rho^2+\frac{s}{\eta_{DF}}\right)+k_{D3}\cdot\sqrt{\left(\rho^2+\frac{s}{\eta_{D3}}\right)}}}\right]\right]\cdot\left[F_{CD_f}\cdot\left(\rho^2+\frac{s}{\eta_{Df}}\right)+k_{D1}\cdot\sqrt{\left(\rho^2+\frac{s}{\eta_{D1}}\right)}-k_{D2}\cdot\sqrt{\left(\rho^2+\frac{s}{\eta_{D2}}\right)}\right]}\cdot d\rho$$

4.7.1 Final fractured-well pressure equation for asymmetric reservoir

Since the integration is an even function in ρ, the above equation can be simplified, as the final equation for the wellbore pressure in the Laplace domain, for an asymmetric reservoir system bounding the fractured-well and the fault nearby, is:

Equation 93

$$\overline{p}_{wD} = \frac{2}{s}\int_0^{\infty} \frac{1 - \left[e^{-2\sqrt{\left(\rho^2+\frac{s}{\eta_{D2}}\right)}\cdot d_F}\left[\frac{1 - \frac{k_{D2}\cdot\sqrt{\left(\rho^2+\frac{s}{\eta_{D2}}\right)}}{F_{CD_F}\cdot\left(\rho^2+\frac{s}{\eta_{DF}}\right)+k_{D3}\cdot\sqrt{\left(\rho^2+\frac{s}{\eta_{D3}}\right)}}}{1 + \frac{k_{D2}\cdot\sqrt{\left(\rho^2+\frac{s}{\eta_{D2}}\right)}}{F_{CD_F}\cdot\left(\rho^2+\frac{s}{\eta_{DF}}\right)+k_{D3}\cdot\sqrt{\left(\rho^2+\frac{s}{\eta_{D3}}\right)}}}\right]\right]}{\left[F_{CD_f}\cdot\left(\rho^2+\frac{s}{\eta_{Df}}\right)+k_{D1}\cdot\sqrt{\left(\rho^2+\frac{s}{\eta_{D1}}\right)}+k_{D2}\cdot\sqrt{\left(\rho^2+\frac{s}{\eta_{D2}}\right)}\right]+\left[e^{-2\sqrt{\left(\rho^2+\frac{s}{\eta_{D2}}\right)}\cdot d_F}\left[\frac{1 - \frac{k_{D2}\cdot\sqrt{\left(\rho^2+\frac{s}{\eta_{D2}}\right)}}{F_{CD_F}\cdot\left(\rho^2+\frac{s}{\eta_{DF}}\right)+k_{D3}\cdot\sqrt{\left(\rho^2+\frac{s}{\eta_{D3}}\right)}}}{1 + \frac{k_{D2}\cdot\sqrt{\left(\rho^2+\frac{s}{\eta_{D2}}\right)}}{F_{CD_F}\cdot\left(\rho^2+\frac{s}{\eta_{DF}}\right)+k_{D3}\cdot\sqrt{\left(\rho^2+\frac{s}{\eta_{D3}}\right)}}}\right]\right]\cdot\left[F_{CD_f}\cdot\left(\rho^2+\frac{s}{\eta_{Df}}\right)+k_{D1}\cdot\sqrt{\left(\rho^2+\frac{s}{\eta_{D1}}\right)}-k_{D2}\cdot\sqrt{\left(\rho^2+\frac{s}{\eta_{D2}}\right)}\right]} \cdot d\rho \quad (93)$$

The reservoir is assumed to be an asymmetric reservoir bounding the fractured-well and the fault nearby $(k_1 \neq k_2 \neq k_3)$.

4.7.2 Fractured well pressure equation for symmetric reservoir

Equation 94

$$\overline{p}_{wD} = \frac{2}{s}\int_0^{\infty} \frac{1-\left[e^{-2\sqrt{m}}\cdot d_F\left[\frac{1-\frac{k_D\cdot\sqrt{\left(\rho^2+\frac{s}{\eta_D}\right)}}{F_{CD_F}\cdot\left(\rho^2+\frac{s}{\eta_{DF}}\right)+k_D\cdot\sqrt{\left(\rho^2+\frac{s}{\eta_D}\right)}}}{1+\frac{k_D\cdot\sqrt{\left(\rho^2+\frac{s}{\eta_D}\right)}}{F_{CD_F}\cdot\left(\rho^2+\frac{s}{\eta_{DF}}\right)+k_D\cdot\sqrt{\left(\rho^2+\frac{s}{\eta_D}\right)}}}\right]\right]}{\left[F_{CD_f}\cdot\left(\rho^2+\frac{s}{\eta_{Df}}\right)+2\cdot k_D\cdot\sqrt{\left(\rho^2+\frac{s}{\eta_D}\right)}\right]+\left[e^{-2\sqrt{m}}\cdot d_F\left[\frac{1-\frac{k_D\cdot\sqrt{\left(\rho^2+\frac{s}{\eta_D}\right)}}{F_{CD_F}\cdot\left(\rho^2+\frac{s}{\eta_{DF}}\right)+k_D\cdot\sqrt{\left(\rho^2+\frac{s}{\eta_D}\right)}}}{1+\frac{k_D\cdot\sqrt{\left(\rho^2+\frac{s}{\eta_D}\right)}}{F_{CD_F}\cdot\left(\rho^2+\frac{s}{\eta_{DF}}\right)+k_D\cdot\sqrt{\left(\rho^2+\frac{s}{\eta_D}\right)}}}\right]\right]\cdot\left[F_{CD_f}\cdot\left(\rho^2+\frac{s}{\eta_{Df}}\right)\right]} \quad (94)$$

The reservoir is assumed to be a symmetric reservoir bounding the fractured-well and the fault nearby $(k_1 = k_2 = k_3)$.

4.8 Overall Solution Behaviour: Observations and Discussions

FracFault-model Code: MATLAB software package was used to code the solution in dimensionless form. The code is capable of running an unlimited number of different scenarios and type curves and can be used to match pressure data of field cases. It also accounts for specific properties for the fracture, fault and all the three regions.

The reservoir models discussed here use the following reservoir and fluid properties:

$h = 100\ ft$
$k_1 = k_2 = k_3 = 1\ md$
$\varphi = 0.15$
$\beta = 1.0$ rb/stb
$\mu = 0.7\ cp$
$c_t = 3.0\ e^{-6}\ \ psi^{-1}$
$w_f\ and\ w_F = 1.0\ foot$
$d_F = 10000.0\ foot$

For the more general case of a fractured-well in a reservoir with a fault, the corresponding type-curves of dimensionless time versus dimensionless pressure and its log-derivative have been plotted, for different dimensionless fracture and fault conductivities with distinctive features, shown in the Figures presented in this section. The fractured well pressure behaviour, from this solution, shows identical pressure profiles, provided all regions are of the same quality: ($k_1 = k_2 = k_3$). The run consists of four sets with reservoir and fluid properties as follows:

Set-1: A well in a homogenous reservoir;

Set-2: A fractured-well in a homogenous reservoir with fault nearby:
F_{cf} =2 (md ft) and F_{cF} =1e6 (md ft);

Set-3: A fractured-well in a homogenous reservoir with fault nearby:
F_{cf} =200 (md ft) and F_{cF} =1e7 (md ft);

Set4: A fractured-well in a homogenous reservoir with fault nearby:
F_{cf} =3000 (md ft) and F_{cF} =1e8 (md ft).

For all the four sets, the fault is located at a distance of 10,000 ft.

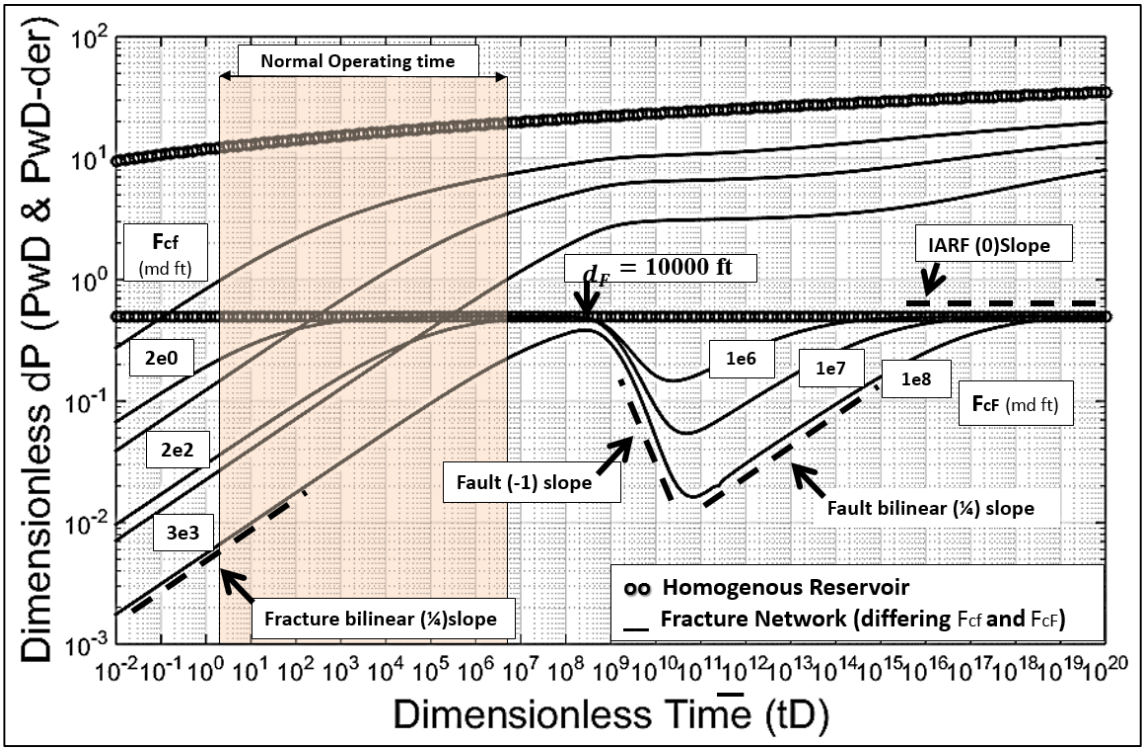

Figure 32- Dimensionless pressure and pressure derivative vs. dimensionless time.

The corresponding type curve solution of dimensionless time versus dimensionless pressure and its log-derivative has been plotted, for these different dimensionless fracture and fault conductivities with distinctive features, shown in Figure 32. At early times, the curve signifies a ¼ slope as a result of a bilinear flow from the two linear flow regimes along and into the fracture. Subsequently, a radial flow regime demonstrating the transient flow in the matrix bounding the fracture. A "down-turn" is then evident, with a negative unit slope, indicating the start of a conductive fault and enhancement of rock quality followed, by an "up-turn" with a bilinear flow regime reflecting the finite nature of fault and succeeded by a radial flow regime of the bounding blocks, at late times.

It is worth mentioning that the normal operating hours are shaded from (from $2.8e^0$ to $6.7e^6$). A synthetic case was run to reflect a welltest scenario with realistic well and reservoir properties. The shaded area, in Figure 33, is replicating the normal operating hours, for a more realistic case.

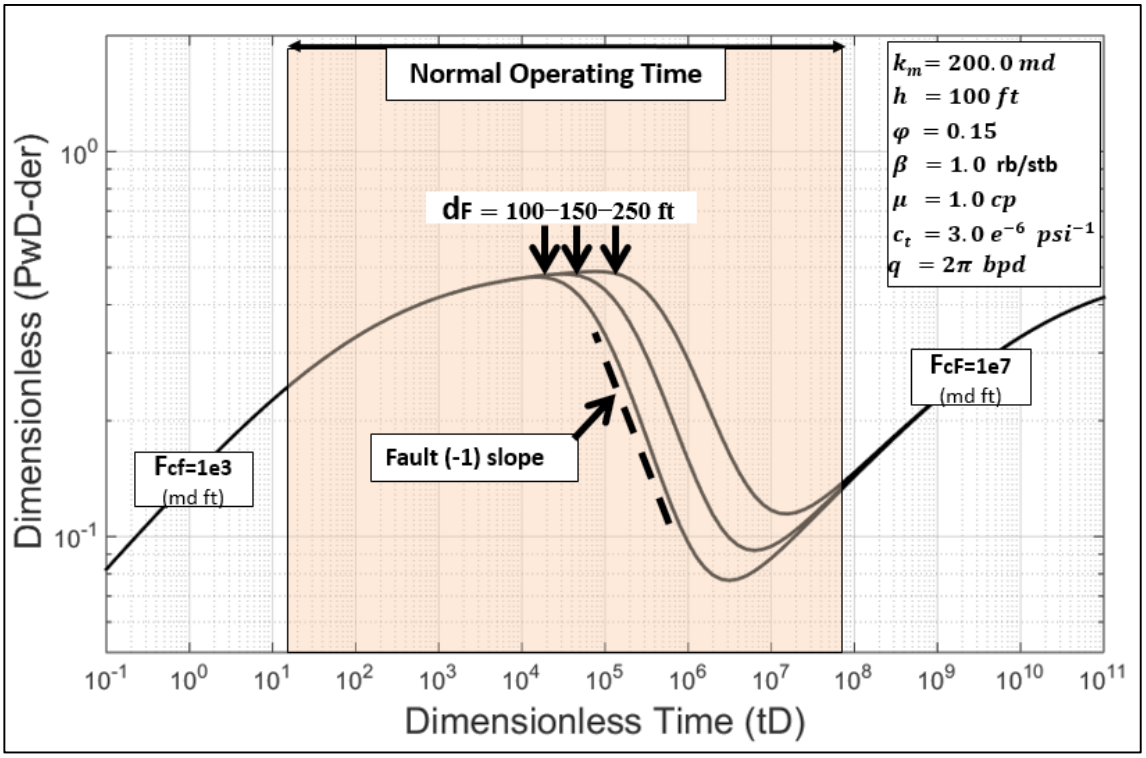

Figure 33- Dimensionless pressure derivative versus dimensionless time by the FracFault-model for a more realistic case.

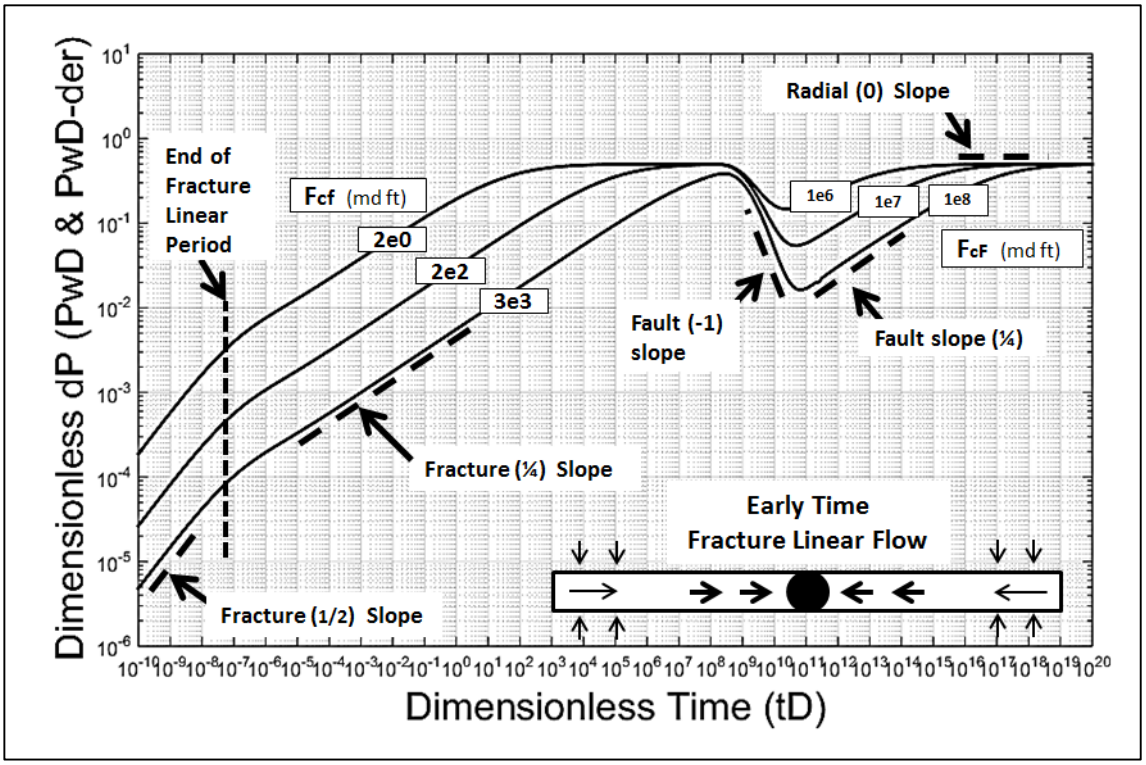

Figure 34- Dimensionless time vs. dimensionless pressure derivative by the FracFault-model exhibiting the Early Fracture Linear Flow regime.

Similarly, the type curves, in Figure 34, exhibit a distinctive feature of an early fracture linear flow regime at very early times expressing the first fluid flow into the well from the fracture only, and validates the stability of the solution even at a very early time.

4.8.1 Sensitivity runs

This section is highlighting the solution behaviour. Below are series of sensitivity runs in "a simple to complex order":

1. A well in a homogenous reservoir for various permeability.
2. A well in a linear composite reservoir.
3. A fractured well in a linear composite reservoir.
4. A fractured well in a three-region reservoir with a fault.
5. Effect of differing fault distances on flow profile.
6. Effect of differing fault conductivities on flow profile
7. A fractured well near a fault in a linear composite reservoir
8. Adding well-bore storage and skin to the solution.

Well in a homogenous reservoir with differing regions qualities: Case-1

Below are three sensitivities were run of varying matrix permeability for a homogenous reservoir, using the following reservoir and fluid properties:

$h = 100\ ft$
$\varphi = 0.15$
$\beta = 1.0$ rb/stb
$\mu = 0.7\ cp$
$c_t = 3.0\ e^{-6}\ \ psi^{-1}$
$w_f\ and\ w_F = 1.0\ foot$

The runs consisted of the following four sets:

Set-1 all the three Regions are of the same permeability, $(k_1 = k_2 = k_3 = 1md)$,

Set-2 Region-1 is different from Regions 2&3, $(k_1 = 1md\ \boldsymbol{and}\ k_2 = k_3 = 5md)$ and

Set-3 assigns the arithmetic average of Set-2 to all regions, $(k_1 = k_2 = k_3 = 3md)$.

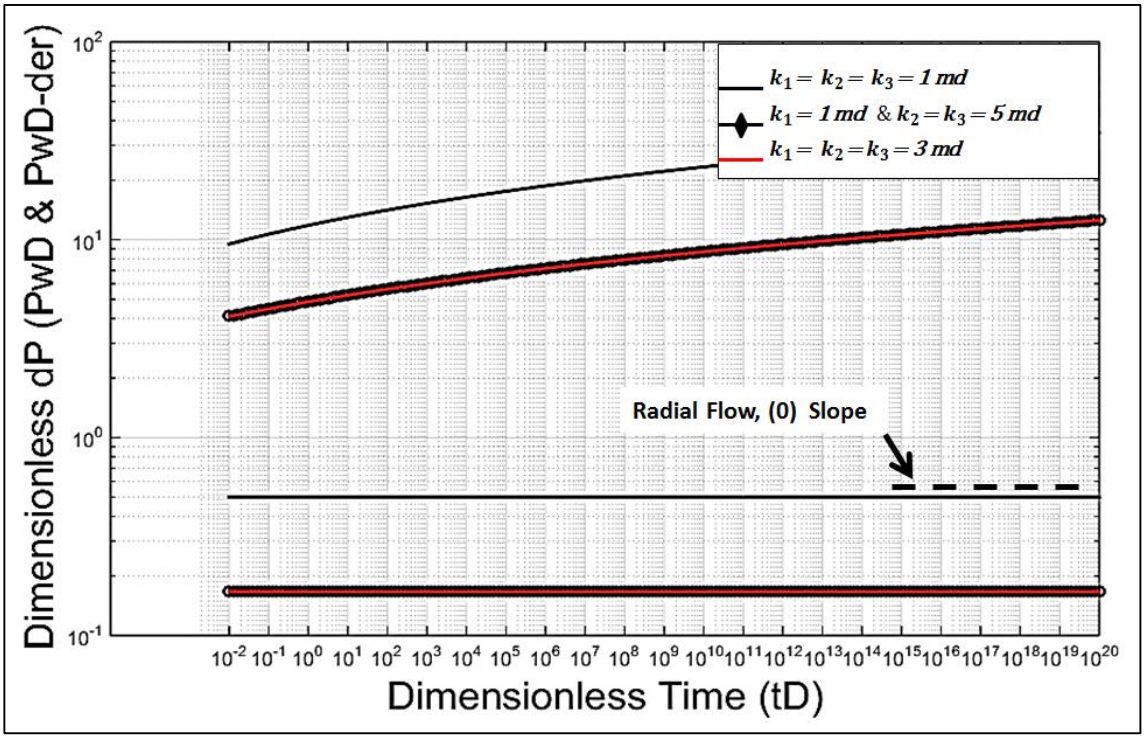

Figure 35- Dimensionless time vs. dimensionless pressure for the three sets.

Figure 35 confirms that the athematic average is calculated by the solution and **Set-2** and **Set-3** are generating identical results.

A well in a linear composite reservoir: Case 2

This sensitivity is devoted to showing that the solution can also be used to model a well in a linear composite reservoir by simply setting the fracture and fault apertures to zero ($w_f = w_F = 0$) and changing the mobilities of the regions. For the same reservoir properties, with $k_3 \geq k_1 \; and \; k_2$, four sets were run as follows:

Set-1 Homogenous and same quality reservoir, ($k_1 = k_2 = k_3 = 1md$),

Set-2 Regions 1&2 are different from Region 3, ($k_1 = k_2 = 1\,md \;\; and \; k_3 = 6\,md$)

Set-3 Regions 1&2 are different from Region 3, ($k_1 = k_2 = 1\,md \;\; and \; k_3 = 4\,md$)

Set-4 Regions 1&2 are different from Region 3, ($k_1 = k_2 = 1\,md \;\; and \; k_3 = 2\,md$)

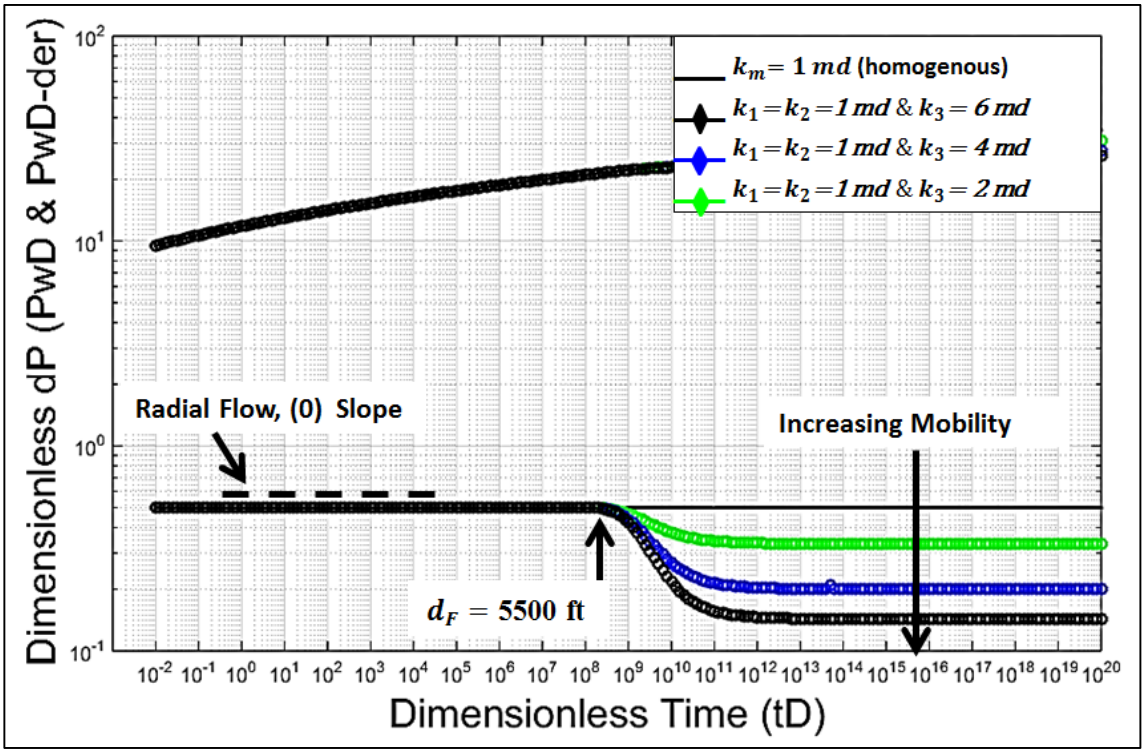

Figure 36- A well model in a linear composite reservoir with an increasing mobility.

Figure 36 demonstrates, correctly, a linear composite behaviour with a second lower stabilisation capturing increasing reservoir quality away from the well as that of Region 3 is higher than 1and 2.

Similarly, for the same reservoir properties four additional sets were also run, but this time with $k_3 \leq k_1 \; and \; k_2$, as follows:

Set-1 Homogenous and same quality reservoir, ($k_1 = k_2 = k_3 = 1md$)

Set-2 Regions 1&2 are different from Region 3, ($k_1 = k_2 = 1\,md \;\; and \; k_3 = 0.025\,md$)

Set-3 Regions 1&2 are different from Region 3, ($k_1 = k_2 = 1\,md \;\; and \; k_3 = 0.25\,md$)

Set-4 Regions 1&2 are different from Region 3, ($k_1 = k_2 = 1\,md \;\; and \; k_3 = 0.75\,md$)

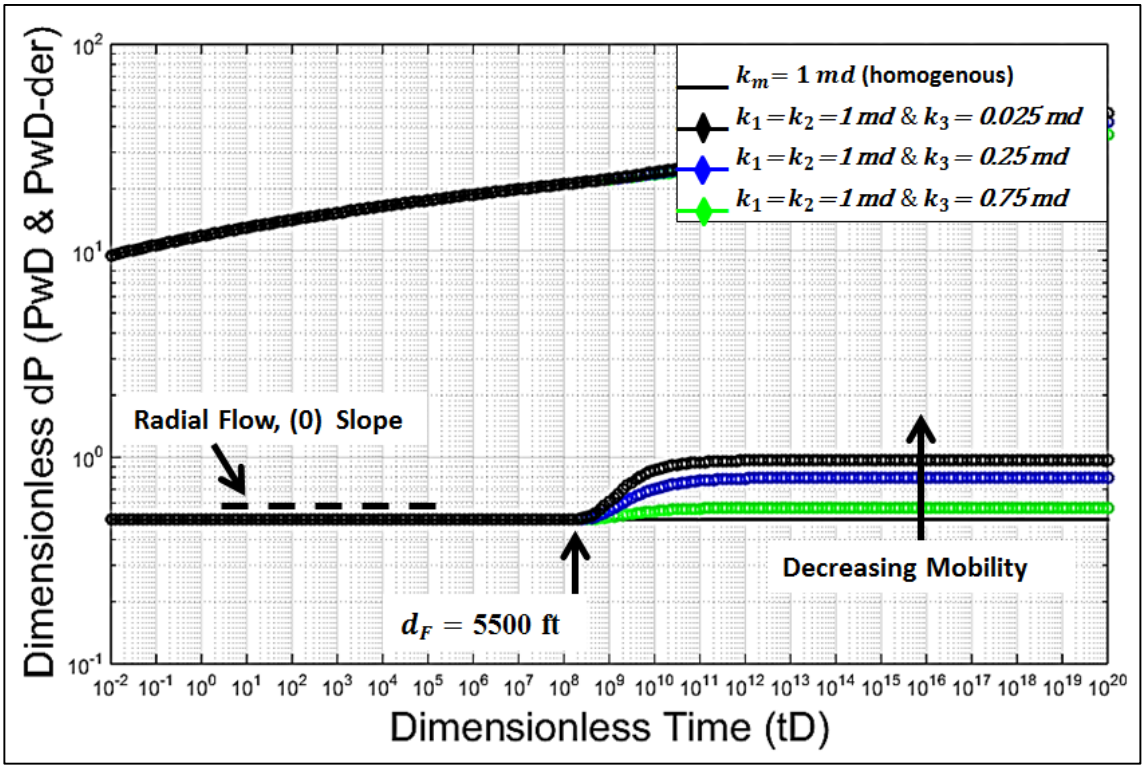

Figure 37- A well model in a linear composite reservoir with a decreasing mobility.

Figure 37 exhibits, again, a linear composite behaviour with a second higher stabilisation capturing decreasing reservoir quality away from the well as Region 3 is of a lower quality than 1&2.

A fractured well in a linear composite reservoir: Case 3

This sensitivity is presented to model a fractured well in a linear composite reservoir, where fault aperture was set to zero ($w_F = 0$). Here, for the same reservoir properties four sets were also run,

Set-1 Homogenous and same quality reservoir, ($k_1 = k_2 = k_3 = 1md$);

Set-2 Regions 1&2 are different from Region 3, ($k_1 = k_2 = 1\ md\ \ and\ k_3 = 6\ md$) with fractured well; F_{cf} =10 (md ft);

Set-3 Regions 1&2 are different from Region 3, ($k_1 = k_2 = 1\ md\ \ and\ k_3 = 4\ md$) with fractured well; F_{cf} =10 (md ft);

Set-4 Regions 1&2 are different from Region 3, ($k_1 = k_2 = 1\ md\ \ and\ k_3 = 2\ md$) with fractured well; F_{cf} =10 (md ft).

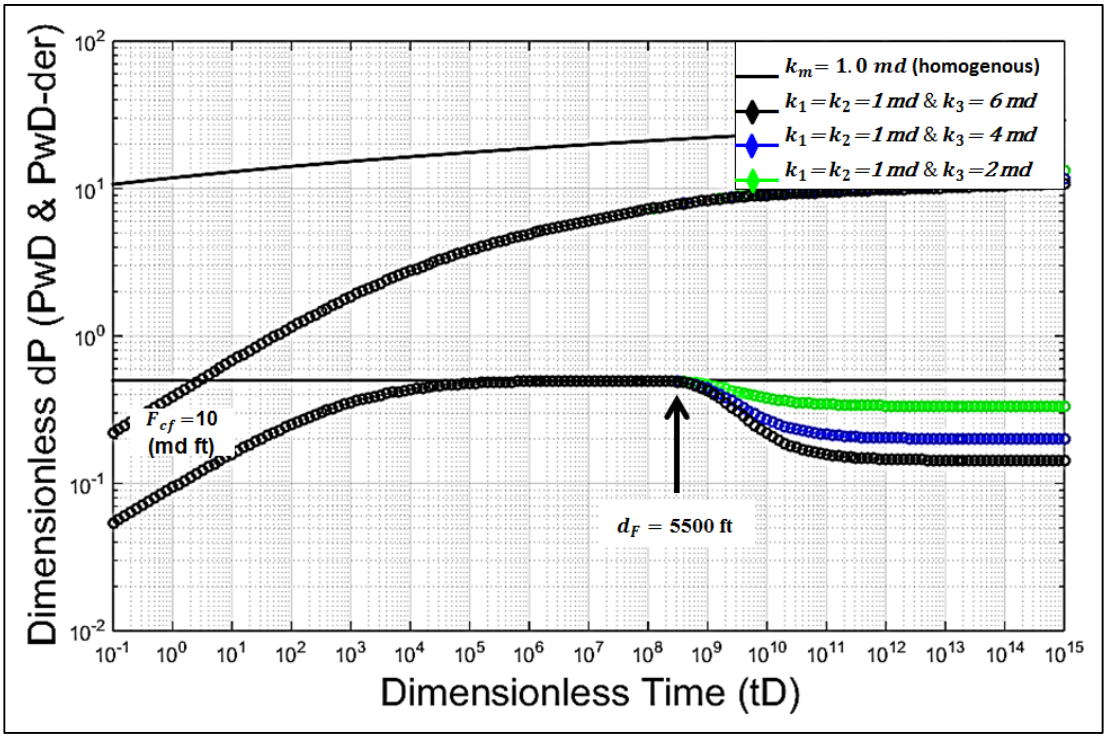

Figure 38- A fractured-well model in a linear composite reservoir with increasing mobility.

Figure 38 demonstrates, correctly, a fractured-well in a linear composite behaviour with a second lower stabilisation capturing increasing reservoir quality away from the well, as that of Region 3 is of higher quality than that of 1 and 2. The ¼ slope fracture signature is also observed at early time. Moreover, Figure 39 exhibits the expected fractured-well behaviour in a linear composite reservoir with decreasing reservoir quality away from the well, as Region 3 is of lower quality than 1&2 for the following sets:

Set-1 Homogenous and same quality reservoir, ($k_1 = k_2 = k_3 = 1md$);

Set-2 Regions 1&2 are different from Region 3, ($k_1 = k_2 = 1\,md$ and $k_3 = 0.025\,md$) with fractured well; F_{cf} =10 (md ft);

Set-3 Regions 1&2 are different from Region 3, ($k_1 = k_2 = 1\,md$ and $k_3 = 0.25\,md$) with fractured well; F_{cf} =10 (md ft);

Set-4 Regions 1&2 are different from Region 3, ($k_1 = k_2 = 1\,md$ and $k_3 = 0.75\,md$) with fractured well; F_{cf} =10 (md ft).

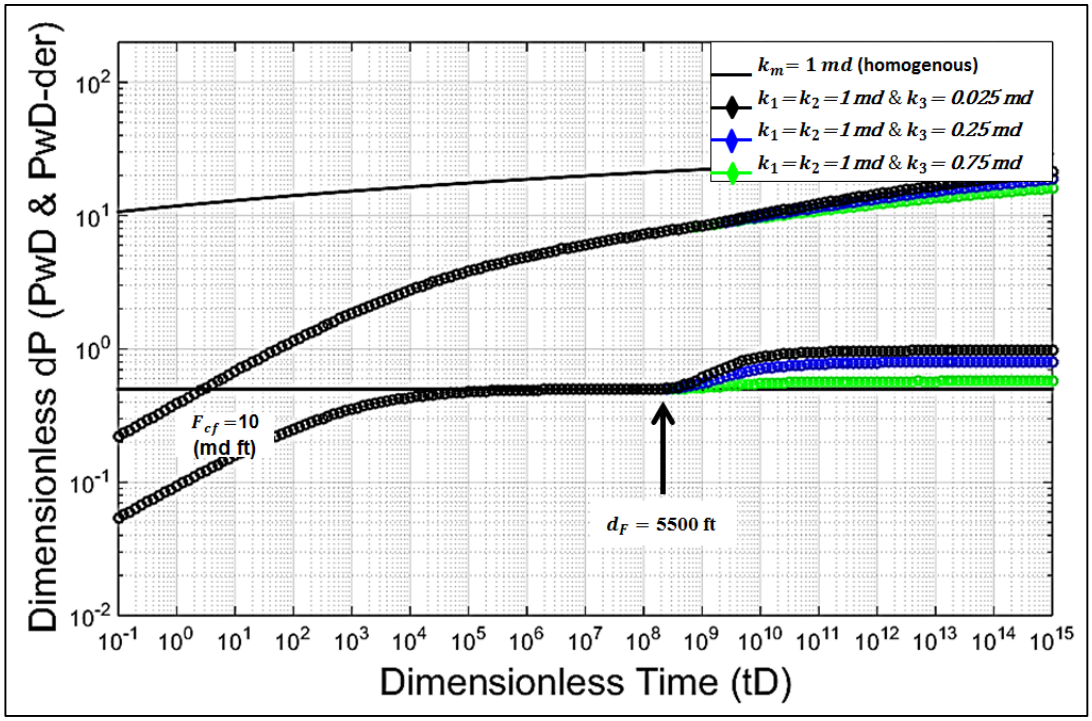

Figure 39- A fractured-well model in a linear composite reservoir with decreasing mobility.

A three-region reservoir with a fracture and a fault: Case 4

For the same reservoir properties four sets were also run to analyse the behaviour of the given solution with different matrix permeabilities but similar fracture and fault conductivities, as follows:

Set-1 Homogenous and same quality reservoir, $(k_1 = k_2 = k_3 = 1md)$;

Set-2 All regions are of the same quality, $(k_1 = k_2 = k_3 = 1md)$ with fractured well and fault nearby; F_{cf} =10 (md ft) and F_{cF} =1e7 (md ft);

Set-3 Region-1 is different than Regions 2&3, $(k_1 = 1md\ and\ \ k_2 = k_3 = 3\ md)$ with fractured well and fault nearby; F_{cf} =10 (md ft) and F_{cF} =1e7 (md ft);

Set-4 All regions are of the same quality, $(k_1 = k_2 = k_3 = 2\ md)$ with fractured well and fault nearby; F_{cf} =10 (md ft) and F_{cF} =1e7 (md ft).

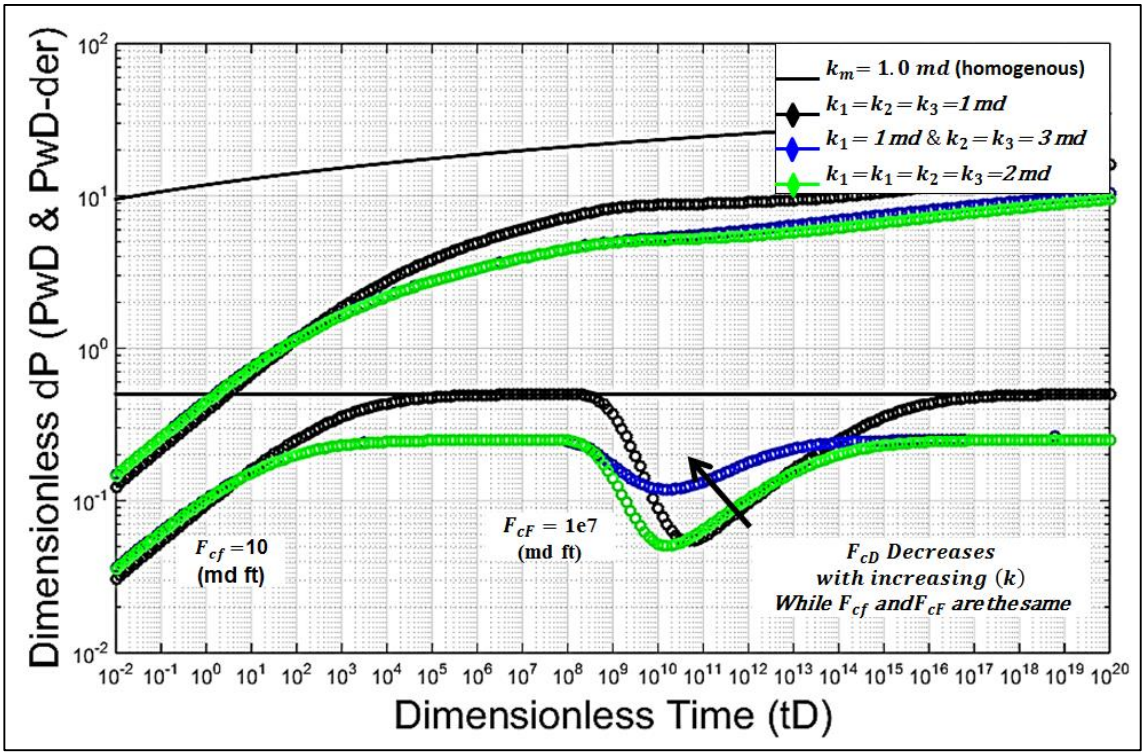

Figure 40- Dimensionless time vs. dimensionless pressure for the three sets.

From Figure 40 it can be seen that the total permeability is increasing as Regions 2 and 3 permeabilities are increasing. It should be noted that the conductivity of the fault is constant, but the dimensionless fault conductivity decreases due to increasing matrix permeability, as defined by the definition of dimensionless fracture and fault conductivities:

and $F_{CDF} = \frac{k_F w_F}{k_{rF} r_w}$, where: $k_{rF} = \frac{k_2+k_3}{2} = k_{23}$.

This effect, which results in the downturn, is clearly observed over the period of $1e8$ to $1e14$ of the dimensionless time in Figure 40.

The dimensionless fracture conductivity of Set-3 is the same as that of Set-4, since the average matrix permeability around the fracture is the same (2 md) for both cases:

$F_{CDf} = \frac{k_f w_f}{k_{rf} r_w}$, Where: $k_{rf} = \frac{k_1+k_2}{2}$.

Effect of differing fault distances on flow profile: Case 5

To study the effect of the fault and its distance from the well, a fractured-well with a fracture conductivity of $(F_{Cf} = 10\ md\ ft)$ is placed in a homogenous reservoir $(k_m = 1\ md)$ with a fault at differing distances ($d_F = 500, 1000, 2000$ & $4000\ ft$), Figure 41. The figure correctly shows the middle time, dip due to fault and second plateau signatures. It also shows that, at the same fault conductivity ($F_{CF} = 1e6\ md\ ft$), the pressure drop at the well (p_{wD}) is directly proportional to the fault distance; it increases as the fault distance from the well increases.

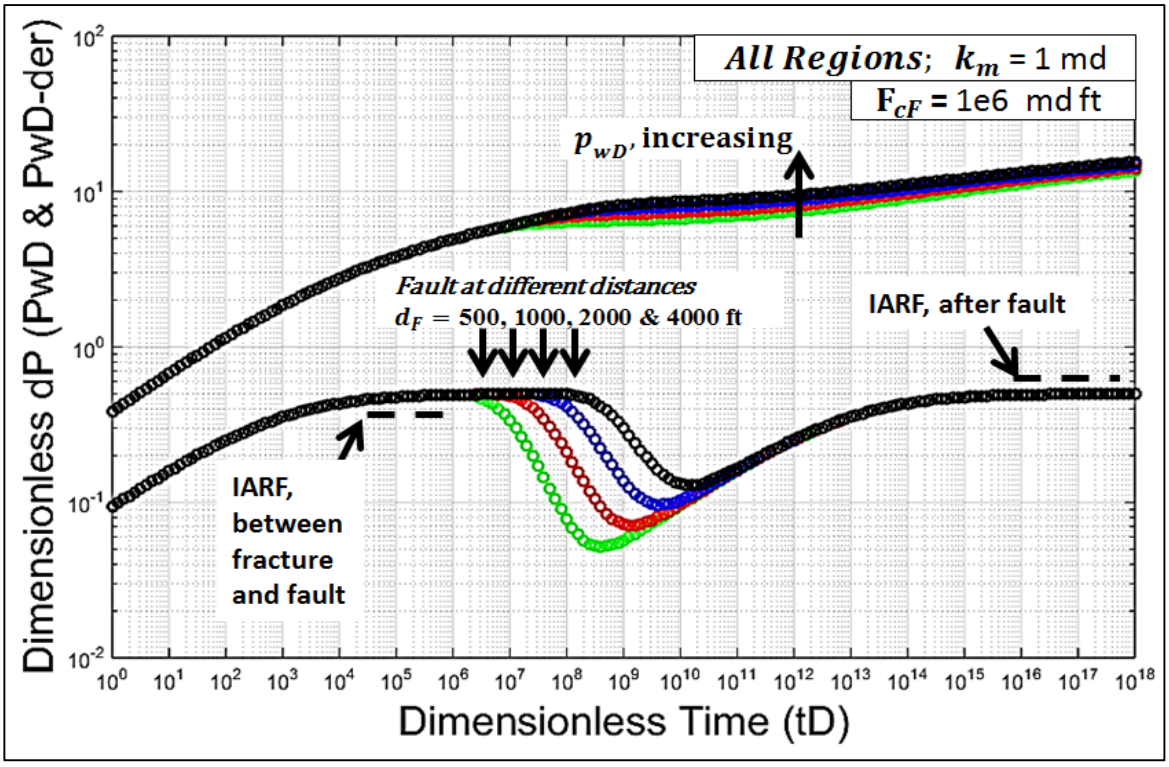

Figure 41- A fractured-well in a reservoir with a finite conductivity fault at different distances from the well.

Hence, the valley shape, in the derivative curve, is manifested later and gets shallower, reflecting the increase in the pressure drop in the pressure curve. The rationale for this occurrence could be that it is producing at a constant rate, regardless of the fault location. Therefore, a higher pressure drop is required to deliver the same rate from faults located at larger distance from the producing well.

Effect of differing fault conductivities on flow profile: Case 6

For a fractured-well model with a fracture conductivity of $(F_{Cf} = 10\ md\ ft)$ in a homogenous reservoir of $(k_m = 1\ md)$ at a fixed fault distance of $(d_F = 500\ ft)$ and changing fault conductivities, $(F_{CF} = 1e7, 1e6, 1e5\ \&\ 1e4\ \ md\ ft)$ produced the flow profiles presented in Figure 42.

Since the pressure drop at the well (p_{wD}) is inversely proportional to the fault conductivity, it increases as the fault conductivity decreases. Therefore, the valley shape gets shallower with decreasing fault conductivity.

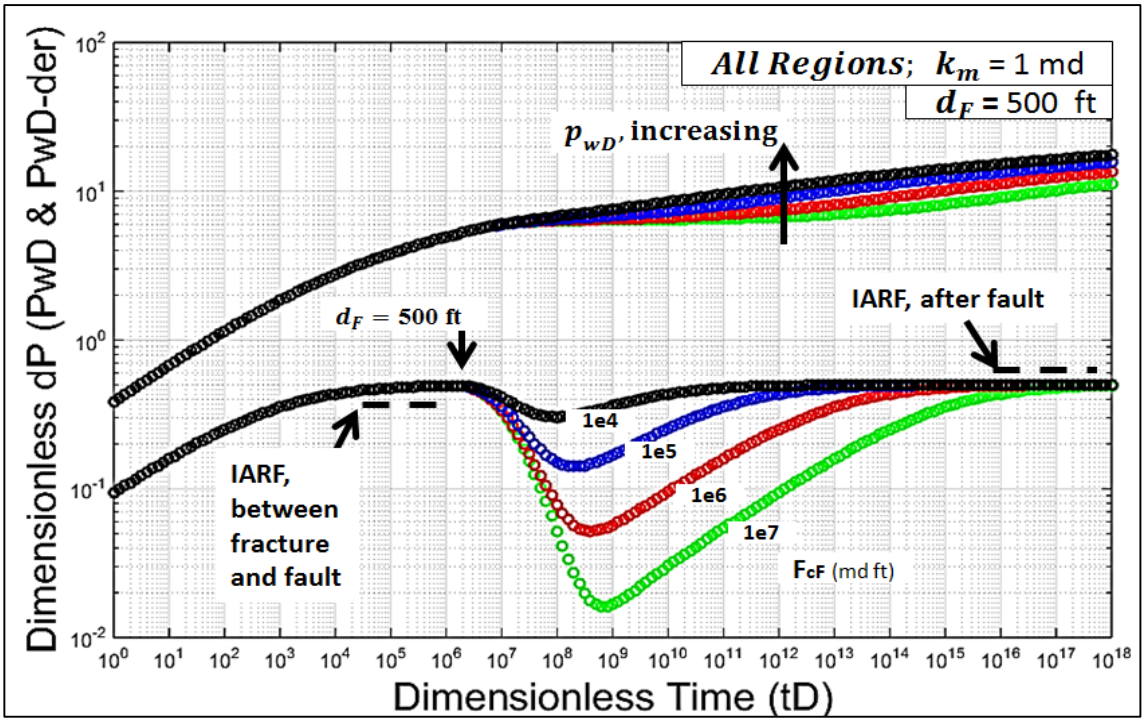

Figure 42- A fractured-well in a reservoir with a finite conductivity fault at different fault conductivities.

The physics of this occurrence could be, once more, due producing at a constant rate, regardless of the fault conductivity. Therefore, a higher pressure drop is required with a lower fault conductivity to deliver the same rate.

A fractured well near a fault in a linear composite reservoir: Case 7

The derivative curves in Figure 43 describe a fractured-well in a reservoir with a finite conductivity fault with different reservoir mobilities for Region-3. From this figure, a higher pressure drop, can be observed for low mobilities, to sustain the fixed rate and vice-versa.

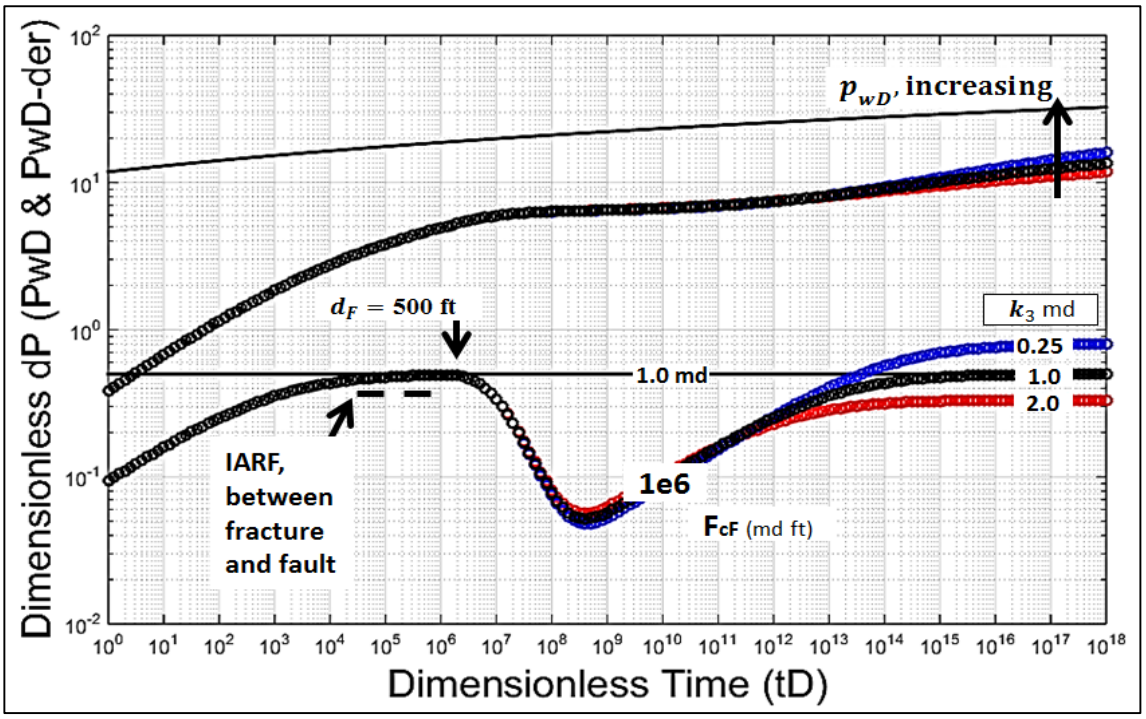

Figure 43- A fractured well near a fault in a linear composite reservoir with differing mobility at Region-3.

Adding well-bore storage and skin to the solution: Case 8

As shown in Figure 44 , the well-bore storage (WBS) can also be added. The same model with well-bore storage and skin is also presented in Figure 88.

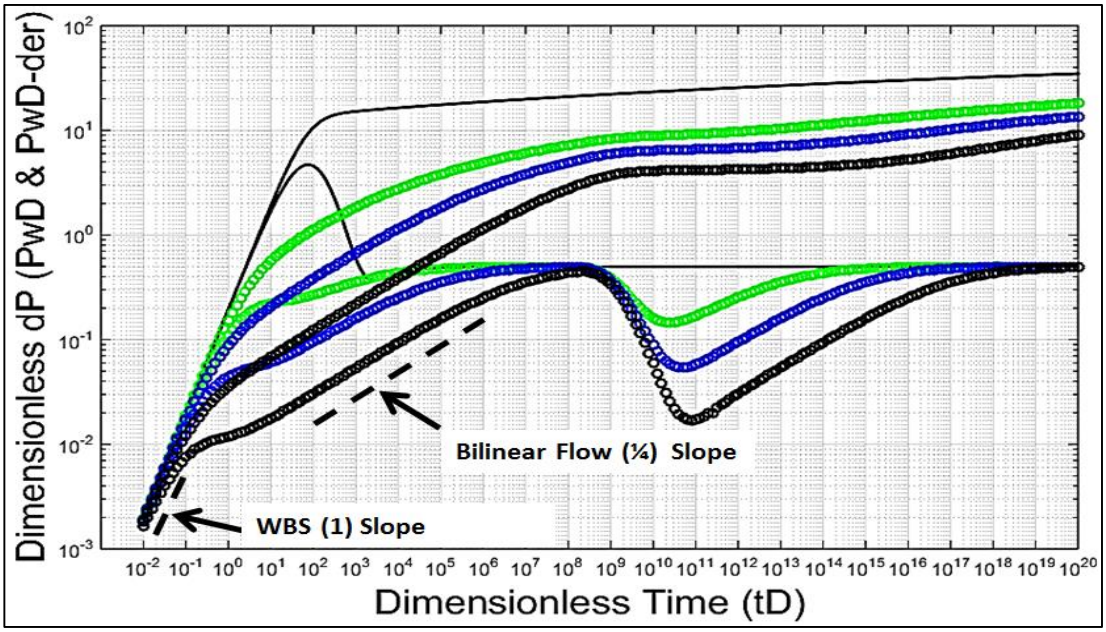

Figure 44- The curves reflect a fractured-well in a reservoir with a finite conductivity fault with different fracture and fault conductivities and well-bore storage.

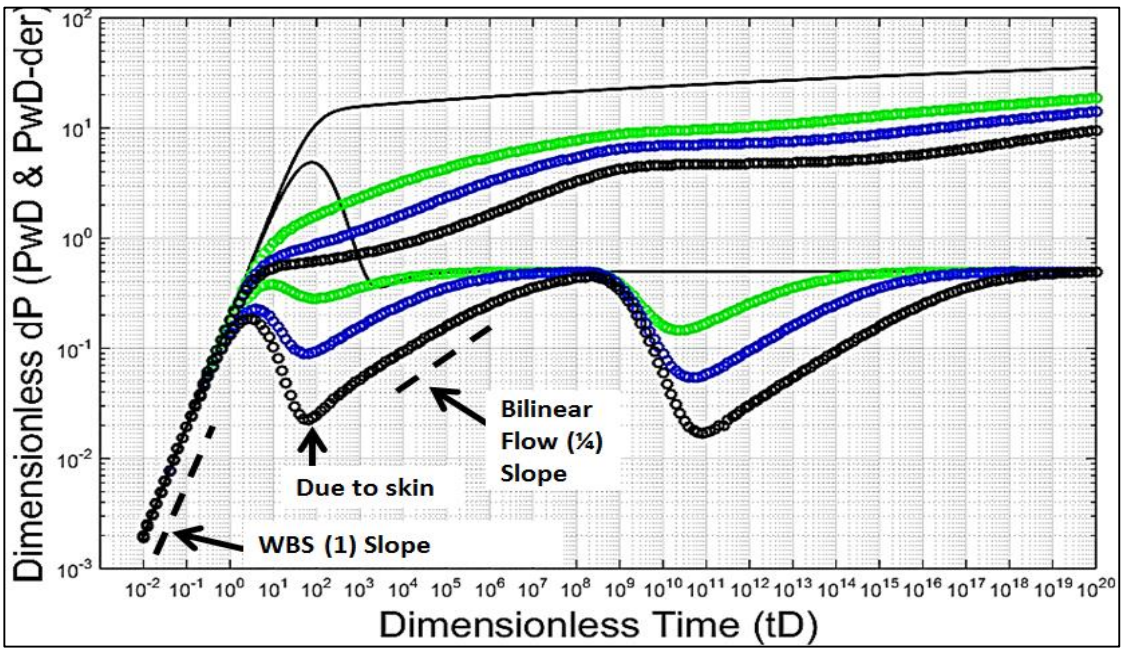

Figure 45- A fractured-well in a reservoir with a finite conductivity fault with different fracture and fault conductivities, well-bore storage and skin.

As pointed out earlier in Chapter 3, Kucuk and Ayestaran's (1985) dimensionless equations are limited to positive skin only. Figure 45 shows the unit slope, followed by a hump, indicating a transition zone that signifies the increase in pressure drop due to skin.

Summary

In Chapter 4, the reservoir is assumed to be asymmetric, complementing the efforts carried over from Chapter 3, by modelling a fractured well between three differing quality regions: 1, 2 and 3, where all the three regions have their own specific permeabilities, separated by the fractured well (between Regions 1 and 2) and the fault (between Regions 2 and 3). The solution, FracFault-model, also accounts for matrix radial flow along x and y-planes in all the three regions.

The type curve solutions of dimensionless time versus dimensionless pressure and its log-derivative for different dimensionless conductivities were presented in the Laplace domain. The proposed solution is characterised, at early times by a bilinear flow resulting from fracture/formation flows, radial flow period from the matrix bounding the fracture-well, and negative unit slopes, at middle time period, followed, at late times, by a fault bilinear flow period and a late radial flow period from the bounding blocks.

The reliability of the proposed solution was demonstrated using a number of synthetic cases. Two synthetic cases were carried-out to assure its stability. The results proved to be consistent with the expected correct physics, i.e. the total permeability was sensitive to the change in permeabilities of any region in the model around the fault. In addition to that, models for different well and geological settings were also constructed, to demonstrate the rationality of the solution, i. e. a vertical well/fractured well in a linear composite reservoir, the effect of differing fault distance on flow profile, the effect of differing fault conductivities on flow profile and a fractured-well near a fault in a linear composite reservoir. The validity confirmation of the proposed solution will then be established further through analysing a number of field cases, in Chapter 6.

The next chapter will discuss a new approach to estimate (i) the effective fracture half-length, contributing length, for an infinite fracture length and (ii) to calculate flux distribution in and alongside the fracture plane.

CHAPTER 5 – FLUX DISTRIBUTION AND EFFECTIVE FRACTURE HALF-LENGTH ESTIMATION

5.1 Introduction

Chapter 5 introduces an approach to estimate the matrix-flux distribution alongside the fracture plane, the fracture-flux and fracture's effective half-length. The objectives of this chapter were achieved by deploying the flux term in the corresponding equation and solving for the effective fracture half-length (x_{fe}). This approach calculates the fracture half-length for the infinite fracture length, when the change in pressure across the fracture-matrix interface becomes practically zero. In other words, the procedure for x_{fe} calculations is based on the assumption that extremely insignificant fluid flow will occur when the difference in pressure across the fracture plane is approaching zero ($\Delta p \approx zero$). It also estimates the fracture pressure distribution, the fracture flux and flux distributed along and into the fracture.

It is worth mentioning that, the other methods are limited to finite fracture lengths, and therefore, reflect tip effects, i.e. an increase in flux towards the fracture toe. This phenomenon is occurring, due to the greater pressure drop (per unit distance) at the fracture tips, Figure 46.

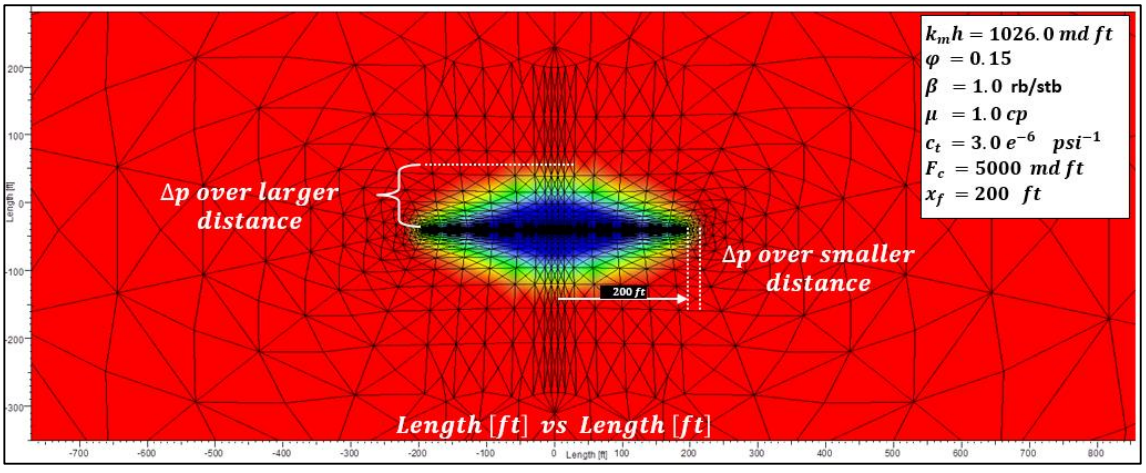

Figure 46- A fractured-well numerical model by Ecrin-KAPPA Software, illustrates the pressure drop per unit distance around a finite conductivity fractured-well.

As mentioned before, in the FracFault-model, the fracture is assumed to be of infinite length, yet the contributing "effective" length (x_{fe}) is finite. This case is more realistic,

as the transient time, drawdown time, may not be long enough to reach the tips of the fracture, or in cases where the fracture is very long, several kilometres, as is evident in some carbonate reservoirs. The method will equip reservoir engineers with an easy approach to estimate effective fracture half-length in cases of very long fractures or short flow periods are in hand.

5.2 Flux Distribution along a Finite Conductivity Fracture

The nature of "Finite Conductivity Fractures" dictates the form of un-even flux distribution. Explicitly, the flux distribution over the fracture plane is non-uniform, as the fracture pressure (p_f) along the fracture is considerably smaller closer to the well and gets larger towards the tip of the fracture. In other words, flux distribution is a function of fracture conductivity, and therefore, fracture pressure; the lower the fracture conductivity (F_{CDf}), the higher the pressure drop across the fracture face, between matrix and fracture, Figure 47.

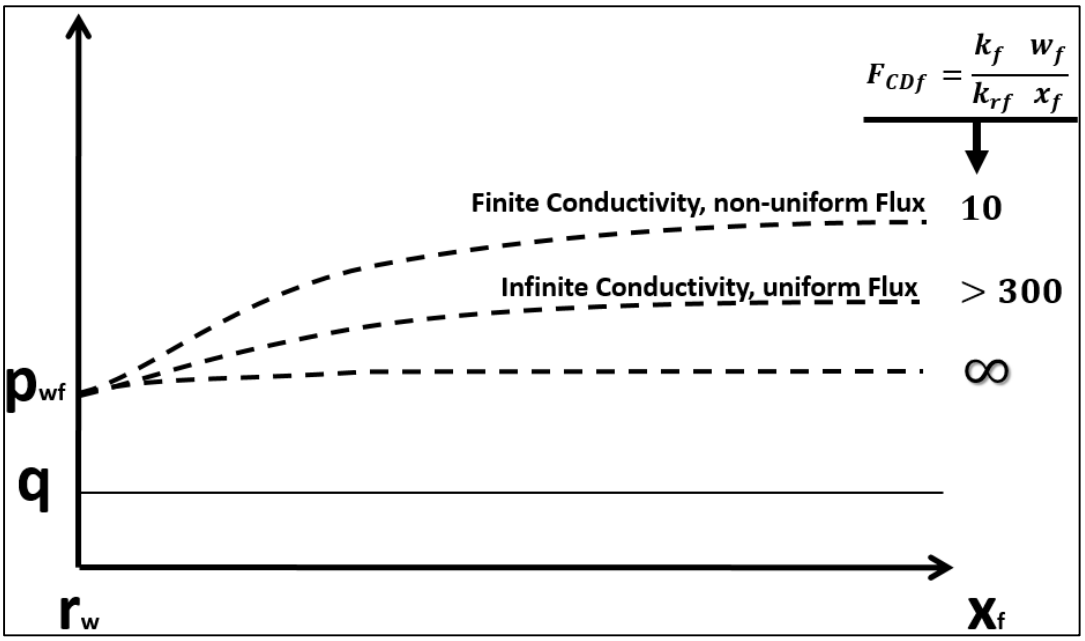

Figure 47- Schematic of fracture pressure distribution along the fracture and as a function of fracture conductivity at a constant rate.

In the FracFault-model, the fracture half-length (x_f) is assumed to be infinite, therefore, the effective fracture half-length cannot be directly calculated from the given solution. Here, in this Chapter, a solution is presented to estimate the actual fracture half-length, also referred to as: "Effective Fracture Half-length (x_{fe})". The assumption is made based on the following: the effective fracture half-length will be equal to the

conventional fracture half-length at a distance from the well where the flux from matrix is almost zero, Figure 48. At this point, the pressure drop across the fracture-matrix interface decreases and approaches zero, i.e. at $q_{Dm} \approx 0 \;\Rightarrow\; x_{fe} \approx x_f$.

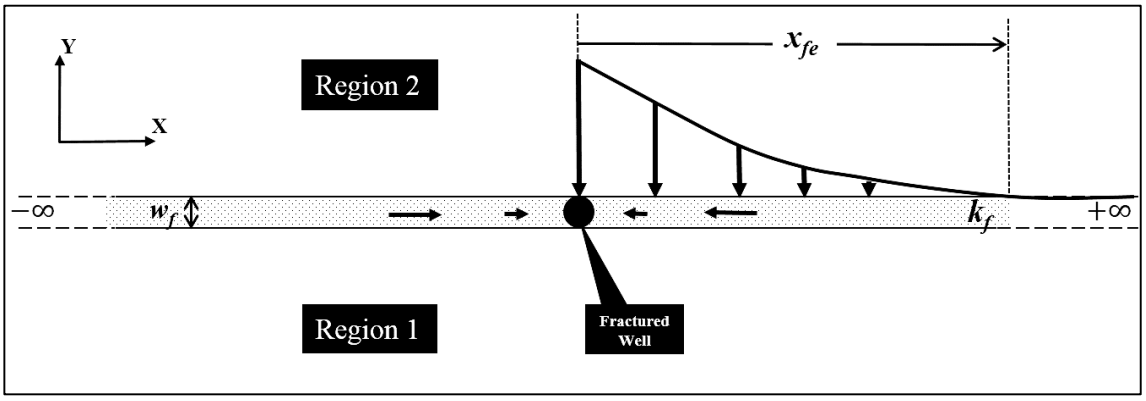

Figure 48- Schematic of the flux along a finite conductivity fracture.

5.2.1 Flux distribution from one side of the fracture on x-y plane

Assuming the flux is only from one side, along the y-direction, then:

for: ($\overline{\overline{q}}_{\mathrm{Dm}} = \left.\frac{d\overline{\overline{p}}_D}{dy_D}\right|_{y_D=0}$)

$$\overline{\overline{q}}_{\mathrm{Dm}} = \frac{1}{F_{CDf}}\left[(k_D)\cdot \left.\frac{d\overline{\overline{p}}_D}{dy_D}\right|_{y_D=0}\right]$$

And Equation 37

$$\left.\frac{d\overline{\overline{p}}_D}{dy_D}\right|_{y_D=0} = \overline{\overline{p}}_{Df}\cdot\sqrt{\left(\rho^2+\frac{s}{\eta_D}\right)}$$

$$\Rightarrow \quad \overline{\overline{q}}_{\mathrm{Dm}} = \frac{k_D}{F_{CDf}}\cdot\overline{\overline{p}}_{Df}\cdot\sqrt{\left(\rho^2+\frac{s}{\eta_D}\right)}$$

And Equation 39 with the flow from one side of the fracture only, becomes:

$$\overline{\overline{p}}_{Df} = \frac{\sqrt{2\pi}}{s.\left[F_{CDf}\cdot\left(\rho^2+\frac{s}{\eta_{Df}}\right)+(k_D).\sqrt{\left(\rho^2+\frac{s}{\eta_D}\right)}\right]}$$

Then

$$\overline{\overline{q}}_{\mathrm{D}} = \frac{k_D}{F_{CDf}} \cdot \frac{\sqrt{2\pi}}{s.\left[F_{CDf}\cdot\left(\rho^2+\frac{s}{\eta_{\mathrm{Df}}}\right)+(k_D).\sqrt{\left(\rho^2+\frac{s}{\eta_{\mathrm{D}}}\right)}\right]}.\sqrt{\left(\rho^2+\frac{s}{\eta_{\mathrm{D}}}\right)}$$

Taking the inverse of the Fourier transformation with respect to (ρ) for reverting it back to the variable (x_D) in the Laplace domain:

From

$$F^{-1}\left\{\overline{\overline{q}}_{\mathrm{Dm}}\right\} = \frac{1}{\sqrt{2\pi}}\int_{-\infty}^{\infty}\left[\overline{\overline{q}}_{\mathrm{Dm}}\right]\cdot e^{-i\rho x_D}\,d\rho = \overline{q}_{Dm}(x_D,s),$$

$$\overline{q}_{Dm}(x_D,y_D=0,s) = \frac{1}{s}\int_{-\infty}^{\infty}\frac{e^{-i\cdot x_D\cdot\rho}}{\left[\left(\frac{F_{CDf}{}^2.\left(\rho^2+\frac{s}{\eta_{Df}}\right)}{k_D.\sqrt{\left(\rho^2+\frac{s}{\eta_D}\right)}}\right)+F_{CDf}\right]}\cdot d\rho$$

$$\overline{q}_{Dm}(x_D,y_D=0,s) = \frac{1}{s}\int_{-\infty}^{\infty}\frac{e^{-i\cdot x_D\cdot\rho}}{\left[\left(\frac{F_{CDf}{}^2.\left(\rho^2+\frac{s}{\eta_{Df}}\right)}{k_D.\sqrt{\left(\rho^2+\frac{s}{\eta_D}\right)}}\right)+F_{CDf}\right]}\cdot d\rho$$

$$\overline{q}_{Dm}(x_D,y_D=0,s) = \frac{1}{s}\left[\int_0^{\infty}\frac{e^{-i\cdot x_D\cdot\rho}}{\left[\left(\frac{F_{CDf}{}^2.\left(\rho^2+\frac{s}{\eta_{Df}}\right)}{k_D.\sqrt{\left(\rho^2+\frac{s}{\eta_D}\right)}}\right)+F_{CDf}\right]}\cdot d\rho + \int_{-\infty}^{0}\frac{e^{-i\cdot x_D\cdot\rho}}{\left[\left(\frac{F_{CDf}{}^2.\left(\rho^2+\frac{s}{\eta_{Df}}\right)}{k_D.\sqrt{\left(\rho^2+\frac{s}{\eta_D}\right)}}\right)+F_{CDf}\right]}\cdot d\rho\right]$$

$$= \frac{1}{s}\left[\int_0^{\infty}\frac{e^{-i\cdot x_D\cdot\rho}}{\left[\left(\frac{F_{CDf}{}^2.\left(\rho^2+\frac{s}{\eta_{Df}}\right)}{k_D.\sqrt{\left(\rho^2+\frac{s}{\eta_D}\right)}}\right)+F_{CDf}\right]}\cdot d\rho + \int_0^{\infty}\frac{e^{i\cdot x_D\cdot\rho}}{\left[\left(\frac{F_{CDf}{}^2.\left(\rho^2+\frac{s}{\eta_{Df}}\right)}{k_D.\sqrt{\left(\rho^2+\frac{s}{\eta_D}\right)}}\right)+F_{CDf}\right]}\cdot d\rho\right]$$

$$\Rightarrow \overline{q}_{Dm}(x_D,y_D=0,s) = \frac{1}{s}\left[\int_0^{\infty}\frac{e^{-i\cdot x_D\cdot\rho}+e^{i\cdot x_D\cdot\rho}}{\left[\left(\frac{F_{CDf}{}^2.\left(\rho^2+\frac{s}{\eta_{Df}}\right)}{k_D.\sqrt{\left(\rho^2+\frac{s}{\eta_D}\right)}}\right)+F_{CDf}\right]}\cdot d\rho\right]$$

And for:

$$e^{-i\cdot x_D\cdot\rho} + e^{i\cdot x_D\cdot\rho} =$$

$$[\cos(x_D\,\rho) - i\,.\sin(x_D\,\rho)] + [\cos(x_D\,\rho) + i\,.\sin(x_D\,\rho)] = 2\,.\cos(x_D\,\rho)$$

Then, the flux from one side of the fracture can be described by:

$$\overline{q}_{Dm}(x_D, y_D = 0, s) = \frac{-2}{s}\int_0^{\infty} \frac{\cos\,(x_D\,\rho)}{\left[\left(\frac{F_{CDf}{}^2\cdot\left(\rho^2+\frac{s}{\eta_{Df}}\right)}{k_D\cdot\sqrt{\left(\rho^2+\frac{s}{\eta_D}\right)}}\right)+F_{CDf}\right]}\cdot d\rho$$

Or

Equation 95

$$\overline{q}_{Dm}(x_D, y_D = 0, s) = \frac{-2}{s}\int_0^{\infty} \frac{\cos\,(x_D\,\rho)}{\left[\left(\frac{F_{CDf}\cdot\left(\rho^2+\frac{s}{\eta_{Df}}\right)}{\sqrt{\left(\rho^2+\frac{s}{\eta_D}\right)}}\right)+k_D\right]}\cdot d\rho \qquad (95)$$

Plotting:

q_{Dm} *Versus* x_D, Or q_{Dm} *Versus* x_f

Will yield the estimated effective fracture half-length (x_{fe}) with respect to fracture conductivity and reservoir permeability, where the dimensionless forms are:

$q_{Df} = \frac{q_f\cdot(2\pi\,h\;x_{fe})}{q_w\cdot\beta}$, $q_f = Fracture\ Rate\ (bpd)$ and $q_w = Well\ Rate\ (bpd)$

$x_D = \frac{x_f}{r_w}$ And $x_f\big|_{q_{Dm}=0} = x_{fe}$

$F_{CDf} = \frac{k_f\,w_f}{k_{fr}\,r_w}$, $k_{fr} = \frac{k_{R1}+k_{R2}}{2}$, arithmetic average of Regions' 1 & 2 permeabilities.

In this case k_{R1} and k_{R2} are equal, therefore, $k_{rf} = k_{matrix}$

5.2.2 Flux distribution from two sides of the fracture on x-y plane

Assuming the flux is from two sides of the fracture, along x- and y-plane, then:

For: ($\overline{\overline{q}}_{Dm} = \left.\frac{d\overline{\overline{p}}_D}{dy_D}\right|_{y_D=0}$)

$$\overline{\overline{q}}_{Dm} = \frac{1}{F_{CDf}}\left[(k_{D2})\cdot\left.\frac{d\overline{\overline{p}}_{D2}}{dy_D}\right|_{y_D=0} - (k_{D1})\cdot\left.\frac{d\overline{\overline{p}}_{D1}}{dy_D}\right|_{y_D=0}\right]$$

From Equation 37

$$\left.\frac{d\overline{\overline{p}}_{D1}}{dy_D}\right|_{y_D=0} = \overline{\overline{p}}_{Df}\cdot\sqrt{\left(\rho^2+\frac{s}{\eta_{D1}}\right)}$$

$$\left.\frac{d\overline{\overline{p}}_{D2}}{dy_D}\right|_{y_D=0} = -\overline{\overline{p}}_{Df}.\sqrt{\left(\rho^2+\frac{s}{\eta_{D2}}\right)}$$

$$\Rightarrow \quad \overline{\overline{q}}_{Dm} = \frac{-1}{F_{CDf}}\left[(k_{D2})\cdot\overline{\overline{p}}_{Df}.\sqrt{\left(\rho^2+\frac{s}{\eta_{D2}}\right)}+(k_{D1})\cdot\overline{\overline{p}}_{Df}.\sqrt{\left(\rho^2+\frac{s}{\eta_{D1}}\right)}\right]$$

And Equation 39 becomes:

$$\overline{\overline{p}}_{Df} = \frac{\sqrt{2\pi}}{s.\left[F_{CDf}.\left(\rho^2+\frac{s}{\eta_{Df}}\right)+(k_{D1}).\sqrt{\left(\rho^2+\frac{s}{\eta_{D1}}\right)}+(k_{D2}).\sqrt{\left(\rho^2+\frac{s}{\eta_{D2}}\right)}\right]}$$

Then

$$\overline{\overline{q}}_{Dm} = \frac{-\sqrt{2\pi}}{s\,.\,F_{CD}}\cdot\frac{(k_{D1}).\sqrt{\left(\rho^2+\frac{s}{\eta_{D1}}\right)}+(k_{D2}).\sqrt{\left(\rho^2+\frac{s}{\eta_{D2}}\right)}}{\left[F_{CDf}.\left(\rho^2+\frac{s}{\eta_{Df}}\right)+(k_{D1}).\sqrt{\left(\rho^2+\frac{s}{\eta_{D1}}\right)}+(k_{D2}).\sqrt{\left(\rho^2+\frac{s}{\eta_{D2}}\right)}\right]}$$

Taking the inverse of Fourier transformation with respect to (ρ) for reverting it back to the variable (x_D) in Laplace domain:

From

$$F^{-1}\left\{\overline{\overline{q}}_{Dm}\right\} = \frac{1}{\sqrt{2\pi}}\int_{-\infty}^{\infty}\left[\overline{\overline{q}}_{D}\right]\cdot e^{-i\rho x_D}\,d\rho = \overline{q}_D\,(x_D,s),$$

Similarly to the steps carried over from section (5.2.1), it gives:

Equation 96

$$\overline{q}_{D(xy)}(x_D,y_D=0,s) = \frac{-2}{s}\int_0^{\infty}\frac{\cos\,(x_D\,\rho)}{\left[\left(\frac{\left[F_{CDf}.\left(\rho^2+\frac{s}{\eta_{Df}}\right)+(k_{D1}).\sqrt{\left(\rho^2+\frac{s}{\eta_{D1}}\right)}+(k_{D2}).\sqrt{\left(\rho^2+\frac{s}{\eta_{D2}}\right)}\right]}{(k_{D1}).\sqrt{\left(\rho^2+\frac{s}{\eta_{D1}}\right)}+(k_{D2}).\sqrt{\left(\rho^2+\frac{s}{\eta_{D2}}\right)}}\right)\right]}\cdot d\rho \qquad (96)$$

5.2.3 Flux distribution from two sides of the fracture along y-axis

Similarly; by eliminating the Fourier space variable in the matrix, (x_D) in terms of the parameter (ρ), the flow along the y-axis only is:

Equation 97

$$\overline{q}_{Dy}(x_D,y_D=0,s) = \frac{-2}{s}\int_0^{\infty}\frac{\cos\,(x_D\,\rho)}{\left[\left(\frac{\left[F_{CDf}.\left(\rho^2+\frac{s}{\eta_{Df}}\right)+(k_{D1}).\sqrt{\left(\frac{s}{\eta_{D1}}\right)}+(k_{D2}).\sqrt{\left(\frac{s}{\eta_{D2}}\right)}\right]}{(k_{D1}).\sqrt{\left(\frac{s}{\eta_{D1}}\right)}+(k_{D2}).\sqrt{\left(\frac{s}{\eta_{D2}}\right)}}\right)\right]}\cdot d\rho \qquad (97)$$

5.2.4 Fracture Flux Distribution along fracture

The flux along the fracture can be expressed using this equation:

$$\overline{q}_{Df}(x_D, y_D = 0, s) = -F_{CDf} \cdot \frac{d\overline{p}_{Df}}{dx_D}$$

And the fracture pressure distribution with respect to the x-axis,

$F^{-1}\left\{\overline{\overline{p}}_{Df}\right\} = \frac{1}{\sqrt{2\pi}} \int_{-\infty}^{\infty} \overline{\overline{p}}_{Df}\, e^{-i\rho x_D}\, d\rho = \overline{p}_{Df}\,(x_D, s)$, inverted back to Laplace space

Substitute Equation 41 then (repeating the steps above):

Equation 98

$$\overline{p}_{Df}(x_D, y_D = 0, s) = \frac{-2}{s} \int_{-\infty}^{\infty} \frac{\cos\,(x_D\,\rho)}{\left[\left(F_{CDf}\cdot\left(\rho^2+\frac{s}{\eta_{Df}}\right)\right)+\left((k_{D1})\cdot\sqrt{\left(\rho^2+\frac{s}{\eta_{D1}}\right)}\right)+\left((k_{D2})\cdot\sqrt{\left(\rho^2+\frac{s}{\eta_{D2}}\right)}\right)\right]} \cdot d\rho \quad (98)$$

Plotting:

$\overline{p}_{Df}$, $\overline{q}_{Df}$, $\overline{q}_{Dy}$ *and* $\overline{q}_{Dxy}$ *Versus* x_f,

will present the pressure and flux distribution along (x) and determine (x_{fe}) at a flux and/or pressure depletion of value $\geq 99.99\%$ of the total calculated value. It should be noted that the value for this criterion can be altered, but in the FracFault-model it was noted that it reasonably matches the fracture half-length of many numerically built cases. Furthermore, in reality, if there is a fracture length part that contributes less than 0.01% would not be dominating the flow behaviour and hence can be ignored.

5.3 Overall Solution Behaviour: Observations and Discussions

Here the effect of a number of variables, on the solution of flux distribution and effective fracture half-length is studied;

$\boldsymbol{q = 2\pi\ to\ 2000\pi}$ $(\boldsymbol{bpd})$

$\boldsymbol{k_m = 1.0\ \ to\ \ 10000}$ $(\boldsymbol{md})$

$\boldsymbol{h\ = 100.0}$ $(\boldsymbol{ft})$

$\boldsymbol{r_w = 0.25}$ $(\boldsymbol{ft})$

$\boldsymbol{\varphi\ = 15.0}$ (%)

$\boldsymbol{\beta\ = 1.0}$ $(\boldsymbol{rb/stb})$

$\boldsymbol{\mu\ = 0.7}$ $(\boldsymbol{cp}$

$\boldsymbol{c_t\ = 3.0\,e^{-6}}$ $(\boldsymbol{psi^{-1}})$

$\boldsymbol{F_{Cf}\ = 1.0e^{1}\ \ to\ \ 1.0e^{6}}$ $(\boldsymbol{md\ ft})$

$\boldsymbol{w_f\ = 1.0}$ $(\boldsymbol{foot})$

For simplicity, the author selected to fix the fracture width to be always one foot, ($w_f = 1.0 \ \ foot$). This has no effect on the results and makes simple comparison possible with other analytical, numerical and field data. The type curve of a well intersecting a finite conductivity fracture located between two different regions, has been reproduced as shown in Figure 49. In this case, both regions (1&2) are of the same quality (1.0 md).

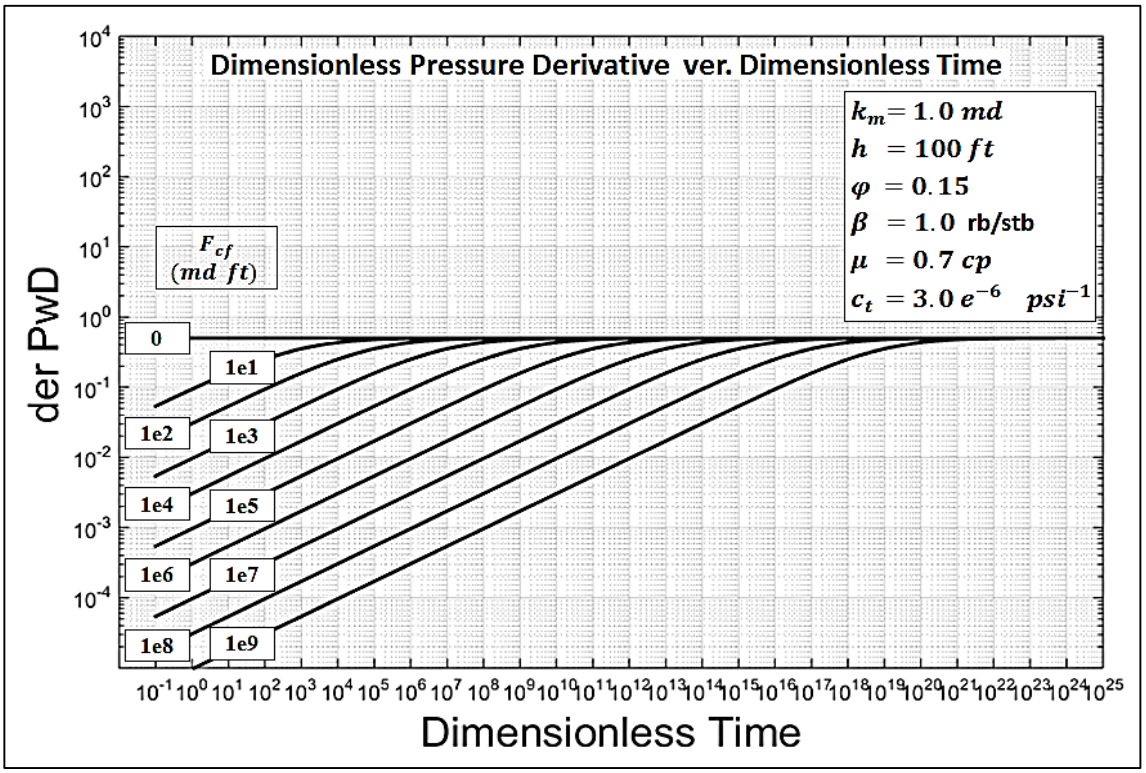

Figure 49- Dimensionless Pressure Derivative versus Dimensionless Time at different fracture conductivities.

5.3.1 Sensitivity Runs

Comparison between fluxes of matrix calculated on x-y plane and y-Axis: Case-1

This approach allows for more realistic transient and flux calculation, as it is accounting for the matrix flow on the x-y plane (q_{Dxy}). Other studies account for the flow in the y-plane only, (q_{Dy}). A case scenario was run to compare the two approaches, as presented in Figure 50 and Figure 51. The two approaches are in good agreement, as they both have the same trend. The solution over the x-y plane represent a more realistic pattern of the fluid flow in the porous media. The presence of scattered data may be due to numerical issues, but it can also be attributed to the diagonal flow nature and convergence into the fracture, which need to be investigated further. However, it is

important to mention that, the extremely small y-scale (10^{-6}) largely magnifies the plotted data. At this stage it is assumed that the two solutions are similar, and in fact, for the effective fracture length calculation, the y-axis flow is the only solution considered. It has to be added that the solution of equations in the x-y plane allows us to observe the radial flow signature after the bilinear flow signature. To the best of the author's knowledge, in some of the existing software, the radial flow is not calculated but graphically added to the solution. The two curves are superimposed and shown in Figure 52.

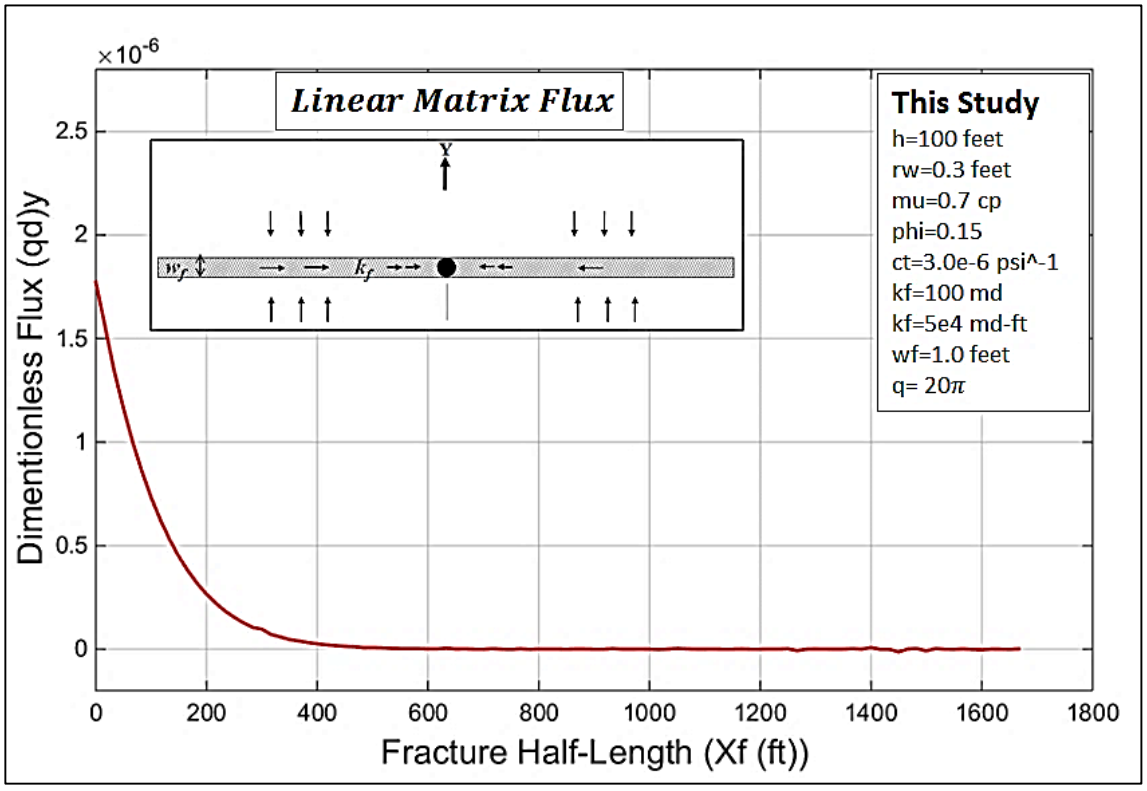

Figure 50- Matrix "Linear" flux distribution along the fracture on the y-plane.

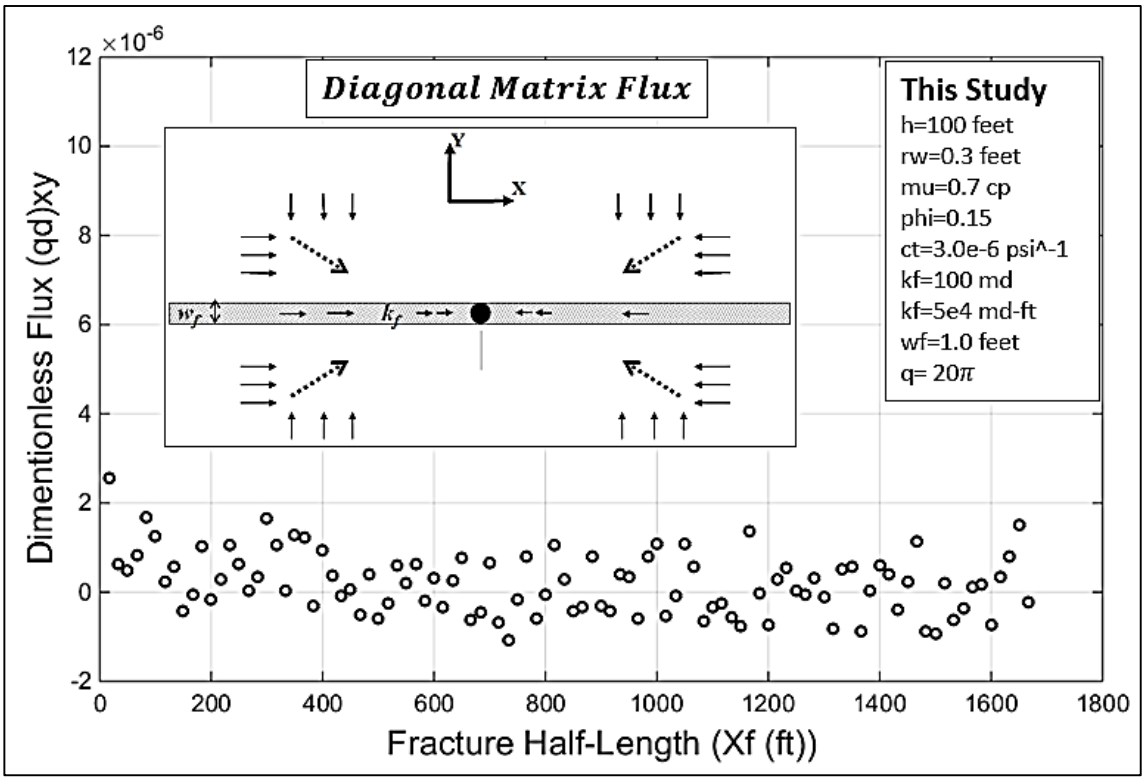

Figure 51- Matrix "Diagonal" flux distribution along the fracture on the x-y plane.

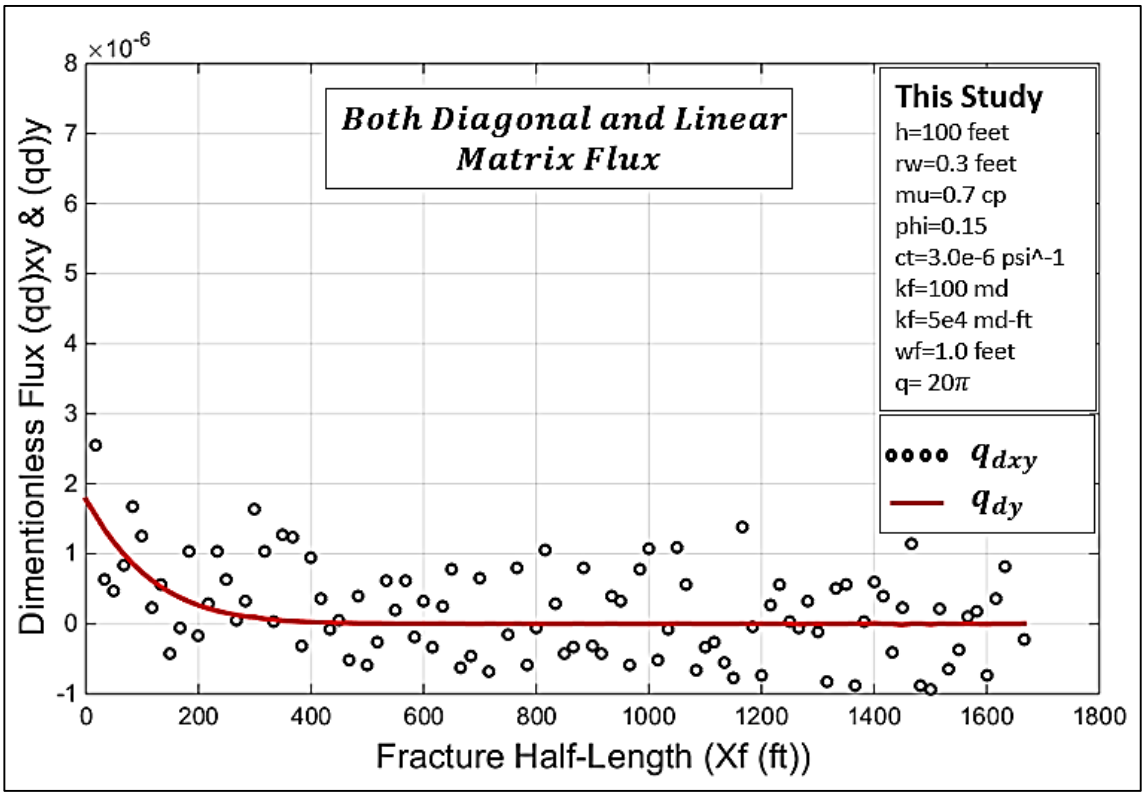

Figure 52- Both "Linear" and "Diagonal" Matrix flux distribution along the fracture on the x-y plane.

Effect of matrix permeability on flux magnitude: Case-2

Figure 53 shows the effect of the matrix permeability on the amount of flux accumulation at the origin $(x_D = 0)$. For a fracture conductivity of $(k_f = 1e3)$, three-permeability matrix cases were run: 100, 200 and 300 md, with results showing that the contribution from the matrix to the fracture increases with increasing permeability. In other words, at a constant fracture conductivity and pressure drop, the fluids flow more along the matrix due to increased permeability.

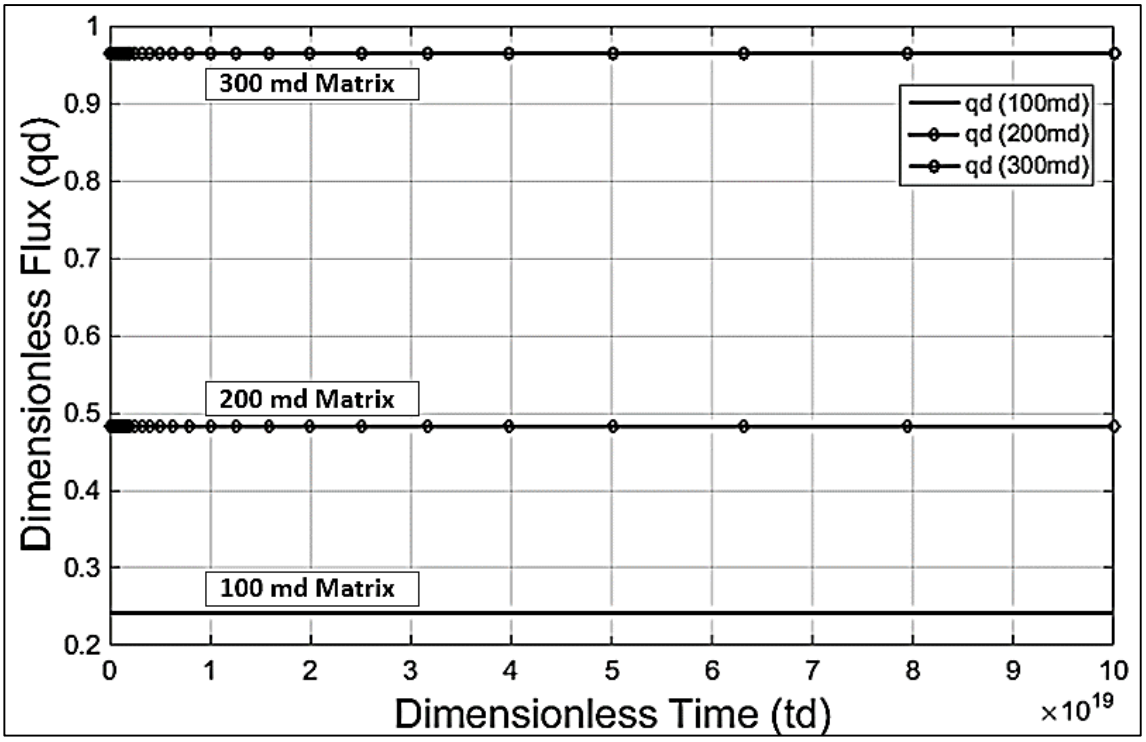

Figure 53- Matrix flux accumulation sensitivity case for differing matrix permeability.

Effect of fracture conductivity on flux quantity: Case-3

Figure 54, shows the effect of the fracture conductivity on the amount of flux accumulation at the origin $(x_D = 0)$. In a matrix permeability of 100 md, three-fracture conductivity cases were run: 1000, 2000 and 4000 md-ft with results showing that the contribution from the matrix decreases with increasing fracture conductivity for the same applied pressure drawdown. At high conductivity values, the fracture acts as a source of fluid supply, confirming the observation also first noted by Maghsood and Cinco-Ley (1995). Fluids tend to be supplied by the fracture itself, as the pressure-drop across the fracture is exceptionally small; hence, the fluids' flow along the fracture plane, i.e. the

fracture linear flow regime, is more than the fluids' flow from the matrix supplying the fracture, i.e. the formation linear flow regime.

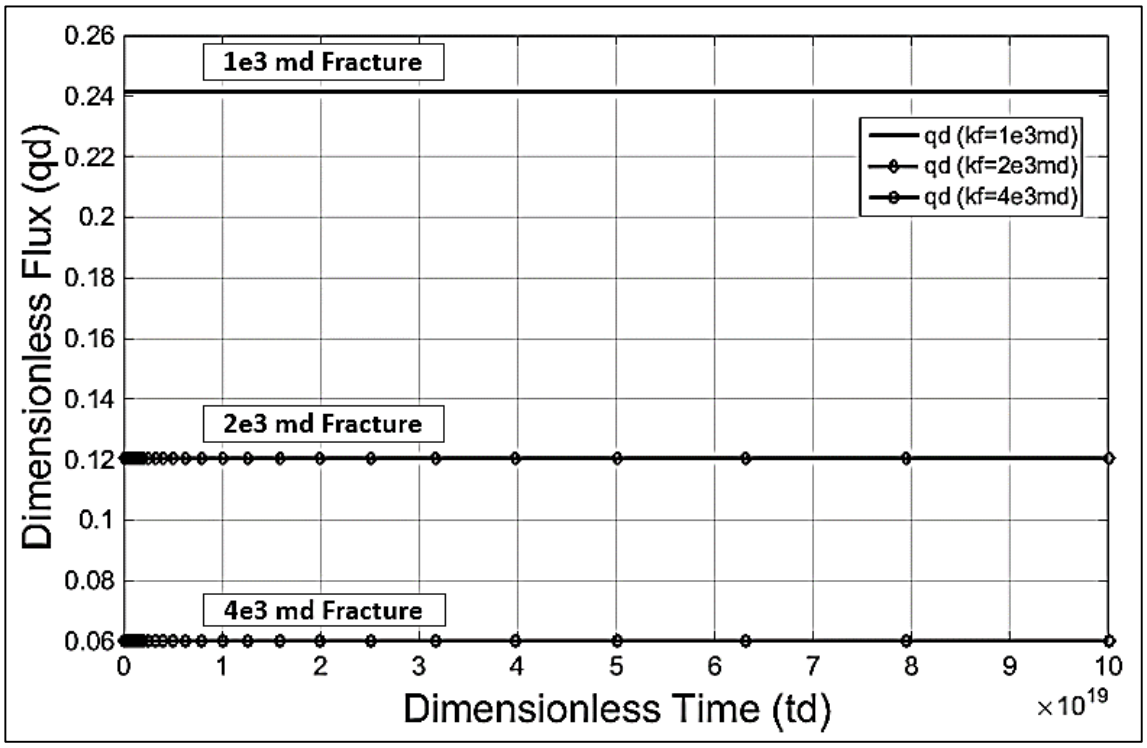

Figure 54- Matrix flux accumulation sensitivity case for differing fracture conductivity.

Effect of fracture conductivity on source of fluids and fracture half-length: Case-4

Assuming the well is a source (injector), Figure 55 below clearly shows the profile distribution of the fracture pressure along the fracture aperture at the same wellbore flow rate for all considered cases. At lower fracture conductivity values (black curve), the fracture pressure at $x = 0$, is higher, as it is harder to inject into the fracture and is lower as the conductivity is higher, hence, fluids tend to dissipate into the matrix more at lower fracture conductivities. Therefore, at high conductivity values (green and blue Curves), the fracture takes the fluid injected, confirming the observation also first reported by Maghsood and Cinco-Ley (1995), where they noted it becomes a source of fluid in the case of a sink (producer). As a result, smaller fracture half-length is expected at lower fracture conductivities as clearly shown in Figure 55. A very interesting observation is noted at ($x_{fe} \approx 60\ ft$), where the trend of pressure values changes at some distance along the fracture length from being higher at lower k_f to being lower. This deflection may be attributed to smaller fracture pressure distribution along the fracture at high fracture conductivity values, hence, a more uniform flux

distribution along the fracture length. This observation confirms that, at low conductivity fractures, a non-uniform distribution flux is expected.

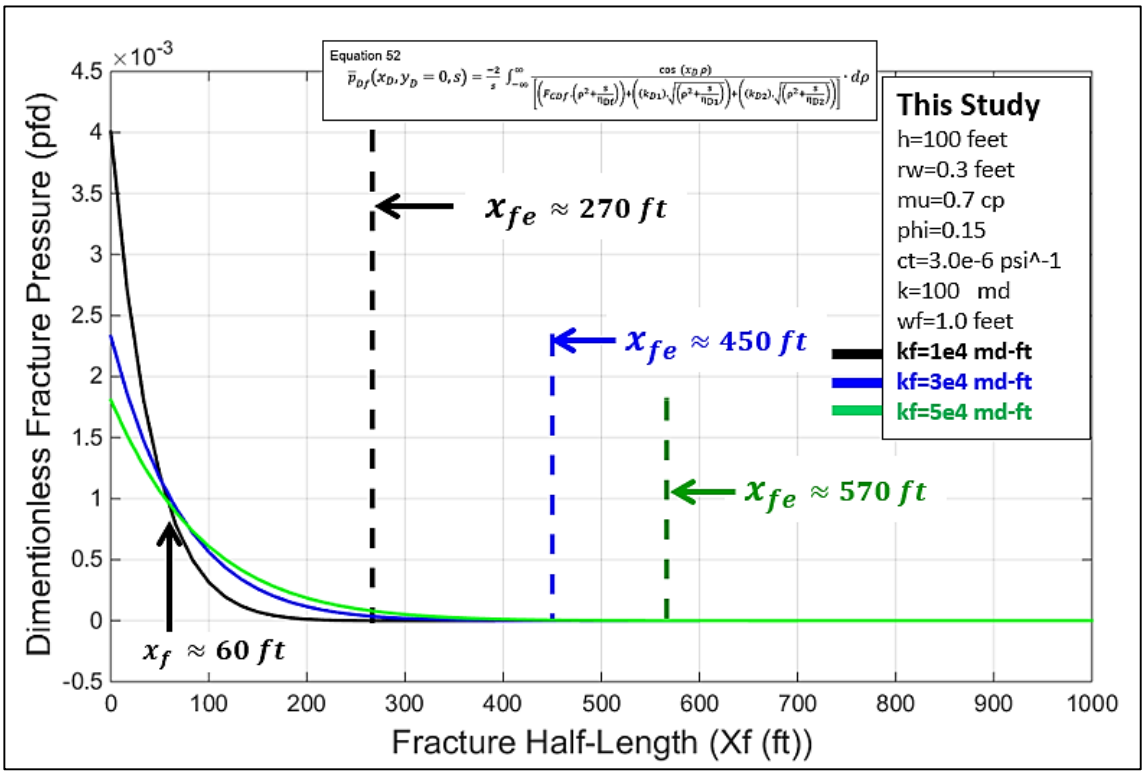

Figure 55- Fracture pressure distribution alongside the fracture and fracture half-length estimation at different fracture conductivities and a well-rate of 2π bpd.

Figure 56, below, shows the fracture flux distribution along the fracture aperture. It is noted that, at larger fracture conductivity, the fracture accepts more fluid in an "injector scenario". Fluids tend to be supplied through the fracture itself, as the pressure-drop across the fracture is exceptionally small; hence, fluids are flowing along the fracture plane, i.e. the fracture linear flow regime, enormously faster than the fluids flowing from the matrix supplying the fracture, i.e. the formation linear flow regime. It is worth mentioning that the flux values are very small, due to the high quality fractures and relatively low injection rate (2π). The slight difference in fracture half-length estimation between Figure 55 and Figure 56 is due to the criteria used in the FracFault-model. That is, it is largely affected by the fact that (x_{fe}) is estimated at the remaining 0.01% of the pressure drop in Figure 48 and total flux in Figure 49.

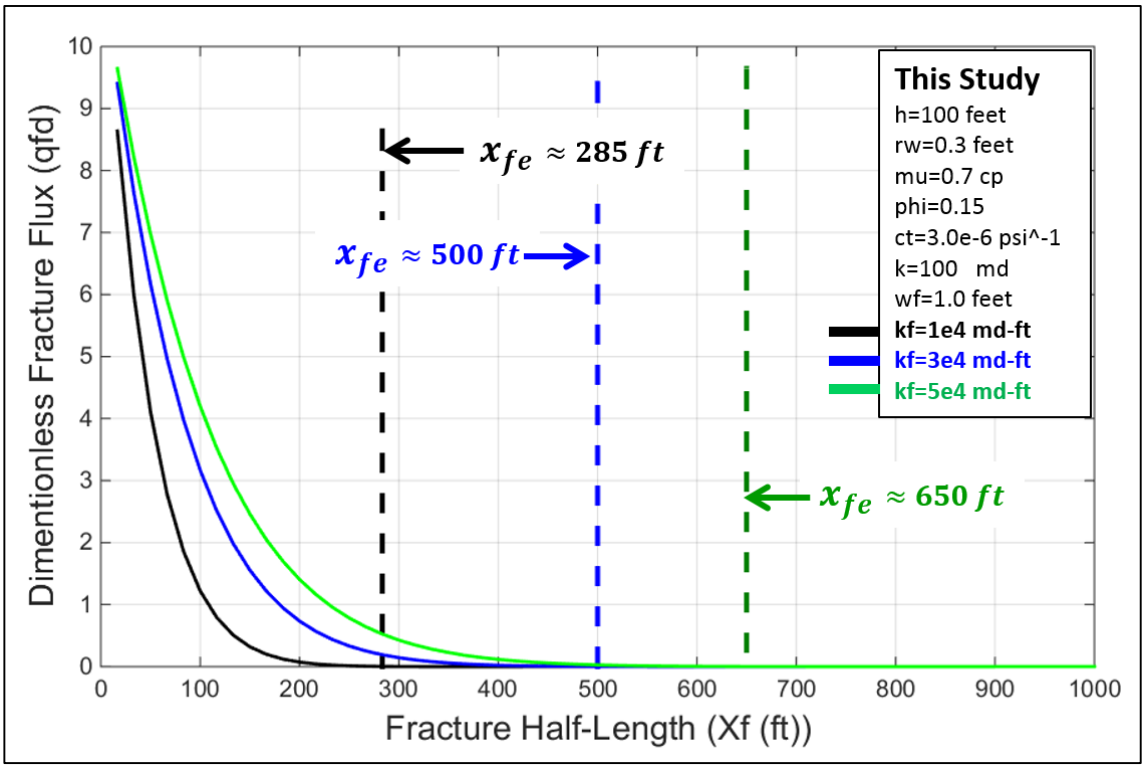

Figure 56- Fracture flux distribution alongside the fracture and fracture half-length estimation at different fracture conductivities and a well-rate of 2π bpd.

Figure 57, below, shows that the matrix flux distribution confirms the observations mentioned above. Specifically, the fracture conductivity becomes larger, the fracture accepts more fluid in an "injector" scenario, and thus less fluid is dissipated into the matrix (green curve). In other words, more flux is taken/contributed by the matrix at lower fracture conductivity values (black curve).

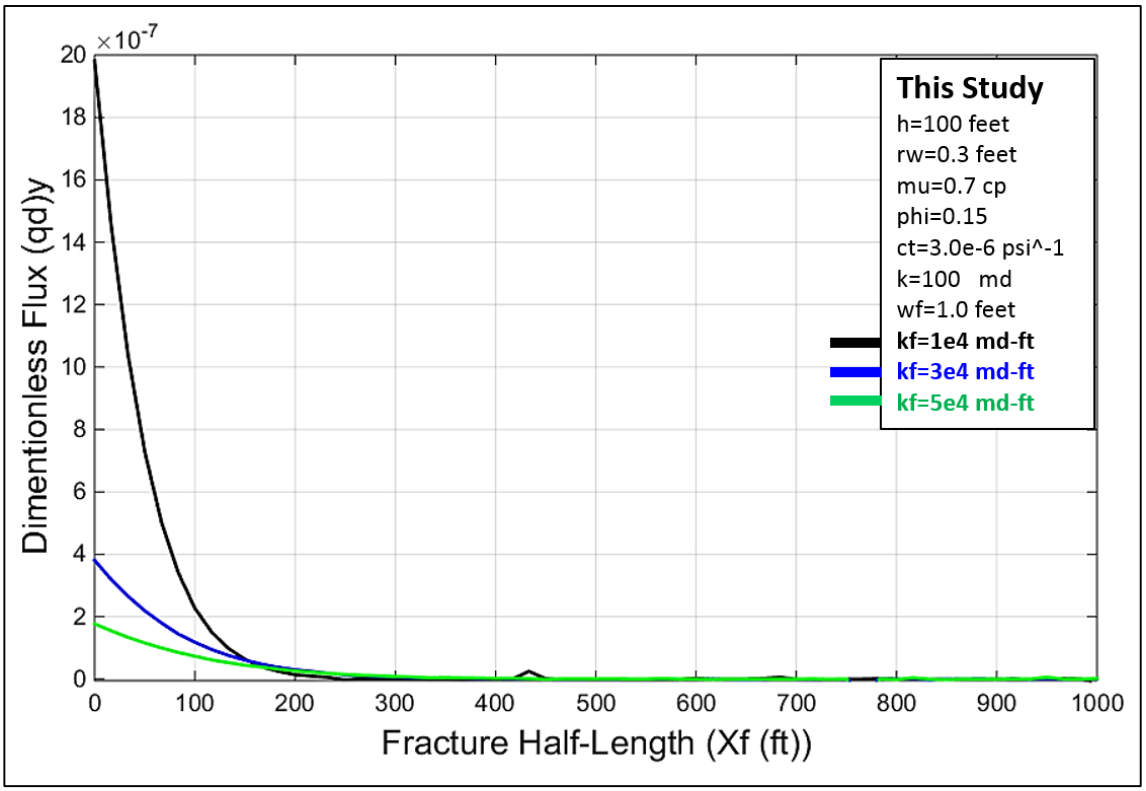

Figure 57- Matrix Linear flux distribution alongside the fracture and fracture half-length estimation at different fracture conductivities and a well-rate of 2π bpd.

Effect of matrix permeability on effective fracture half-length: Case-5

Changing the matrix permeability has a clear effect on the estimation of effective fracture half-length (x_{fe}). Figure 58, shows three dimensionless pressure curves with differing matrix permeabilities (i.e. 100, 300 and 500 md). The curves were superimposed estimating different fracture half-length (x_{fe}) of 530 ft, 415 ft and 365 ft, respectively. That is, in a "source" case, the lower the matrix permeability, the longer the fracture, to allow the same injected fluid.

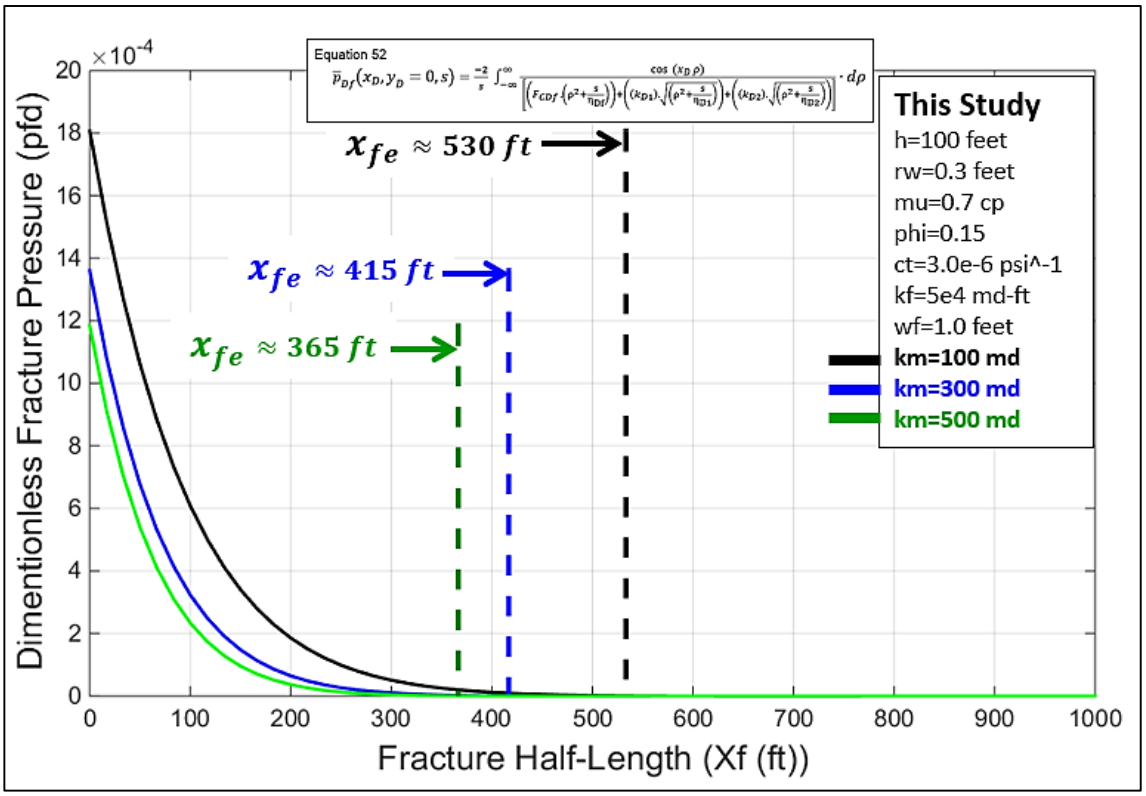

Figure 58- Dimensionless fracture pressure along fracture aperture versus fracture half-length estimation at different matrix permeabilities.

Another interesting observation is noted at ($x_{fe} \approx 80\ ft$), Figure 59, where the matrix fluxes lean towards reversing in trend at some distance along the fracture length. This deflection may be attributed to the higher fracture conductivity for the lower matrix quality case that contributed to the increase of the flux from or into the matrix after the deflection point. It should be noted that the total flux is constant for all the three cases.

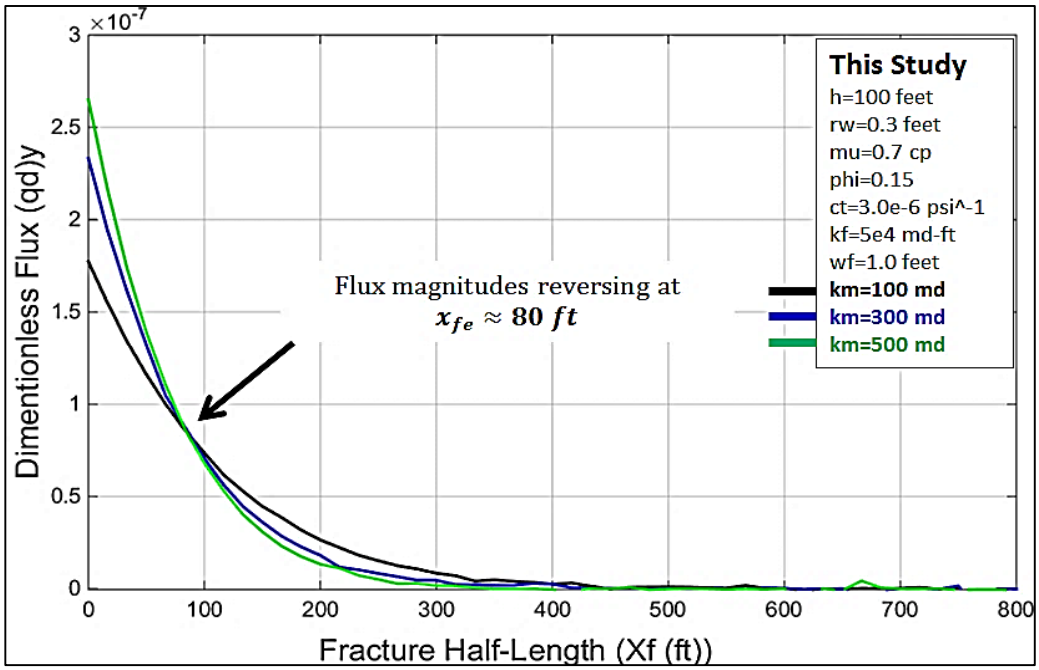

Figure 59- Dimensionless linear flux distribution alongside the fracture and fracture plane at different matrix permeabilities.

Effect of two-region composite system on fracture/matrix fluxes and effective fracture half-length: Case-6

The solution can handle a two-region composite reservoir across the fracture. Two sets of data were run simultaneously to show and validate the solution:

Set-1: Homogenous (same quality reservoir); $(k_1 = k_2 = 10\ md)$

with fractured-well; $F_{cf} = 5e4\ md\ ft$,

Set-2: Composite regions (differing quality reservoir); $(k_1 = 100md\ \ and\ \ k_2 = 10\ md)$ with fractured-well; $F_{cf} = 5e4\ md\ ft$,

Basically, Set-2 is reflecting a permeability equal to the arithmetic average of Regions 1 and 2 ($k_1 and\ k_2 = 55\ md$), which is different from that of Set-1, and hence, reflects a higher quality reservoir. The curves of Set-1 and Set-2 were superimposed and estimated different fracture effective half-lengths (x_{fe}) of 985 ft and 685 ft, respectively. The lower the matrix permeability, the longer the fracture, to accept more of the injected fluid. Again, for higher quality, Set-2, the matrix contributes/accepts flow at larger scale than with the lower quality. As for the fracture, it is the opposite, where the fracture for the low quality matrix, Set-1, is the main source to contribute/accept fluids, Figure 60 and Figure 61.

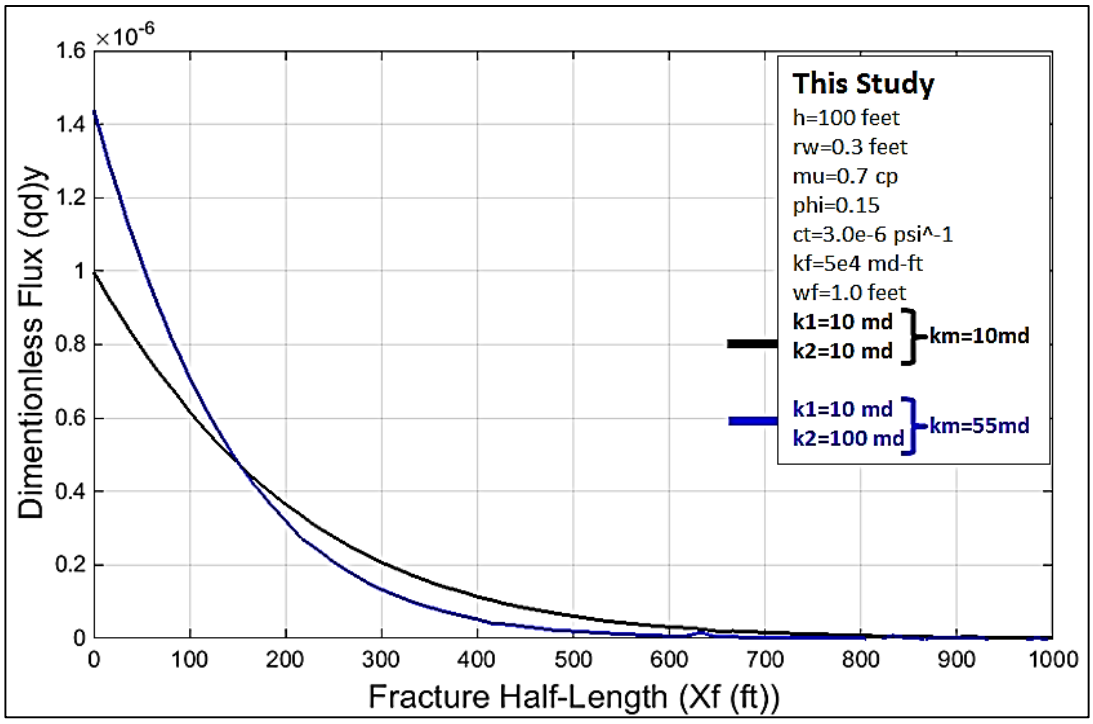

Figure 60- Dimensionless flux distribution alongside the fracture and fracture half-length estimation for a composite reservoir.

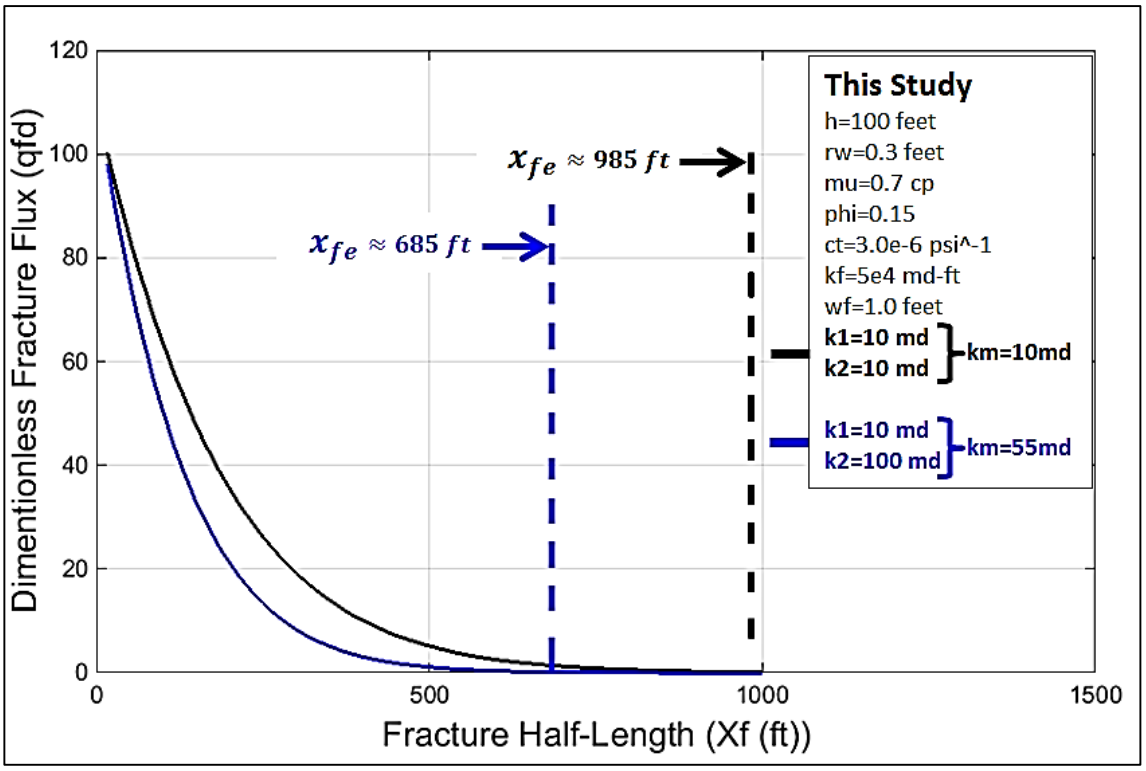

Figure 61- Dimensionless flux distribution along the fracture aperture for composite reservoir.

Effect of well-rate on fracture/matrix fluxes and effective fracture half-length: Case-7

This scenario is run with a reasonable matrix permeability (100 md) and fracture conductivity of ($5e4$ md-ft) more than two orders of magnitude, to replicate a real case at different well rates of (2π, 20π and 200π). At higher rates, understandably, matrix and fracture contributions are larger, Figure 62 and Figure 63, confirming the accurate behaviour and physics of the solution.

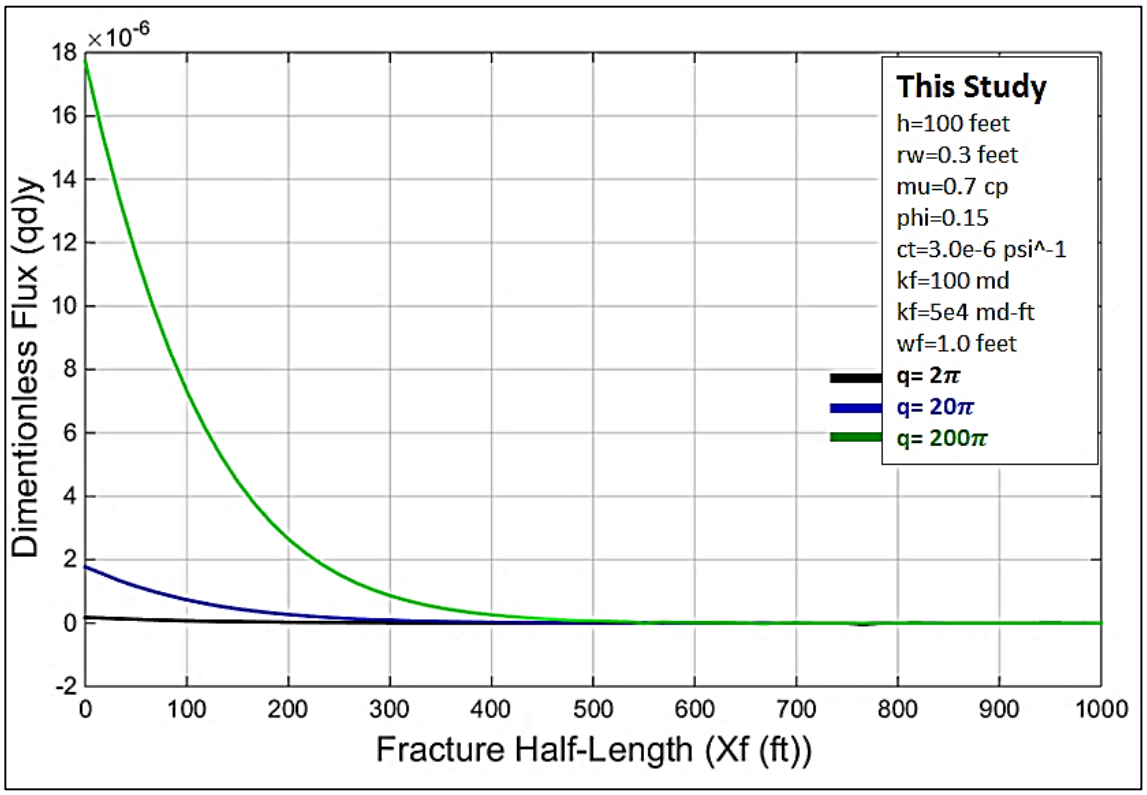

Figure 62- Matrix flux distribution versus effective fracture half-length at different well rates.

The rate magnitude should not have any effect on the effective fracture half-length: changing the rate induces different pressure amplitudes, the larger the rate, the larger the pressure amplitude. For small rate changes the disturbance is infinitely small and may be immeasurable: however, the radius of the pressure transient should be the same, at different rates. This is consistent with the principle and assumptions of estimating the radius of investigation; the correlation is not a function of well-rate, but it measures how far into the reservoir, the transient effects have covered.

Equation 99

$$r_{inv} = \sqrt{\frac{\text{kt}}{948 \cdot \varphi \mu c_t}} \tag{99}$$

Figure 63, confirms this understanding by calculating the effective fracture half-length to be the same at different rate values, ($x_{fe} \approx 650\ ft$).

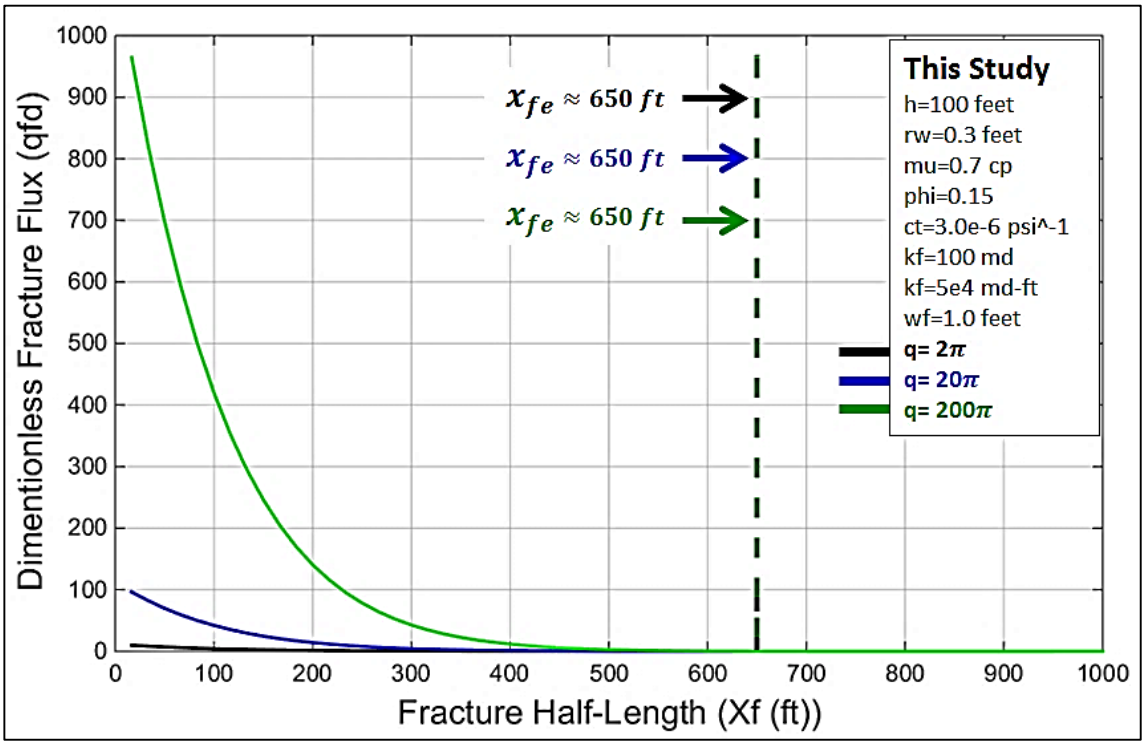

Figure 63- Fracture flux distribution versus effective fracture half-length at different well rates.

Summary

Chapter 5 has introduced an approach to estimate the fracture flux distribution and the matrix flux distribution alongside the fracture plane. It also presented a new method to estimate the fracture effective half-length by deploying the flux term in Equation 19 and solving for fracture half-length. The procedure is based on the assumption that particularly small fluid flow occurs when the difference in pressure across the fracture plane, in an infinite length fracture, is approaching zero ($\Delta p \approx zero$). Therefore, it can estimate the fracture pressure distribution, the fracture-flux into the fracture and matrix-flux distributed along the fracture. The other methods, available in the literature, are limited to finite fracture lengths, and therefore, reflect tip effects, i.e. an increase in flux towards the toe of the fracture, due to increased pressure drop per unit distance.

The solution was validated through synthetic and field cases with different complexities. Also, the effect of different parameters on the effective fracture half-length (x_{fe}) and flux distribution were investigated.

The main observations are as follows:

1. By comparing between matrix fluxes calculated on the x-y plane and y-axis, it was noted that the two approaches were in good agreement, as they both had the same trend and values.

2. The linear flow along the (y-axis) is the solution considered in calculating the effective fracture half-length due to its stability.

3. It was noted that: when using the pressure and flux distribution to determine (x_{fe}), at a flux and/or pressure depletion of $\geq 99.99\%$ of the first calculated value, it reasonably matches the fracture half-length of many field and numerically built cases.

4. Effect of matrix permeability on flux magnitude: results showed that the contribution from/to matrix increased with increasing matrix permeability.

5. Effect of matrix permeability on effective fracture half-length: in a "source/injection" case, the lower the matrix permeability, the longer the fracture, to accept more of the injected/produced fluid.

6. Effect of fracture conductivity on flux quantity: it was noted that the contribution from/to matrix decreased with increasing fracture conductivity.

7. Effect of fracture conductivity on source of fluids: at high conductivity values, the fracture accepts/produces more of the fluid injected/produced.

8. Effect of fracture conductivity on fracture half-length: the higher the conductivity, the larger the fracture half-length.

9. Effect of well-rate on fracture/matrix fluxes and effective fracture half-length: at higher rates, matrix and fracture contributions are larger but fracture half-length is constant.

The next chapter will discuss solution, automation and validation using synthetic and field data.

CHAPTER 6 – SOLUTION COMPETENCY AND VALIDATION USING SYNTHETIC AND FIELD DATA

6.1 Solution for Different Reservoir Complexities

Here some of the key features of the developed models are reviewed before discussing the synthetic data. The code FracFault-model is capable of handling different cases namely:

6.1.1 Homogenous Reservoir

a. Radial homogenous reservoir,
b. Fractured well in homogenous reservoir,
c. Finite conductivity fault in a homogenous reservoir,
d. Fractured well in a reservoir with finite conductivity fault

6.1.2 Three-Region Linear Composite System

(Well is located between Regions 1 and 2)

a. Three-region linear composite system,
b. Fractured well in three-region linear composite system,
c. Finite conductivity fault in three-region linear composite system,
d. Fractured well in a reservoir with finite conductivity fault in three-region linear composite system.

6.2 Dimensionless Parameters

In order to superimpose this solution to external models or data, in dimensionless form, the code uses the following dimensionless terms:

$$(t_D)_{ex} = \left(\frac{0.000264\, k_r t}{\varphi \mu c_t\, {r_w}^2}\right)_{ex}$$

$$(dp_{wD})_{ex} = \left(\frac{k_r h}{141.2 q \beta \mu}\, dp_w\right)_{ex}$$

$$\left(\frac{dp_{wD}}{dt_D}\right)_{ex} = \left(\frac{k_r h}{141.2 q \beta \mu}\, \frac{dp_w}{dt_D}\right)_{ex}$$

where (ex), is the external model/data.

The well test derivative is expressed as: $dt_D \cdot \frac{dp_{wD}}{dt_D}$

Reservoir Reference Permeability: In this code, a reference permeability of $(k_r = 1.0)$ is used to retain the effect of the dimensionless permeability to be the same as the dimensional permeability;

$$k_{Di} = \frac{k_i}{k_r}, \qquad where;\ i = 1, 2, 3, \ldots \ and \ k_r = 1.0$$

Fracture Reference Permeability: The calculation of the fracture dimensionless conductivity, in the FracFault-model, reflects the influence of the two reservoirs, Figure 64, as follows:

$$F_{CDf} = \frac{k_f \,.\, w_f}{k_{rf} \,.\, r_w}, \quad where; \quad k_{rf} = \frac{k_1 + k_2}{2}$$

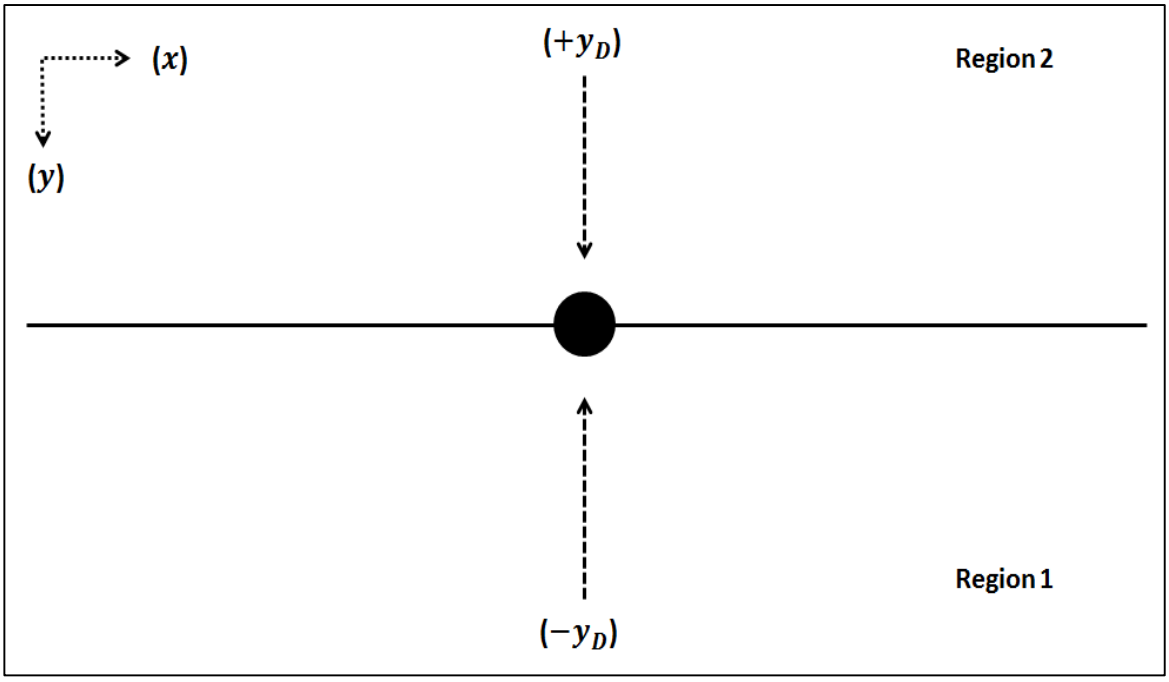

Figure 64: The fractured well is located in the centre between Regions 1 and 2.

Fault Reference Permeability: The calculation of the nearby fault's dimensionless conductivity reflects the influence of the second region matrix, Figure 65, as follows:

$$F_{CDF} = \frac{k_F \,.\, w_F}{k_{rF} \,.\, r_w} \quad where; \quad k_{rF} = \frac{k_2 + k_3}{2}$$

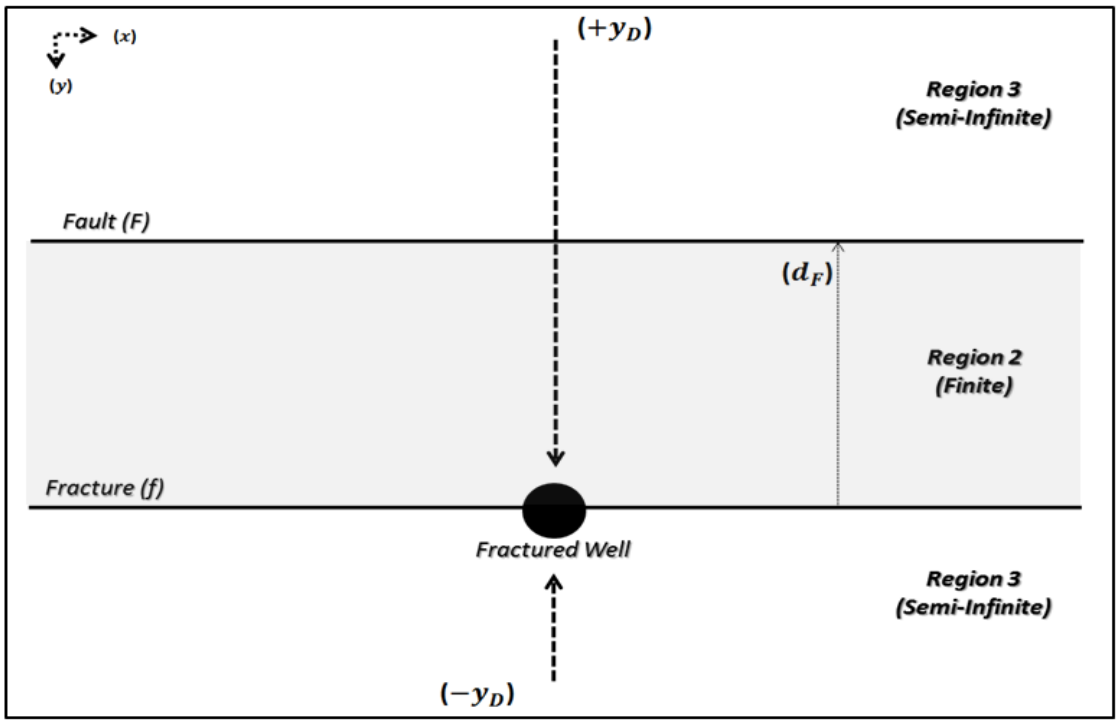

Figure 65: Region-2 is separating the fractured-well from the fault.

6.3 Dimensionless Skin and Wellbore Storage (WBS)

As mentioned before, this solution is also enabled with dimensionless skin and wellbore storage (WBS) using Kucuk and Ayestaran's (1985) dimensionless equations and limited to positive skin only.

6.4 Solution Parameters

The solution will provide the following results:

- Reservoir permeabilities: (k_1, k_2 and k_3)
- Fracture permeability: (k_f)
- Fracture width: (w_f)
- Fracture conductivity: ($k_f \cdot w_f$)
- Effective fracture half-length: (x_{fe})
- Dimensionless fracture conductivity: ($F_{CDf} = \frac{k_f w_f}{k_{rf}\ r_w}$)
- Fault permeability: (k_F)
- Fault width: (w_F)
- Fault conductivity: ($k_F \cdot w_F$)
- Dimensionless fault conductivity: ($F_{CDF} = \frac{k_F w_F}{k_{rF}\ r_w}$)
- Distance to fault: (d_F)
- Dimensionless positive skin: ($S_D \geq 0$)
- Dimensionless Well Bore Storage: (WBS_D)

6.5 Validation of Solution via Numerical, Analytical and Field Cases

Here the author will validate the proposed final solution by the use of synthetic and field cases as follows:

6.5.1 Analytical Cases

Analytical data from the commercial well-test Software: Analytical Data Set-1

A hydraulically fractured well analytical model was constructed using the commercial well test software (Saphir-KAPPA, 2012) and the pressure derivative signatures were extracted and then compared with those of the proposed solution, to validate the integrity of solution presented in the FracFault-model. The well and reservoir properties are shown in Table 2. The match, as presented in Figure 66, is good. The slight pressure discrepancy, between the times $2e6$ to $2e8$, can be attributed to the conversion of the Saphir model data from dimensional to dimensionless, the numerical inversion of this model from Laplace space to real space and the infinite fracture half-length supposition used in the FracFault-model. A comparison between the analytical model and this solution, shown in Table 3, reflects a perfect agreement between the two data sets of reservoir parameters.

Table 2: Well and reservoir properties of the field data set-1.

Property	Value
Wellbore Radius, ft	0.3
Pay Zone, ft	30.0
Porosity, %	10.0
Formation Volume Factor, bbl/STB	1.0
Viscosity, cp	1.0
Total Compressibility, psi^{-1}	$3.0e^{-6}$

Table 3: Comparison between the results obtained from the FracFault-model and the analytical model available in the used well-test package.

Saphir-KAPPA-Software Analytical Model			**Frac Model**		
x_f (ft)	F_{Cf} -F_{CF} (md ft)	k (md)	x_f (ft)	F_{Cf} -F_{CF} (md-ft)	k_1 -k_2 -k_3 (md)
2000	8e3 - 0	3.3	-	8e3 - 0	3.3

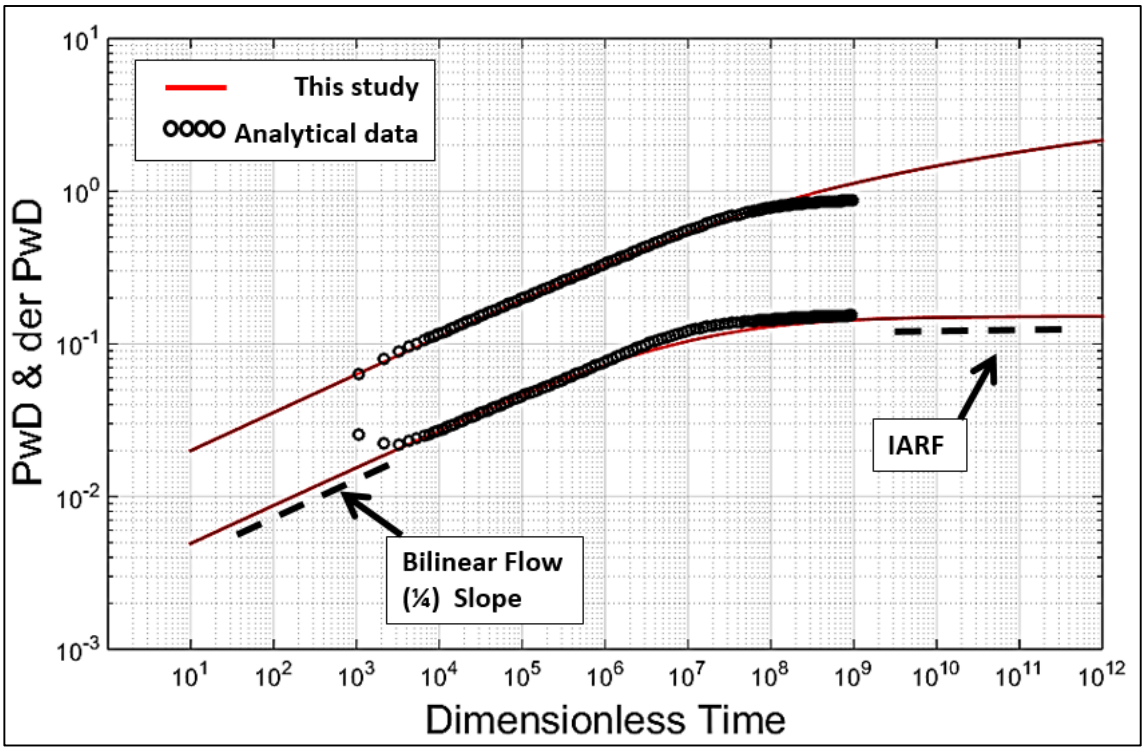

Figure 66- Pressure and derivative match of the synthetic data-1 with a type curve of the numerical model available in the used well-test package.

6.5.2 Numerical cases

Basic Homogenous Numerical Model:

Numerical models are very flexible in terms of the complexity of the model, such as number and types of wells, number of intersected fractures and non-intersected ones. However, they can introduce numerical, errors due to the approximations of pressure calculations over the studied flow problem using discrete grids, especially if they do not have the optimum size. Therefore, setting the exact inner and outer boundaries (constraints) are extremely important for valid comparison exercises.

Numerical data from a Ecrin-Software reservoir simulator: the numerical linear model used as part of Ecrin-Software is a single phase numerical simulator using "automatic grid generation" based upon the work of Voronoï (1908), where the well pressure (p_{wb}) is solved numerically (Houze et al., 2008).

The used gridding type and specification: in addition to the initial discussion in section (1.1-Problem Statement), and in order to set-up a numerical model and validate the semi-analytical solution of the FracFault-model, there is also a brief discussion here of the gridding used. The Voronoi grids, also referred to as PEBI grids (Perpendicular Bisector), adopt an automatic gridding technique and honour reservoir outer and inner boundaries (reservoir contours and well). This gridding technique is based on generating a series of smartly positioned points in the reservoir (nodes) and can be anywhere, regardless of the position of the other nodes. This tactic is what brands the Voronoi grids as "Unstructured" (Houze et al., 2008). The grids are built radially around the vertical wells and select a more complex shape around horizontal, fractured wells or other geological features represented in the model, to follow the expected fluid flow for each case.

Considering these parameters, a synthetic numerically-built homogenous 2D model of a vertical well in a circular reservoir, using Ecrin-Software numerical well-test package, is studied here to validate the solution. The reservoir properties and model dimensions are listed in Table 4 and Table 5.

Table 4: Reservoir Properties of data set-1.

Reservoir Properties	**Value**
Wellbore Radius, ft	0.3
Reservoir	homogenous
Pay Zone, ft	100.0
Porosity, %	15.0
Formation Volume Factor, bbl/STB	1.0
Viscosity, cp	0.7
Total Compressibility, psi^{-1}	$3.0e^{-6}$

Table 5: Model Dimensions of data set-1.

Model Dimensions	**Value**
Reservoir Model Radius, ft	10000.0
Circular Boundaries	Sealing
Numerical Model Type	2-D
Numerical Model View	3-D
Grid Type	Voronoi
Grid Setup Mechanism	Automatic

Figure 67, shows the pressure distribution of a drawdown test from a vertical well, specified above, in a circular, 2D, numerical model using Ecrin-Software by KAPPA Engineering.

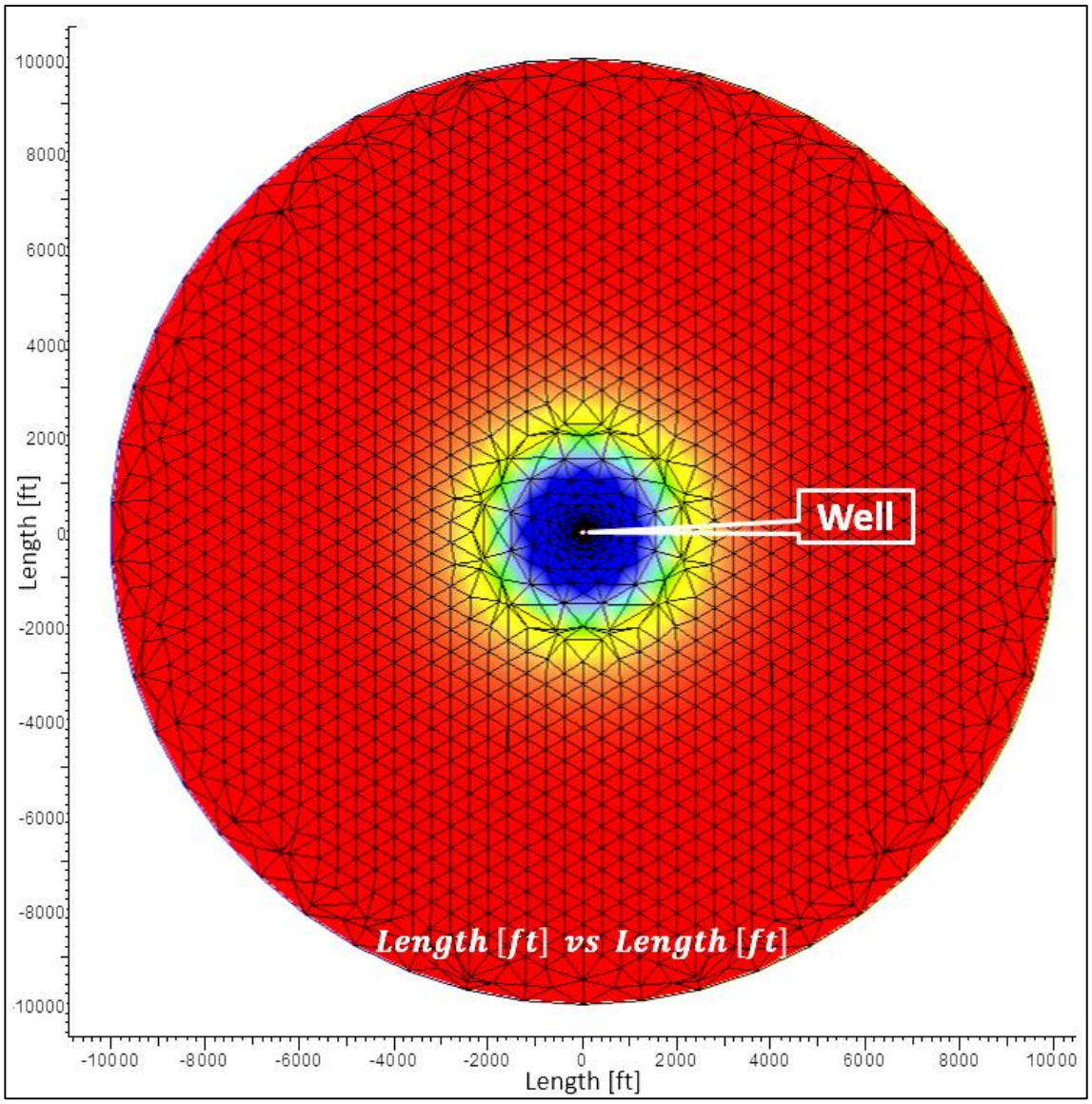

Figure 67- Pressure distribution in a circular, 2D, numerical model of a drawdown test from a vertical well using Ecrin-Software by KAPPA Engineering.

The derivative plot was generated and matched the plot from this solution and is presented in Figure 68. The match is excellent for both the well pressure drop and its derivative, except for a slight deviation at early times, between the times $1e2$ to $1e3$, where the radial grids are affecting the wellbore pressure calculation. This exercise further confirms the accuracy and reliability of the proposed solution.

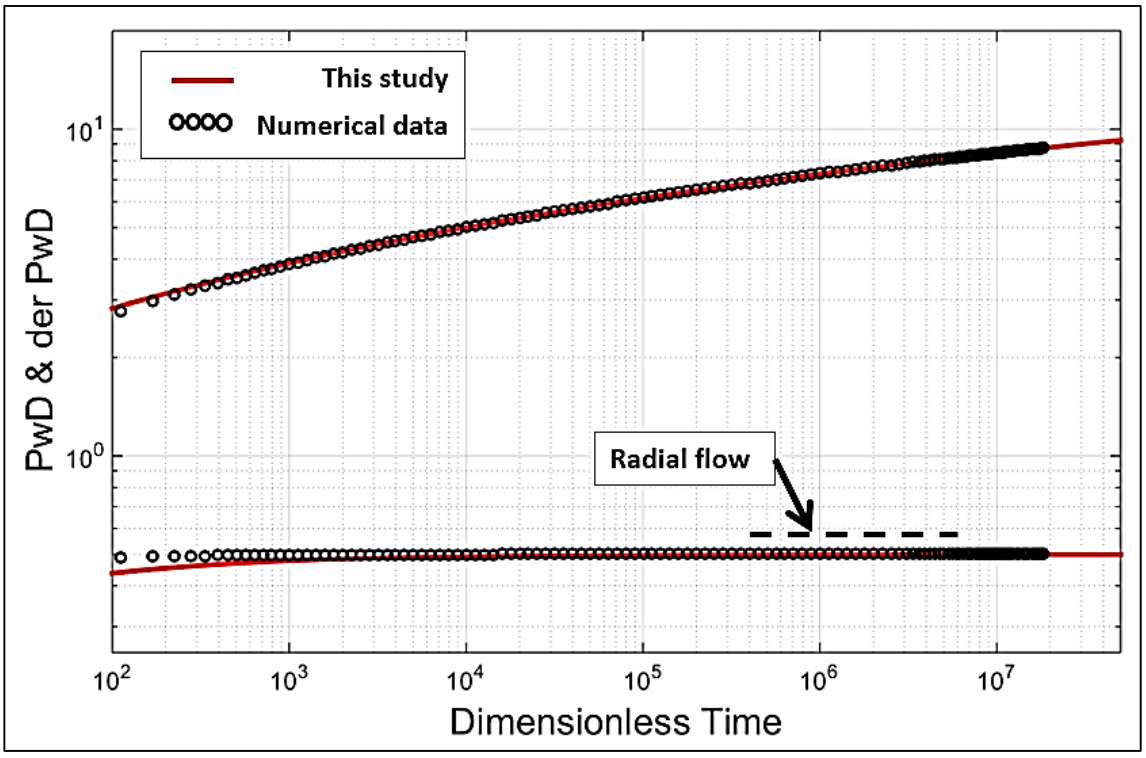

Figure 68- Pressure and derivative match of the Synthetic data-1 from the FracFault-model with a numerical model from Ecrin-Software package.

Table 6 shows the input data to the numerical model and results obtained by super-imposing the pressure data of the numerical simulator on the type curve proposed in the FracFault-model.

Table 6: Comparison between the results of a numerically based model and the new solution.

Saphir-KAPPA Software Numerical Model			**FracFault Model**		
x_f (ft)	F_{Cf} -F_{CF} (md ft)	k (md)	x_f (ft)	F_{Cf} -F_{CF} (md ft)	k1-k2-k3 (md)
-	0 - 0	10	-	0 - 0	10

Fractured well numerical model: Data Set-1

A synthetic numerically-built asymmetric reservoir model of a well intersecting a finite conductivity fracture was constructed and the pressure transient data were generated, and analysed by Ecrin-Software well-test package and this solution, using well and reservoir properties in Table 7.

Again, a good agreement between the two is noted. Similarly to synthetic data set-2, the slight deviation in the match between t_D of $5.0e7$ to $5.0e9$ is possibly attributed to the conversion of the numerical model (data) from dimensional to dimensionless, the numerical inversion of this model from Laplace space to real space and the infinite fracture half-length supposition used in the FracFault-model.

Table 7: Well and reservoir properties of the field data set-1.

Property	Value
Wellbore Radius, ft	0.3
Pay Zone, ft	30.0
Porosity, %	10.0
Formation Volume Factor, bbl/STB	1.0
Viscosity, cp	1.0
Total Compressibility, psi^{-1}	$3.0e^{-6}$

Table 8 shows the input data to the numerical model and results obtained by super-imposing the pressure data of the numerical simulator on the type curve proposed in the FracFault-model.

Table 8: Comparison between the results of a numerically based model and the new solution.

Saphir-KAPPA Software Numerical Model			**Frac Model**		
x_f (ft)	F_{Cf} -F_{CF} (md ft)	k (md)	x_f (ft)	F_{Cf} -F_{CF} (md ft)	k1-k2-k3 (md)
2000	8e3 - 0	3.3	-	8e3 - 0	3.3

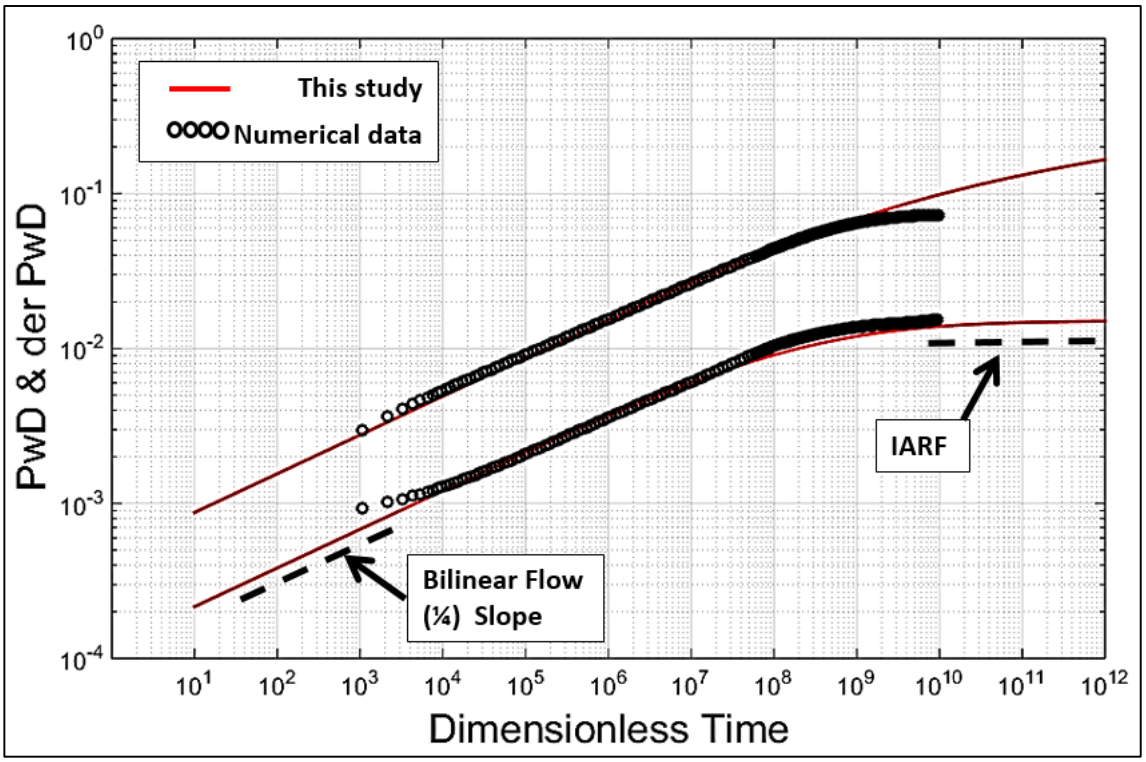

Figure 69- Pressure and derivative match from the FracFault-model with Synthetic Numerical Data.

Numerical data from the commercial software: Data Set-2

A synthetic numerically-built case, of a well intersecting a fracture, was constructed and the pressure data were generated to be analysed in the well-test package. Results were obtained by super-imposing the pressure data of the numerical simulator on the proposed type curve. An excellent agreement between the two is noted in Table 9, Figure 70 and Figure 71.

Table 9: Comparison between the results of a numerically-based model and this solution.

Saphir-KAPPA Software Numerical Model			**Frac Model**		
x_f (ft)	F_{Cf} (md ft)	k (md)	x_{fe} (ft)	F_{Cf} (md ft)	k (md)
1050	5.0e5	500	1040	5.0e5	500

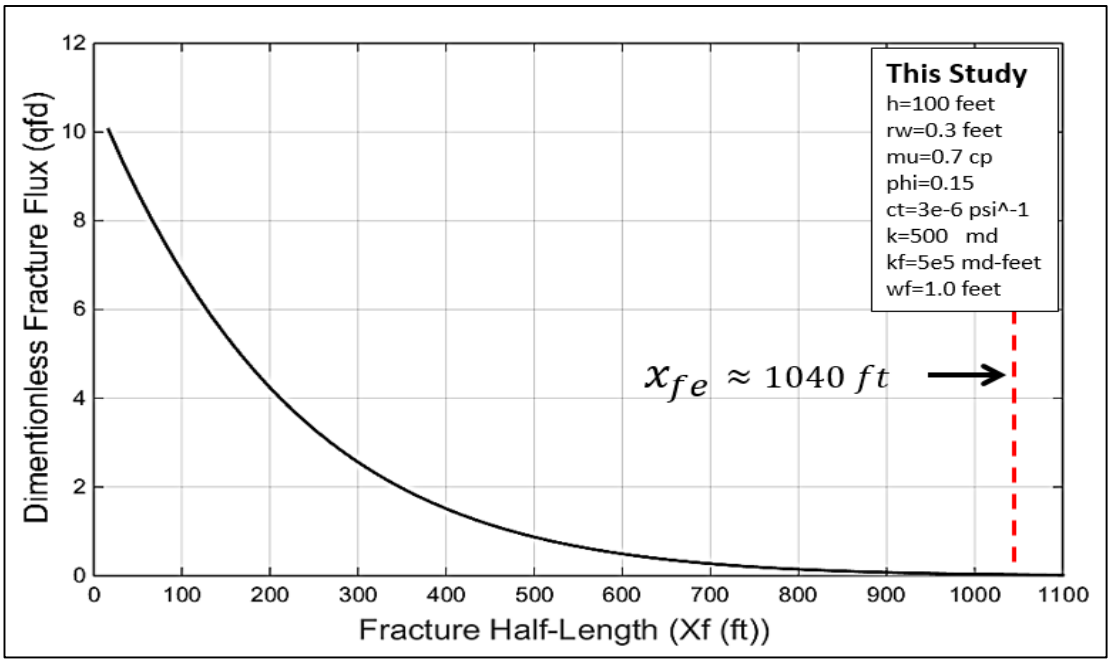

Figure 70- Dimensionless fracture flux distribution alongside the fracture and fracture half-length estimation using the FracFault-model.

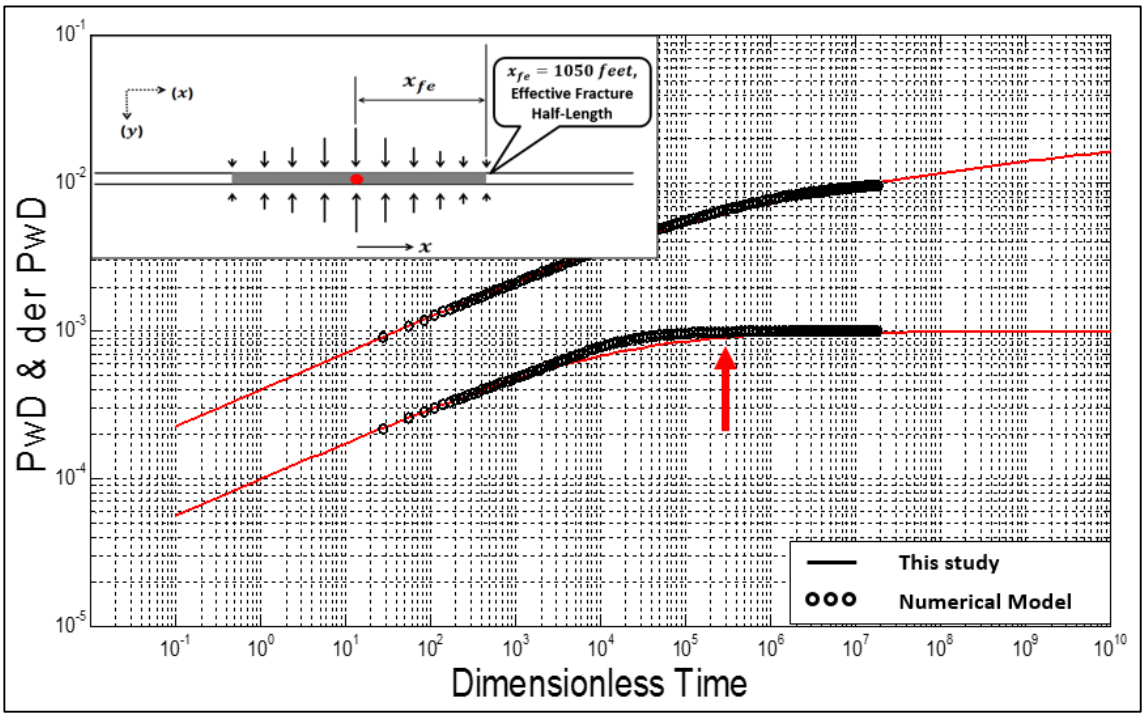

Figure 71- Pressure and derivative match using the Frac-model with Synthetic Numerical Model.

Finite conductivity fault (non-intersected fault): Numerical Data Set-3

A synthetic numerically-built reservoir model of a well near a finite conductivity fault was constructed using the well-test package to validate the proposed semi-analytical solution, Figure 72. The production, well and reservoir data are listed in Table 10 and Table 11.

Table 10: Production data of the field data set-3.

Well Type	Vertical	
Production Rate, STBD	10000 Oil 0 Water	0% Water cut
Test Type	Build-up	

Table 11: Well and reservoir properties of field data set-3.

Property	**Value**
Wellbore Radius, ft	0.25
Pay Zone, ft	100.0
Porosity, %	15.0
Formation Volume Factor, bbl/STB	1.0
Viscosity, cp	0.7
Total Compressibility, psi^{-1}	$36e^{-6}$

Table 12, shows the input data to the numerically based constructed model and results obtained by super-imposing pressure data of this solution on the proposed type curve. An outstanding agreement between the two is noted in both Table 12 and Figure 73.

Table 12: Comparison; between the results of the numerically based constructed model and the FracFault-model.

Saphir-KAPPA Software Numerical Model			**FracFault Model**		
d_F (ft)	F_{CF} (md-ft)	k (md)	d_F (ft)	F_{CF} (md-ft)	k (md)
550	5e5	7	550	5e5	7

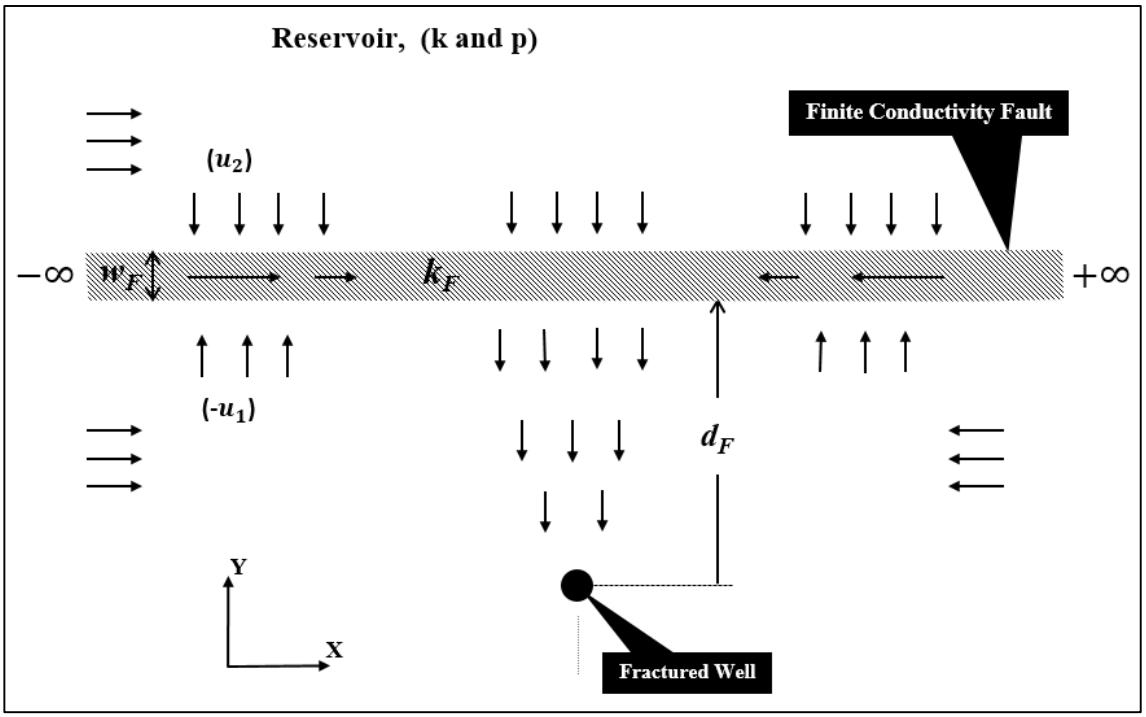

Figure 72- Schematic of a well located in a reservoir with a finite conductivity fault for synthetic data set-3.

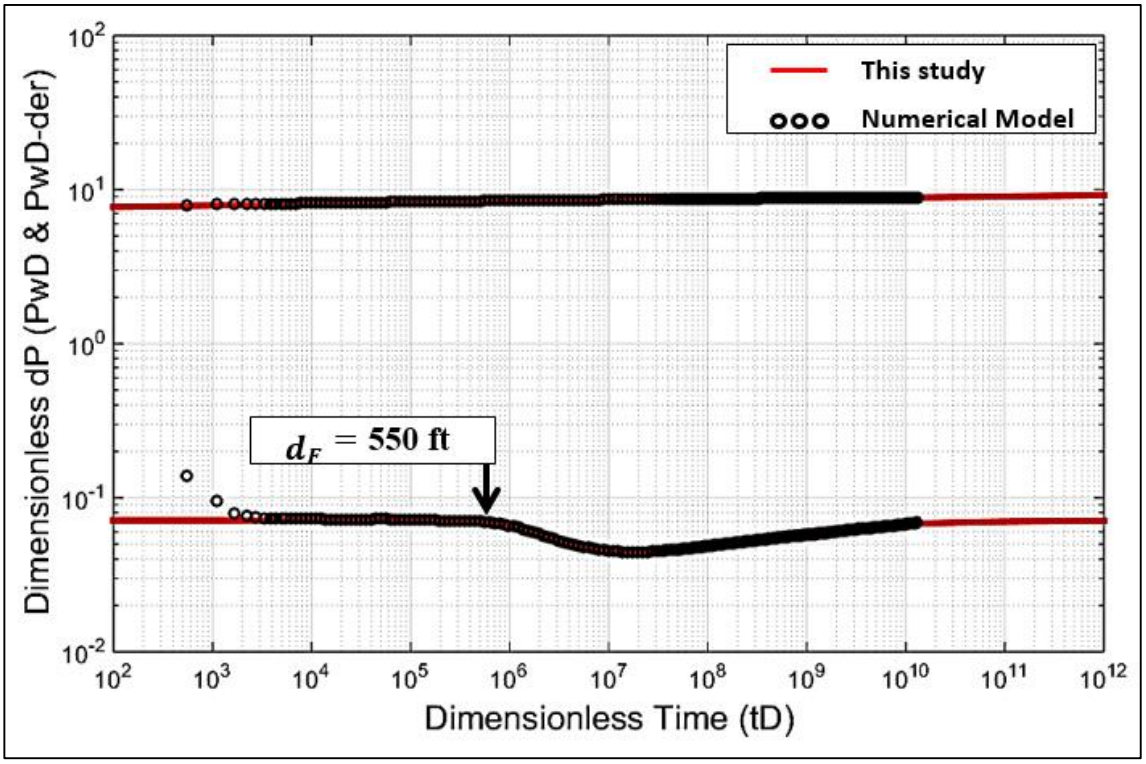

Figure 73- Pressure and derivative match of the FracFault-model and the numerical model available in the used well-test package for synthetic data set-3.

Fractured well near a finite conductivity fault: Numerical Data Set-4

A synthetic numerically-built model of a well intersecting a finite conductivity fracture in a reservoir with a finite conductivity fault, was constructed, Figure 74. The pressure transient data were generated to be analysed in the well-test package. The production, well and reservoir data are listed in Table 13 and Table 14.

Table 13: Production data for the field data set-4.

Well Type	Vertical	
Production Rate, STBOD	**10000 (Intersected)**	0% Water cut
Test Type	Build-up	

Table 14: Well and reservoir properties of field data set-4.

Property	**Value**
Wellbore Radius, ft	0.30
Pay Zone, ft	30.0
Porosity, %	10.0
Formation Volume Factor, bbl/STB	1.0
Viscosity, cp	1.0
Total Compressibility, psi^{-1}	$3.0e^{-6}$

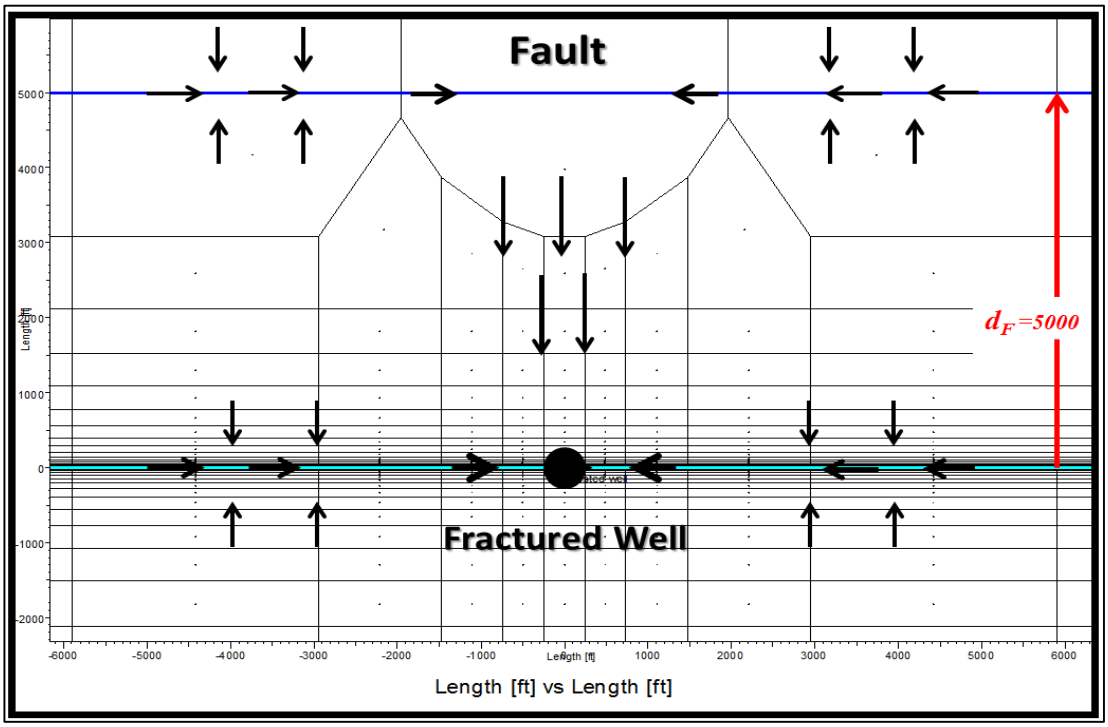

Figure 74- Numerical model with different grid sizes around and between the fracture and fault.

Table 15 shows the input data to the numerical model and results obtained by super-imposing the pressure data of the numerical simulator on the proposed type curve. An excellent agreement between the two is noted in both Table 15 and Figure 75. The slight deviation in the match at middle and late times is possibly attributable to the large grid sizes around the fault in the numerical simulator, Figure 75. The effective fracture half-length, corresponding to ($q_{Df} \approx 0$), shown in Figure 76, is also very good.

Table 15: Comparison between the results of a numerically based model and the new solution.

Saphir-KAPPA-Software Numerical Model				**This Solution**			
x_f (ft)	d_F (ft)	F_{Cf} -F_{CF} (md ft)	k (md)	x_f (ft)	d_F (ft)	F_{Cf} -F_{CF} (md ft)	k (md)
2.0e5	5000	1e5 - 1e8	33	2.0e5	5000	1e5 - 1e8	33

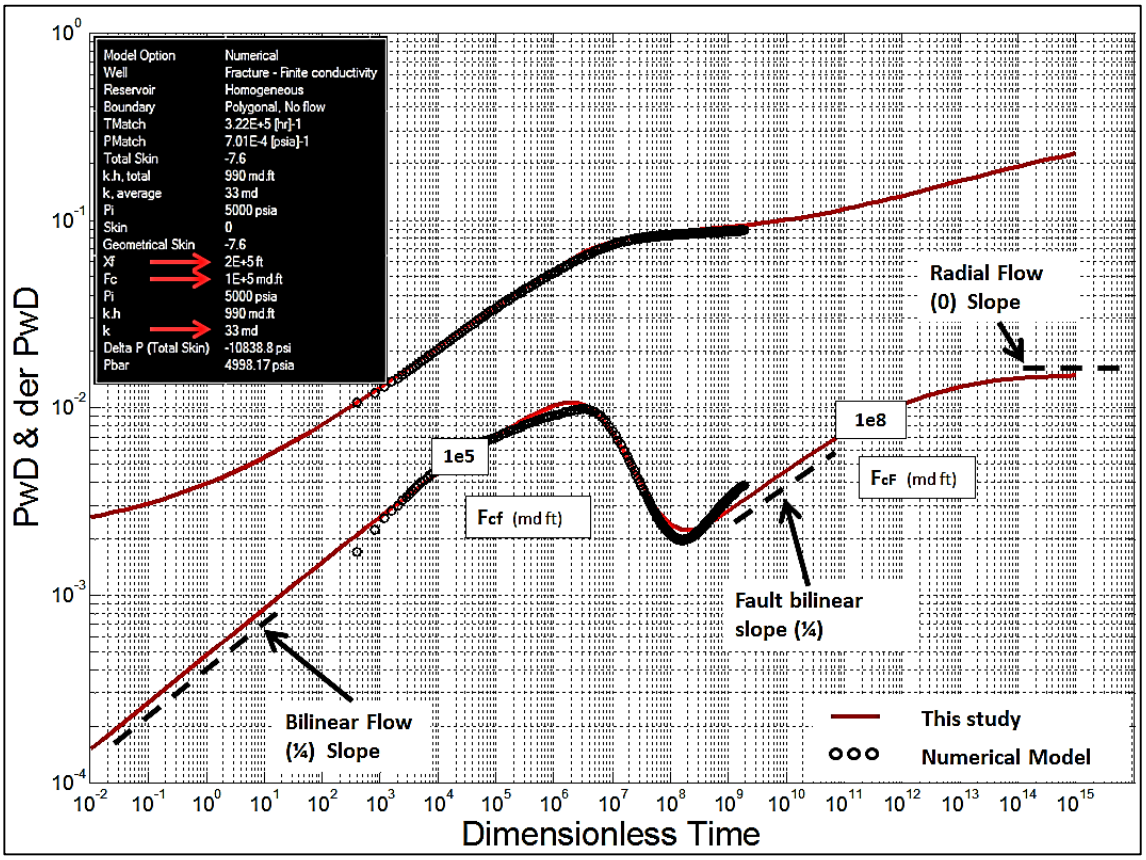

Figure 75- Pressure and derivative match using the FracFault-model to Synthetic Numerical Data.

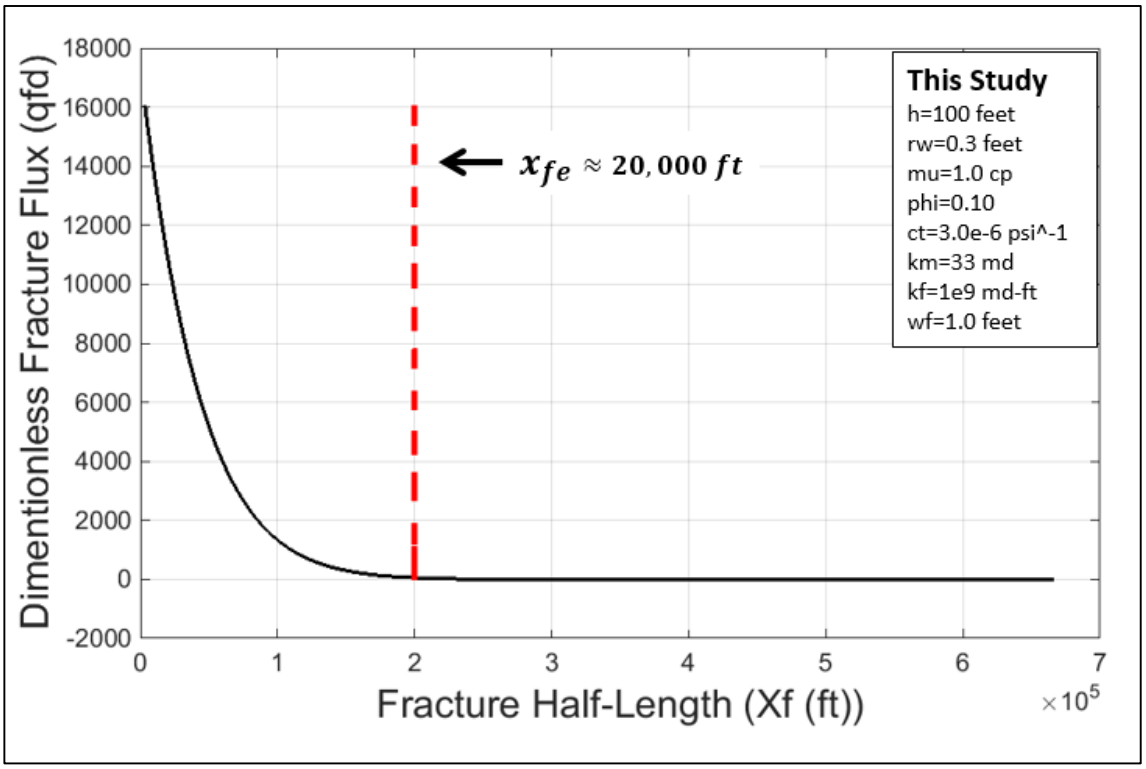

Figure 76- Fracture flux distribution alongside the fracture and fracture half-length estimation.

6.5.3 Field Cases

In this section, the different examples provided are arranged as follows:

1. **Field Data Set-1:** Fractured vertical well in a sandstone reservoir,
2. **Field Data Set-2:** Fractured horizontal well in a carbonate reservoir,
3. **Field Data Set-3 and 4**: Well near a finite conductivity fault, two cases.
4. **Field Data Set-5:** Well near a finite conductivity fault and later hydraulically fractured, one case but two sets.
5. **Field Data Set-6:** Hydraulically fractured well near a finite conductivity fault, one case.

A fractured vertical well in a sandstone reservoir: Field Data Set-1:

The first field case example data set corresponds to a vertical well intersecting a finite conductivity fracture in a sandstone reservoir. The objective here is to evaluate the reliability of the proposed solution for a practical field example, where the flow is dominated by the bi-linear flow regime and followed by a radial flow regime. A fracture skin and the wellbore storage flow regime are also evident in the early-time data. Table 16 summarises well and reservoir properties.

Table 16: Well and reservoir properties of the field data set-1.

Property	Value
Wellbore Radius, ft	0.23
Pay Zone, ft	100.0
Porosity, %	19.0
Formation Volume Factor, bbl/STB	1.39
Viscosity, cp	0.35
Total Compressibility, psi^{-1}	$7.17e^{-6}$

The pressure transient data have been matched to a type curve provided by the new solution, Figure 77. The results have also been validated by those obtained based on the Cinco et al. (1978) solution, Figure 78, available in the used well test software. The flow capacity to oil has been found to be 2500 md-ft from this solution and 2500 md-ft from the solution of Cinco et al. (1978). The fracture conductivities are also identical as shown in

Table 17. The fracture half-length was estimated using the approach that was detailed in Chapter 5.

Table 17: Comparison between the results obtained for the field data set-1 by the solution proposed by the FracFault-model and the Cinco et al. (1978) solution available in the used well test package.

Cinco's and Samaniego's solution				**FracFault Model**				
x_f (ft)	F_{Cf} (md-ft)	F_{CDf}	k (md)	x_f (ft)	F_{Cf} (md-ft)	F_{CDf}	k_1 (md)	k_2 (md)
240	12.6e3	2.0	25	300	12.6e3	2.0	30	20
							$k_{av} = 25$	

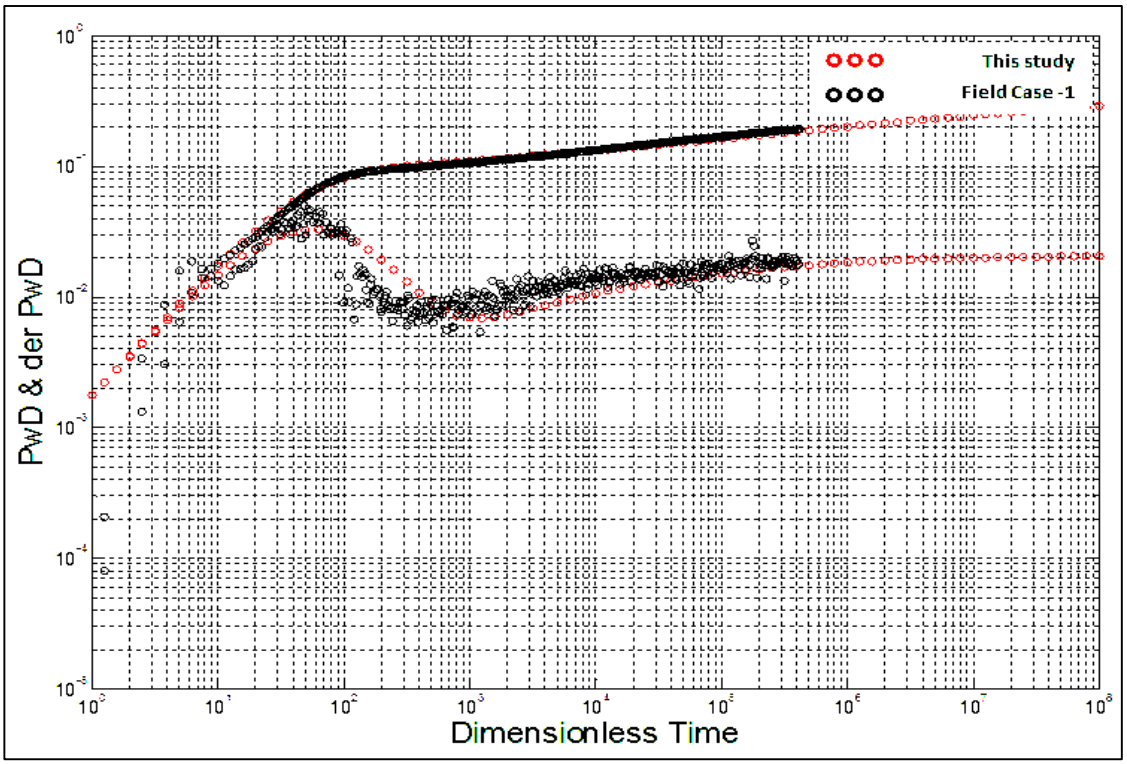

Figure 77- Pressure and derivative match of the field data set-1 with a type curve of the solution proposed by the FracFault-model.

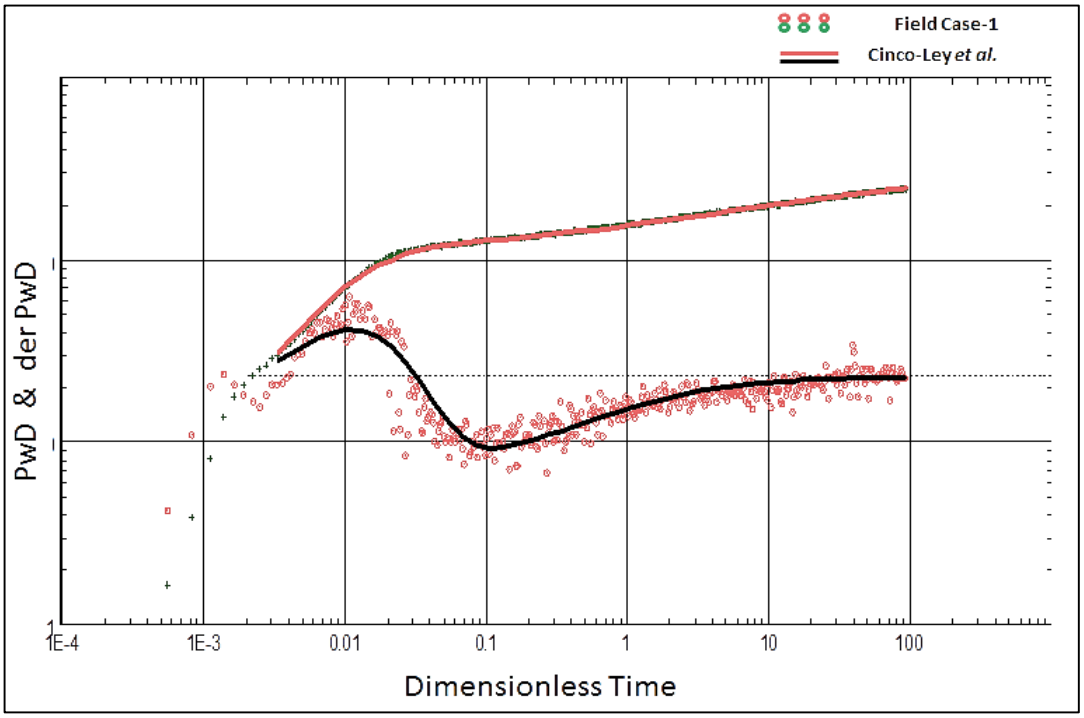

Figure 78- Pressure and derivative match of the field data set-1 with a type curve of the Cinco et al. (1978) solution available in the used well-test package.

A fractured horizontal well in a carbonate reservoir: Field Data Set-2

At this stage, the field case example considered was the data set of a horizontal well with 2050 ft length ($L_e = 680$ ft) that was placed in the top of the formation where the highest reservoir quality is and intersecting a finite conductivity fracture in a carbonate reservoir. Figure 79, shows the Formation Analysis Log interpretation and the horizontal trajectory is shown in Figure 80. It is likely that the horizontal well intersects vertical fractures, as most of the natural fractures in this field are vertical and of a north-east/south-west direction. The aim is to evaluate the reliability of this solution for a practical field example where the flow is completely dominated by the fracture. The early-time data has been slightly distorted due to wellbore storage and phase segregation.

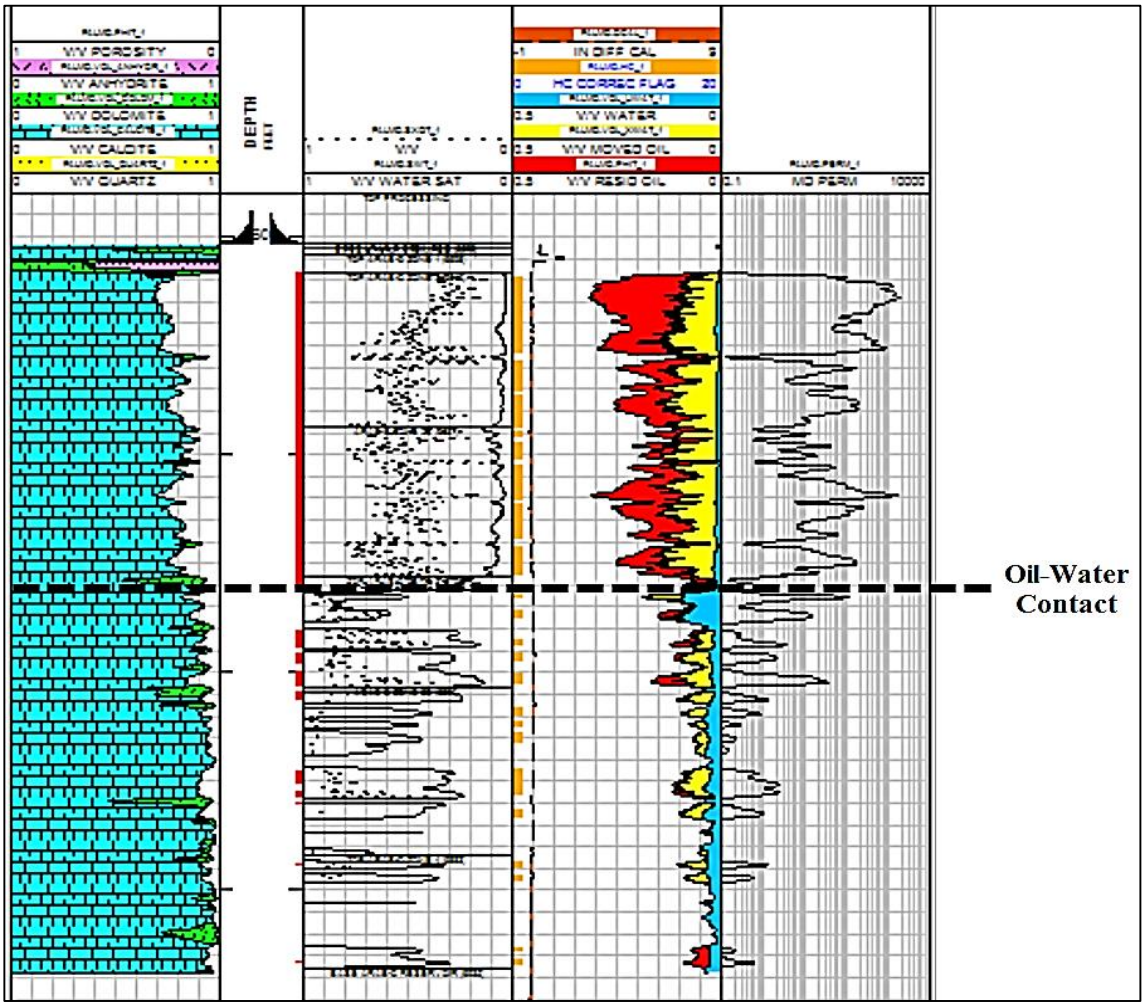

Figure 79 Formation Analysis Log.

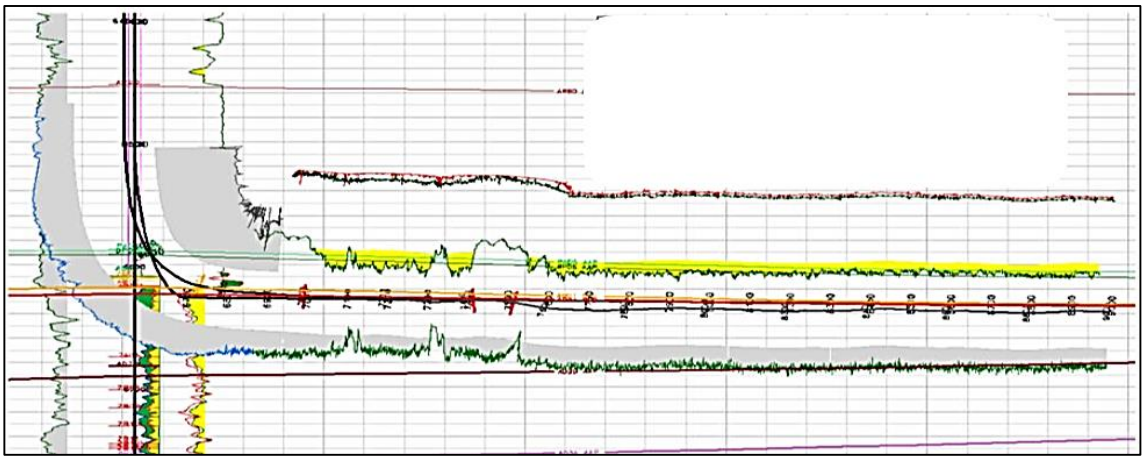

Figure 80: Horizontal Trajectory of 2050 ft.

The production data, well and reservoir properties are listed in Table 18 and Table 19.

Table 18: Production data of the field data set-2.

Well Type	Horizontal	
Production Rate, STBD	8,700 Oil	2.2% Water cut
	180 Water	
Test Type	Build-up	

Table 19: Well and reservoir properties of the field data set-2.

Property	Value
Wellbore Radius, ft	0.26
Pay Zone, ft	140.0
Porosity, %	15.0
Formation Volume Factor, bbl/STB	1.39
Viscosity, cp	0.73
Total Compressibility, psi^{-1}	$7.8e^{-6}$

The proposed solution was used to match the pressure data, Figure 82, and compared with the numerical model available in the used well-test software for a well intersecting a finite conductivity fracture in a symmetrical reservoir, Figure 83 and Figure 84. Both solutions capture the 1/4 slope bilinear flow signature corresponding to flow along and into the fracture, followed by a radial flow-period corresponding to the reservoir section. It should be noted that, as mentioned before, this solution is developed for more complex geological systems (two regions), but it can correctly handle a simpler system considered here. As clearly shown in Table 20, the consistency of the solution is confirmed, as the estimated reservoir parameters are in excellent agreement, i.e. the parameters estimated using both solutions are identical.

Table 20: Results obtained for the field data set by the approach proposed by the FracFault-model.

Field Case			**Frac Model**		
x_f (ft)	F_{Cf} (md ft)	k (md)	x_{fe} (ft)	F_{Cf} (md ft)	k (md)
242	1.0e7	190	295	1.0e7	190

The estimated x_{fe} from the proposed solution is higher than the one calculated by the analytical solution, due to the approximation nature of the method (i.e. at a flux and/or pressure depletion of: value ≥ 99.99% of the first value calculated).

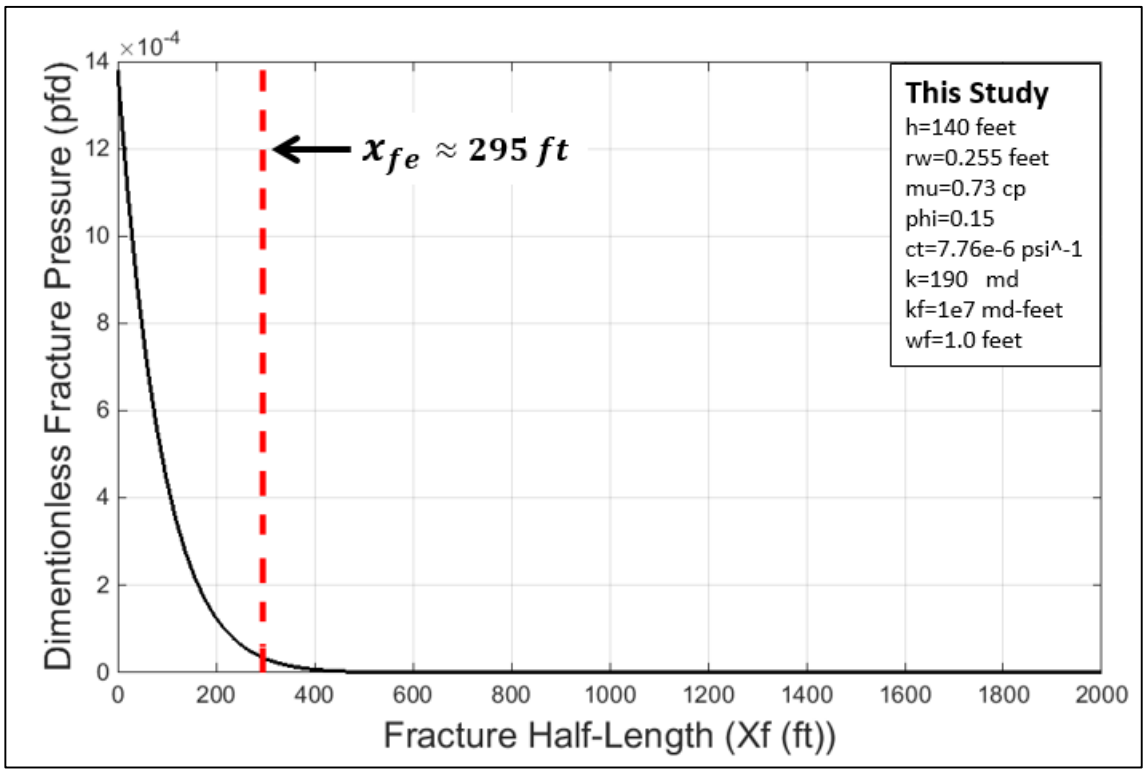

Figure 81- Flux distribution alongside the fracture and fracture half-length estimation of the given field case using the FracFault-model.

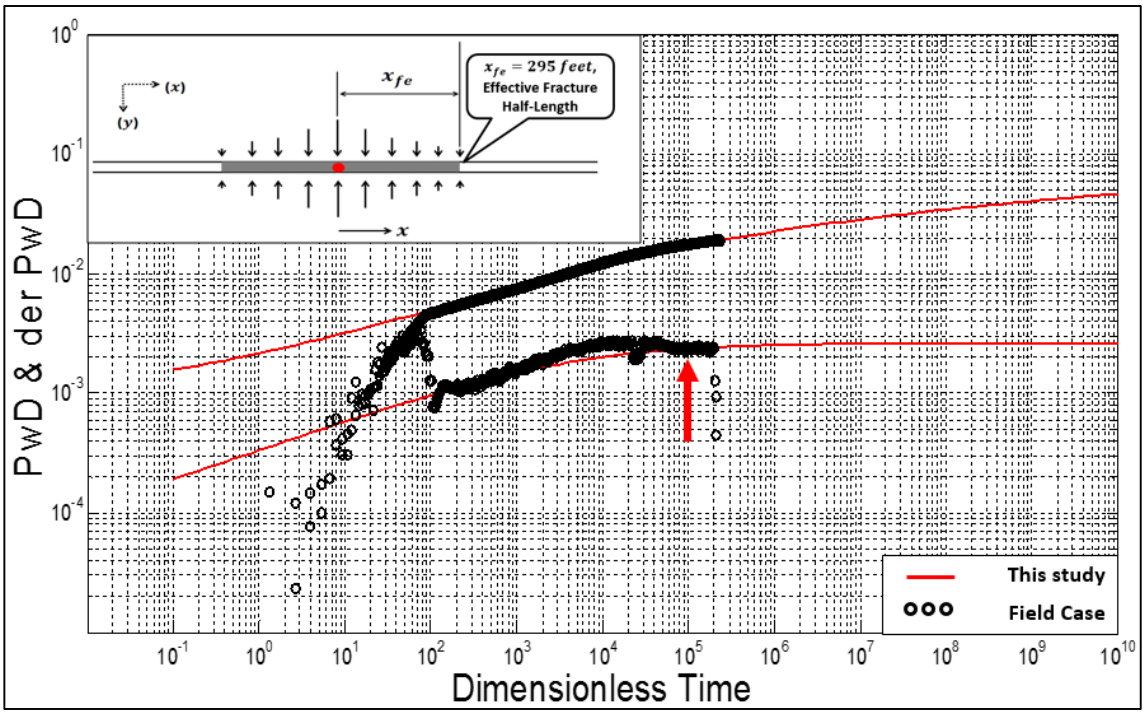

Figure 82- Pressure and derivative match of the field case with a type curve of the solution proposed by the FracFault-model.

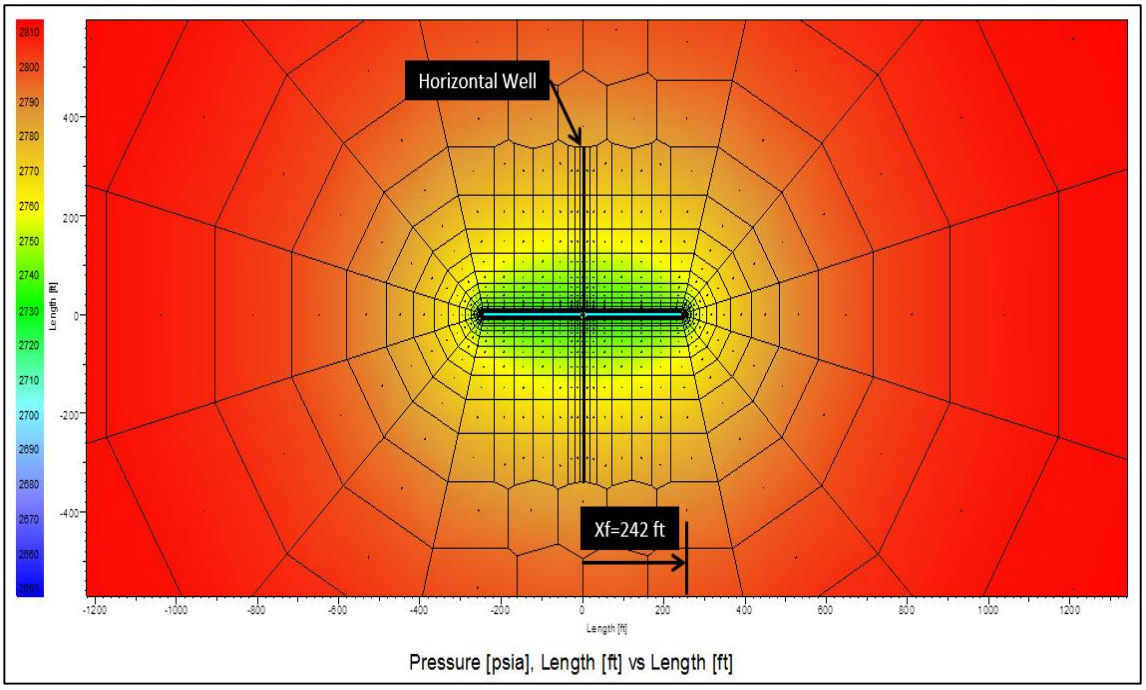

Figure 83- 2D Geometry Plot Pressure Distribution field data set-2 by the used software.

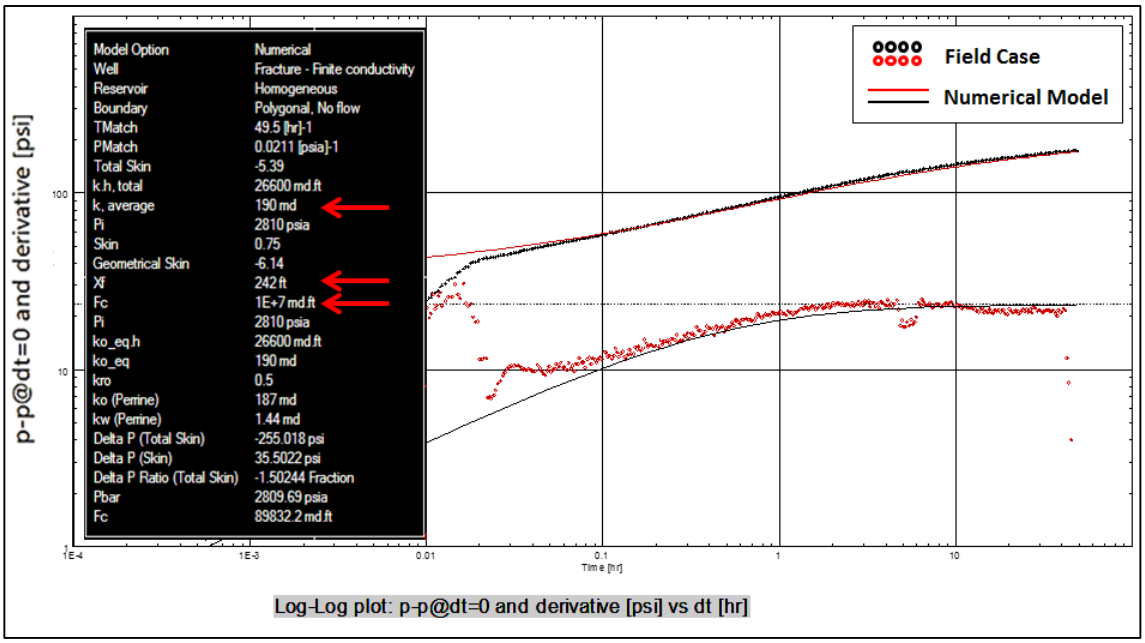

Figure 84- Pressure and derivative match of the field case-2 with a type curve of the numerical model from software available in the used well-test package.

Well near a finite conductivity fault: Field Data Set-3

The production, well and reservoir data are listed in Table 21 and Table 22.

Table 21: Production data of the field data set-3.

Well Type	Vertical	
Production Rate, STBD	3100 Oil 450 Water	12.7% Water cut
Test Type	Build-up	

Table 22: Well and reservoir properties of field data set-3.

Property	Value
Wellbore Radius, ft	0.354
Pay Zone, ft	200.0
Porosity, %	17.0
Formation Volume Factor, bbl/STB	1.28
Viscosity, cp	0.71
Total Compressibility, psi^{-1}	1. $36e^{-5}$

The proposed solution was used to match the pressure data and then compared with results of a numerical model that used the software, both considering a well near a finite conductivity fault in a symmetrical reservoir. In other words, the data is matched to the curve provided by the FracFault-model, Figure 85, and validated by a numerical model available in the used commercial well-test software package, Figure 86 and Figure 87. Again, it should be noted that, the proposed semi-analytical solution is developed for

more complex geological systems (three regions), but it can correctly handle a simple system as well. As shown in Table 23, the consistency of the solution is confirmed, as the estimated reservoir parameters, using these two tools, are in excellent agreement, apart from the matrix permeability, which is slightly lower in the proposed solution.

Table 23: Comparison between the results obtained for the field data set-3 by the solution proposed by the FracFault-model and the numerical solution available in the used well test package.

Saphir-KAPPA-Software Numerical Model			**FracFault Model**		
d_F (ft)	F_{CF} (md-ft)	k (md)	d_F (ft)	F_{CF} (md-ft)	k_{avg} (md)
100	8e5	55	100	8e5	50

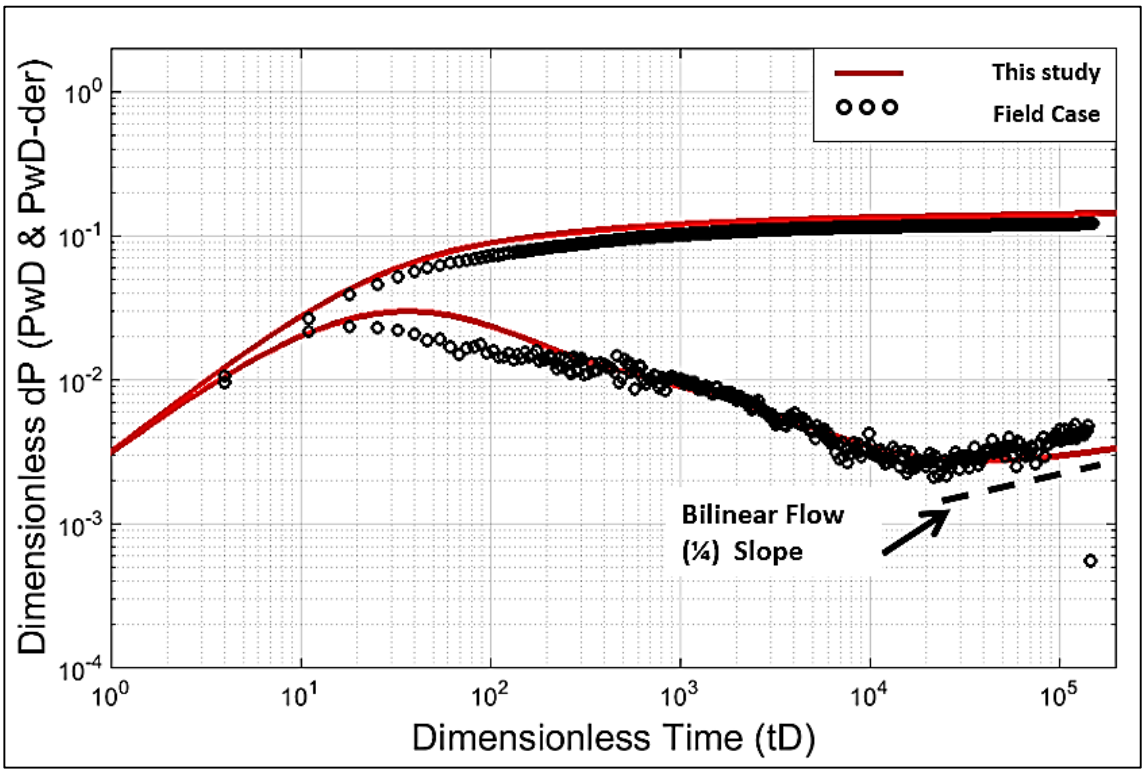

Figure 85- Pressure and derivative match using the FracFault-model to field data set-3.

It should be noted that, in order to match the field pressure data, the commercial software calculated a negative skin of -1.3 (Figure 87, blue curve), however, the proposed model cannot account for negative skin; hence, the pressure curve was not matched.

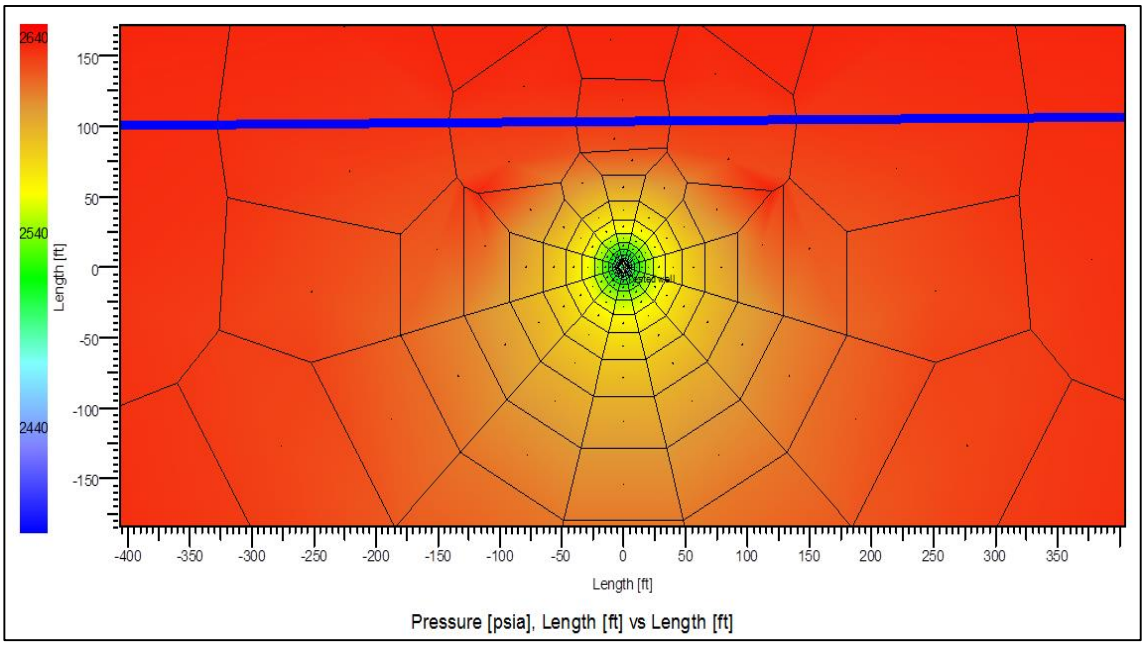

Figure 86- 2D Geometry Plot Pressure Distribution field data set-3, by the used commercial software.

So as to show the skin effect on the pressure curve, three iterations on skin magnitude were carried out (i.e. skin values of -1.3, 0 and 5) and are presented in Figure 87. It is evident that higher skin value will result in increased pressure drop.

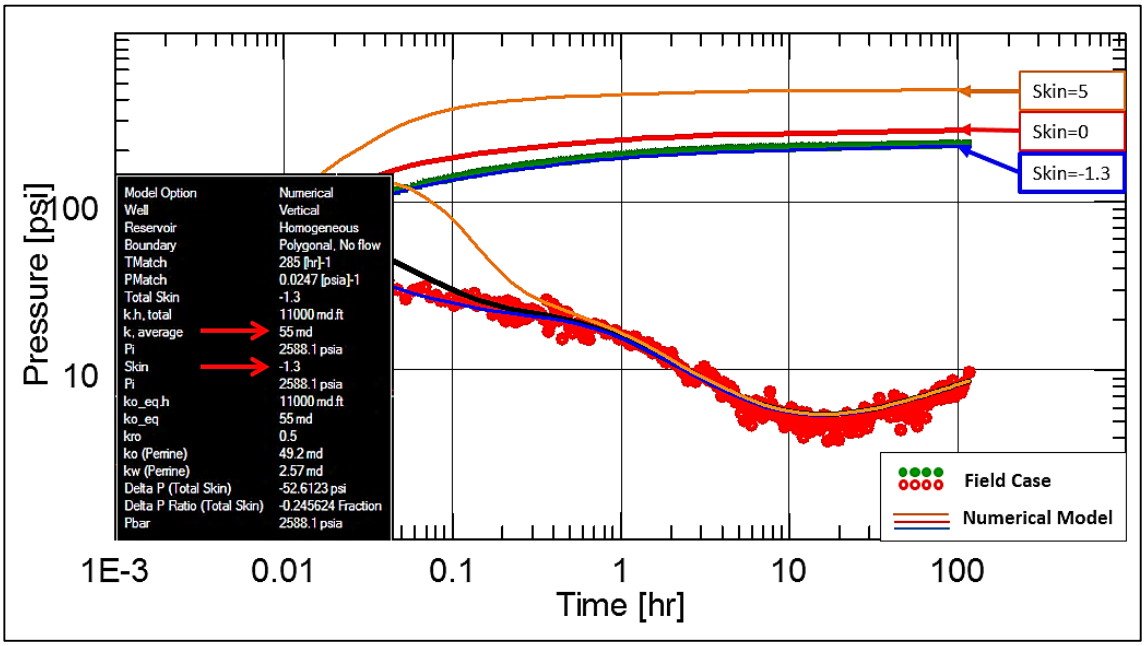

Figure 87- Pressure and derivative match using numerical model with different skin values of (-1.3, 0 and 5), from the used commercial software to field data set-3.

Well near a finite conductivity fault: Field Data Set-4

The production, well and reservoir data are listed in Table 24 and Table 25.

Table 24: Production data for the field data set-4.

Well Type	Vertical	
Production Rate, STBD	9825 Oil 0 Water	0% Water cut
Test Type	Build-up	

Table 25: Well and reservoir properties of field data set-4.

Property	Value
Wellbore Radius, ft	0.25
Pay Zone, ft	178.0
Porosity, %	18.5
Formation Volume Factor, bbl/STB	1.51
Viscosity, cp	0.36
Total Compressibility, psi^{-1}	$3.55e^{-6}$

The proposed solution was used to match the pressure data and then compared to the results of the numerical model, available in the used commercial software, for a well near a finite conductivity fault in a symmetrical reservoir. Table 26, shows the results of both approaches to the field data set-4, which are very close.

Table 26: Comparison between the results obtained for the field data set-4 by the solution proposed by the FracFault-model and the numerical solution available in the used well test package.

Saphir-KAPPA-Software Numerical Model			**FracFault Model**		
d_F (ft)	F_{CF} (md-ft)	k (md)	d_F (ft)	F_{CF} (md-ft)	k_{avg} (md)
150	1.5e8	600	180	1.1e8	600

The data is matched to the curve provided by the FracFault-model, Figure 88, and validated by a numerical model, Figure 89 and Figure 90. Again, this study does not handle negative skin, and hence, the pressure curve was not matched, while the commercial model used calculated a negative skin of (-0.7), so as to match the field pressure data.

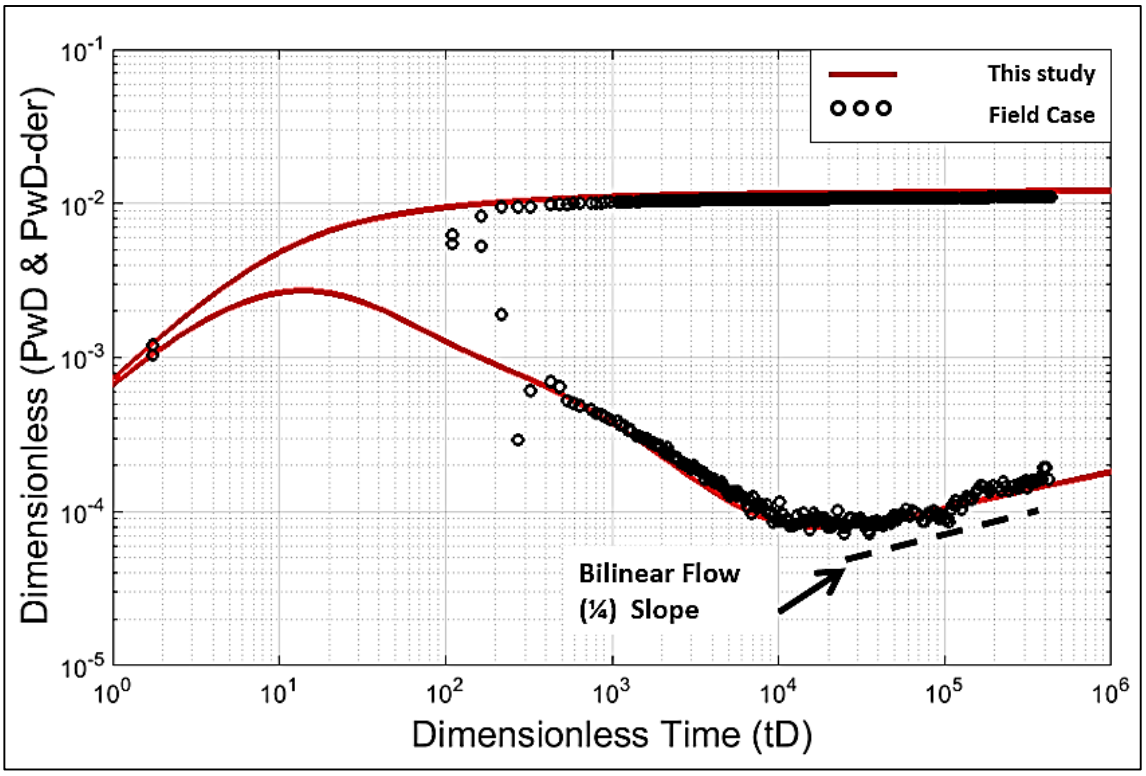

Figure 88- Pressure and derivative match using the FracFault-model to field data set-4.

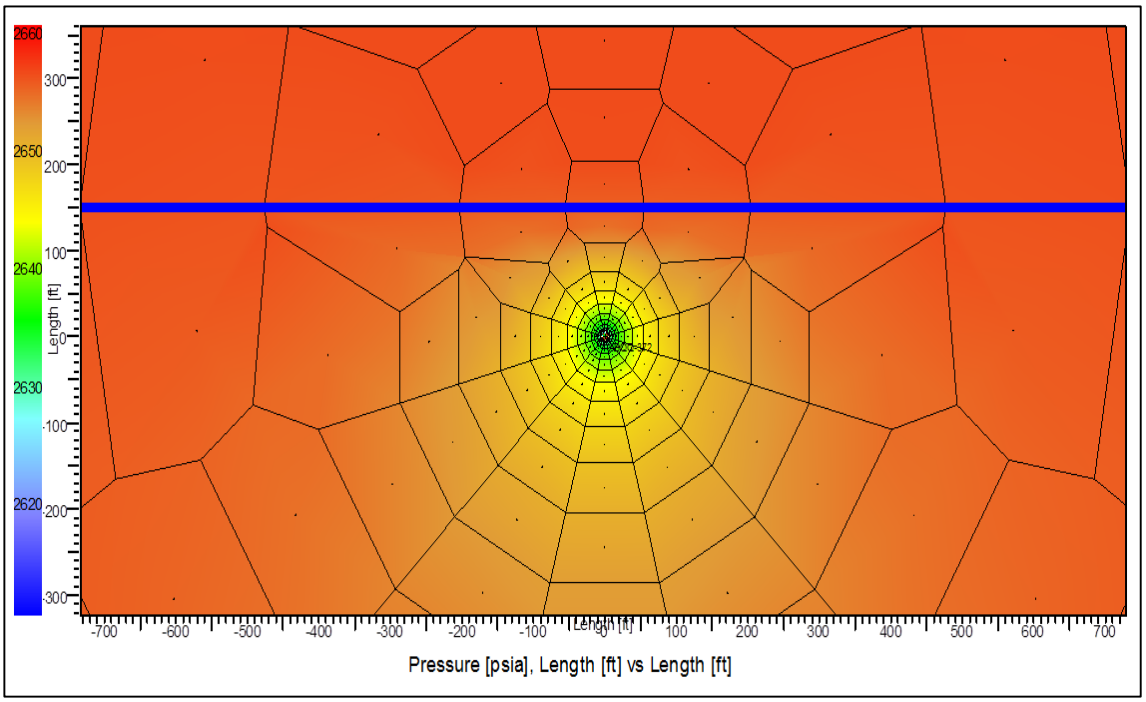

Figure 89- 2D-Geometry Plot Pressure Distribution field data set-4 by the used commercial software.

With the intention of showing the skin effect on the pressure curve, three iterations on skin magnitude were carried out in this case study (i.e. skin values of -0.7, 0 and 5) and the corresponding pressure drop curves are shown in Figure 90, displaying increased pressure drop at higher skin.

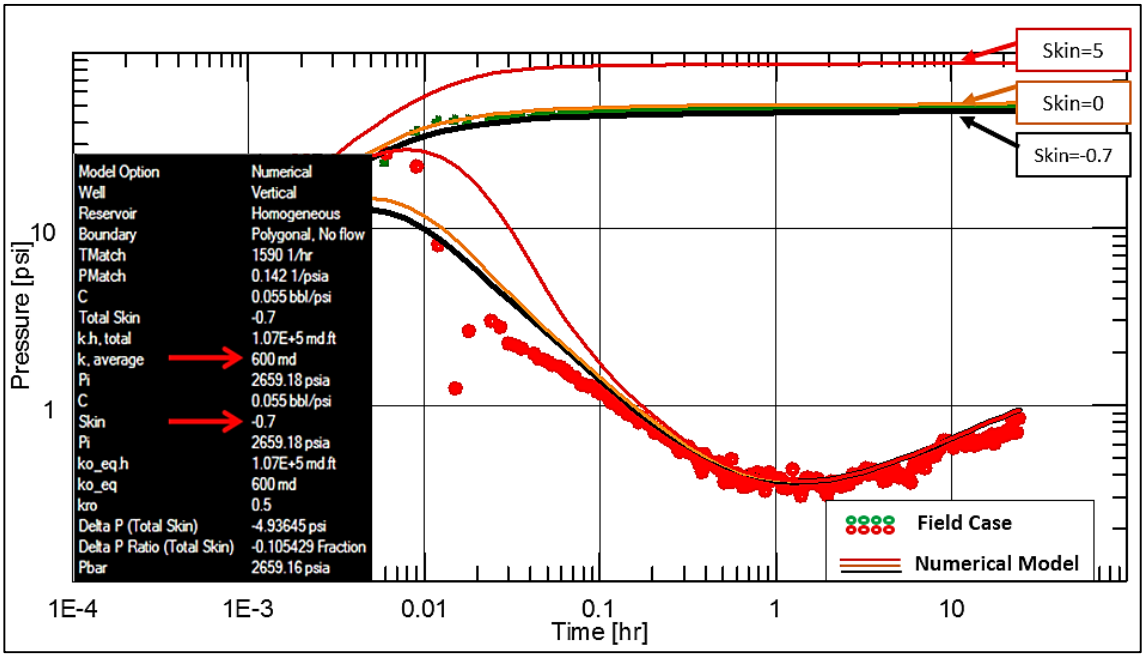

Figure 90- Pressure and derivative match using numerical model with different skin values of (-0.7, 0 and 5), from the used commercial software to field data set 4.

Hydraulically fractured well communicating with a fault: Field Data Set-5

The well was drilled with limited reservoir penetration and a non-intersected conductive fault nearby was observed, via pressure data. Later, the well was hydraulically fractured and connected to the nearby fault. The production, well and reservoir data are listed in Table 27 and Table 28.

Table 27: Production data for the field data set-5.

Well Type	Vertical	
Production Rate, STBOD	-10800 Intersected	0% Water cut
	-8500 Non-intersected	
Test Type	Fall-off	

Table 28: Well and reservoir properties of field data set-5.

Property	**Value**
Wellbore Radius, ft	0.25
Pay Zone, ft	110.0
Porosity, %	18.0
Formation Volume Factor, bbl/STB	1.02
Viscosity, cp	0.45
Total Compressibility, psi^{-1}	$3.88e^{-6}$

The data is matched to the curve provided by the FracFault-model, Figure 91 and Figure 92, and compared to the analytical model of a well in a reservoir with a finite conductivity fault, available in the used commercial well-test software package, Figure 93. The flow capacities to oil, have been found by to be 4,950 md-ft, which resulted in a permeability of 45 md by both approaches. The fracture and fault conductivities are also identical, as can be seen in Table 29, shows the results of applying both tools to the field data set-5. The fault conductivities calculated from both models were close but not identical.

Table 29: Comparison between the results obtained for the field data set-5 by the solution proposed by the FracFault-model and the numerical solution available in the used well test package.

Saphir-KAPPA-Software Numerical Model			**This Solution**		
d_F (ft)	$F_{Cf} = F_{CF}$ (md-ft)	k (md)	d_F (ft)	$F_{Cf} = F_{CF}$ (md-ft)	k_{avg} (md)
70	3.5e6 -1e6	45	80	3.5e6 - 1e6	45

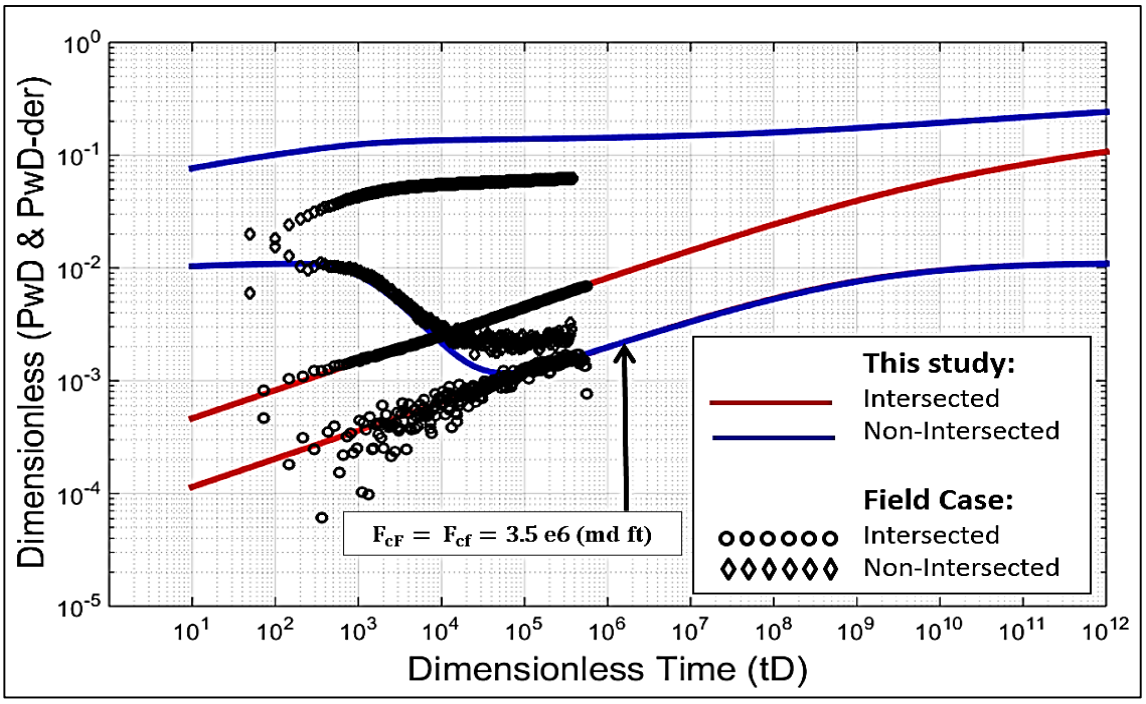

Figure 91- Pressure and derivative match to field data set-5 using the FracFault-model, with similar fracture and fault conductivity values.

It is believed that the fault conductivity values from both cases, pre- and post-fracture pressure data, should be equal. However, to obtain a better match, the conductivity is reduced for the non-intersected case (blue curve) as shown below in Figure 92.

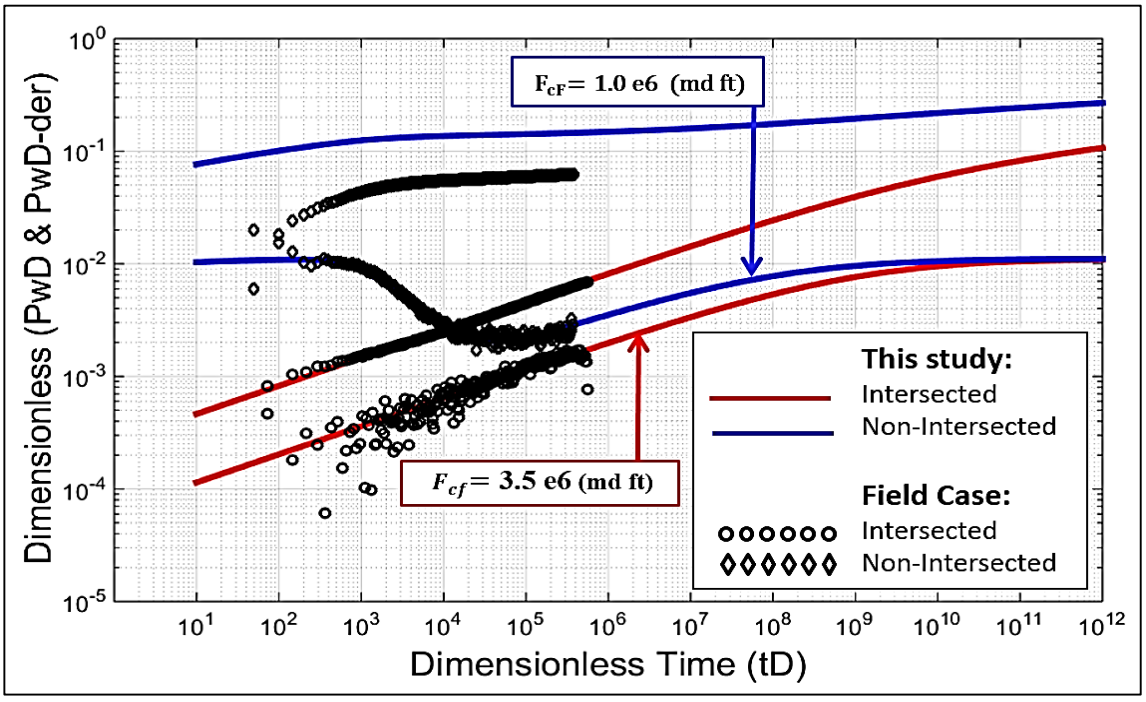

Figure 92- Pressure and derivative match to field data set-5 using the FracFault-model with different fracture and fault conductivity values.

Figure 93, shows the results of the analytical model(s) match to the pressure data by from the used well-test software.

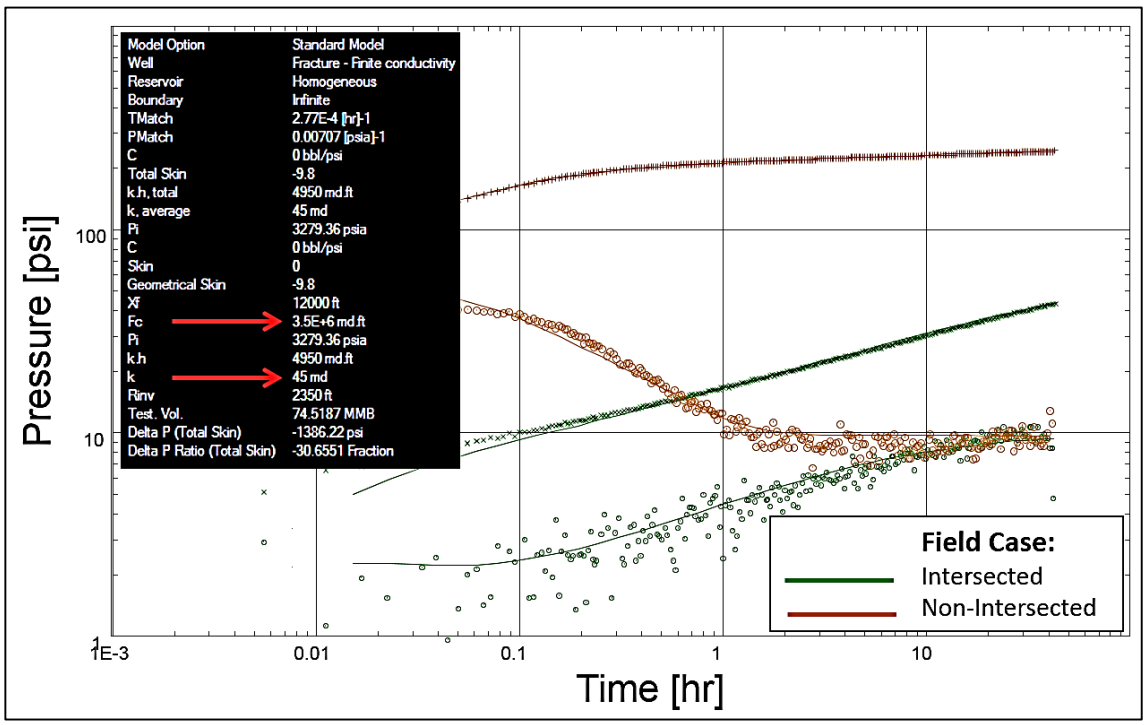

Figure 93- Pressure and derivative match to field data set-5 using the commercial software.

It is worth mentioning that unlike the commercial software used, the FracFault-model does not account for the well's long production history. In addition, the software is empowered with a "Rate Normalization" feature; hence, the resultant derivative calculation/shape will be affected and not match the actual field data. Hence, it is believed that the fracture and fault conductivities of 5e7 md ft are considered to be more accurate.

Fractured vertical well near a finite conductivity fault: Field Data Set-6

The objective here is to evaluate the reliability of the proposed solution for a practical field example that combines all the flow regimes presented in the FracFault-model. This field case example data set corresponds to a vertical well intersecting a finite conductivity fracture in a tight carbonate reservoir with a finite conductivity fault nearby.

Table 30 and Table 31 summarise production, well and reservoir properties.

Table 30: Production data for the field data set-6.

Well Type	Vertical	
Production Rate, STBOD	3730 OIL	20% Water cut
	932 Water	
Test Type	Build-up	

Table 31: Well and reservoir properties of the field data set-6.

Property	**Value**
Wellbore Radius, ft	0.27
Pay Zone, ft	236.0
Porosity, %	18.0
Formation Volume Factor, bbl/STB	1.4
Viscosity, cp	0.32
Total Compressibility, psi^{-1}	$1.92e^{-5}$

The flow, in this example, is dominated by the fracture bi-linear flow regime after a short wellbore storage period, at early times, followed by a hump, due to, possibly, a geological fault skin or "geochoke", based on Corbett et al. (2005). There is a sharp drop in the derivative, with a negative unit slope, followed by a bilinear flow regime which is a characteristic of a nearby non-intersected finite conductivity fault, Figure 94.

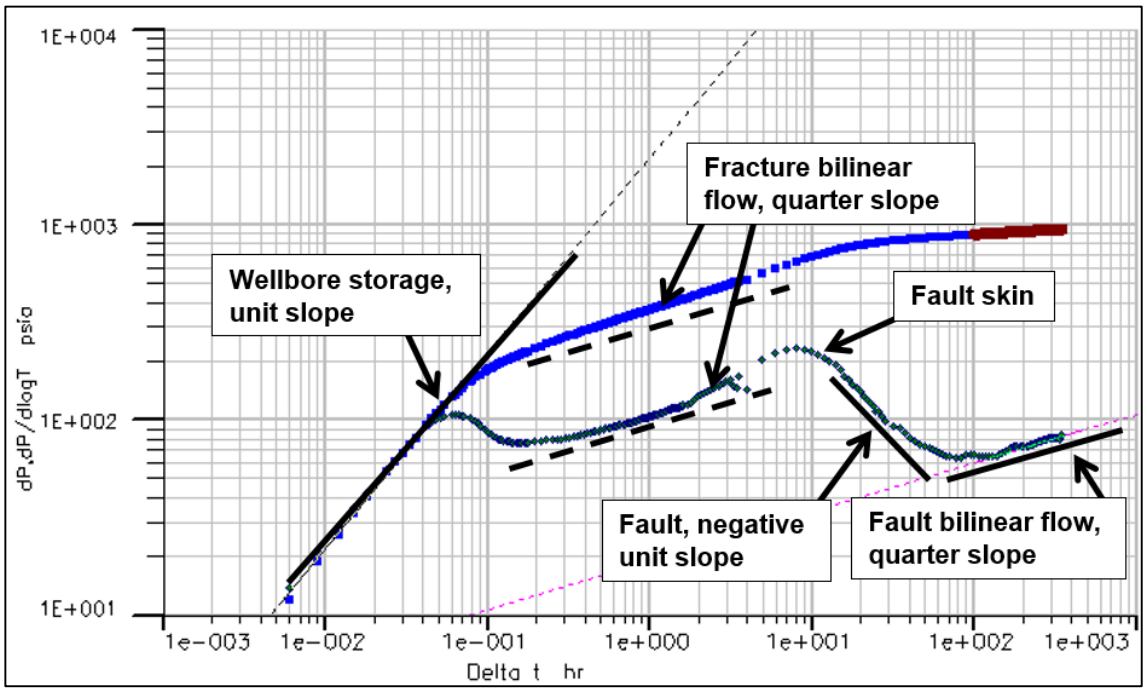

Figure 94: The derivative plot of the subject well with four flow regimes, reflecting the hydraulic and natural fractures.

Based on the pressure data response and the evidence of faults and fractures from seismic and production data, presented in Chapter 1, a numerical model was built. Firstly, using Saphir-KAPPA software package, a fractured well with low conductivity nature, was modelled across the well, before the fault nearby was introduced. It should be noted that a good match to the early-time pressure data was obtained with fracture conductivity, F_{Cf} , of 480 md-ft and a fracture half-length, x_f, of 50 feet. Then, a finite conductivity fault was introduced to the numerical model to match the rest of the pressure data, which showed up from 10 hours of shut-in time and lasted to the end of the test. This was accomplished by placing a fault at a distance, d_F of 80 feet away from the well and parallel to the fractured well. Figure 95 shows Voronoi grids (PEBI grids) generated across the fracture and nearby fault. It is quite challenging to completely match the pressure data due to the difficulty in constructing the grids at the fault, the software uses an automated gridding technique.

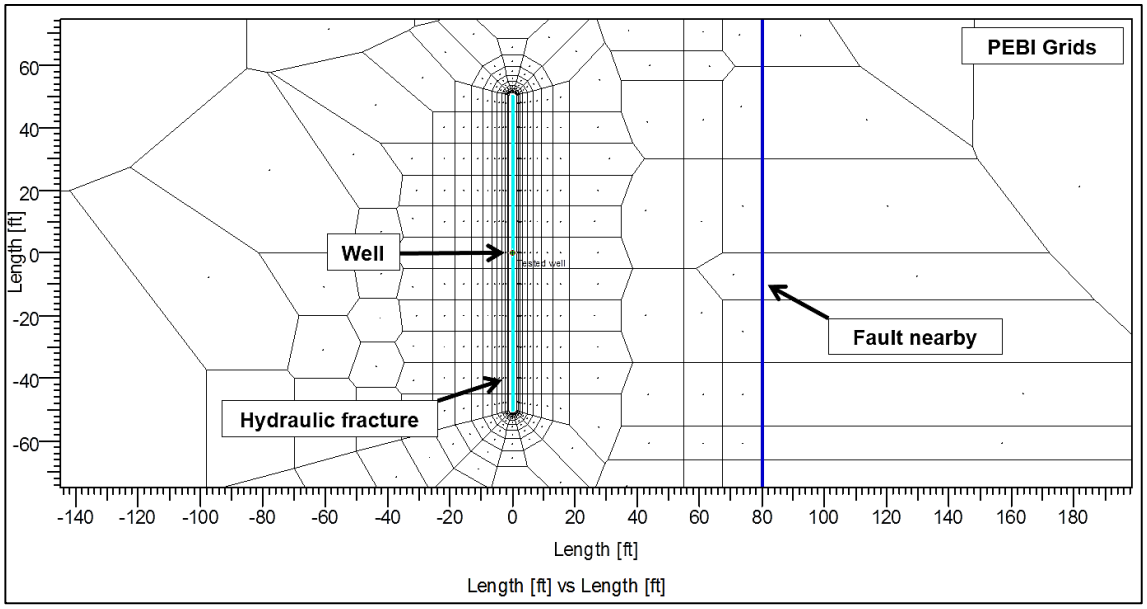

Figure 95: (PEBI) grids generated around well and along fracture and nearby fault by Saphir-KAPPA-Software.

The width of the fault, w_F, was 1.0 foot, resulted in fault conductivity (F_{CF}) of 2.5e4 md-ft. A reasonable match was obtained, as shown in Figure 96.

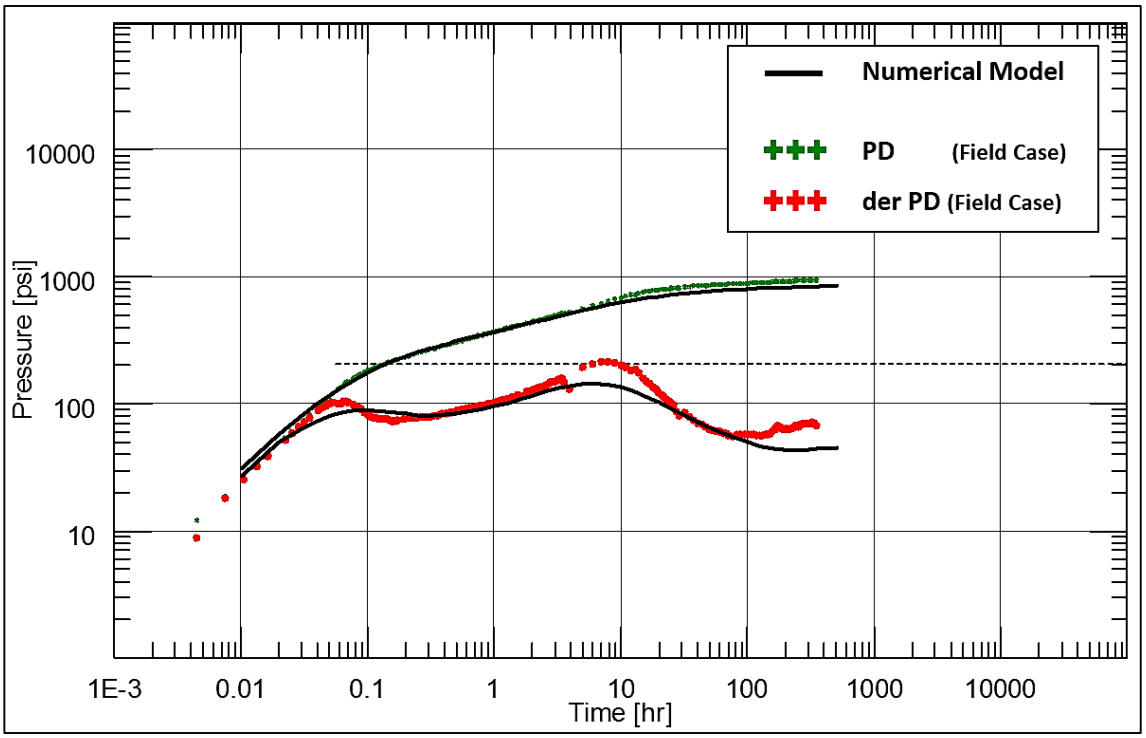

Figure 96: Numerical model match to the pressure data by Saphir-KAPPA-Software.

The data is also matched to a type curve provided by the solution proposed, Figure 97, with and without wellbore storage. The results were validated by those obtained based on the numerical solution mentioned above. The flow capacities to oil and the fault conductivities are identical and the fracture conductivities are relatively analogous, as shown in Table 32.

Table 32: Comparison between the results obtained for the field data set-6 by the solution proposed by the FracFault-model and the numerical solution available in the used well test package.

Saphir-KAPPA-Software Numerical Solution				**FracFault Model**			
x_f (ft)	d_F (ft)	F_{Cf} -F_{CF} (md-ft)	k (md)	x_f (ft)	d_F (ft)	F_{Cf} -F_{CF} (md-ft)	k (md)
50	80	480 – 2.5e4	2.8	78	105	310 – 2.5e4	2.8

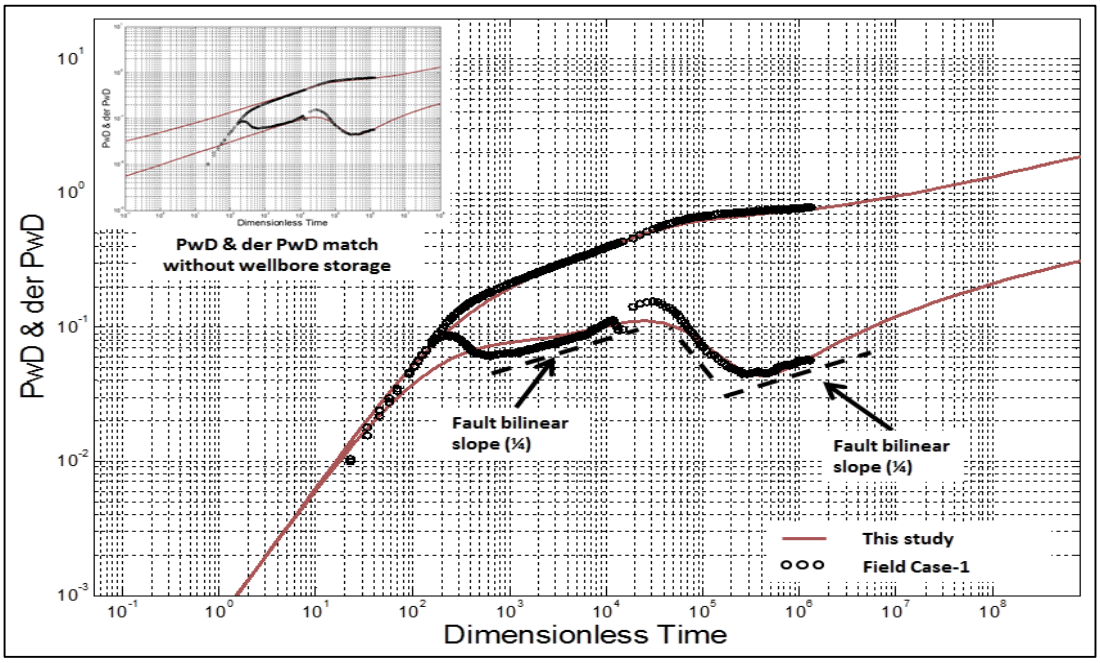

Figure 97- Pressure and derivative match of the field data set-6 with a type curve of the solution proposed by the FracFault-model.

The effective fracture half-length, shown in Figure 98, is estimated to be 78 feet and it is realistically reasonable, compared to the one estimated by the numerical model, of 50 feet, as both reveal a relatively short hydraulic fracture (<100 feet).

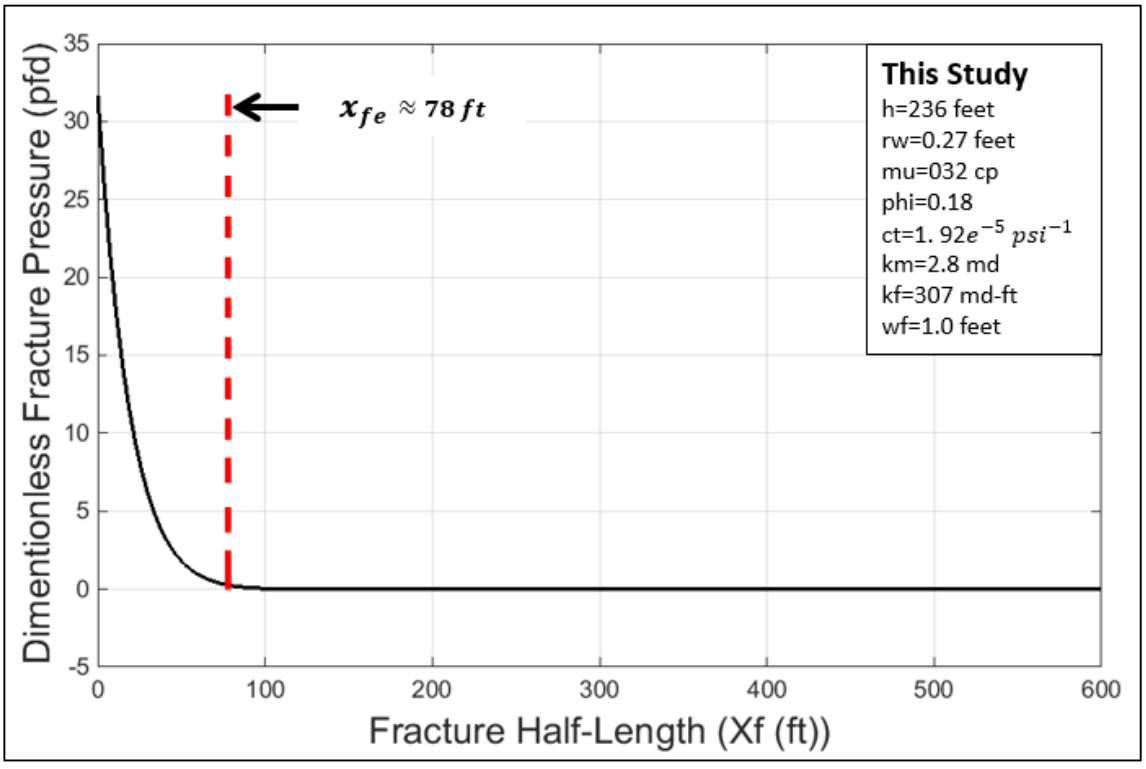

Figure 98- Fracture pressure distribution alongside the fracture and fracture half-length estimation.

Summary

In this chapter, the proposed solutions were validated by the use of analytically and numerically built synthetic and field cases, as follows:

First, the model was matched to an analytical solution. Then one homogenous numerical model and four numerical models were constructed using Ecrin-KAPPA software and compared to the proposed solution in a simple to complex order. After establishing a good understanding of the accuracy and reliability of the model, six field examples' data sets from carbonate and sandstone reservoirs, were analysed using the proposed semi-analytical solution and compared to a numerical models obtained by the commercial software (Saphir-KAPPA, 2012). The FracFault model related to the proposed solution is capable of multi-matching, as many scenarios as required, and also superimposes models with different colours and sets of parameters.

The next chapter will discuss conclusions, observations and recommendations by this study.

CHAPTER 7 – CONCLUSIONS, OBSERVATIONS AND RECOMMENDATIONS

7.1 Conclusions

1. The FracFault-model presents a novel solution for pressure transient data of a fractured-well in a three-region reservoir with a finite conductivity fault. This is in-line with meeting current industry requirements, with increased production from naturally faulted geological settings and unconventional reservoirs; hence, the importance of developing appropriate solutions for their accurate modelling and performance predictions. In addition, the existence of such complex geology and well flow geometries is commonly documented over the increasing number of image, production logs and dynamic data yet, the amount of these data is very limited relative to the field size. Consequently, analysis of dynamic data has become a primary tool for the identification, characterisation and modelling of such geological features.

2. The FracFault-model presents a suitable model for a fractured well in an asymmetric reservoir with a fault nearby. This general model validated the reliability of the specific numerical models normally used to match the pressure data. The proposed solutions uncover more flexible schemes to easily carry out modelling of other complex structures; e.g. fractured well in a linear composite reservoir with differing quality reservoir units across the fault plane. The final wellbore pressure-drop equation, Equation 93, in the Laplace domain is:

$$\bar{p}_{wD}=\frac{2}{s}\int_0^{\infty}\frac{1-\left[e^{-2\sqrt{\left(\rho^2+\frac{s}{\eta_{D2}}\right)}\cdot d_F}\left[\frac{1-\frac{k_{D2}\cdot\sqrt{\left(\rho^2+\frac{s}{\eta_{D2}}\right)}}{F_{CD_F}\cdot\left(\rho^2+\frac{s}{\eta_{DF}}\right)+k_{D3}\cdot\sqrt{\left(\rho^2+\frac{s}{\eta_{D3}}\right)}}}{1+\frac{k_{D2}\cdot\sqrt{\left(\rho^2+\frac{s}{\eta_{D2}}\right)}}{F_{CD_F}\cdot\left(\rho^2+\frac{s}{\eta_{DF}}\right)+k_{D3}\cdot\sqrt{\left(\rho^2+\frac{s}{\eta_{D3}}\right)}}}\right]\right]}{\left[F_{CD_f}\cdot\left(\rho^2+\frac{s}{\eta_{Df}}\right)+k_{D1}\cdot\sqrt{\left(\rho^2+\frac{s}{\eta_{D1}}\right)}+k_{D2}\cdot\sqrt{\left(\rho^2+\frac{s}{\eta_{D2}}\right)}\right]+\left[e^{-2\sqrt{\left(\rho^2+\frac{s}{\eta_{D2}}\right)}\cdot d_F}\left[\frac{1-\frac{k_{D2}\cdot\sqrt{\left(\rho^2+\frac{s}{\eta_{D2}}\right)}}{F_{CD_F}\cdot\left(\rho^2+\frac{s}{\eta_{DF}}\right)+k_{D3}\cdot\sqrt{\left(\rho^2+\frac{s}{\eta_{D3}}\right)}}}{1+\frac{k_{D2}\cdot\sqrt{\left(\rho^2+\frac{s}{\eta_{D2}}\right)}}{F_{CD_F}\cdot\left(\rho^2+\frac{s}{\eta_{DF}}\right)+k_{D3}\cdot\sqrt{\left(\rho^2+\frac{s}{\eta_{D3}}\right)}}}\right]\right]\cdot\left[F_{CD_f}\cdot\left(\rho^2+\frac{s}{\eta_{Df}}\right)+k_{D1}\cdot\sqrt{\left(\rho^2+\frac{s}{\eta_{D1}}\right)}-k_{D2}\cdot\sqrt{\left(\rho^2+\frac{s}{\eta_{D2}}\right)}\right]}\cdot d\rho$$

3. This model can also be used for simpler cases, such as the fracture and fault in a symmetric reservoir, a fractured well, and linear composite reservoir, with the ability to model a wide range of reservoir and fracture properties. Unlike other studies, when dealing with a fractured-well scenario, this work accounts for the matrix flow on the x-y plane. The reliability of the proposed solution was demonstrated in a systematic

approach, including synthetic and numerically-built models, constructed from the simulated flow geometry by the commercial software used. In addition to that, the validity was further confirmed through analysing a number of field cases in sandstone and carbonate reservoirs.

4. The effective fracture half-length calculated from the proposed approach reasonably matched the corresponding values inputted into the numerical simulations that generated the well tests' signatures observed in the field data. The solution is described by the flux distribution, Equation 97, from the two sides of the fracture, along the x-axis as follows:

$$\overline{q}_{D(xy)}(x_D, y_D = 0, s) = \frac{-2}{s} \int_0^{\infty} \frac{\cos\,(x_D\,\rho)}{\left[\left(\frac{\left[F_{CDf}\cdot\left(\rho^2+\frac{s}{\eta_{Df}}\right)+(k_{D1})\cdot\sqrt{\left(\rho^2+\frac{s}{\eta_{D1}}\right)}+(k_{D2})\cdot\sqrt{\left(\rho^2+\frac{s}{\eta_{D2}}\right)}\right]}{(k_{D1})\cdot\sqrt{\left(\rho^2+\frac{s}{\eta_{D1}}\right)}+(k_{D2})\cdot\sqrt{\left(\rho^2+\frac{s}{\eta_{D2}}\right)}}\right)\right]} \cdot d\rho$$

The results of FracFault-model may enable reservoir engineers to carry out modelling of such complex reservoir/well geometries with increasing certainty and long-term benefits. In summary, the solution can be used to describe a three-region, linear, composite reservoir with or without a fractured-well. Table 33, summarises the similarities and differences between the present study and Cinco et al. (1978), Maghsood and Cinco-Ley (1995) and Rahman et al. (2003).

Table 33: Comparison between this study and Cinco et al. (1978), Maghsood and Cinco-Ley, (1995) and Rahman et al. (2003).

Paper #	Conductive Fracture(f) / Fault(F)						Matrix Flow	Number of Regions	Remarks
	Intersected by Well?								
	Yes			No					
	x_f	F_{cf}	S_f	d_F	F_{cF}	S_F			
SPE 24704 (1978) Cinco-Ley and Samaniego	✓	✓	X	**Intersected fracture only**			Linear y-axis	**1**	1.Finite conductivity nature 2.Homogenous reservoir 3.Transient effects along fracture are **not neglected** 4.Matrix flow along y-axis only
SPE 24704 (1992) Abbaszadeh and Cinco-Ley	**Non-intersected fracture only**			✓	✓	✓	Linear **y-axis**	**1**	1.Finite conductivity nature. 2.Allows reservoir flow from left and right towards the fault. 3.Transient effects along fault **are neglected.** 4.Zero fault capacity, net cumulative flux in/out of fault is zero. 5.Calculates Fault distance, skin and conductivity. 6.Different reservoir properties of the two side of the fault plane (using S_f). 7.Each reservoir zone is semi-infinite in the x-direction and has an interface with the fault zone. 8.Both reservoir zones and the fault zone are infinite in the y-direction. 9.Matrix flow along y-axis only.
SPE 84295 (2003) Anisur Rahman et al.	**Non-intersected fracture only**			✓	✓	✓	Linear **y-axis**	**2**	1. Finite conductivity nature. 2.Allows reservoir flow from left and right towards the fault. 3.Transient effects along fault **are not neglected.** 4.Calculates fault distance, skin and conductivity. 5.Different reservoir properties of the two side of the fault plane (two regions). 6.Each reservoir zone is semi-infinite in the x-direction and has an interface with the fault zone. 7.Both reservoir zones and the fault zone are infinite in the y-direction. 8.Matrix flow along y-axis only.
This Study (2016)	✓	✓	X	✓	✓	X	Both Linear and Diagonal **x-y plane**	**3**	1.Finite conductivity nature. 2.Allows reservoir flow from both sides towards the Fault. 3.Allows reservoir flow from both sides towards the fracture. 4.Transient effects along fault are not neglected. 5.Calculates fault distance and conductivity. 6.Calculates fracture half-length and conductivity. 7.Different reservoir properties of the two sides of the fault plane and fracture (Three regions and one fracture and one fault). 8.Reservoir zone one is semi-infinite in the Y-direction and has an interface with the fracture zone. 9.Reservoir zone three is semi-infinite in the Y-direction and has an interface with the fault zone. 10.Reservoir zone two is finite in the Y-direction and has an interface with the fracture zone from one side and fault zone from the other side. 11.Both reservoir zones and the fault zone are infinite in the x-direction. 12.Matrix flow along both x- and y- plane only.

7.2 Major Findings

Fractured Well Solution:

1. Introduced and validated a finite conductivity fractured-well semi-analytical solution, accounting for the flow in the reservoir along the x-y plane, in symmetric and asymmetric reservoirs (two different regions bounding the fracture plane).

2. The average permeability calculated from this solution is the arithmetic average of the two bounding (different) regions. This was confirmed by comparing it to another case for a well located in a homogenous reservoir (without a fracture) and with a single reservoir permeability equal to the average of the two bounding regions (by super-imposing the two derivatives).

3. A fracture-linear flow is evident at very early times confirming the physics, accuracy and stability of the solution.

4. The solution of the equation in the x-y plane allows us to observe the radial flow signature after the bilinear flow signature. To the best of author's knowledge, in some of the existing software, the radial flow is not calculated, but graphically added to the solution.

A well intersecting a finite conductivity fracture near a finite conductivity fault in an asymmetric reservoir:

1. The FracFault-model confirmed the flow behaviour observed in several field data sets and different simulated numerical models of a fractured-well in a three-region composite reservoir with a finite conductivity fault.

2. The proposed solution exhibits the following flow regimes: at early times, the curve signifies a ¼ slope as a result of a bilinear flow from the two linear flow regimes along and into the fracture. Subsequently, a radial flow, demonstrates the transient flow in the matrix bounding the fracture. A "down-turn" is then evident, with a negative unit slope indicating the start of a conductive fault and enhancement of rock quality, followed by an "up-turn" with a bilinear flow regime demonstrating the finite nature of the fault and proceeded by a radial flow regime of the bounding blocks, at late times.

3. The solution can be used to model a well in a linear composite reservoir with and without a fault nearby.

4. It also can be used to model a fractured-well in a linear composite reservoir with and without a fault nearby.

Flux distribution and effective fracture half-length estimation:

1. The flow profile dictates a non-uniform inflow-flux distribution along the fracture plane, as there is a larger fracture pressure drop, Δp_f, closer to the well.

2. A good assessment of the effective fracture half-length (x_{fe}), was achieved, noting that the actual fracture half-length (x_f) is assumed to be infinite. This verified the validity of the assumption that led to the solution of the effective fracture half-length, $\boldsymbol{x_{fe}}$ i.e. the approach is based on the notion that, practically, an extremely small quantity of fluid flow will occur when the difference in pressure across the fracture plane in an infinite length fracture is approaching zero (Δp ≈zero). This criterion was deployed in the flux term of the fractured-well equation, and the resultant equation was solved for effective fracture half-length (x_{fe}).

3. In the FracFault-model, it was noted that, when using the pressure and flux distribution to determine (x_{fe}), at a flux and/or pressure depletion of $\geq 99.99\%$ of the first calculated value, a reasonable match was obtained between the effective fracture half-length calculated by the proposed approach and that of many numerically built cases. Furthermore, in reality, if there is a fracture length part that contributes less than 0.01%, it would not be dominating the flow behaviour and hence can be ignored.

4. The method can also be used to calculate the matrix and fracture fluxes into and along the fracture aperture, $q_{Dm}\ and\ q_{Df}$, respectively.

5. Differently from previous works, this solution solves for matrix-flow on the x-y plane in all the three regions, while other studies account for the matrix linear-flow only. The validity of the reservoir linear flow along the y-axis was verified by this solution. That is, a case scenario was set-up and the outcome of the two approaches were compared. It was noted that both approaches are in exact agreement as they both reflected the same trends

and flux values. However, as mentioned above, the solution accounting for the x- and y-directions allows the observation of radial flow.

6. The presence of scattered data in plotting the flux distribution from the x-y plane approach may be due to numerical issues, but it can also be attributed to the diagonal flow nature and convergence into the fracture, which need to be investigated further. At this stage it is assumed that the two solutions are similar, and the linear flow (y-axis) is the solution considered in calculating the effective fracture half-length, due to its stability.

7. It was shown that for a constant rate and fracture conductivity, the contribution from the matrix to the fracture increases with increasing matrix permeability, due to the decrease in pressure drop across the matrix-fracture interface.

8. For a constant injection rate and matrix permeability, a high conductive fracture acts more like a source of fluid supply, confirming the observation also introduced by Maghsood and Cinco-Ley (1995). That is, fluids tend to be supplied by the fracture itself when the pressure-drop across the fracture is exceptionally small.

9. The fracture half-length is a function of fracture conductivity. At low conductivities, the fracture pressure is higher, as it is harder to inject into the fracture (source case); hence, fluids tend to dissipate into the matrix more. As a result, you get smaller fracture half-length with lower fracture conductivities.

10. The fracture half-length is also a function of matrix permeability. For a source case, the lower the matrix permeability, the longer the fracture, to accept more injected fluid for a constant rate solution.

11. The fracture half-length is not a function of well rate. That is, the rate magnitude has no effect on the effective fracture half-length. Changing the rate induces different pressure amplitudes, the larger the rate, the larger the pressure amplitude; however, the extent of the pressure transient should be the same, at different rates. This is consistent with the principle and assumptions of estimating the radius of investigation. At high rates, understandably, matrix and fracture contributions are larger.

7.3 Business Impact

The identification and characterisation of conductive fractures and faults presents great technical and economic challenges to reservoir engineers and geoscientists. The FracFault-model tackles some of these challenges by presenting semi-analytical solutions for improved interpretation of their transient well test pressure data. The materials discussed here:

- Provide a better understanding of the reservoir fluid movements in intersected fractures and reservoirs with conductive faults, and thus improve reservoir development plans,
- Improve well test interpretation by using more comprehensive semi-analytical solutions.
- Validate numerical approach with the presented semi-analytical solutions.
- Harness the power of simulation by directly linking numerical well-test models, validated by analytical solutions, to simulation models. The current practice is done through Geological Models, which reduces its effect, due to restricting the use of dynamic data to flow capacity (kh) values only.
- Capitalize on the real-time pressure transient analysis from the Intelligent-Field initiative by adopting suitable and accurate analytical and semi-analytical solutions.

7.4 Recommendations for Future work

For future work, this study recommends the following to improve the solution:

Well skin using the effective radius method

The Effective Radius tactic is usually used to represent the well's skin analytically when dealing with negative skin values. The solution proposed in this study, is solved to describe the well pressure without accounting for well treatment (stimulation effect). Here Kucuk and Ayestaran's (1985) dimensionless equations, are used to add "a positive skin dimensionless pressure drop" to the total pressure drop, as was explained earlier. Therefore, it is suggested to include the negative skin in the form of effective wellbore radius. That is:

$$r_w' = r_w \,.\, e^{-s_w} \quad \Rightarrow \quad \Delta p\,(r_w', s_w = 0) = \Delta p\,(r_w, s_w)$$

Where,

r_w : Wellbore radius, r_w' : Effective wellbore radius and s_w: Well Skin

Superposition for varying rates

The superposition effect is owing to the pressure variations, due to multiple flow rates, and is equal to the sum of the pressure drops from the different rates collectively. The proposed solution is solved for describing the pressure distribution due to production caused by a constant rate from a single well. To better represent the pressure behaviour when solving for complex flow problems, it is suggested to include the effect of rate changes on derivative calculation. In other words, a more generalised solution is recommended. That is, the solution should consider changing rates, since, in reality, varying rates from a single well and/or several wells operating at the same time, are common features of actual field data.

Fault-face skin

A "thin skin baffle" along the fault plane, occasionally resembling a situation similar to a sealing fault, is observed in many field data. This geological deformation is referred to in the literature, sometimes, as "Fault Skin" or "Geochoke". Maghsood and Cinco-Ley (1995), Figure 99, and Rahman et al. (2003), Figure 100, accounted for fault skin. For future work, the author intends to include a fault skin, around the fault.

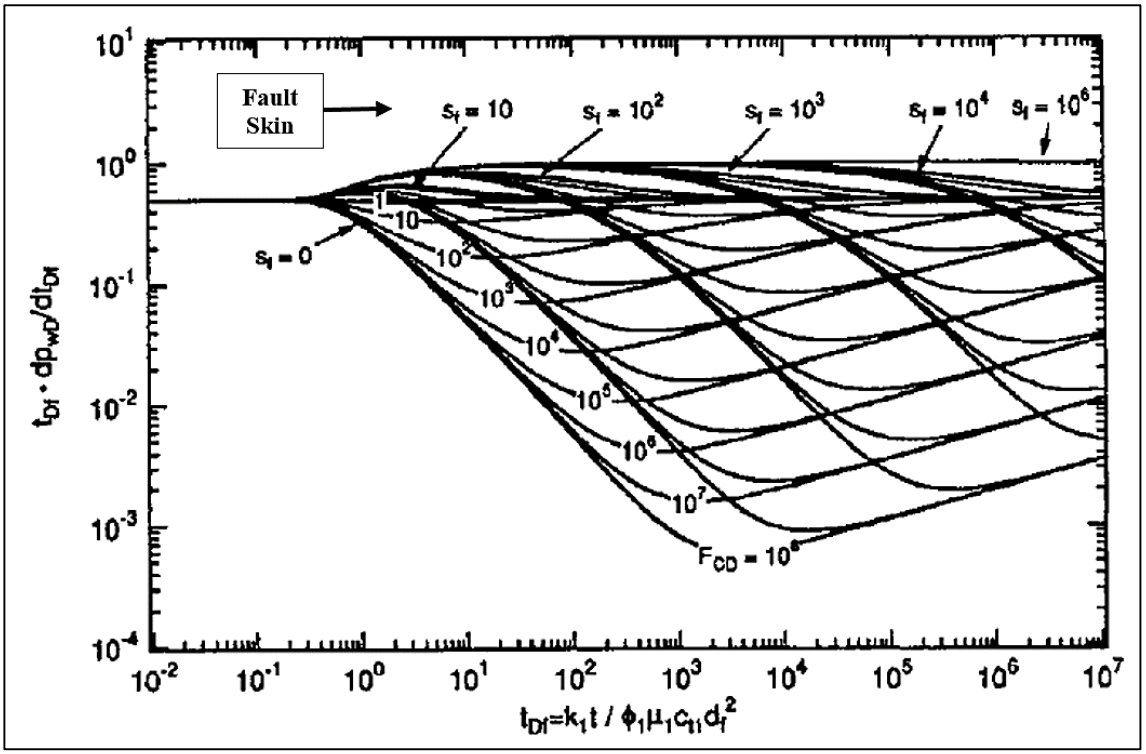

Figure 99: Generalized derivative type-curve for a finite conductivity fault (after Maghsood and Cinco-Ley, 1995)

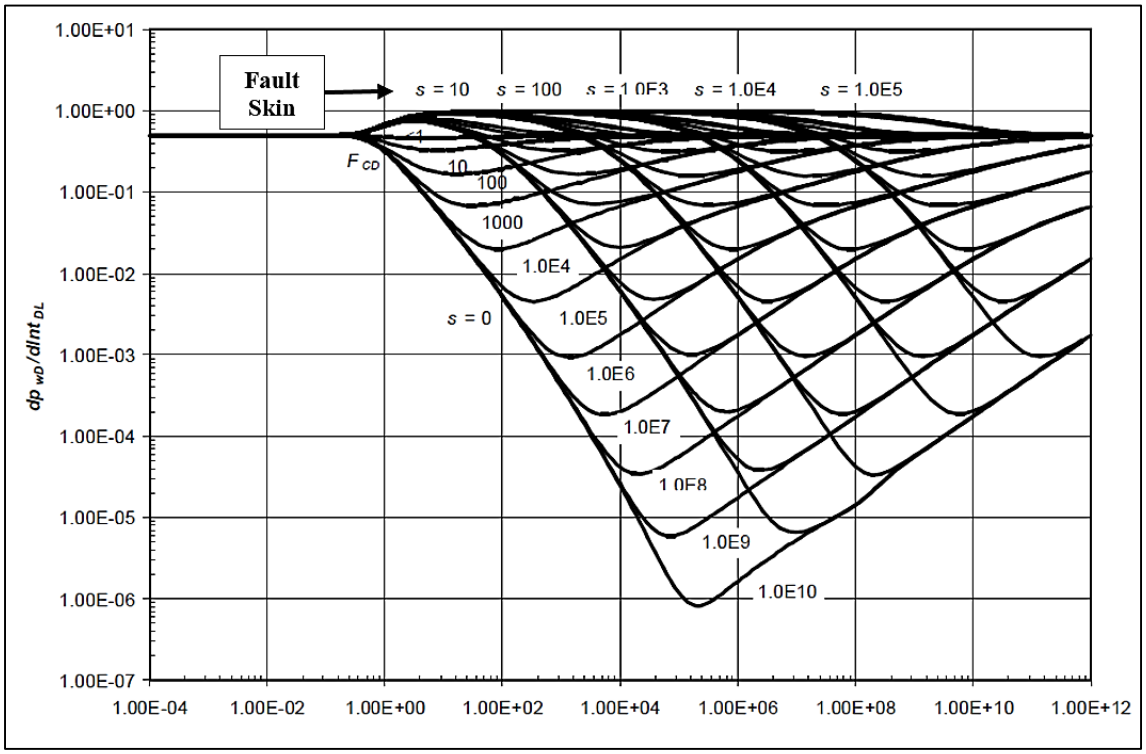

Figure 100: Generalised derivative type-curve for a finite conductivity fault (after Rahman et al., 2003)

Fault core effect

The author suggests studying the effect of the fault core on the shape and slope of the derivative plot, as it reflects a more realistic structure of conductive faults. Fault cores (zones) act as barriers, conduits, or mixed conduit/barrier systems to reservoir fluids, hence, it can be identified via transient data, Figure 101.

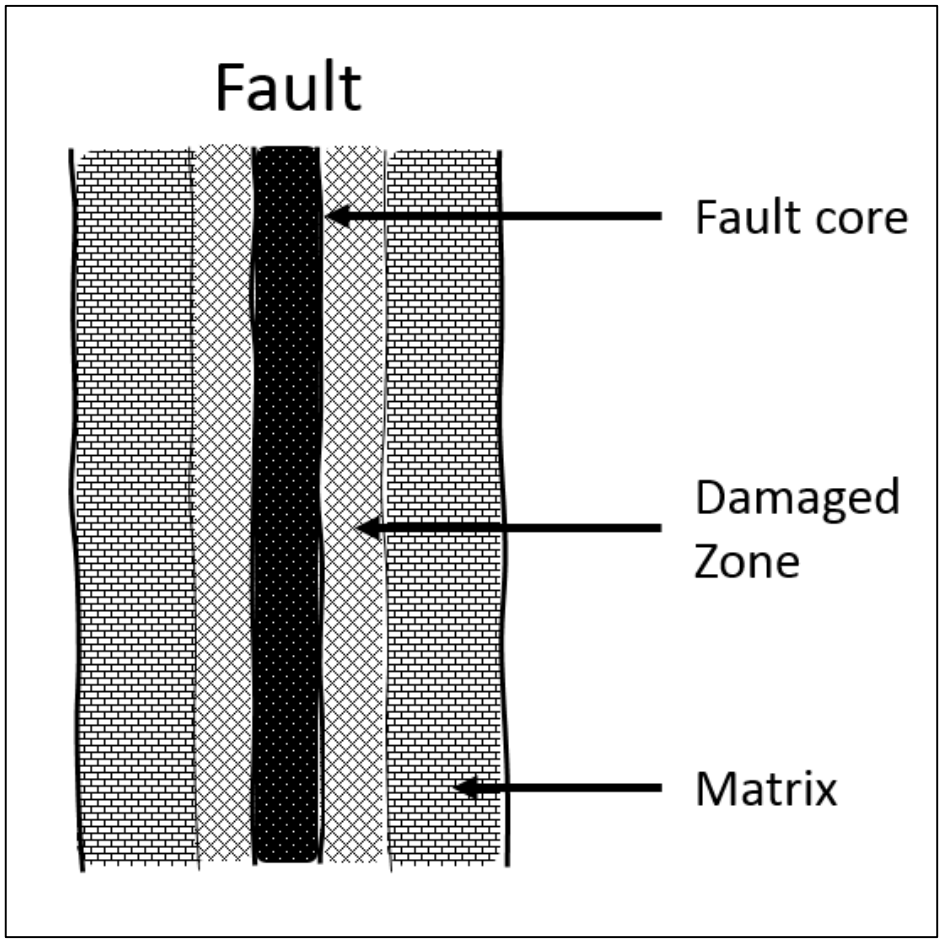

Figure 101: Schematic of the fault components.

This geological feature has been a subject of study in the literature by many researchers. Evans et al. (1997) stated that well-developed damaged zones (fractured zones) around the fault core may lead to enhanced fluid flow through a relatively thin tabular region parallel to the fault plane, yet the fault core restricts fluid flow across the fault. Figure 102 below shows a fault zone architecture, modified after Evans et al. (1997).

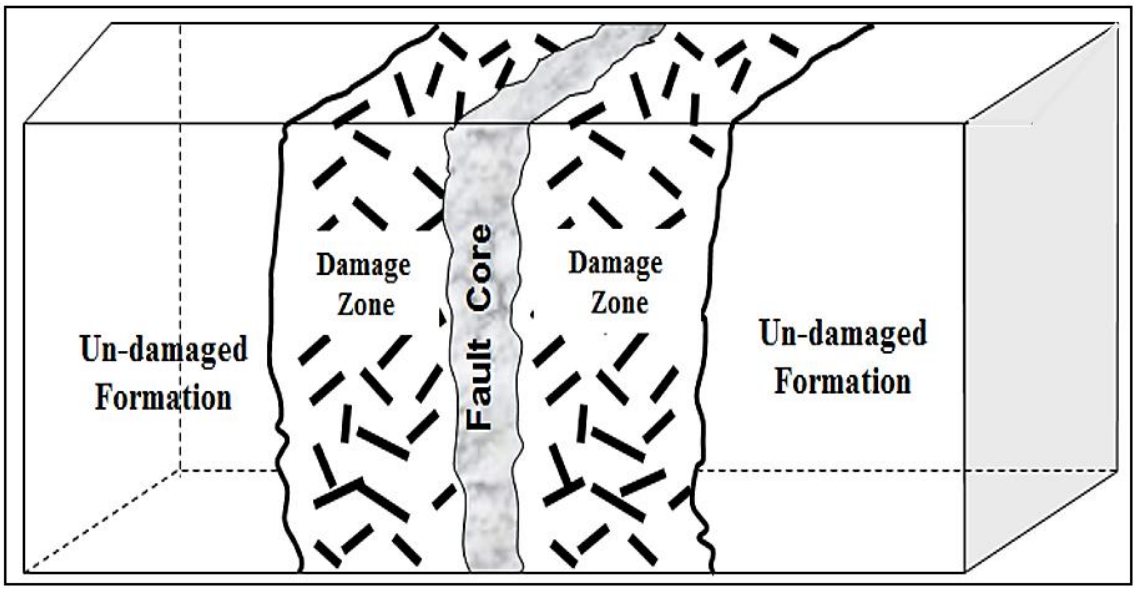

Figure 102: Schematic of the damaged zones around the fault (after Evans et al., 1997).

To understand the effect of the different fault core leakage factors on the shape and slope of the derivative, a numerical model, since there is no analytical solution available yet, was built using the software package, Figure 103, consists of a well near a fault zone. The fault zone was modelled with sealing/leaking fault (fault core) bounded by two conductive faults.

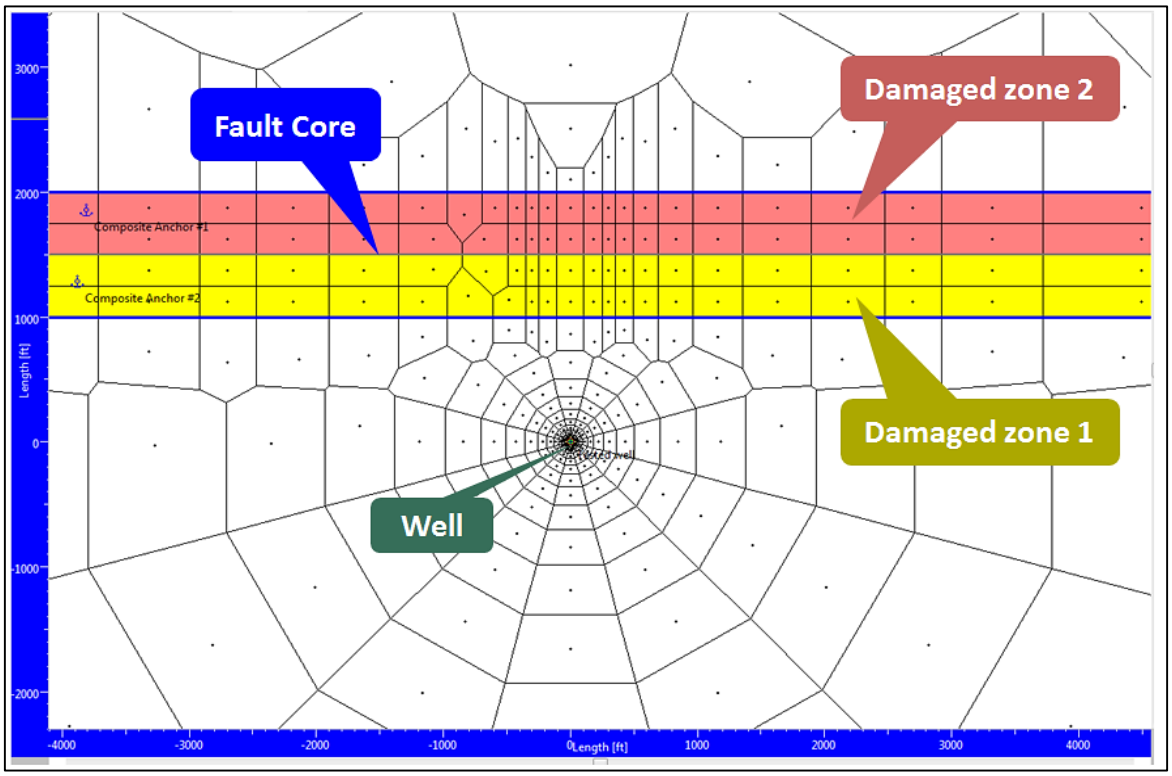

Figure 103: A numerically-built model of the damaged zones around the fault core.

Three sensitivity cases were carried out as follows:

Curve 1 (Red Curve), 0% Leakage factor (completely sealing fault-core),

Curve 2 (Green Curve), 5% Leakage factor (partially leaking fault-core),

Curve 3 (Blue Curve), 100% Leakage factor (completely leaking fault-core).

In Figure 104, it is very clear that the curves will deviate from the linear/bilinear slope as a result of different fault-core leak-ability.

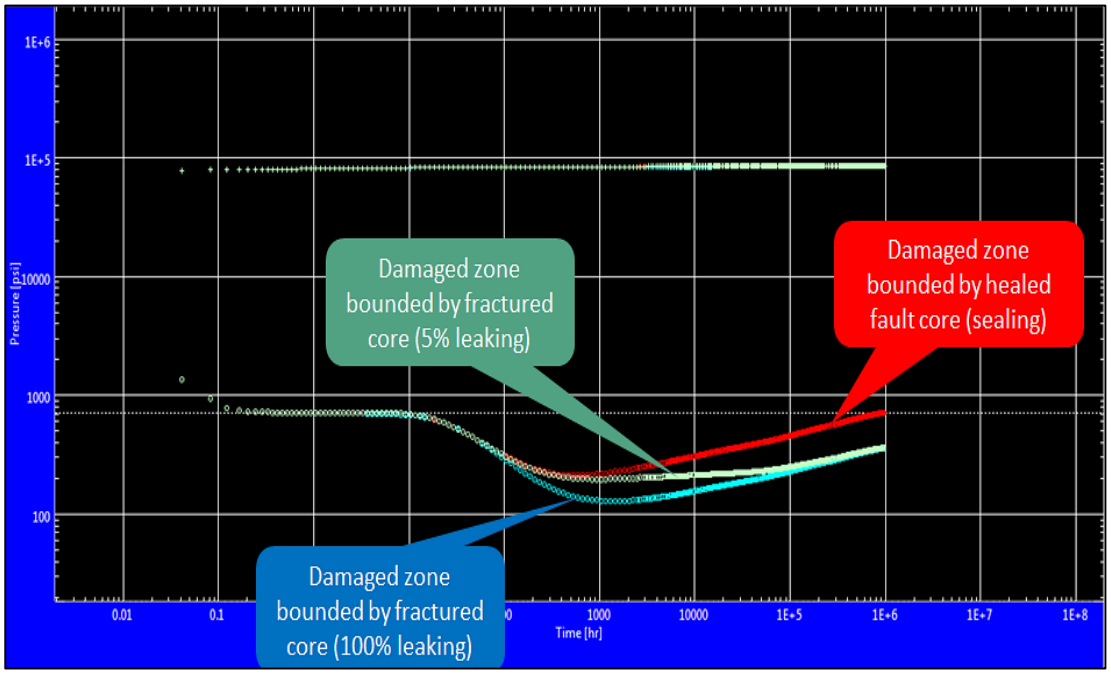

Figure 104: Derivative plot reflecting effect of different leakage factors (0%, 5% & 100%) on flow profile.

Curve 1 (Red Curve), shows a lower conductivity fault, due to the sealing nature of the fault-core that will result in a thinner fault, and hence, lower conductivity.

Curve 2 (Green Curve), reflects a partially leaking fault-core, 5%, and gradually (slowly) leaks all the fluids to the other side of the fault. In fact, it looks like a linear composite reservoir flow behaviour.

Curve 3 (Blue Curve), represents a completely leaking fault core and resulting in a greater fault conductivity, due to the increase in width of the fault core.

Finally, a fourth sensitivity case was run as follows:

Curve 4 (Red Curve), 1% leakage factor (partially leaking fault core).

This run shows a very interesting observation: a hump, reflecting the resistance to fluid flow across the leaking fault core, is evident at a very low leakage factor ~1% only, Figure 105.

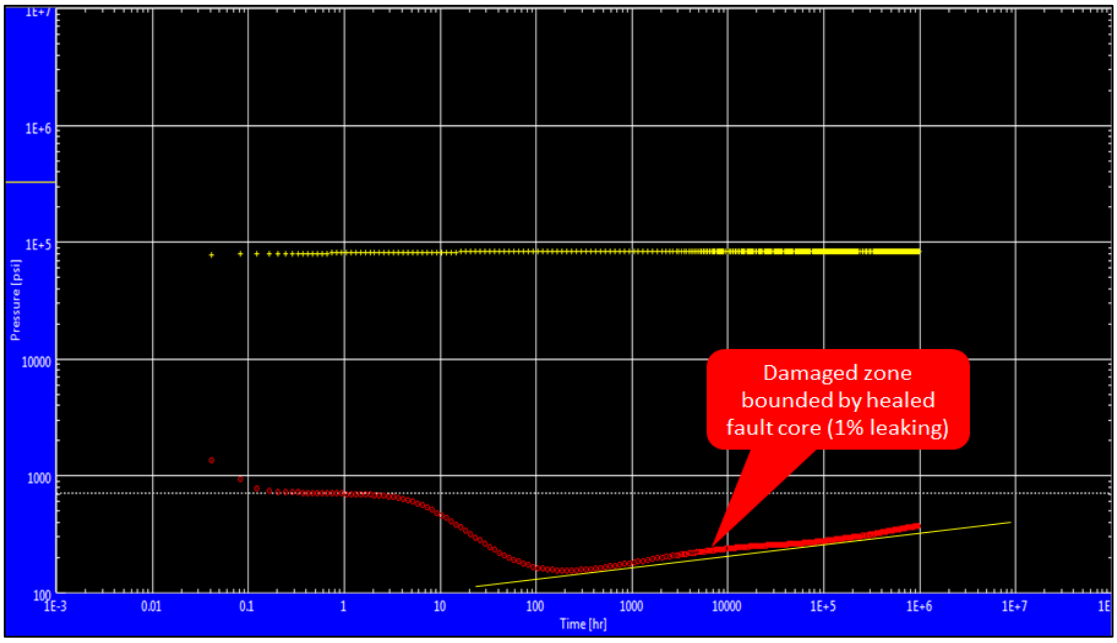

Figure 105: Derivative plot reflecting effect of a 1% leakage factor on flow profile.

Earlier, Corbett et al. (2005) highlighted that this could also occur due to the short restriction in flow that represents depletion of the high permeability zones and the delay in recharging from other patches away from the well, i.e. the "geochoke" response. They have shown a pronounced, humped, middle time region in a well test build-up from a field example, Figure 106.

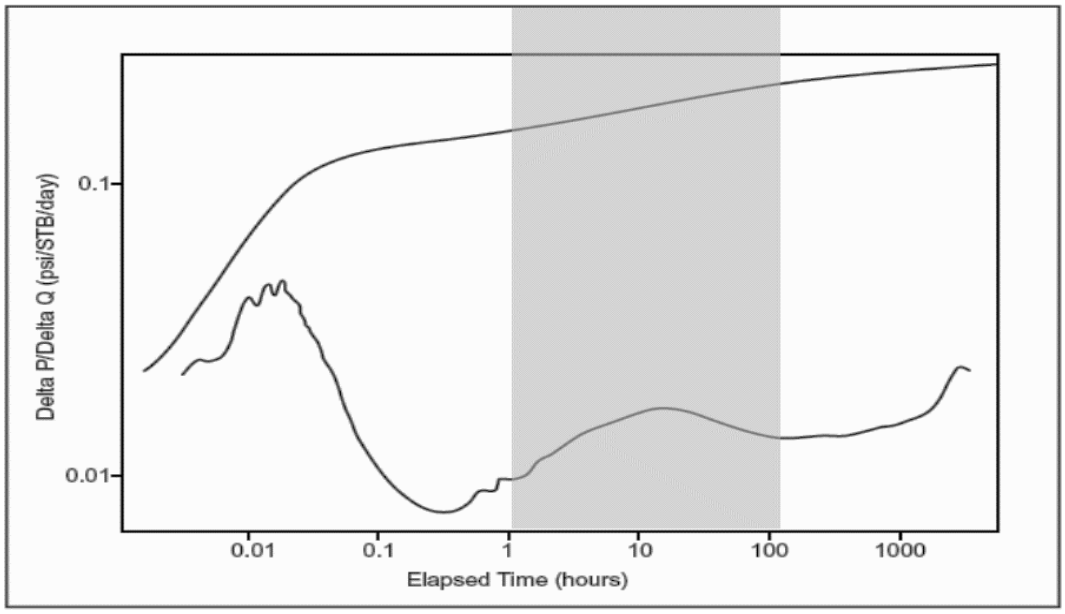

Figure 106: Field example from a braided fluvial reservoir in a North African fluvial reservoir example (after Corbett et al., 2005).

Non-Darcy flow systems

This work can be extended to include the application of the non-Darcy flow systems, or in general terms, inertial effect, in the developed formulae. It can be accomplished by solving for the **effective fracture conductivity** rather than the **absolute fracture conductivity**, similar to the approach by Mahdiyar et al. (2011) discussed earlier in the literature review, section (2.2)

Main Program

Available to Heriot-Watt University, Institute of Petroleum Engineering:

Professor, Mahmoud Jamiolahmady

(Jami.Ahmady@pet.hw.ac.uk)

REFERENCES

Allan, U. S. (1989). Model for hydrocarbon migration and entrapment within faulted structures. AAPG Bulletin 73(7): 803-811.

Althawad, F. M., A. Al-Shahri, A. Al-Gattan and K. Al-Hawas (2000). Optimizing Horizontal Well Placement in the Faulted Ghawar Field by Integrating Pressure Transient and 3D Seismic. Presented at SPE Annual Technical Conference and Exhibition, 1–4 October, Dallas, Texas. SPE 62986.

Althawad, F. M., S. Bin-Akresh and R. Al-Obaid (2001). Characterisation of Fractures/Faults Network from Well Tests; Synergistic Approach. Prepared for presention at SPE Annual Technical Conference and Exhibition, 30 September–3 October, New Orleans, Louisiana. SPE 71578-MS.

Althawad, F. M. and M. Jamiolahmady (2014). A Novel Semi-Analytical Solution for Transient Pressure Data Interpretation of a Fractured Well in an Asymmetric Reservoir. Presented at the International Petroleum Technology Conference, Kuala Lumpur, Malaysia, 10-12 December. IPTC 17785-MS.

Ambastha, A., P. McLeroy and A. Grader (1989). Effects of a partially communicating fault in a composite reservoir on transient pressure testing. Journal Paper, Formation Evaluation 4(02): 210-218. SPE 16764-PA.

Antonellini, M. and A. Aydin (1994). Effect of faulting on fluid flow in porous sandstones: petrophysical properties. Journal Paper, AAPG Bulletin 78(3): 355-377. SPE 21045-PA.

Bilhartz Jr, H. and H. J. Ramey Jr (1977). The combined effects of storage, skin, and partial penetration on well test analysis. Prepared for presentation at SPE Annual Fall Technical Conference and Exhibition, Society of Petroleum Engineers. SPE 6753-MS.

Bixel, H., B. Larkin and H. Van Poollen (1963). Effect of linear discontinuities on pressure build-up and drawdown behavior. Journal of Petroleum Technology 15(08): 885-895.

Bourdet, D. (2002). Well Test Analysis: the Use Of Advanced Interpretation Models, Handbook Of Petroleum Exploration & Production. Vol 3, Elsevier.

Bourdet, D., J. Ayoub and Y. Pirard (1989). Use of pressure derivative in well test interpretation. SPE Formation Evaluation 4(02): 293-302. SPE 12777-PA

Bourdet, D., T. Whittle, A. Douglas and Y. Pirard (1983). A new set of type curves simplifies well test analysis. World Oil 196(6): 95-106.

Boussila, A., D. Tiab and J. Owayed (2003). Pressure behavior of well near a leaky boundary in heterogeneous reservoirs. SPE Production and Operations Symposium, Society of Petroleum Engineers. SPE 80911-MS.

Bouvier, J., C. Kaars-Sijpesteijn, D. Kluesner, C. Onyejekwe and R. Van der Pal (1989). Three-dimensional seismic interpretation and fault sealing investigations, Nun River Field, Nigeria. AAPG Bulletin 73(11): 1397-1414.

Bruce, W. (1943). An electrical device for analyzing oil-reservoir behavior. paper SPE-943112-G. Transactions of the AIME 151(01): 112-124.

Caine, J. S., J. P. Evans and C. B. Forster (1996). Fault zone architecture and permeability structure. Geology 24(11): 1025-1028.

Cinco-Ley, H. (1981). Transient pressure analysis for fractured wells. Journal of Petroleum Technology 33(09): 1,749-741,766. SPE 7490-PA.

Cinco, L., V. Samaniego and A. Dominguez (1978). Transient pressure behavior for a well with a finite-conductivity vertical fracture. Society of Petroleum Engineers Journal 18(04): 253-264. SPE 6014.

Cooper, H. H. and C. Jacob (1946). A generalized graphical method for evaluating formation constants and summarizing well-field history. Eos, Transactions American Geophysical Union 27(4): 526-534.

Corbett, P. W., Y. Ellabad, J. I. K. Egert and S.-Y. Zheng (2005). The geochoke well test response in a catalogue of systematic geotype curves. SPE Europec/EAGE Annual Conference, Society of Petroleum Engineers. SPE-93992-MS.

Darcy, H. P. G. (1856). Dètermination des lois d'ècoulement de l'eau à travers le sable.

Dyes, A., C. Kemp and B. Caudle (1958). Effect of fractures on sweep-out pattern. SPE 1071-G. SPE-1071-G.

Earlougher, R. C. (1977). Advances in well test analysis. AIME, Henry L. Doherty series, Monograph 5.

Ecrin Software Ver. 4.30.08 (2012). Sophia Antipolis, France, Kappa Engineering.

Evans, J. P., C. B. Forster and J. V. Goddard (1997). Permeability of fault-related rocks, and implications for hydraulic structure of fault zones. Journal of Structural Geology 19(11): 1393-1404, Elsevier.

Gibson, R. G. (1994). Fault-zone seals in siliciclastic strata of the Columbus Basin, offshore Trinidad. AAPG Bulletin 78(9): 1372-1385.

Grattan-Guinness, I. and J. B. J. Fourier (1972). Joseph Fourier, 1768-1830; A survey of his life and work, based on a critical edition of his monograph on the propagation of heat. Presented to the Institut de France in 1807, MIT Press.

Gringarten, A. C. (1987). Type-curve analysis: what it can and cannot do. Journal of Petroleum Technology 39(01): 11-13. JPT SPE Journal Paper - 2015.

Gringarten, A. C., H. J. Ramey Jr and R. Raghavan (1974). Unsteady-state pressure distributions created by a well with a single infinite-conductivity vertical fracture. Society of Petroleum Engineers Journal 14(04): 347-360. SPE 4051.

Guppy, K. H., H. Cinco-Ley and H. Ramey Jr (1982a). Non-Darcy flow in wells with finite-conductivity vertical fractures. Society of Petroleum Engineers Journal 22(05): 681-698. SPE 8281-PA.

Guppy, K. H., H. Cinco-Ley and H. Ramey Jr (1982b). Pressure buildup analysis of fractured wells producing at high flow rates. Journal of Petroleum Technology 34(11): 2,656-652,666. SPE 10178-PA.

Hamdi, H., P. Reulland, P. Bergey and P. W. M. Corbett (2014). Using geological well testing in the improved selection of appropriate reservoir models. Petroleum Geoscience 20(4): 353-368.

Harding, T. and A. Tuminas (1988). Interpretation of footwall (lowside) fault traps sealed by reverse faults and convergent wrench faults. AAPG Bulletin 72(6): 738-757.

Horner, D. (1951). Pressure build-up in wells. 3rd World Petroleum Congress, 28 May-6 June, the Hague, the Netherlands. WPC-4135.

Houze, O., D. Viturat and O. Fjaere (2008). Dynamic Flow Analysis: The Theory and Practice of Pressure Transient and Production Analysis & the Use of Data from Permanent Downhole Gauges. France, KAPPA. v4. 10.01.

Houze, O. P., R. N. Horne and H. J. Ramey Jr (1988). Pressure-transient response of an infinite-conductivity vertical fracture in a reservoir with double-porosity behavior. SPE Formation Evaluation 3(03): 510-518. SPE 12778-PA.

Huang, H. and J. A. Ayoub (2007). Modeling non-Darcy flow and perforation convergence for vertically fractured wells. European Formation Damage Conference, Society of Petroleum Engineers, Scheveningen, The Netherlands, 30 May-1 June. SPE 107853-MS.

Issaka, M. and A. Ambastha (1999). A generalized pressure derivative analysis for composite reservoirs. Journal of Canadian Petroleum Technology 38(13).

Jackson, M., J. Percival, P. Mostaghimi, B. Tollit, D. Pavlidis, C. Pain, J. Gomes, A. H. Elsheikh, P. Salinas and A. Muggeridge (2015). Reservoir modeling for flow simulation by use of surfaces, adaptive unstructured meshes, and an overlapping-control-volume finite-element method. SPE Reservoir Evaluation & Engineering 18(02): 115-132.

Jacob, C. (1940). On the flow of water in an elastic artesian aquifer. Eos, Transactions American Geophysical Union 21(2): 574-586.

Jacob, C. and H. Cooper Jr (1946). A generalized graphical method for evaluating formation constants and summarizing well field history, Am. Geophys. Union Trans 27: 526-534.

Jelmert, T. (1993). Theory and application of polynomial type curves. Low Permeability Reservoirs Symposium, 26-28 April, Denver, Colorado. SPE 25876-MS.

Kamal, M. M. (2008). Transient well testing, SPE Monograph Series, vol. 23. Society of Petroleum Engineers, Richardson, TX.

Khan, N. A., A. Ara, A. Yildirim and E. Yuluklu (2010). Approximate solution of Helmholtz equation by differential transform method. World Applied Sciences Journal 11(12): 1509-1511, IDOSI Publications. ISSN 1818-4952.

Knipe, R. (1992). Faulting processes and fault seal. Structural and tectonic modelling and its application to petroleum geology: 325-342. Edited by R.M. Larsen, H. Brekke, B.T. Larsen, E. Talleraas. Elsevier.

Kucuk, F. and L. Ayestaran (1985). Analysis of simultaneously measured pressure and sandface flow rate in transient well testing (includes associated papers 13937 and 14693). Journal of Petroleum technology 37(02): 323-334. SPE 12177-PA.

Landa, J., M. Kamal, C. Jenkins and R. Horne (1996). Reservoir Characterisation Constrained to Well Test Data: A Field Example. SPE Annual Technical Conference and Exhibition, Society of Petroleum Engineers. SPE 36511-MS.

Lee, John (1982). Well Testing. SPE Textbook Series. Society of Petroleum Engineers, Richardson, TX.

Lorenz, J. C., N. R. Warpinski and L. W. Teufel (1996). Natural fracture characteristics and effects. Society of Exploration Geophysicists. The Leading Edge 15(8): 909-911.

Maghsood, A. and H. Cinco-Ley (1995). Pressure-transient behavior in a reservoir with a finite-conductivity fault. SPE Formation Evaluation 10(01): 26-32. SPE-24704-PA.

Mahdiyar, H., M. Jamiolahmady and M. Sohrabi (2011). Improved Darcy and non-Darcy flow formulations around hydraulically fractured wells. Journal of Petroleum Science and Engineering 78(1): 149-159.

Marquis de Laplace, P. S. (1820). Théorie analytique des probabilités, V. Courcier.

Matthews, C. S. and D. G. Russell (1967). Pressure buildup and flow tests in wells. Society of Petroleum Engineers of AIME, Dallas, TX.

McGuire, W. and V. Sikora (1960). The effect of vertical fractures on well productivity. Journal of Petroleum Technology 12(10): 72-74. SPE 1618-G.

McKinley, R. (1971). Wellbore transmissibility from afterflow-dominated pressure buildup data. Journal of Petroleum Technology 23(07): 863-872. SPE 2416-PA.

Meehan, D. N. (1989). Hydraulically fractured wells in heterogeneous reservoirs: Interaction, interference, and optimization, Stanford University, CA (USA), thesis (Ph. D.)

Meyer, B. R. and R. H. Jacot (2005). Pseudosteady-state analysis of finite conductivity vertical fractures. SPE Annual Technical Conference and Exhibition, Society of Petroleum Engineers. SPE 95941-MS.

Nelson, R. (2001). Geologic analysis of naturally fractured reservoirs, Gulf Professional Publishing.

Pirard, Y. and A. Bocock (1986). Pressure derivative enhances use of type curves for the analysis of well tests. International Meeting on Petroleum Engineering, Society of Petroleum Engineers. SPE 14101-MS.

Pittman, E. D. (1981). Effect of fault-related granulation on porosity and permeability of quartz sandstones, Simpson Group (Ordovician), Oklahoma. AAPG Bulletin 65(11): 2381-2387.

Raghavan, R. (1977). Pressure behavior of wells intercepting fractures. SPE 11030-PA.

Rahman, N., M. D. Miller and L. Mattar (2003). Analytical solution to the transient-flow problems for a well located near a finite-conductivity fault in composite reservoirs. SPE Annual Technical Conference and Exhibition, Society of Petroleum Engineers, 5-8 October, Denver, Colorado. SPE 84295-MS.

Ramey Jr, H. J. (1976). Practical use of modern well test analysis. SPE California Regional Meeting, Society of Petroleum Engineers, 7-9 April, Long Beach, California. SPE 5878-MS.

Sagawa, A., P. W. Corbett and D. R. Davies (2000). Pressure transient analysis of reservoirs with a high permeability lens intersected by the Wellbore. Journal of Petroleum Science and Engineering 27(3): 165-177.

Schlische, R. W. (1995). Geometry and origin of fault-related folds in extensional settings. AAPG Bulletin 79(11): 1661-1678.

Settari, A., A. Bale, R. Bachman and V. Floisand (2002). General correlation for the effect of non-Darcy flow on productivity of fractured wells. SPE Gas Technology Symposium, Society of Petroleum Engineers. SPE 75715-MS.

Smith, L., C. Forster and J. P. Evans (1990). Interaction between fault zones, fluid flow and heat transfer at the basin scale, in: Hydrogeology of low Permeability environments, International Association of Hydrological Sciences selected papers in Hydrogeology, v. 2, p. 41-67.

Smith, M., A. Bale, L. Britt, L. Cunningham, J. Jones, H. Klein and R. Wiley (2004). An investigation of non-Darcy flow effects on hydraulic fractured oil and gas well performance. SPE Annual Technical Conference and Exhibition, Society of Petroleum Engineers, 26-29 September, Houston, Texas. SPE 90864-MS.

Stewart, G. and A. Gupta (1984). The interpretation of interference tests in a reservoir with sealing and partially communicating faults. European Petroleum Conference, Society of Petroleum Engineers, 22-25 October, London, United Kingdom. SPE12967-MS.

Suri, Y., A. Dutt and A. Mandal (2014). A comparative analysis of offshore and onshore fields using derivative and second derivative plot (without type curves). Petroleum Science and Technology 32(5): 535-542.

Theis, C. V. (1935). The relation between the lowering of the piezometric surface and the rate and duration of discharge of a well using ground water storage. US Department of the Interior, Geological Survey, Water Resources Division, Ground Water Branch Washington, DC.

Villinger, H. (1985). Solving cylindrical geothermal problems using the Gaver-Stehfest inverse Laplace transform. Geophysics 50(10): 1581-1587.

Voronoï, G. (1908). Nouvelles applications des paramètres continus à la théorie des formes quadratiques. Deuxième mémoire. Recherches sur les parallélloèdres primitifs. Journal Für Die Reine und Angewandte Mathematik 134: 198-287.

Warren, J. and P. J. Root (1963). The behavior of naturally fractured reservoirs. Society of Petroleum Engineers Journal 3(03): 245-255. SPE 426-PA.

Wattenbarger, R. A., A. H. El-Banbi, M. E. Villegas and J. B. Maggard (1998). Production analysis of linear flow into fractured tight gas wells. SPE rocky mountain regional/low-permeability reservoirs symposium, Society of Petroleum Engineers, 5-8 April, Denver, Colorado. SPE 39931-MS.

Wenzel, L. K. and V. C. Fishel (1942). Methods for determining permeability of water-bearing materials, with special reference to discharging-well methods, with a section on direct laboratory methods and bibliography on permeability and laminar flow. US Govt. print. off. Series number 887.

Yaxley, L. (1987). Effect of a partially communicating fault on transient pressure behavior. SPE Formation Evaluation 2(04): 590-598. SPE 14311-PA.